Spring 2006

Boundary Interference Assessment and Correction for Open Jet Wind Tunnels Using Panel Methods

Wael Ahmed Mokhtar
Old Dominion University

BOUNDARY INTERFERENCE ASSESSMENT AND CORRECTION FOR OPEN JET WIND TUNNELS USING PANEL METHODS

by

Wael Ahmed Mokhtar
B.S. July 1994, M.S. May 2001, Alexandria University, Egypt

A Dissertation Submitted to the Faculty of Engineering
Old Dominion University in Partial Fulfillment of the
Requirement for Degree of

DOCTOR OF PHILOSOPHY

AEROSPACE ENGINEERING

OLD DOMINION UNIVERSITY
May 2006

Approved by:

Colin P. Britcher (Director)

Osama A. Kandil (Member)

Drew Landman (Member)

ABSTRACT

BOUNDARY INTERFERENCE ASSESSMENT AND CORRECTION
FOR OPEN JET WIND TUNNELS USING PANEL METHODS

Wael Ahmed Mokhtar
Old Dominion University, 2006
Director: Dr. Colin P. Britcher

The presence of nearby boundaries in a wind tunnel can lead to aerodynamic measurements on a model in the wind tunnel that differ from those that would be made when the boundaries of the moving fluid were infinitely far away. The differences, referred to as boundary interference or wall interference, can be quite large, such as when testing aircraft models developing high lift forces, or whose wingspan is a large fraction of the wind tunnel width, or high drag models whose frontal area is a large fraction of the tunnel cross section. Correction techniques for closed test section (solid walled) wind tunnels are fairly well developed, but relatively little recent work has addressed the case of open jet tunnels specifically for aeronautical applications.

A method to assess the boundary interferences for open jet test sections is introduced. The main objective is to overcome some of the limitations in the classical and currently used methods for aeronautical and automotive wind tunnels, particularly where the levels of interference are large and distortion of the jet boundary becomes significant. The starting point is to take advantage of two well-developed approaches used in closed wall test sections, namely the boundary measurement approach and adaptive wall wind tunnels. A low-order panel code is developed because it offers a relatively efficient approach from the computational point of view, within the required accuracy. It also gives the method more flexibility to deal with more complex model geometries and test section cross sections.

The method is first compared to the method of images. Several lifting and non-lifting model representations are used for both two- and three-dimensional studies. Then the method is applied to results of a test of a full-scale Wright Flyer replica inside the Langley Full Scale Tunnel. The study is extended to include the effect of model representation and the test section boundaries (closed, open and 3/4 open) on the interference. The method is also used during a test of full scale NASCAR inside the NASA Langley Research Center 14- by 22- Foot Subsonic Wind Tunnel. This part includes the effects of test section length and the inclusion of the nozzle in the solution on the predicted boundary interference. Finally, a test is conducted at the $1/15^{th}$ scale Langley Full Scale Tunnel using a generic automotive model ("Davis" model) to validate the prediction of the boundary distortion and to investigate the effect of the collector.

The developed method showed reliability when compared to the classical method of images. Through the studied wind tunnel tests, the method showed enough flexibility to be applied to solve both aeronautical and automotive models and several test section configurations with a reasonable computational efficiency.

Co-Directors of Advisory Committee: Dr. Osama A. Kandil

Dr. Drew Landman

ACKNOWLEDGEMENTS

A journey is easier when you travel together. Interdependence is certainly more valuable than independence. This dissertation is the result of more than four and half years of work whereby I have been accompanied and supported by many people. It is a pleasant aspect that I have now the opportunity to express my gratitude for all of them.

The first person I would like to thank is my faculty advisor Professor Colin Britcher, Chair of the Aerospace Engineering Department. His overly enthusiasm and integral view on research and his mission for providing 'only high-quality work and not less', have made a deep impression on me. I owe him lots of gratitude for having me shown this way of research. He could not even realize how much I have learned from him. Besides of being an excellent supervisor, Dr. Britcher was as close as a relative and a good friend to me. I am really glad that I have come to know him in my life.

I would like to thank Professor Osama Kandil who kept an eye on the progress of my work and always was available when I needed his advises. I have been working with him since I jointed Old Dominion University in 2001. During these years I have known Dr. Kandil as a sympathetic and principle-centered person. I really leaned a lot from him professionally and personally.

I am very grateful to Professor Drew Landman for introducing me to the wind tunnel testing. Also he was the center person in most of the wind tunnel tests presented in this dissertation. I am also very grateful to all the faculty, students, and staff who participated in these wind tunnel tests inside the Langley Full Scale Tunnel and the NASA Langley 14 by 22 foot subsonic wind tunnel.

I will also give a special thanks to Professor Kamel Elshorbagui, Mechanical Engineering Department, Alexandria University, for introducing me to experimental fluid mechanics.

I feel a deep sense of gratitude for my father and mother who formed part of my vision and taught me the good things that really matter in life. The happy memory of my father still provides a persistent inspiration for my journey in this life.

Last but not least, I am very grateful for my wife, for her support and patience during the PhD period. One of the best experiences that we lived through in this period was the birth of our son Omar, who provided an additional and joyful dimension to our life mission.

TABLE OF CONTENTS

LIST OF FIGURES

NOMENCLATURE

A^* = nozzle reference area.
A_C = collector area.
A_M = model frontal area.
A_N = nozzle exit area.
B = test section width.
b = wing span.
C = test section area.
C_L = lift coefficient.
C_D = drag coefficient.
$C_{D\,m}$ = measured drag coefficient.
$C_{D\,c}$ = corrected drag coefficient.
C_p = pressure coefficient.
c = chord length.
G = Green's function.
G = Glauert factor[1].
H = test section height.
L = test section length.
l or L_M = model length.
M = Mach number.
n = unit vector normal to the test section boundaries.
p = static pressure.
q = dynamic pressure.
R_C = equivalent duplex collector radius.
R_N = equivalent duplex nozzle radius.
r = position vector.
S = wing reference area.
s = unit vector tangent to the test section boundaries.
t = model equivalent diameter.
u = velocity component in x direction.
U^* = reference upstream velocity.
U_∞ = free stream velocity / nozzle exit average velocity.
U_N = nozzle exit average velocity.
V_M = model volume.
v = velocity component in y direction.
w = velocity component in z direction.
x = streamwise Cartesian coordinate.
x_M = distance from the nozzle exit to the model center.
x_S = distance from the nozzle exit to the point source.
y = spanwise Cartesian coordinate.
z = vertical Cartesian coordinate.
ΔH = boundary deformation.
$\Delta\alpha$ = angle of attack correction factor, $\Delta\alpha = \frac{w_{int}}{U_\infty}$.
β = Prandtl-Glauert compressible factor, $\beta = (1-M^2)^{1/2}$.

γ = vortex strength in 2D, $\gamma = 1/2\ U_\infty\ c\ C_L$.
Γ = vortex strength in 3D, $\gamma = 1/4\ U_\infty\ S\ C_L$.
δ = upwash factor, $\delta = \frac{w_{int}}{U_\infty}\frac{C}{SC_L}$.
ε = blockage factor, $\varepsilon = \frac{u_{int}}{U_\infty}$.
ε_C = blockage factor due to collector effect.
ε_N = blockage factor due to nozzle effect.
ε_S = blockage factor due to jet expansion.
ε_W = blockage factor due to wake effect.

λ = body shape factor.
μ = doublet strength
φ = potential function.
η = running coordinate in x direction.
θ = deformed boundary slope.
ξ = running coordinate in y direction.
σ = source panel strength.
τ = tunnel shape factor.

Subscript:
c = corrected.
D = Dirichlet boundary condition.
i or int = interference component.
f = free-air condition.
g = global coordinate system.
m = model component.
N = Neumann boundary condition.
A_M = model frontal area.
p = panel coordinate system.
w = wall component.

CHAPTER I

I. INTRODUCTION

The early wind tunnel designed by Prandtl in 1919 for his aerodynamic works had an open test section. It has the advantage of free accessibility to the model in the test section and easy installation of both the model and measuring equipment. Nowadays, it is often preferred to test large models inside open rather than closed test sections because the latter may experience severe flow field disturbance or even flow breakdown for large relative model sizes. Further, open test sections are still widely used in automotive wind tunnels to a much greater extent than aeronautical. Some reasons are that for some automotive testing the focus is not external aerodynamics of the tested vehicle (rather internal aerodynamics, such as cooling systems for example) and the blockage ratio may be as high as 100%. The open jet is more forgiving for such large relative model sizes. Some large full-scale open test section wind tunnels are still in operation for both aeronautical and automotive testing, such as the Langley Full Scale Tunnel (LFST) operated by Old Dominion University. It is also important to mention that for some specific applications, such as aero-acoustic testing, the open test section is still superior.

The presence of nearby boundaries in a wind tunnel test section - whether the boundaries are in the form of solid walls or a shear layer around a free jet - can lead to aerodynamic measurements on a model in the wind tunnel that differ from those that would be made when the boundaries of the moving fluid were infinitely far away. The differences, referred to as boundary interference or wall interference, can be quite large, such as when testing aircraft models developing high lift forces, or whose wingspan is a large fraction of the wind tunnel width (more than 50%), or high drag models whose frontal area is a large fraction of the tunnel cross section (more than 10% for low subsonic test conditions). Correction techniques for closed test section (solid walled) wind tunnels are fairly well developed, but relatively little recent work has addressed the case of open jet tunnels specifically for aeronautical applications. The following sections give an overview of some of the classical and contemporary methods used for closed and open test section boundary corrections.

1.1 Method of images

Concerns about test section boundary interference started as early as the 1920s when Glauert introduced the method of images to obtain boundary interference of a rectangular closed test section.[1] In the method of images, the model is represented by simple singularities and the boundaries are simulated by an infinite array of images of the model singularities with appropriate strength and sign for solid or open boundaries. Later, Theodorsen used the method of images to obtain the boundary interference for several test section configurations, including three, two, one, and no solid boundaries.[2] He noticed that open and closed boundaries tend to have similar interference effects, but with opposite signs. So he reported that an interference free test section might be achieved by a combination of open and closed boundaries. Krynytzky and Ewald listed the assumptions of the classical wall interference theory as follows[3]:

1. Linear potential flow
2. Perturbation flow at the tunnel boundaries
3. Small model relative to the tunnel
4. Constant tunnel cross-sectional area extending infinitely far upstream and downstream of the model

Following the same reference,[3] the potential Φ is assumed to be expressible as the superposition of a uniform onset stream, the model potential, and the wall potential.

$$\Phi(x,y,z) = -U_\infty x + \varphi_m(x,y,z) + \varphi_w(x,y,z) \quad (1)$$

Where x, y and z are the Cartesian coordinates, U_∞ is the free stream velocity and the subscripts m and w refer to the model and the wall respectively. With the assumption of a small model and perturbation velocities at the boundaries, only the far-field flow around the model is represented. The far-field influence of the model can be summarized as follows: model shape and volume, which causes a displacement of streamlines around the model, model lift force, which causes a redirection of the stream momentum, and model drag, which results in an outward displacement of streamlines around the viscous wake. These three effects are presented in the method of images using elementary analytical singularities such as a doublet, point source, horseshoe vortex, etc. Despite the limitations the method of images imposes on the relative model size and on the geometry of the

model and the test section, it is still a valuable reference to validate any new approach. Figure (1-1) shows an example of using the method of images to correct data obtained during a test of a wing inside a rectangular test section. The wing is represented by a single horseshoe vortex and interference of the test section boundaries is simulated using an array of images. The summation of the velocity induced by these singularities represents the boundary interference. Further details about the method of images and the different boundary conditions used for open and closed test sections are presented in Chapter (3).

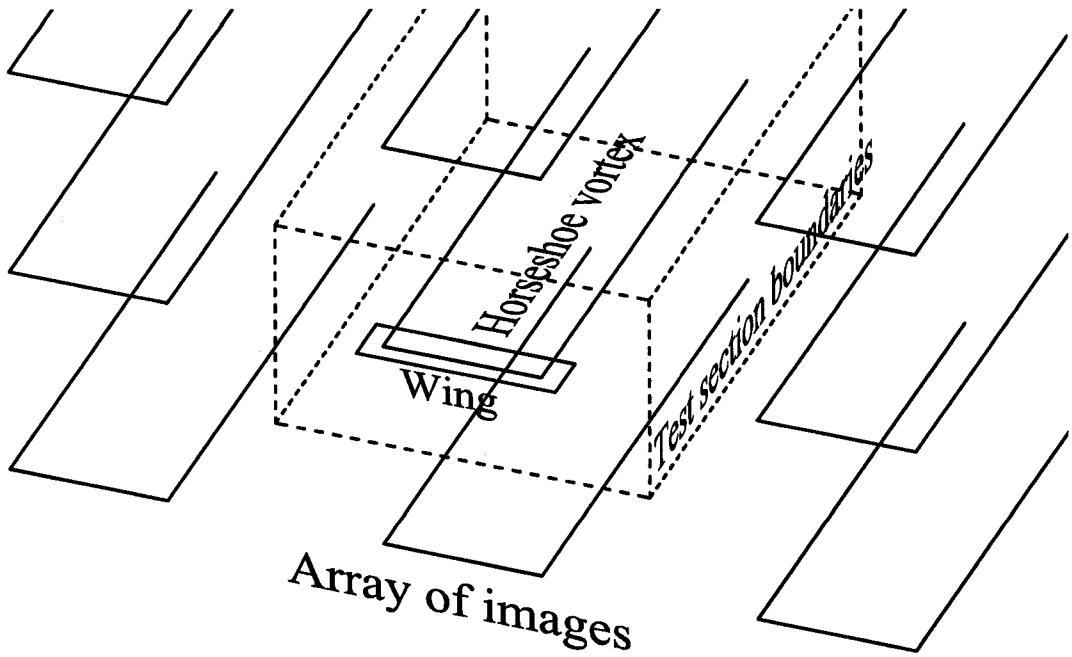

Figure (1-1) Sketch illustrating the method of images.

1.2 Boundary measurement methods

The calculation of wall interference using measurements of the wall pressures in closed-wall test sections were proposed in the early 1940's. Ashill reported that reliable bases for calculating wind tunnel wall interference corrections in general cases were not developed until the 1970s[4,5], namely the boundary measurement methods. In these techniques either one or two variables are measured on the test section walls to obtain the wall interference.

Hackett developed the single-variable measurement method by measuring static pressure on the walls at limited number of points and obtaining strengths of a small number of singularities representing the model.[6,7] Then the wall interference is obtained using the images of model singularities in a way similar to the method of images. Figure (1-2) shows an example of one of the test sections (NASA Langley Research Center 14 by 22 Foot Subsonic Wind Tunnel) that use the wall signature method for assessment of wall corrections. Twelve rows of pressure taps are distributed over the sidewalls and the ceiling. The photo also shows a full-scale NASCAR model, which was subjected to a back-to-back test inside closed and open test sections. The details of this are discussed in Chapter (5) of the present dissertation[8]. A typical measured wall signature in shown is Figure (1-3).

The major disadvantage of the single-variable method, as developed by Hackett, is that it uses a small number of elementary singularities to represent the tested model. This adds some difficulties in applying it to models with complex geometries especially those of large sizes. On the other hand, the two-variable method derives the interference directly from the measurements taken at the walls without using any information about the model geometry; however model information is still needed to apply the corrections.[5]

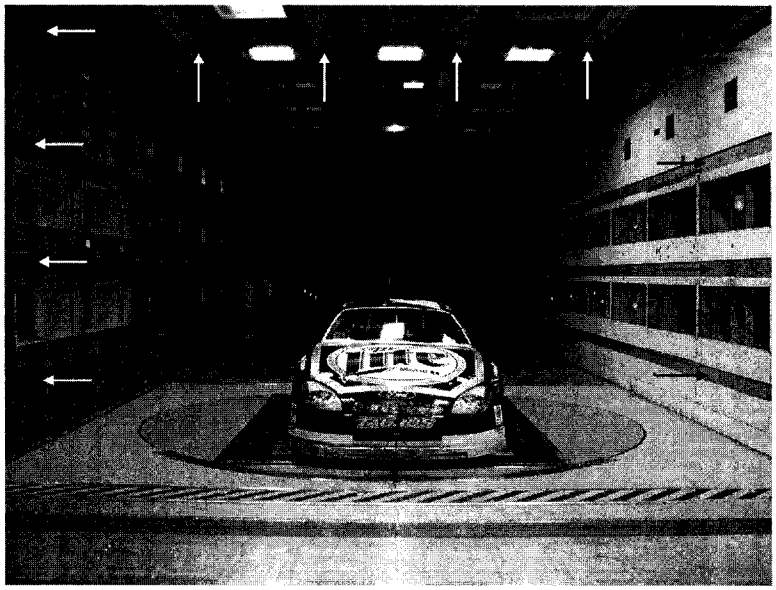

Figure (1-2) The test section of the NASA Langley Research Center 14 by 22 Foot Subsonic Wind Tunnel during a test of a full scale NASCAR model.
(Arrows show the rows of pressure taps).

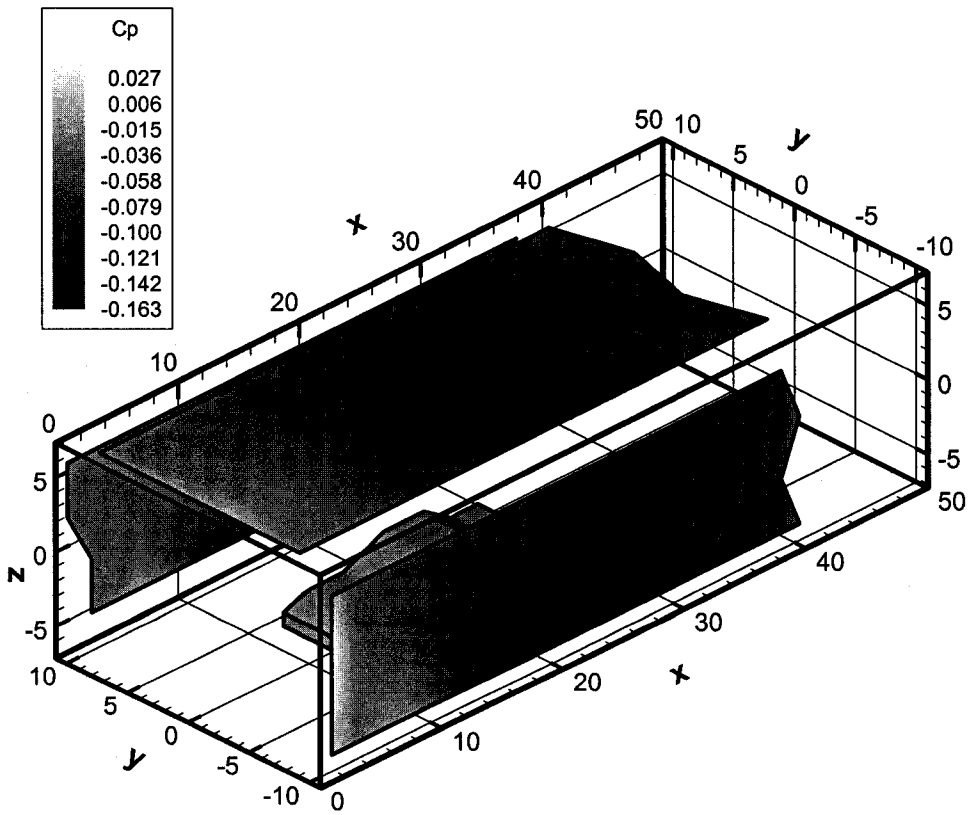

Figure (1-3) A typical wall signature during the test of a full scale NASCAR inside the NASA Langley Research Center 14 by 22 Foot Subsonic Wind Tunnel [8].

For low subsonic flow conditions, the far field can be well represented by internal singularities, determined from the model geometry and measured loads as reported by Rizk[9]. The assumptions used for both methods, that the normal velocity component is zero on the solid boundary, is equivalent to neglecting the interaction between the inviscid flow field and the wall boundary layer. For each case the validity of this assumption has to be assessed because in some cases where the flow perturbations are large, viscous interaction cannot be ignored. For example, this occurs for flows where shock waves reach the test section wall or when massive separation exists. Further details about the limits of the boundary measurement methods are discussed by Ashill.[4,5]

The boundary measurement methods are also widely used in correcting results from ventilated test sections. Despite the non-linearity of the cross-flow properties and their dependence on the wall boundary layers, the boundary measurement methods which are based on idealized linear boundary conditions have retained a great deal of appeal, as reported by Ashill et al[4]. For the single-variable measurement method, a static pressure plate (rail) mounted on the wall in the direction parallel to the mainstream with instrumented pressure orifices is usually used for two-dimensional test sections. For three-dimensional test sections a pipe replaces the static pressure plate. A second row of orifices is added when the two-variable method is used. There are still some difficulties in making the necessary flow measurements in ventilated test sections and in post-processing them. The boundary measurement methods are also used in correcting slotted wall transonic tunnels, as reported by Iyer et al.[10] Further details about the use of the wall signature methods for ventilated wind tunnels may be found in the work presented by Ulbrich.[11]

Although boundary measurement methods are relatively reliable and accurate, especially for subsonic testing, to the best of the author's knowledge, they are not used for open test sections due to experimental difficulties in detecting the boundaries of the open test section and in measuring the flow properties over them.

1.3 Adaptive wall wind tunnels

Another approach to solve the wall inference problem is to produce an interference free wind tunnel by "streamlining" the walls. This approach is referred to as the adaptive wall wind tunnel. In this section some information about this type of wind tunnel, more specifically the methods used to predict the wall streamlining, are presented as a part of the introduction to the boundary deformation technique employed in the present work for open jet test sections.

Adaptive wall test sections were first introduced in the mid 1930s at the National Physical Laboratory (NPL) in England, as discussed by Wedemeyer et al[12]. Due to the required computational power and the complexity of the operation by manually deforming the walls, interest was soon transferred away from the adaptive wall approach. The technical and operational simplicity of the slotted wall tunnel, which was introduced in the 1940's, may have led to the decision to abandon the adaptive wall approach in the 1950's, as mentioned by Mokry[13]. In the 1970s, as reported by Goodyer[14], adaptive wall techniques re-emerged with substantial advances in the field of automation and computation. In the flexible-walled wind tunnel (the predominant version of adaptive wall wind tunnels) the test section boundaries are mechanically contoured ("streamlined") to have a shape close to the shape of the streamlines that would occur around the same model in free air. The adaptation is done by a control system, which reads the flow properties on the walls, computes wall position, and adapts its geometry, typically by means of jacks. Due to practical limitations, the walls cannot be completely streamlined, particularly in 3D, so small residual corrections may still be necessary. Figure (1-4) shows a sketch of an adaptive wall test section.

Generally speaking, two main approaches are used in predicting the wall adaptation (a third technique is also mentioned later). In the first approach, the interface-matching technique, wall-induced perturbations are used to predict the required deformation and the adaptation is gauged purely from the assessments of the admissibility of the adapted wall boundary conditions. The method presented later in the current work for open jet

tunnels uses the one-step method, which is one of these techniques. In the second approach, the target line technique, the wall-induced perturbations are used in predicting the deformation as in the first approach except that the deformation is gauged by both the boundary conditions on the adaptive walls and the desired minimum interference level along lines passing through the test section. The concept of wall streamlining is well described by Goodyer[15] for 2D applications. A summary of the different methods used for predicting wall adaptation can be found in Erickson[16]. Several updates were then presented by Wolf[17] and Meyer and Nitsche[18]. Wolf and Goodyer[19] present a fully detailed description of the one-step method, the interface matching method used in the present work.

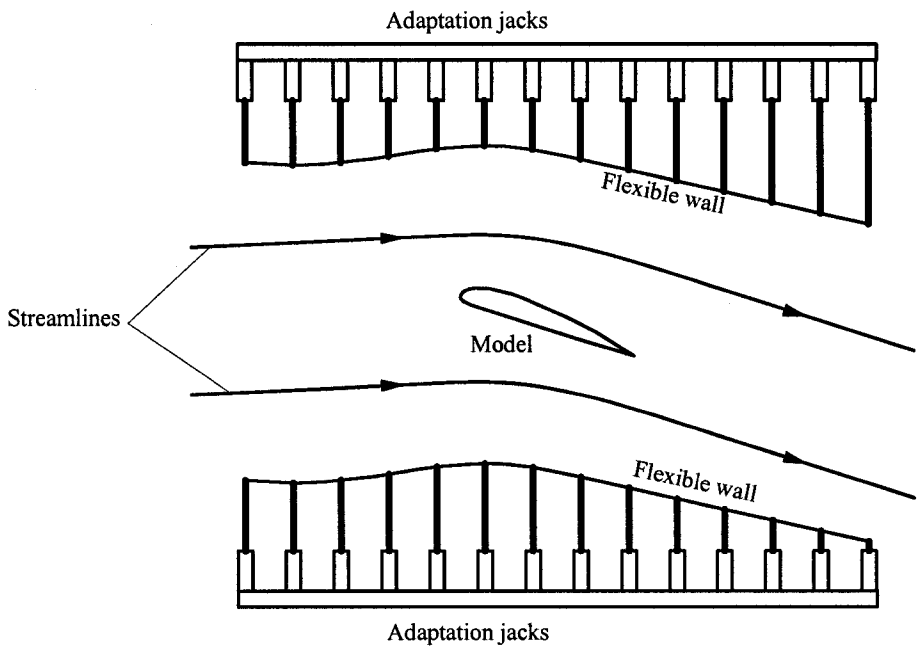

Figure (1-4) Sketch of a flexible wall test section.

The forms of wall adaptation may be categorized into two broad groups. In the first group the profiles of flexible walls are modified to manipulate the flow conditions on the surface of the test section walls. In the second group the flow near to the walls is manipulated by controlling the test section ventilation through fixed walls, as shown in Figure (1-5). The flexible walled test sections have the advantage of well-defined control surfaces and measurements of the boundary conditions are relatively easy, while this is

not the case in ventilated test sections. On the other hand, the finite number of jacks used puts limits on the flexible wall test section accuracy and residual wall interferences sometimes need to be corrected. The unconfined flow conditions are not expected to be precisely attained even in the "full" adapted stages as reported by Mokry[13]. In his work he showed through some examples the assessment and correction of the adaptive wall test section boundary interference using one and two-variable measurements methods.

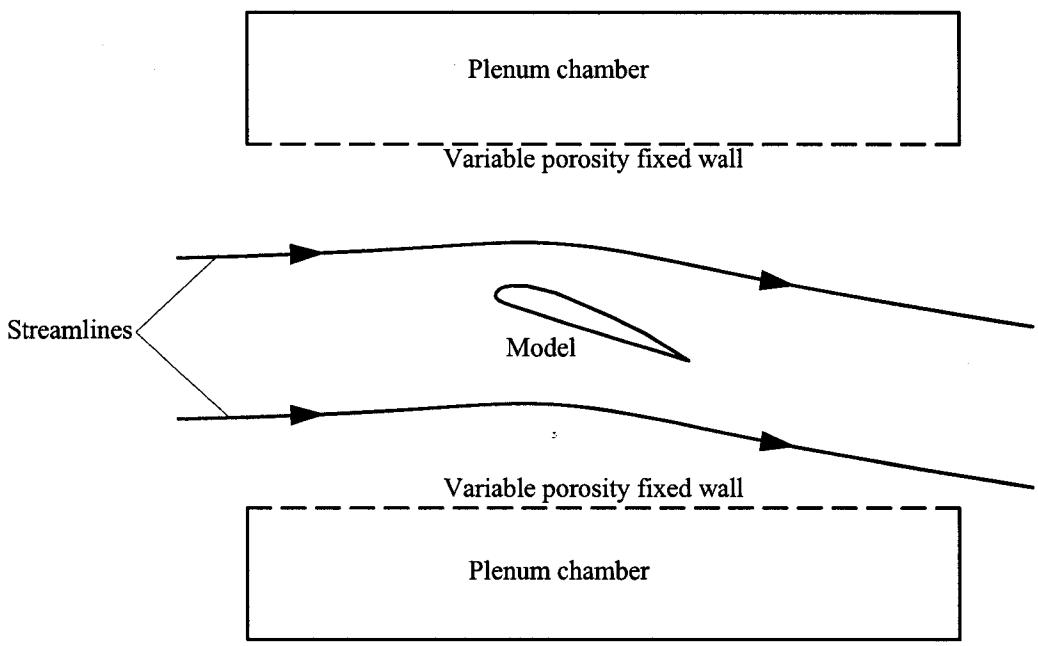

Figure (1-5) Sketch of a ventilated test section.

A third category was recently added to the abovementioned two categories in the mid 1990's, which is referred to as adaptive slotted test sections. It is a combination of flexible wall and the ventilated test sections. Its advantages, as reported by Meyer and Nitsche[18], are a simple mechanical setup compared to the regular adaptive wall tunnel and a low cost of converting existing slotted test sections to a fully 3D adaptation capability. The idea of this method is to use a common adaptation procedure for flexible walls and convert the calculated interference reducing wall shapes to particular slot arrangements. Only procedures that calculate the required wall deflection in a single step can be used for that task. Figure (1-6) shows a sketch of an adaptive slotted wall test section.

In this work, Meyer and Nitche[18] performed a calibration test in the Technical University of Berlin wind tunnel against the existing adaptive wall test using an empty test section and using CAST 7 airfoil. The results of the pressure and flow field measurements showed correlation within the measurement accuracy. Also, a commercial CFD code TASCflow3D is used to study the flow through the slots. Further investigations are still needed for this relatively new method before it can be widely used.

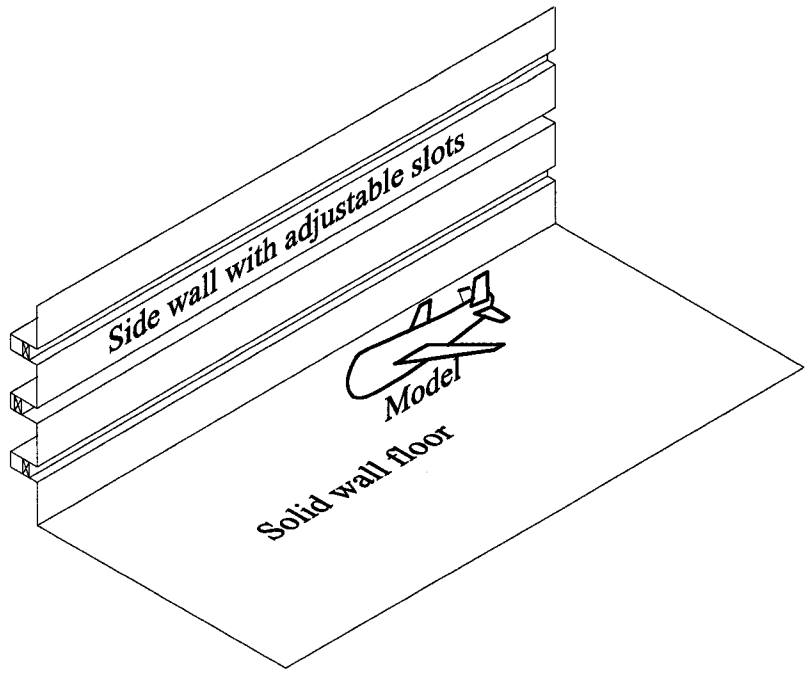

Figure (1-6) Sketch of an adaptive slotted test section.

Several examples of early and recent use of adaptive wall tunnels exist in the literature. A list of the adaptive wind tunnels up till 1990 is presented by Ladson[20]. More recently in Europe, Bottin et al[21] used a Cauchy integral adaptation method, which is an interface-matching technique, in the adaptive wind tunnel at von Karman Institute (VKI). They showed good agreement between their results and the interference free results for the NACA 0012 airfoil section. For the same airfoil section Russo et al[22] presented a comparison between the adaptive wall tunnel and several wall interference methods including the method of images and the boundary measurement methods. They obtained a good agreement at moderate angles of attack between the reference data (interference

free) and the data obtained in both the adaptive wall test and the fixed wall with corrections calculated using the two variable method. The classical correction method of images showed large deviations from the reference data.

Also in the U.S., Mineck[23] presented a comparison between the adaptive wall technique and the classical analytical wall correction method. A common airfoil model (CAST 10-2/DOA 2) was tested in the adaptive-wall test section of the NASA Langley 0.3-Meter Transonic Cryogenic Tunnel (0.3-m TCT) and in the ventilated test section of the National Aeronautical Establishment (NAE) Two-Dimensional High Reynolds Number Facility (HRNF). The TCT test section has four solid walls with flexible top and bottom walls. The one-step method, an interface-matching technique, is used for wall adaptation. The NAE test section has solid sidewalls and the top and the bottom walls are porous. Three sets of data are obtained from the NAE test: uncorrected, corrected for sidewalls only, and corrected for all four walls. The analytical wall correction technique presented by Mokry and Ohman[24] which is based on the Fast Fourier Transforms, is employed in the study. Good agreement between the results was obtained indicating that both the adaptive-wall and the analytical correction techniques do an adequate job correcting for the top- and bottom-wall interference. In China, Huaxing et al[25] presented a study of using the adaptive wall section for half-model testing in the Northwestern Polytechnic University (NPU). They used the target line technique for wall adaptation.

1.4 Panel methods

One of the more recent and promising methods used for wall interference correction in closed test sections is the panel method, using a surface distribution of singularities on the test section boundaries. The panel method relies on the same basic principles as does the method of images. The panel code solves for the strengths of all the singularities by applying the boundary condition at each panel control point. Then the wall panels produce the same incremental flow field as the entire collection of images. Figure (1-7) shows sketches of the panel method and the method of images. One of the advantages of the panel method compared to the method of images is that it enables the analysis of large complex models and arbitrary tunnel cross-sectional shapes. It also offers a fast and computationally efficient tool compared to other numerical methods, which may include generating complex grids and solving the Euler or full Navier-Stokes Equations. Krynytzky and Ewald[3] reported in their closing remarks about panel methods: "The successes of panel methods over wide ranges of sub-critical flow conditions suggests their use not only in routine testing applications within their accepted range of validity, but also as a touchstone against which advanced methods may be tested."

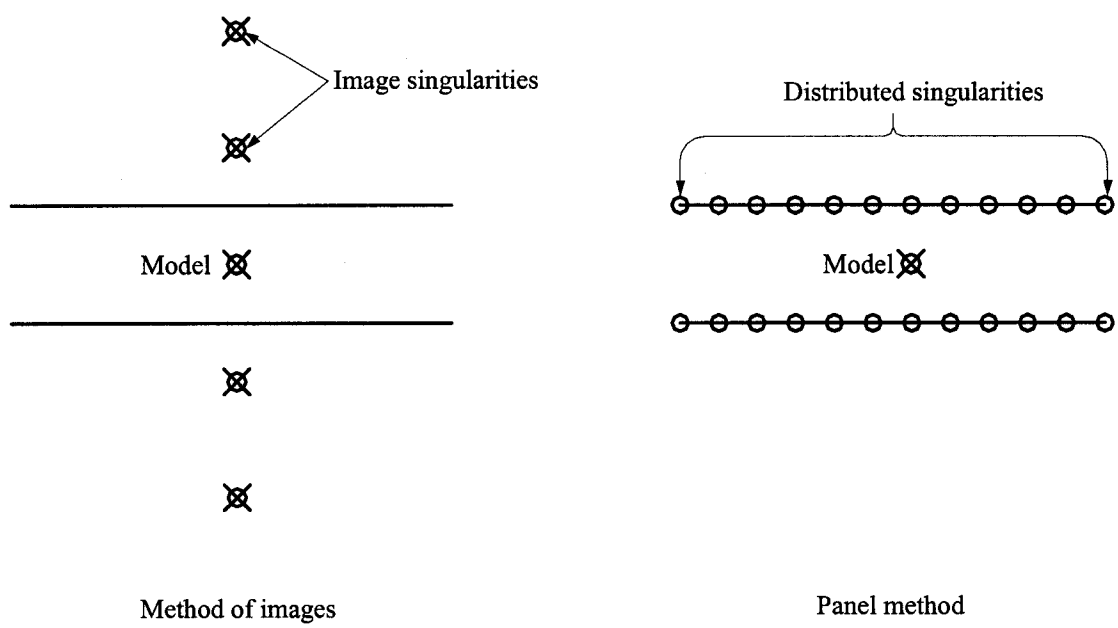

Figure (1-7) Sketches of the method of images and the panel method.

Commonly used singularities include vortex lines for vortex lattice codes, constant strength sources or doublets for simple panel codes, and higher order source or doublet panels for higher order panel codes. Models can be represented by a few singularities with strengths derived from the measured loads if their geometries are simple enough. Alternatively model singularities may be left as unknowns and in this case boundary conditions have to be applied on both the walls and the model panels. Hybrid approaches are possible where part of the model aerodynamics may be specified.

One of the earliest published works was by Joppa.[26] He calculated the upwash interference in closed wall tunnels of arbitrary cross sections by representing the walls using a tubular vortex sheet composed of vortex rings. His study included a uniformly loaded finite span horseshoe vortex at the center of a circular, square and rectangular tunnel. His results indicate that a length of one diameter (for circular tunnels) upstream and downstream of the wing will be accurate enough to represent the tunnel walls.

Later Holt and Hunt [27] presented further details about using panel methods for 2D and 3D closed wall interference correction. Their study indicated that representing the test section as a closed box with solid horizontal floor and ceiling and solid vertical streamwise walls with other vertical faces perpendicular to the flow carrying a uniformly distributed velocity vector into and out of the box does not work. It generates an infinite number of different singularity distributions on these six surfaces able to satisfy the required boundary conditions. They recommended instead the use of a long open-ended tube installed in an external flow field parallel to it. The extension of this tube and the density of the panels around the cross section depend on the form of singularity used to simulate the walls. For example in their study, they employed source panels for a numerical test section eight times root-chord upstream and eleven times root-chord downstream of a delta wing model using 192 surface panels.

Lee[28] used a higher order panel code to study the interference of solid and slotted wall tunnels. The study includes the effect of the finite test section length, the corner fillet, model size and location, and the support. The model tested was a rectangular wing with

aspect ratio 8 and spanned two-thirds of the tunnel width. The singularities used were as follows: doublet panels for the solid part of the tunnel walls and wakes, source panels for the support system including the island, strut and pitch assembly and composite panels with sources and doublets for the lifting wing and the slotted test section walls.

In automotive wind tunnels Mokry[29] used a low-order source panel code for blockage corrections. The study included closed, 3/4 open, and slotted wall test sections. In his work, 759 panels were used for the car model and the test section sidewalls and roof. He reported that the source panel code is suitable for this case because the automobile is a non-lifting body, so keeping a portion of the model surface open simulates the wake displacement and the boundary conditions can be easily implemented. In his closing remarks he indicated that the leakage due to enforcing the boundary conditions at only a single point of each source panel is relatively insignificant.

In the above examples panel methods are used to simulate the wind tunnel environment for wall interference correction without using measurements over the walls. Following are some examples of panel methods based on flow measurement. Mokry et al[31] used doublet panel method to correct wall interference of a half-model inside the National Aeronautical Establishment (NAE) 5 ft Tunnel. They used a single-variable boundary measurement method. The wall pressure is measured using longitudinal static pressure tubes. The boundary values of the streamwise component of the wall interference velocity are obtained from the measured boundary pressures and the far field of the free-air flow. A small number of internal singularities are used to represent the model shape and the spanwise distribution of the measured aerodynamic forces. The results correlated well with data from full model wind tunnel tests and from flight test aircraft.

At the NASA Ames 12ft Pressure Wind Tunnel (PWT) Ulbrich and Boone[11] also used a single-variable method (Wall Signature Method) for real time wall corrections. It relies on the same main principle of the method used by Mokry et al[31]. Source and sink singularities are used to represent the fuselage, propulsion simulator, and separation wake volume blockage effects. Semi-infinite line doublets represent lifting effects. They

reported that the location of the test article singularities is selected using simple rules of thumb. The strength of the singularities are derived from the lift force, the propulsion simulator thrust force, and the wall pressure signature measurements. The singularities representing the test article are combined with lift force measurement, propulsion simulation thrust force measurements, least squares fits of wall pressure measurements, data from wall pressure port calibration "empty" test section tests, and solutions of the subsonic potential equation in the form of normalized perturbation velocities to predict Mach number, dynamic pressure and angle of attack corrections. The results presented for blockage and angle of attack corrections compared well with classical methods.

Qian and Lo[32] and Qian[33] described the use of a two-variable method for blockage interference correction assessment in a circular tunnel. They used Prandtl-Glauert equations to describe the subsonic flow field and analytical solutions are obtained using Fourier transformation technique. They compared the use of two model representations: a profile of the body of revolution and a distribution of source-sink singularities. Both methods worked very well. The study is based on numerically produced data obtained using a small perturbation inviscid code TSFOIL and a panel code PMARC.

One of the hardest interference correction problems is that of porous walls in transonic testing. Glazkov et al[34] showed the use of a panel method for this case at the T-128 wind tunnel of TsAGI. The perturbation flow potential comprises the potential of the infinite flow over the model, which can be calculated from the total loads on the model and its geometrical dimensions and the potential of distributed singularities at the flow boundary. The strengths of these singularities are calculated from boundary conditions on the walls specified in the form of distributions of pressure or porosity parameters related to the streamwise and normal perturbation velocity components. The main focus of this study was transport aircraft testing.

Recently Hackett presented a comparison between three of the contemporary methods used for low speed wind tunnel wall interference[35]. These methods are the two-variable method, a single-variable method and a pressure signature method. The checks are made

against benchmarks using the classical method of images. The test cases are totally theoretical, based on the use of single horseshoe vortices, line sources or line doublets. For the two-variable method the panel method code WIHM2V, which is based on Green's formula, is used. The code uses distributed doublet panels. The panel method code ANTARES is used for the single-variable approach. It uses specialized source panels to represent the tunnel surface. For the pressure signature approach the code PRSIG2L is used. In this method only a single row of wall pressures is required. It models the test object using classical images of the line sources, sinks and vortices and no wall panels are required for rectangular tunnels. The study indicates that among the three methods, the pressure signature method is the most economical regarding tunnel instrumentation and data acquisition requirements. The first two methods must employ finite length rather than infinitely long test sections. Corrections may be needed at the inlet and exit that compensate for this. Also, in the pressure signature method some simplifying assumptions have to be made to condense a model's vorticity field to manageable proportions. The three methods show good agreement with the classical method of images. This work[35] may be considered one of the most up-to-date studies about the methods currently used for solid wall interference. It can be seen that the panel method is involved in two of the methods used and showed high reliability.

1.5 Advanced numerical approaches

Currently panel methods are widely used for wall interference corrections. But for some applications where massive separation occurs or when shocks reach the test section walls more advanced methods that employ solutions of the Euler and/or Navier-Stokes Equations may be needed. In this section some of these examples are presented.

Hsing and Lan[36] presented a method based on the pressure signature approach for wall corrections during the test of a 65-deg delta wing and a wing-body-strake configuration in subsonic flow. The ARC3D code is used in the study. This code is based on the three-dimensional Reynolds Averaged Navier-Stokes Equations (RANS) with the thin layer approximation. The interference correction technique used is similar to the pressure signature method except that the wall pressure distribution is calculated with a Navier-Stokes solver instead of being measured. The solver is also used to obtain the uncorrected values of lift, drag and moment coefficient of the model inside the tunnel. Then the wall pressure distribution acts as the forcing function to generate the wall-induced flow field in the test section by solving the Euler equations. Then the blockage and upwash interference factors obtained from the wall-induced flow field are used to correct the lift, drag and moment coefficients obtained in the first step of the solution. It can be seen that the method is totally numerical with no need to take measurements from the tunnel. But it is not a generic approach that may be used for any model because a numerical grid has to be generated for each model geometry, which causes additional computational load each time the method is used.

Lombardi et al[37] presented a similar method based on the pressure signature approach. The correction is calculated from the difference between the values obtained in two different numerical simulations. In the first, the flow over the model in free-air conditions is simulated. In the second one, the measured pressure values over the wind tunnel walls are used as boundary conditions. A full potential flow solver is used in the study. The tested case was an ONERA M5 configuration model inside a slotted wall test section.

Although the potential flow solver makes the method computationally efficient, some computational effort is still needed.

Lessard[38] presented a numerical study of model support and tunnel wall interference for the high-lift Technology Concept Airplane (TCA) during a test conducted in the NASA Langley Research Center 14 by 22 Foot Subsonic Wind Tunnel. The highly swept low aspect ratio wings of the supersonic aircraft decrease their efficiency in the subsonic flight regimes. For that reason the focus of the study is the takeoff condition. The finite volume code CFL3D is used in the study. Three configurations are simulated numerically: model only in free-air conditions, model with post support in free-air condition and model with post support inside the tunnel. The data is compared to experimental measurements. The method employed in this study shows a good example of the labor and computational effort needed for such a complex model geometry. The grids used were generated in several stages. First the Initial Graphics Exchanges Specification (IGES) data were read into the Integrated Computer-Aided Engineering and Manufacturing (ICEM) software system where the grid blocks are generated. The blocks' faces were then refined by GRIDGEN2D to ensure smoothness and orthogonality. The Multi Geometry Grid Embedder (MaGGiE) code is used to determine the interpolation information between the grids. The grids for the post support and tunnel walls were generated with a hyperbolic grid generator (HYPGEN). So it can be seen that generating the grids for this case is not easy, but it is important to acknowledge that this method is more accurate compared to the other methods for this case where massively separated flow is expected.

1.6 Status of boundary correction methods for open jet wind tunnels

Essentially the same techniques used for closed jet test sections can be applied to the open jet case, albeit with a modified boundary condition (constant pressure). However, classical method of images neglects the effects of jet boundary distortion, which have been shown to be significant in cases where the test model is large relative to the test section cross section. In other words, **the correct boundary condition is enforced, but on an incorrect, undistorted boundary.**

SAE has been active in reporting on the development of boundary correction methods for open jet automotive tunnels[39,40]. Wickern[41] described the use of the classical boundary correction methods for open jet and closed test sections during automotive tests. In this application, the ground board represents the ground the vehicle is traveling on and has to be considered part of the tested model, not a test section boundary. To make the situation comparable to the one obtained in aeronautical applications, the model is mirrored at the ground plane and a situation with two models in a test section of twice the height (a duplex tunnel) is obtained. For this case all remaining boundaries are of the same nature (open jet or closed) and the classical method of images, outlined earlier, can be used. Mirror images are used to create the test section boundaries with the appropriate strengths (this will be discussed more fully in Chapter 3) to satisfy the boundary conditions on the test section boundaries. The blockage interference is then calculated by summing the streamwise velocity component induced by the image singularities. Wickern[41] reported that the gradient correction, not accounted for in his method, has to be applied first before the obtained blockage interference. It is important to note that the boundary deformation is not represented in this method. Also all the limitations of the classical method of images such as the assumption of a simple small model inside an infinitely long test section are imposed.

In addition to the above, the finite jet length, not properly accounted for in the classical theories, may be the source of the majority of the boundary interferences in an open jet wind tunnel. Mercker et al[42,43] developed one of the commonly used methods. They

grouped the interference effects into blockage due to jet expansion, empty-tunnel pressure gradients, and nozzle or collector solid blockage effects. They modified the classical formulations to include the additional jet expansion and the additional velocity reduction at the model due to jet deflection caused by the model proximity to the nozzle. For the empty-tunnel pressure gradient they presented a simplified form instead of the full integration of the pressure over the model to obtain the horizontal buoyancy. For the solid blockage due to the nozzle and the collector they used a simple point source and two vortex rings positioned at the nozzle and the collector. The method is relatively efficient in correcting the drag force based on a single point correction approach, but it depends partially on the method of images, which may put some limits on its applicability to complex model geometries.

Several improvements of the above method were later presented. For example, Wickern et al[44] presented a study of the nozzle gradient effect on open jet blockage interference for models of high blockage ratios. The study consisted of three main parts: an analytical model, CFD simulation, and experimental validations. The analytical model was based on the momentum balance and potential flow theory. Its objective was to present a basic analysis of the dependencies of the effect of the model and the wind tunnel properties. A simple streamlined model was represented using a blockage doublet with its axis parallel to the test section centerline aiming toward the upstream direction. In the second step of the study a simplified two-dimensional CFD analysis was performed using the commercial code StarCD™. A rectangular numerical domain was used. Its left boundary represents the nozzle exit section; its right boundary represents the collector entrance section, and the lower boundary represents the ground board. The model is merged to the lower boundary and the upper boundary represents the ceiling of the test section. The layout of the numerical domain used in this study[44] resembles the one used in the present study, (see Chapter (6)), except that the latter is extended to include the nozzle, the collector and the plenum chamber. StarCD™ solves the Reynolds-averaged Navier Stokes equations (RANS) and the k-ε model was used to simulate turbulence. The CFD-calculated values of the drag were corrected using the method developed in the analytical study and compared to a reference case, which was also obtained using CFD, but with

1% blockage. Finally the method was used to correct the effect of the nozzle pressure gradient for some of the published wind tunnel results and showed acceptable success.

Wiedemann et al[45] extended the previous study of the nozzle pressure gradient to include the effect of the boundary layer pre-suction on the ground board upstream to the model. They presented an experimental study conducted in the $1/5^{th}$ scale IVK model wind tunnel in Stuttgart. The study showed that the boundary layer pre-suction appears as a ground simulation increment due to the decreased boundary layer thickness and as a static pressure gradient increment due to the unintended additional pressure gradient. Based on the experimental results they proposed an empirical method to correct this effect by modifying the G-Factors (Glauert-Factor: a factor used to calculate effective volume of the model to correct the buoyancy effect of the empty test section pressure gradient)[1]. In their method they suggest slicing the model into sub-volumes and recommended the use of G-Factors in the order of one or smaller.

Recently, Mercker et al[46] presented a semi-empirical approach to correct the blockage interference by correlating the changes in the measured drag to the pressure gradient over the wake. The results from a test conducted in the model wind tunnel of IVK/FKFS of the University of Stuttgart were used to develop the method. An SAE generic vehicle model was used with four interchangeable rear-end shapes (square-back, hatchback, notchback, and fastback). The pressure gradient downstream of the model was changed by controlling the angle of collector flaps. The authors modified the method developed by Mercker et al[42,43] where the model was represented by a point source singularity and the nozzle and the collector are represented by two vortex rings located at the nozzle exit section and the collector entrance. In the latter method[42,43], the source strength was set to give a semi-infinite body of revolution with same base area as the frontal area of the vehicle. The source was located so that the leading edge of the semi-infinite body was at the front bumper location. This location, as they reported, was arbitrary in this method and they presented some recommended values based on the experimental study[46].

Hoffman et al[47, 48] developed a purely empirical method (linear regression) to assess the boundary interference of Ford/Sverdrup Drivability Test Facility (DTF), Wind Tunnel No. 8. This wind tunnel is used for both aerodynamic and aero-acoustic tests and, as they reported, was in full operational status in 2001. In their first study[47], the objective was to compare two test section configurations: slotted and 3/4 open jet boundaries. Four MIRA (Motor Industry Research Association) automobile shapes and six SUV (Sport Utility Vehicle) shapes are used to represent blockage from 7 to 25%. The tests were conducted in the $1/11^{th}$ scale representation of the Ford's Wind Tunnel No. 8. A reference set of data was obtained by testing the same models inside Sverdrup's sub-scale adaptive wall tunnel. No interference assessment was preformed in this study[45] and the authors reported that the comparison study of the 3/4 open jet, slotted wall and reference results (adaptive wall) showed that the 3/4 open jet offers less aerodynamic interference. This coupled with the acoustic advantage of the open jet drove the decision to strictly employ an open jet configuration in the Ford's Wind Tunnel No. 8.

Later the same group (Hoffman et al [48]) extended the previous study to develop a purely empirical method to determine open jet lift and drag interferences for a wide range of vehicle shapes. The study included sedan, station wagon, pickup, and sport utility vehicle profiles for blockage ratio ranges from 11 to 25%. Again the tests were conducted in the $1/11^{th}$ scale representation of Wind Tunnel No. 8 and the reference data was obtained from Sverdrup's sub-scale adaptive wall tunnel. They reported that the developed method showed effectiveness in correcting for drag interference while the lift correction did not work as well due to the measurement uncertainty. This method might be a simple and easy way to get an acceptable estimate of the boundary interference for the same models, test section and testing configurations. However, it is not a general method that can be safely used to correct other testing conditions. In addition, the method assumes that the reference data obtained from the adaptive wind tunnel is interference free which was proved to be not completely accurate as reported by Mokry.[13]

More recently Mercker et al[49] presented an extension of the semi-empirical method to correct the empty-tunnel pressure distribution, described earlier[46]. The new method is

also semi-empirical and it is based on wind tunnel measurements taken in the model wind tunnel of IVK/FKFS of the University of Stuttgart. The main improvement is that the new method calculated the drag correction by taking two wind tunnel measurements with different pressure gradients. One measurement was made in the standard wind tunnel flow. In the second one, the pressure gradient was introduced by closing the flaps of the collector. They reported that the new method was used to correct the drag using the following procedure. First two drag measurements were taken in two different pressure distributions. Second, based on the calculated static pressure difference between the front end of the vehicle and any downstream location, each of the measured drag coefficients was corrected using the method previously developed by the same authors.[42,43] Then the two corrected drag coefficients obtained were compared. If they were identical, then the correction was found. If not, as they reported, the model had to be moved a small increment downstream and the previous steps were repeated. This work is currently the most up to date regarding boundary interference for automotive open jet wind tunnels. The method is presented by the same authors who developed the well known method described before.[42,43] Again the method might be efficient in correcting the measurements it was based on; however, as they reported, it is semi-empirical and some of its steps depend at least partially on classical methods.

The literature cited above covers most of the previous and the current methods developed during the last decade for open jet boundary correction. The best description of the current status of the boundary interference correction methods for open jet test sections was presented recently by Mokry.[50] He reported, "To date, most corrections for open jet test sections are either semi-empirical or reliant upon modified image-singularity solutions." In this study he proposed a method based on the potential flow formulations and a finite difference solver using successive over-relaxation. The method is computationally efficient, but as he indicated, the main weakness of the method is that the downstream area of the jet is assumed to have the same area as the nozzle area, so no account has been taken of the deformation of the tunnel jet boundary.

1.7 General remarks

Several boundary correction methods for both closed and open test sections have been presented in the previous sections. In this section some statements are made concerning the principal motivations for introducing a new method for open test section boundary corrections.

The method of images is relatively accurate within its limits on the relative sizes of model and test section and their respective geometries. It can be used for both closed and open test sections, albeit with less accuracy in the open test section case because it does not account for the boundary distortions. The methods currently used for open jet test section boundary corrections share some of the limitations of the method of images and are mostly designed for automotive applications with single point correction of the drag force only. The boundary measurement methods are very efficient for closed test section interference corrections. They are not yet used for open test sections due to technical difficulties in taking the necessary boundary measurements. But the main principle may be applied to open jet test sections if the flow properties can be predicted numerically on the deformed test section boundaries. Now the questions are: How the boundaries' location can be predicted and which numerical method can be used?

The answer for the first question comes from the adaptive wall wind tunnels. The methods used in adaptive wall tunnels have shown success through the years in streamlining the walls and the results obtained compared well with reference free-air conditions. These methods can be used in predicting the over-expanding open test section boundary deformation with the application of the correct boundary conditions. The fundamental boundary condition for open jet boundaries is constant pressure (constant velocity). The available model information may be used to the maximum extent possible. This is the antithesis of much research in closed test section tunnels, where it is argued that interferences can (should) be assessed with no model information whatsoever. If the location of the boundary can be estimated based on model information, such as its

geometry and measured forces and moments, then the interference assessment and correction can then follow more-or-less as in the closed wall test section case.

The choice of the numerical methods used will be according to two factors. The first factor is the computational efficiency of the method for real time corrections. In other words the predicted boundary correction factors should be available before the test is completed. Second the accuracy has to be within the measurement uncertainty. Advanced numerical methods such as the finite difference methods offer high accuracy in the expense of their computational efficiency in terms of preparing numerical grids and running codes. In other words, a lot of effort is required to estimate unnecessarily accurate correction factors while the uncorrected measurements might have higher values of experimental uncertainties. On the other hand, the panel method offers an efficient and fast approach with acceptable accuracy compared to other numerical methods. It is widely used for wall interference corrections of closed, ventilated and slotted test sections with high reliability.

1.8 Outline of the present work

The details of the present method are presented in Chapter (2) including the theoretical background of the boundary measurement methods and the adaptive wind tunnels as well as the integration of these well-developed methods currently used in solid wall test sections into a method suitable for open jet test sections. Also the Chapter includes the details of the panel model developed for the present approach.

Then the method is first compared to the method of images. Several lifting and non-lifting model representations are used with different types of surface panels for both two- and three-dimensional studies in Chapter (3). Then the method is used during a test of a full-scale Wright Flyer replica inside the Langley Full Scale Tunnel. The study is extended to include the effect of model representation and the test section boundaries (closed, open and 3/4 open) on the interference in Chapter (4). The method is also used during a test of full scale NASCAR inside the NASA Langley Research Center 14 by 22

Foot Subsonic Wind Tunnel. This part includes the effect of test section length and the inclusion of the nozzle in the solution on the predicted boundary interference in Chapter (5). Finally, a test is conducted at the $1/15^{th}$ scale Langley Full Scale Tunnel using a generic automotive model (a "Davis" model) to validate the prediction of the boundary distortion and to investigate the effect of the collector in Chapter (6).

CHAPTER II

II. PRESENT WORK

The present method for open jet test section boundary interference is based on the concepts of two of the well-developed current approaches, namely boundary measurement wall correction techniques and adaptive wall test sections. Both of them use the measured flow properties on the walls either to assess the wall interference, as in the first approach, or to predict the necessary wall deformation to eliminate the boundary interference inside the test section, as in the second approach. In the first two sections of this chapter, these two concepts are outlined. Then the details of the present method are introduced including an outline of the panel method, model representation, surface panel generation and a parametric study for the appropriate surface panel size.

2.1 Boundary measurement approach

The main concepts used in the boundary measurement methods have been presented several times in the literature. The derivations presented in this section are summarized from Ashill [4] and Ashill et al [5].

The method assumes that the flow is subsonic and everywhere irrotational. For example consider the flow about a model of an aircraft in a wind tunnel, Figure (2-1). When the flow is defined using the velocity potential φ, then

$$\nabla^2\varphi = 0 \tag{2-1}$$

The wall interference φ_i can be defined as the difference between the wind tunnel flow φ and the free-air flow φ_f

$$\varphi_i = \varphi - \varphi_f \tag{2-2}$$

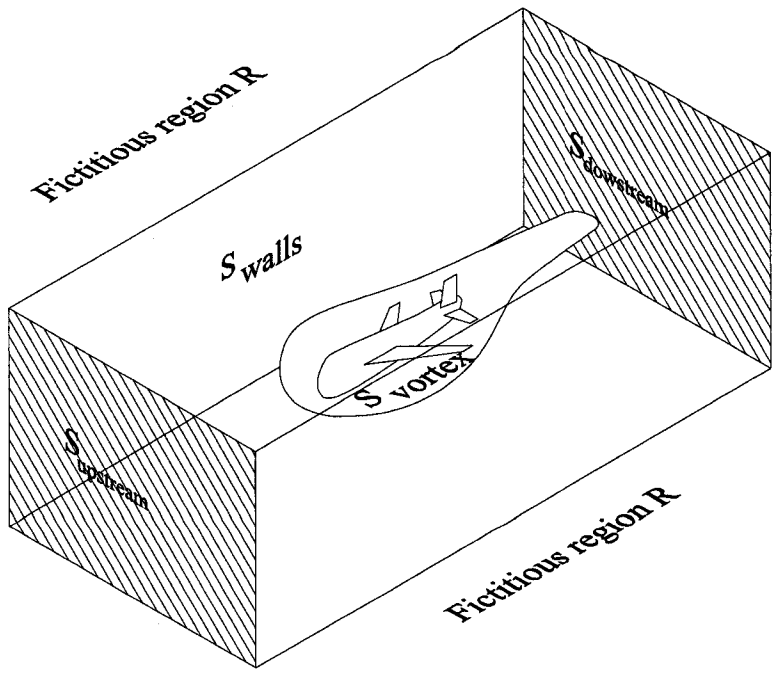

Figure (2-1) A sketch of a closed test section with a model inside.

Equation (2-1) indicates that φ is harmonic within the working section. So it is possible to use Green's formula to write the interference potential at point P in the working section.

$$4\pi\varphi_i(P) = -\int_S \left[\frac{\partial\varphi_i}{\partial n}G - \varphi_i\frac{\partial G}{\partial n}\right]dS \qquad (2\text{-}3)$$

- where n is the normal inward towards the working section and the integration is performed over the boundary surface S ($S = S_{walls} + S_{upstream} + S_{downstream}$). G is a Green's function that is harmonic everywhere within the measurement region except at point P. At this point it behaves like 1/r, where r is the distance between the point P and a variable point in the region. This analysis may be extended to rotational flows if the vorticity is confined to a region surrounding the model as shown in Figure (2-1). The boundary surface of this region S_{vortex} has to be included in the surface of integration S.[5]

Equation (2-3) implies that to determine the wall interference potential in the working section it is necessary to know both the wall interference potential itself and its normal gradient at the measurement surface. If the wall interference potential φ_i in the right hand

side is replaced by the wind tunnel potential φ and the model free-air potential φ_f from Equation (2-2) then,

$$4\pi\varphi_i(P) = -\int_S \left(\left[\frac{\partial\varphi}{\partial n} - \frac{\partial\varphi_f}{\partial n} \right] G - (\varphi - \varphi_f) \frac{\partial G}{\partial n} \right) dS \qquad (2\text{-}4)$$

Now it can be seen that three independent variables are required: the perturbation potential of the wind tunnel flow and its normal gradient at the surface and a representation of the free-air flow around the model. The number of variables can be reduced to two by using the freedom to choose an appropriate Green's function for the boundary-value problem. In the single-variable methods, one flow variable is measured on the walls and the model free-air flow is represented. In the two-variable methods, two flow variables are measured on the walls with no representation for the model.

In the single-variable methods, the appropriate Green's function used depends on the approach of solving the Equation (2-4) as a Dirichlet, a Neumann, or a mixed problem. In the Dirichlet problem, the interference potential is specified on S and the Green's function has to vanish on the measurement surface. Then the interference potential can be defined as follows:

$$4\pi\varphi_i(P) = \int_S (\varphi - \varphi_f) \frac{\partial G_D}{\partial n} dS \qquad (2\text{-}5)$$

This Green's function G_D can be evaluated once the perturbation potentials φ and φ_f are known. For example the static pressure at the outside surface S_{walls} can be used to determine the potential φ by integration of Bernoulli's or Euler equations.

For the Neumann problem, the normal gradient of the interference potential is specified. The required Green's function G_N is the one that has a vanishing normal gradient on S. From Equation (2-4):

$$4\pi\varphi_i(P) = -\int_S \left[\frac{\partial\varphi}{\partial n} - \frac{\partial\varphi_f}{\partial n}\right] G_N \, dS \tag{2-6}$$

This equation implies that the normal component of the velocity has to be specified on the boundaries. This is done easily in solid fixed and flexible wall test sections where the condition of no flow through the walls is applied. For porous and slotted walls this approach is not used due to difficulties in measuring flow angles near to the boundaries with the required accuracy. For these applications the mixed problem is used, which is beyond the scope of the present work. The wall signature method is a good example of the single-variable methods. It uses a complete knowledge of one flow variable at the measurement surface and limited measurements of a second flow variable on the same surface. The signature of the second variable is used to determine the strengths of the singularities representing the model. For solid walls the normal velocity component is zero and the Neumann problem, Equation (2-6), becomes:

$$4\pi\varphi_i(P) = \int_S \frac{\partial\varphi_f}{\partial n} G_N \, dS \tag{2-7}$$

After differentiation in the x direction Equation (2-7) may be expressed as:

$$u(P) = u_f(P) + \frac{1}{4\pi}\int_S \frac{\partial\varphi_f}{\partial n}\frac{\partial G_N}{\partial x} dS \tag{2-8}$$

For point P taken close to the walls, the left hand side can be defined from the static pressure measurements at the walls at a limited number of points. If the same number of singularities represents the model, then Equation (2-8) may be regarded as a linear integral equation for the unknown singularities strengths. If the length of the test section is large enough to be assumed infinite, the integral Equation (2-8) may be replaced by a doubly-infinite sum of singularities representing the image effect of the tunnel walls.[5]

In the two-variable methods, the idea is to eliminate the contribution of the model representation terms from Equation (2-4). So:

$$0 = \int_S \left(\frac{\partial\varphi_f}{\partial n} G - \varphi_f \frac{\partial G}{\partial n}\right) dS \tag{2-9}$$

Ashill [4], Ashill et al [5] and Mokry [13] suggested that the appropriate Green's function is:

$$G = \frac{1}{r} \tag{2-10}$$

- which is the classical solution of the potential flow field developed by Lamb, as reported by Katz and Plotkin[51]. For this Green's function, Green's formula gives:

$$\iint_S \left(\frac{\partial \varphi_f}{\partial n} \frac{1}{r} - \varphi_f \frac{\partial}{\partial n}\left(\frac{1}{r}\right) \right) dS - \int_{Vo} \frac{1}{r} \Delta^2 \varphi_f \, dV = 0 \tag{2-11}$$

Where, Vo refers to the volume integration in the fictitious region R, outside the measurement region, as shown in Figure (2-1). As the perturbation in the free-air region outside the working section is small, the perturbation potential φ_f can be considered harmonic in this region. Then:

$$\iint_S \left(\frac{\partial \varphi_f}{\partial n} \frac{1}{r} - \varphi_f \frac{\partial}{\partial n}\left(\frac{1}{r}\right) \right) dS = 0 \tag{2-12}$$

Thus the Green's function satisfies Equation (2-9). By substituting for G in Equation (2-4), it is seen that the model representation no longer exists and the interference potential can be defined as:

$$4\pi\phi_i(P) = -\iint_S \left(\frac{\partial \varphi}{\partial n} \frac{1}{r} - \varphi \frac{\partial}{\partial n}\left(\frac{1}{r}\right) \right) dS \tag{2-13}$$

The first term in the right hand side under the integral sign is recognized as the contribution of sources of strength $\frac{\partial \varphi}{\partial n}$, which requires the measurement of the normal velocity component at S while the second term is the contribution of doublets and requires the measurement of the streamwise velocity components. For solid fixed and adaptive walls the normal velocity component is well defined to be zero and the main task is to measure the streamwise component. For open boundaries, the normal gradient is likewise zero and the streamwise component is constant, but the location of the boundary is strictly not known.

It has been shown in this section that the wall interference can be derived from the flow properties on the walls with or without using model information. The same concept can be applied to open jet test sections if the required flow properties at the jet boundaries are known from actual measurements or numerical calculations. For closed test sections it may be preferred to take flow measurements at the walls because it is relatively easy. However, for open jet test sections, the numerical approach would be preferred because of the technical difficulties in detecting the jet boundaries and taking the necessary flow measurements with sufficient accuracy.

2.2 Adaptive wall tunnels

There are two main categories of the algorithms used in predicting wall adjustments for adaptive wall wind tunnels, namely target line and interface matching techniques. In the target line techniques, the test section walls are adjusted to minimize the induced interference along a certain line inside the test section, usually the centerline. This approach is not suitable for predicting the deformation of the open jet test section boundaries because in this case the boundary interference is not eliminated and the convergence criteria of the target line techniques will not be met. On the other hand, the interface matching technique uses the flow properties at the boundaries, which are available from the numerical solution, and the convergence criteria can be easily modified to meet the fundamental boundary condition of the open jet test section boundaries (i.e. constant pressure).

This section addresses the main concept of the "one-step" method, which is an interface matching technique. Several versions of this algorithm have been presented in the literature such as Wolf and Goodyer [19], Wedemeyer et al [12], Wolf [17], Erickson [16], and recently Meyer and Nitsche.[18] Following is a description of how the method works in predicting the wall adjustments for the adaptive wall test sections.

Interface matching means that the flow conditions at the adaptive walls are matched with virtual free flow conditions outside the test section. So the predicted wall contour equals a streamline or streamplane and the interferences are eliminated in the entire test section. The determination of a wall contour follows two main steps: first, the wall interferences are calculated, and second the required wall deflections are derived. The method assumes that all the velocity deviations at the walls are small compared to the free flow and the linear theory can be applied. So, the potential function Equation (2-1) can be utilized:

$$\nabla^2\varphi = 0 \tag{2-1}$$

The wall interference in a two-dimensional tunnel flow can be computed by a Cauchy integral:

$$w_{int}(z) = \frac{1}{2\pi i}\oint_C \frac{w(\zeta)}{\zeta - z}d\zeta \tag{2-14}$$

Where the complex variables z and ζ are defined by $z=x+iy$ and $\zeta=\xi+i\eta$. (x,y) are the coordinates in the flow direction and upward while (ξ,η) are the running coordinates in the x and y directions. The complex integral is taken along a counter-clockwise closed pass (C) around the model along the lower wall from upstream to the downstream end of the test section, from there across the test section to the upper wall and along the upper wall upstream and back across the test section to the starting point (Figure 2-2). The complex expression for the perturbation velocity $w(\zeta)$ in the formulation of the Cauchy line-integral at point (ξ,η) is defined with the application of the Prandtl-Glauert transformation:

$$w(\zeta) = \beta\, u(\xi,\eta) - i\, v(\xi,\eta) \tag{2-15}$$

- where, $\beta^2=1-M^2$ and M is the Mach number. The interference velocity $w_{int}(z)$ at point (x,y) is defined as :

$$w_{int}(z) = \beta\, u_{int}(x,y) - i\, v_{int}(x,y) \tag{2-16}$$

Equation (2-14) is the two-dimensional equivalent to Green's formula introduced by Ashill et al [5] for the computation of wall interference in general three-dimensional flow (Equation 2-13). The perturbation velocity in the Cauchy integral can be derived from the measured pressure distribution, C_p, and the measured wall displacement (wall angle θ_o for aerodynamically straight wall test section) as follows:

$$\frac{u}{U_\infty}=-\frac{C_p}{2} \qquad \text{and} \qquad \frac{v}{U_\infty}=\theta_o \tag{2-17}$$

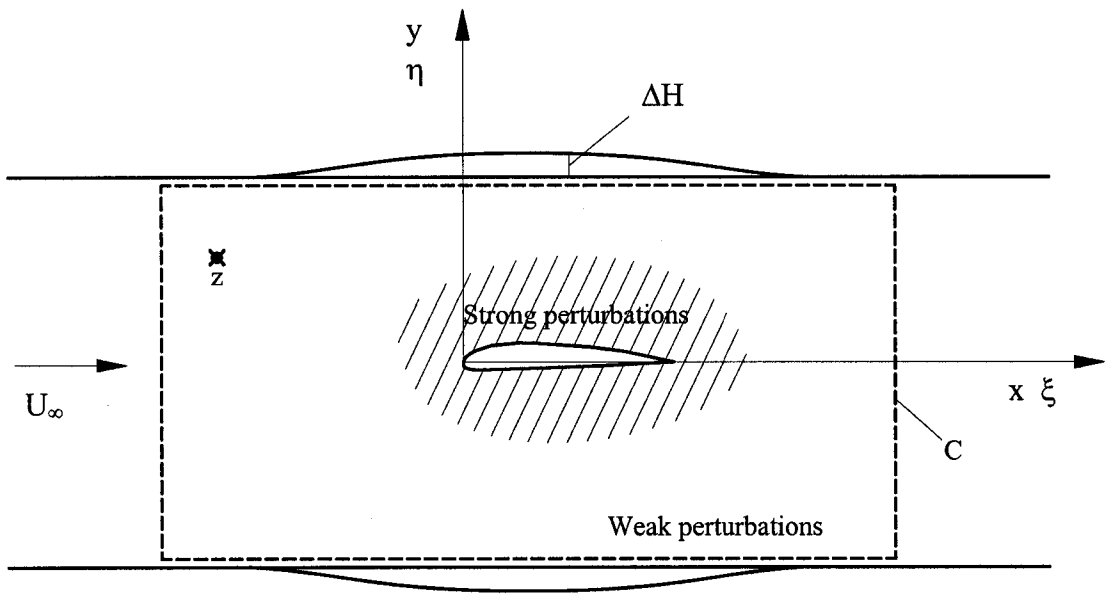

Figure (2-2) Integration area of Cauchy Integral Equation (Equation 2-14)

Equation (2-14) can be used to calculate the interference at any point inside the test section. However, the Cauchy integral is singular for z on the walls ($z=\zeta$). The proper integration is performed by taking the limit value of the integral for z approaching the wall. Then Equation (2-14) becomes

$$w_{\text{int}}(z)=\frac{1}{2}w(z)+\frac{1}{2\pi i}\oint_C \frac{w(\zeta)}{\zeta-z}d\zeta \qquad ;z\in C \tag{2-18}$$

Now, the appropriate wall displacements have to be calculated with the known interference velocities to generate the required counter velocities to cancel the interference velocities. The normal velocity at the wall must be:

$$v_{normal} = v - v_{int} \tag{2-19}$$

and the local slope of the walls θ is:

$$\theta = \frac{v - v_{int}}{U_\infty} \tag{2-20}$$

The required wall displacement ΔH can be calculated in a single step from the local wall angles by integration along the test section wall as follows:

$$\Delta H = \int \theta \, dx = \int \frac{v - v_{int}}{U_\infty} dx \tag{2-21}$$

It has been shown that the flow perturbations and the wall interference can be used directly to predict the required wall adjustment for an interference free test section. In the open jet test section case, a similar approach can be used to predict the over-expanded boundaries. The flow perturbations and the boundary interference can be easily calculated using numerical methods instead of taking direct measurements. But in this case more iterations may be needed and the convergence criteria has to be redefined to match the open jet boundary conditions (constant pressure). Table (2-1) shows a summary of the tangential boundary conditions for the different test section boundaries.

Fixed walls $\frac{\partial p}{\partial x} \neq 0$	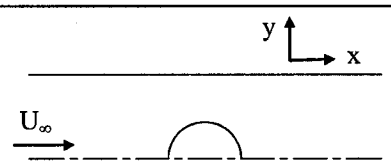
Adaptive wall (free air solution) $\frac{\partial y}{\partial x} = \frac{v}{u} \;\&\; \frac{\partial p}{\partial s} \neq 0$	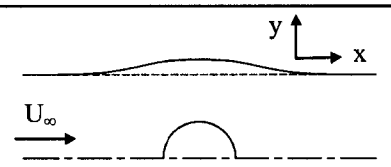
Open jet boundary $\frac{\partial y}{\partial x} = \frac{v}{u} \;\&\; \frac{\partial p}{\partial s} = 0$	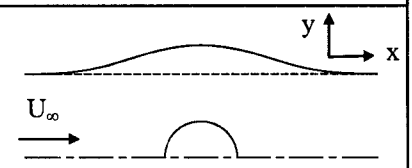

Table (2-1) Summary of the conditions at the test section boundary, where s is the tangential direction.

2.3 Present method

It has been shown in the previous sections that the flow properties at the test section boundaries can be used to derive the boundary interference for the fixed walls and to predict the wall adjustment for adaptive solid walls test sections. For these applications, it is relatively easy to take the necessary flow measurements at the walls. If, for open test sections, numerical methods can predict these flow properties at the boundaries then the interferences can be derived with a more-or-less similar approach.

The present method for open jet test section boundary correction has three main steps. First, the boundary interference is calculated assuming the jet boundaries are fixed solid walls. Second, an iterative algorithm is employed to predict the deformation of the boundaries. Finally, the boundary interference of the open jet test section is calculated

using the deformed boundaries. A panel code that includes these three steps is developed for the study. In the following sections, more details for each step are presented.

2.4 Closed wall solution

The objective of this step is to determine the wall interference induced by the test section boundaries assuming that they are solid fixed walls. The solution is derived using the boundary measurement method. The test section boundaries are first divided into surface panels. For complex models, their surfaces are also divided into panels. For simple models, their geometries are represented by singularities with strengths derived from the measured forces, following the methods discussed in Chapter (1). The strengths of the panels are calculated by applying the Neumann boundary condition to all the surfaces. A numerical wall signature is now calculated using the obtained panel strengths. This step replaces measuring the flow properties at the walls in the boundary measurement methods. Figures (2-3) and (2-4) show samples of the test section surface panels and the obtained numerical wall signature.

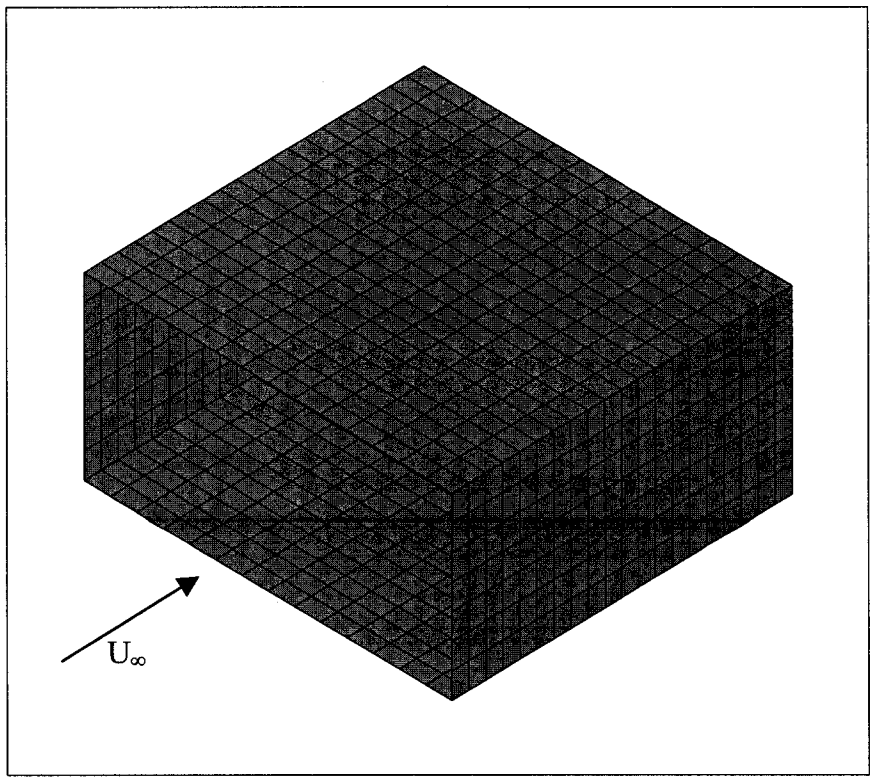

Figure (2-3) A sample of the surface panels used.

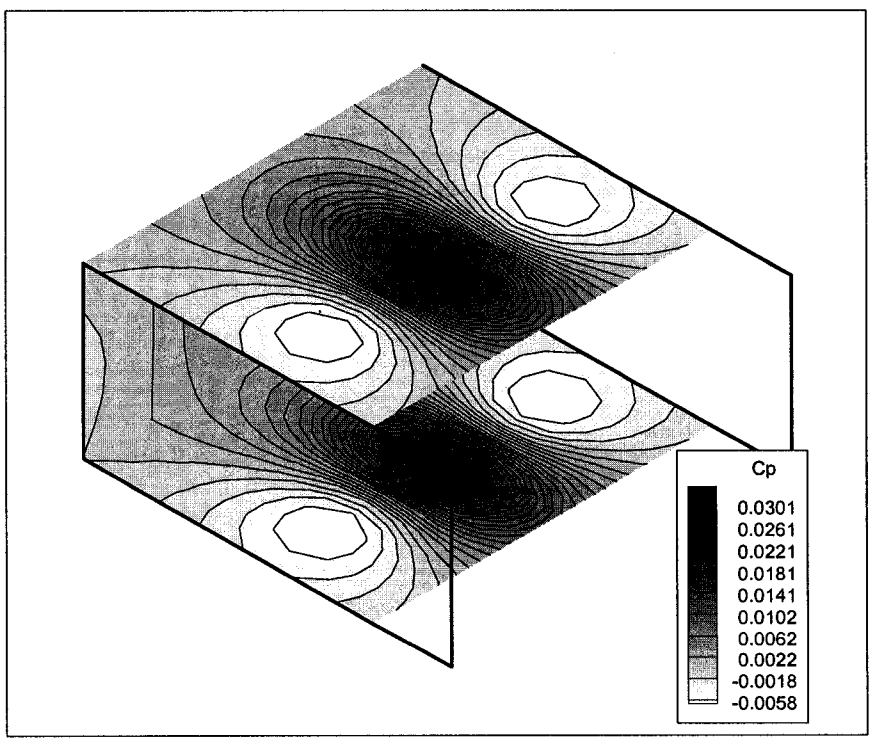

Figure (2-4) A sample of the derived wall signature. The model is a sphere at the test section center.

2.5 Boundary deformation

An iterative algorithm is employed using the one-step method,[16 - 19] Equation (2-20).

$$\Delta H = \int \theta \, dx = \int \frac{v - v_{int}}{U_\infty} dx \qquad (2\text{-}20)$$

The initial values for the flow perturbations v and the boundary interference v_{int} are calculated from the first step of the solution, where the wall interference is calculated from the flow induced by the wall panels. The deformed boundaries are solved again and the new panel strengths are used to calculate new values for the flow perturbations and the boundary interferences. These values are used to predict another boundary deformation and the process is repeated until the open jet boundary condition (constant pressure) is satisfied. The convergence criterion is constant tangential velocity to a prescribed tolerance. Figure (2-5) shows a sample of the predicted test section boundary deformation.

For the three-dimensional case, v and v_{int} in Equation (2-20) are replaced by the velocity component normal to the test section boundaries. For example, in rectangular test sections such as the NASA Langley Research Center 14 by 22 Foot Subsonic Wind Tunnel presented in Chapter (5), initially the horizontal velocity components v and v_{int} are used for the side boundaries and the vertical velocity components w and w_{int} are used for the upper and the lower boundaries. The corner panels are deformed along the diagonal of the test section cross section using the velocity component calculated in the same direction. Then, after the first step of the deformation, the velocity components normal to the new deformed boundaries are used instead. For non-rectangular test section such as the Langley Full Scale Tunnel, as discussed in Chapters (4) and (6), where the test section cross section has horizontal upper and lower boundaries and circular side boundaries, initially the vertical velocity components w and w_{int} are used for the horizontal boundaries and radial velocity components are used for the circular boundaries. Then, again after the first step of the iteration, the velocity components normal to the deformed boundaries are used.

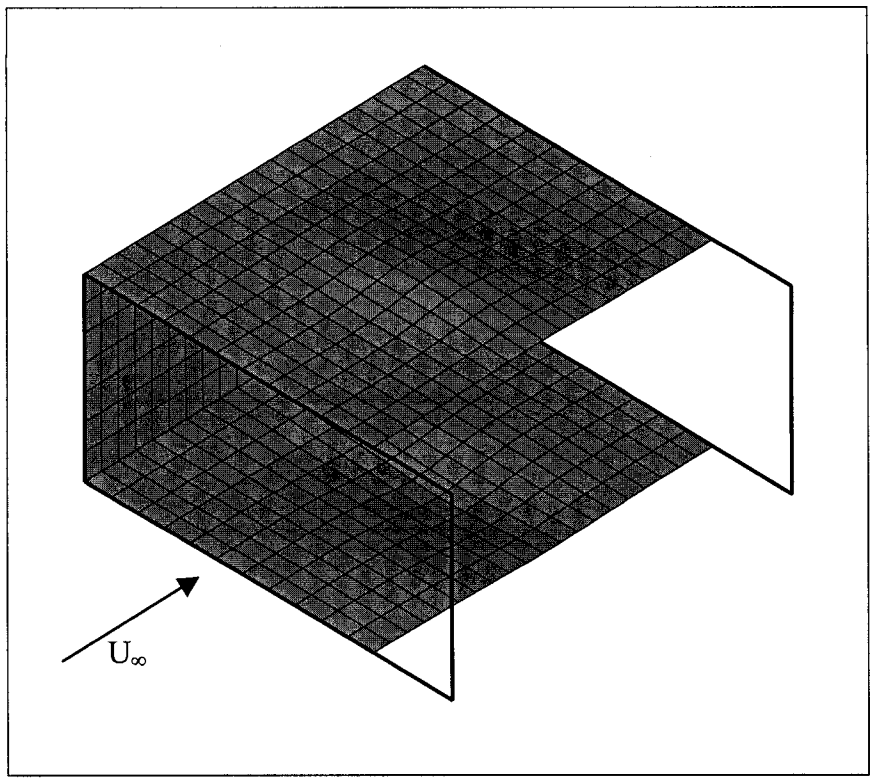

Figure (2-5) A sample of the predicted test section boundary deformation. The model is a sphere at the test section center.

2.6 Boundary interference assessment

At this point of the solution, the deformation of the test section boundaries is predicted and the strength of its surface panels are calculated. The induced flow by these surface panels represents the boundary interferences. Usually the boundary interference is presented as a blockage factor ε and an upwash factor δ. [53]

$$\varepsilon = \frac{u_{int}}{U_\infty} \tag{2-20}$$

$$\delta = \frac{w_{int}}{U_\infty}\frac{C}{SC_L} \tag{2-21}$$

Where u_{int} and w_{int} are the velocity components induced by the test section boundaries panels in the streamwise and upward directions respectively. C is the cross-sectional area of the test section, S is the wing reference area, and C_L is the lift coefficient.

The blockage factor represents the effect of the model shape and volume, which causes a displacement or bulging of the stream around the model. The upwash factor represents the effect of model lift, which results in a redirection of the momentum of the stream. It may be represented as a change in the angle of attack α.

$$\Delta\alpha = \frac{w_{int}}{U_{\infty}} \tag{2-22}$$

The streamwise gradient of the blockage factor is of interest because it imposes a streamwise buoyancy force on the model. Similarly, the streamwise gradient of the upwash is of interest because it indicates the additional streamline curvature, which results in induced camber and apparent changes in the angle of attack at the horizontal tails, leading to changes in trim angles.

Figure (2-6) shows the outline of the panel method used in the present work summarizing the main steps outlined in the previous section (solid wall solution, boundary deformation and interference assessment). More details about the panel model used, the model representation and the surface paneling are presented in the following sections.

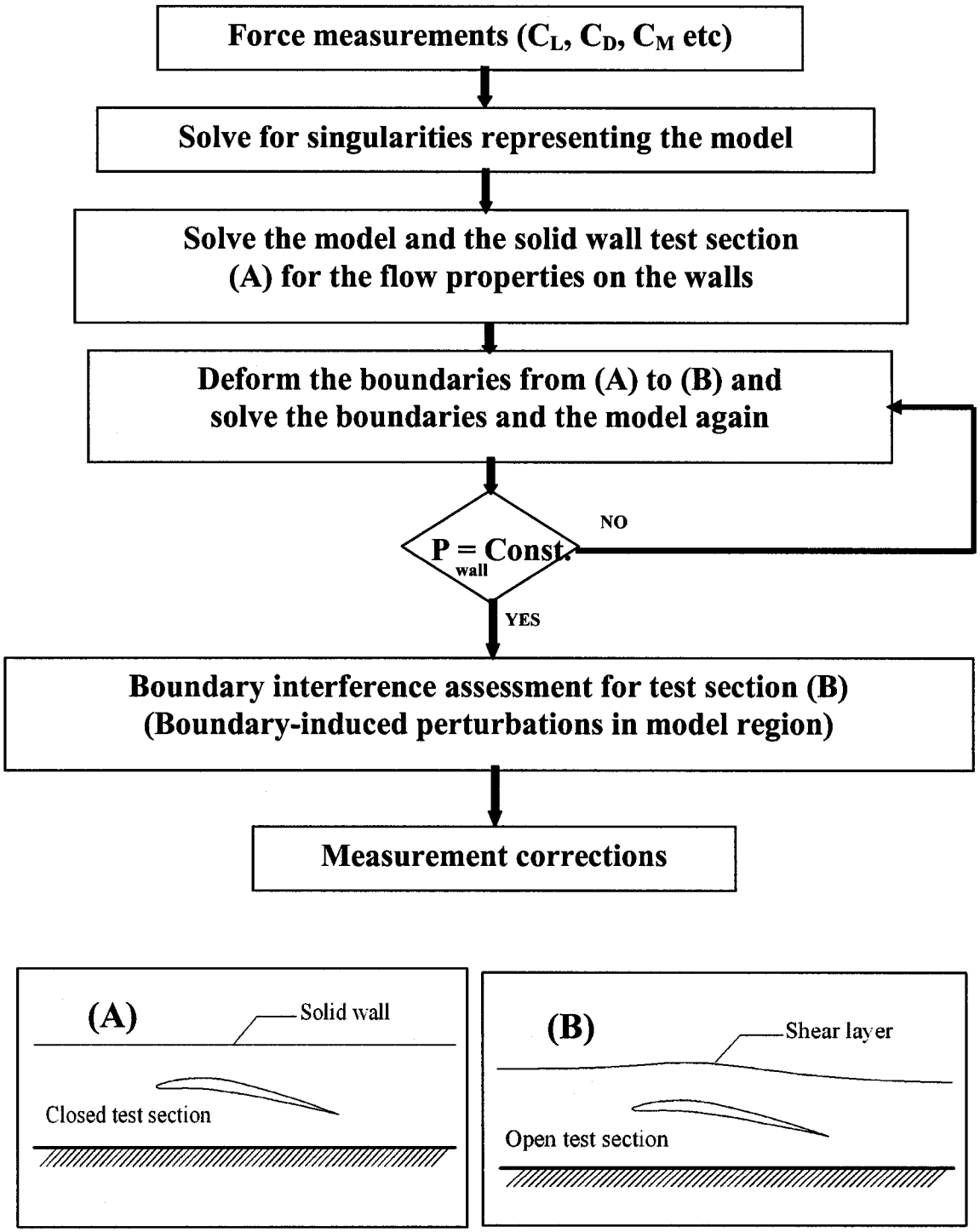

Figure (2-6) Outline of the panel method used in the present work.

2.7 Panel method model

The use of panel method for closed test section wall interference is well developed as outlined in Chapter (1). The majority of the literature modeled the test section only while limited research included the nozzle and/or the diffuser. Three main approaches are used to model the test section. In the first approach, the test section is modeled as a paneled prism with upstream and downstream faces normal to the axis. This approach is used in the panel methods that are based on flow measurements taken on the walls (boundary measurement methods). For example Mokry et al[31] presented a panel method based on the pressure signature for a test conducted inside the National Aeronautical Establishment (NAE) wind tunnel. More recently, Hackett[35] used the WIHM2V code, which uses a panel method based on measuring two flow variables on the test section walls. In this approach, the strengths of the panels on the walls and the upstream and downstream surfaces are obtained by imposing Dirichlet boundary conditions using the measured flow properties. Holt and Hunt[26] reported that this approach is not recommended for fully numerical panel methods where no flow measurements are taken on the walls.

In the second approach, the test section is modeled as a long tube with a far upstream paneled end. The boundary conditions of these panels are used to specify the flow inlet to the test section, and then the Neumann boundary is imposed to obtain the strength of the other wall panels. For example, this approach is used in the Boeing transonic wind tunnel using the panel codes PANAIR as reported by Krynytzky[3]. He recommended that the upstream end should be far enough away to avoid any disturbance to the solution near to the model location.

The third approach is an extension of the previous one by modeling the test section as an open-ended tube embedded in a uniform onset flows. This approach is used by most of the methods introduced in the literature, Chapter (1). For example, for finite length test sections, Joppa[26] and Lee[28] used this approach in developing their panel codes. Also it is used in the panel code PMARC for wall interference as reported by Qian et al[32, 33] for a two-variable boundary measurement method. The same code was also used by Ulbrich[30]

in a fully numerical method with no wall measurements. Ulbrich et al[11] used the open ended tube representation of the test section in a panel code developed to assess the wall interference of the NASA Ames 12ft Pressure Wind Tunnel (PWT). This code is based on the pressure signature method. Hackett[35] reported that this approach is used in the panel code ANTARES, which is based single-variable measurement method. For a long test section (effectively infinite), Holt and Hunt[26] presented the use of panel method in aeronautical applications. In summary this approach is used for both fully numerical and measurement-based panel methods solving both finite length and long test sections.

The panel method used in the present work is not based on flow measurement taken on the test section boundaries, so either the second or the third approach may be used. Since several test section lengths and configurations (including nozzle or the collector representation) are studied, the third approach is found to be more suitable for the purpose of this study.

2.8 Model representation

The first step in the present method is to input the uncorrected wind tunnel measurements (for example the lift, drag, side forces and pitching moment), as shown in the method outline presented in Figure (2-6). Then, the model representation is established. Small, simple models are represented using elementary singularities to induce their far field effect at the test section boundaries. For the comparison with the method of images, the model representation using a single or limited number of elementary singularities is found to be suitable since the method of images assumes small model size relative to the test section, as will be discussed in Chapter (3).

A point vortex singularity is used to represent the lifting effect of a small airfoil inside a two-dimensional test section. For a model (small airfoil) located at the origin (x , y) = (0 , 0), where x and y are the streamwise and the vertical axes, the velocity potential is:[1, 2, 3, 51]

$$\varphi = -\frac{\gamma}{2\pi}\tan^{-1}\left(\frac{y}{x}\right) \tag{2-23}$$

- where, γ is the vortex strength and its sign is adjusted so that the model generates an upwash effect upstream to its center and downwash in the downstream direction as shown in Figure (2-7). The strength of the vortex (γ) is calculated as follows:

$$\gamma = \frac{1}{2}U_\infty c C_L \tag{2-24}$$

For the blockage effect, a point doublet is used to represent a cylinder inside a 2D test section, as show in Figure (2-8). The doublet is aligned with the oncoming stream. The velocity potential of a doublet located at the origin (0 , 0) is as follows:[51]

$$\varphi = \frac{\mu}{2\pi}\left(\frac{x}{x^2 + y^2}\right) \tag{2-25}$$

The doublet strength is related to the cylinder radius R as follows:[51]

$$\mu = 2\pi R^2 U_\infty \tag{2-26}$$

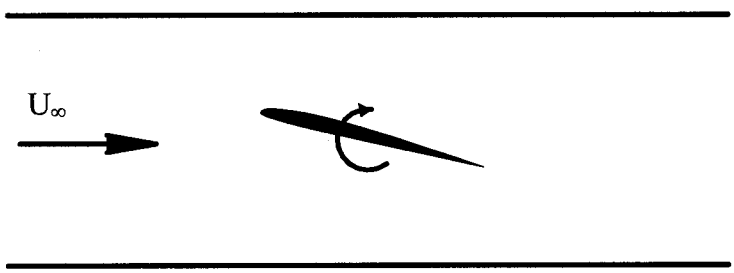

Figure (2-7) Representation of a small airfoil inside a two-dimensional test section using a point vortex.

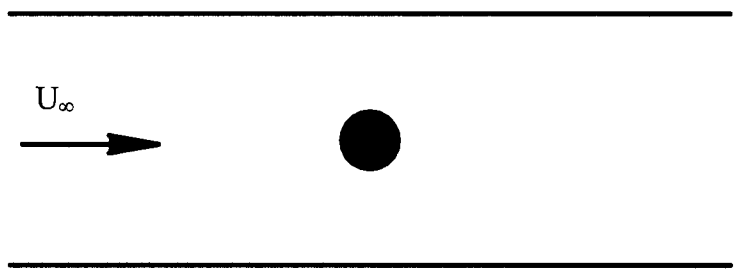

Figure (2-8) Representation of a cylinder a two-dimensional tests section using a point doublet.

A small lifting model is represented using a horseshoe vortex of span 2s as shown in Figure (2-9). The velocity potential is as follows:[3]

$$\varphi = \frac{\Gamma}{2\pi}\left(1 + \frac{x}{\sqrt{x^2 + y^2 + z^2}}\right)\left(\frac{z}{y^2 + z^2}\right) \tag{2-27}$$

- where Γ is the strength of the horseshoe vortex and it is set to induce an upwash upstream of the wing. Its value is related to the wing information and the generated lift as follows:[51]

$$\Gamma = \frac{1}{4} U_\infty S C_L \tag{2-28}$$

- where S is the wing reference area.

It is important to note the accuracy of using a single horseshoe to represent a wing is limited to relatively small wingspan with respect to the test section width (perhaps around 50%).[3] For larger wings, lifting line theory could be used to calculate the load distribution along the wingspan with a set of horseshoe vortices employed. Alternatively

the surface of the wing can be divided into surface panels with their strengths calculated concurrently with the test section boundaries as will be discussed later in this chapter. The application presented in Chapter (4) is a good example of this case (large wingspan) where the wingspan is 67% of the test section width. Both of the methods described above are used to represent the model (full-scale Wright Flyer) inside the Langley Full Scale Tunnel.

The blockage effect of a small sphere tested inside a three-dimensional test section is represented using a 3D point doublet aligned with the oncoming stream as shown in Figure (2-10). Its velocity potential is defined as follows:[51]

$$\varphi = \frac{\mu}{4\pi}\left(\frac{x}{\left(x^2+y^2+z^2\right)^{\frac{3}{2}}}\right) \tag{2-29}$$

The strength of the doublet is related to the sphere radius R and the free stream velocity as follows:[51]

$$\mu = 2\pi R^3 U_\infty \tag{2-30}$$

It is important to note that for models with larger blockage ratios or wingspans the above-discussed representation does not offer enough accuracy and alternative approaches have to be used. In the present work two methods are used for such cases. In the first approach distributed singularities are used and their strengths are calculated from the generated forces. This approach was used to represent the Wright Flyer model inside the Langley Full Scale tunnel (wingspan is 67% of the test section width) where the lifting line theory is used to calculate the load distribution along the wingspan. This case is presented in Chapter (4). Also the same approach was used to represent the NASCAR model inside the NASA Langley Research Center 14 by 22 Foot Subsonic Wind Tunnel, presented in Chapter (5). In this application point-source singularities are distributed over the

geometry of the model and their strengths are calculated from the measured pressure signature during the closed wall test section configuration.

In the second approach the surface of the model is divided into surface panels and their strengths are left as unknowns and calculated with the surface panels of the test section boundary. The Wright Flyer model and the Davis car model are represented using this method in the applications presented in Chapters (4) and (6) respectively. Figures (11) through (13) show examples of the methods used to represent the complex models. Full details of each of these models will be discussed in the following chapters.

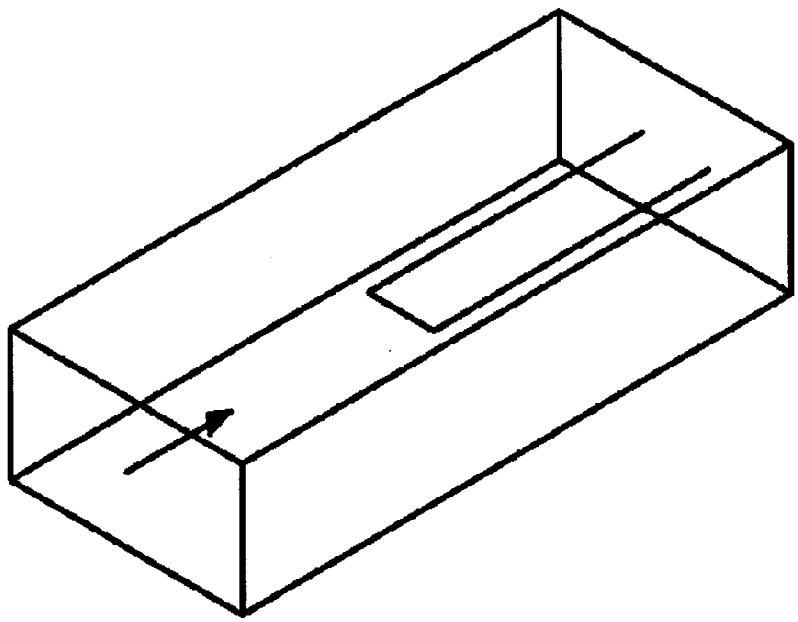

Figure (2-9) Representation of a small wing in a three-dimensional tests section using a horseshoe vortex.

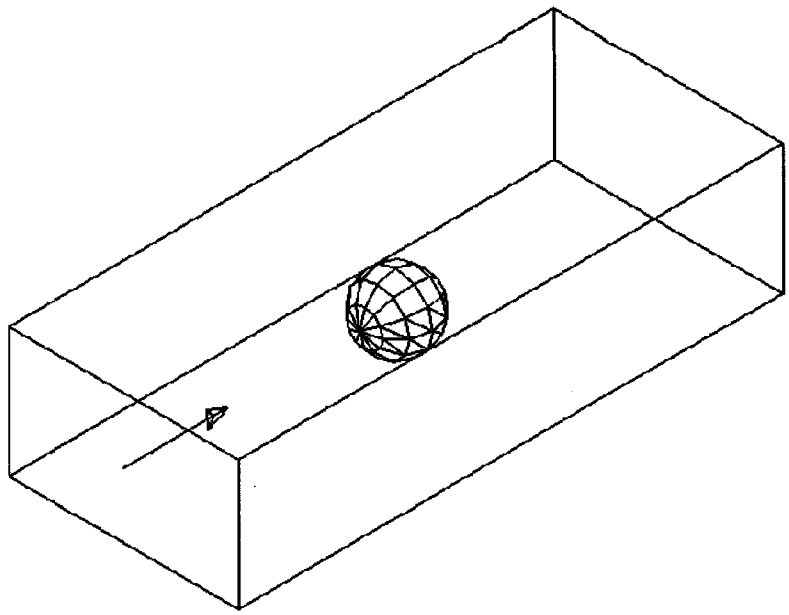

Figure (2-10) Representation of a spherical model in a three-dimensional test section using a point doublet.

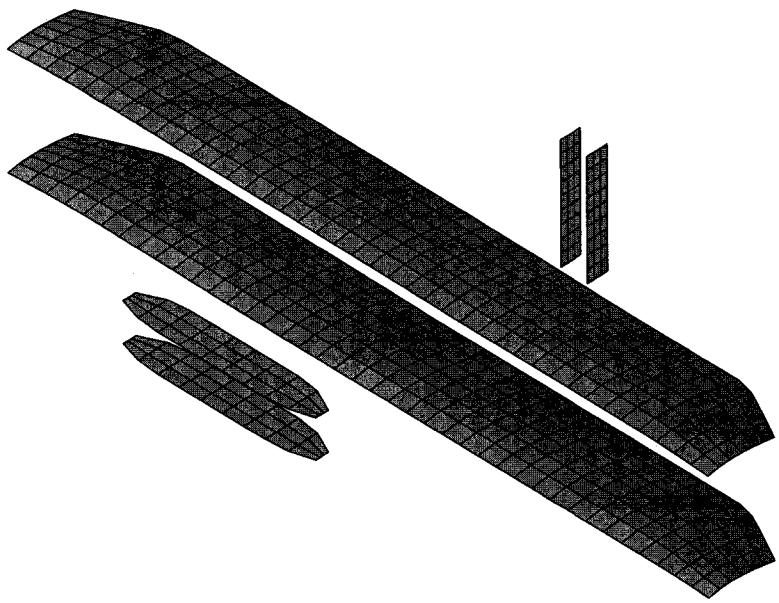

Figure (2-11) 720 vortex ring panels are used to represent the Wright Flyer replica, Chapter (4).

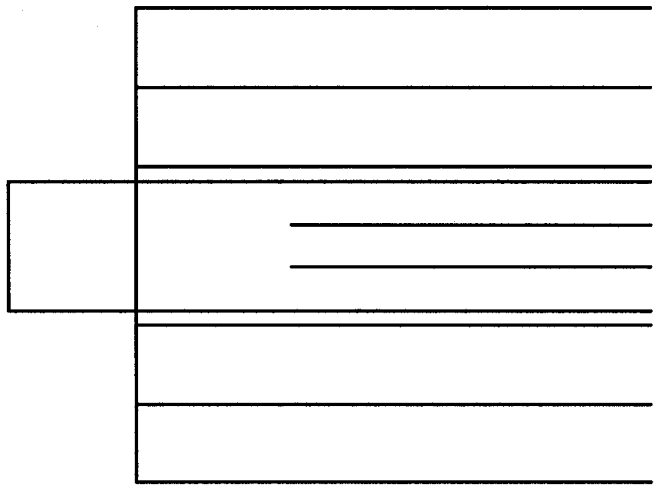

Figure (2-12) Wright Flyer replica represented using horseshoe vortices, Chapter (4).

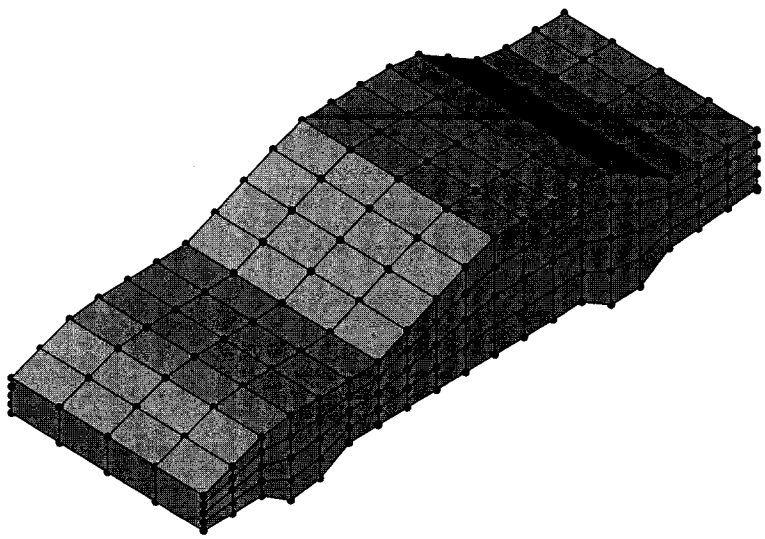

Figure (2-13) 420 point-source singularities are used to represent a NASCAR model, Chapter (5).

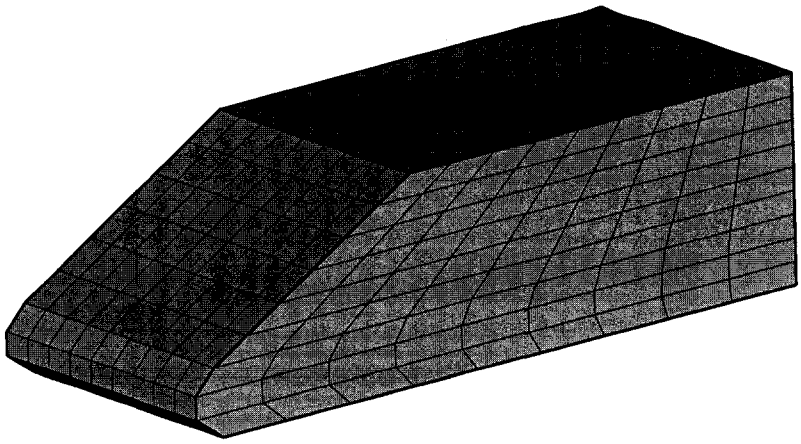

Figure (2-14) 486 vortex ring panels are used to represent a Davis model, Chapter (6).

2.9 Surface panels generation

Low-order surface panels are used in the present method, implemented as flat, constant strength, surface panels in 3D, or straight lines for 2D cases. Three types of surface panels are used in the present panel method: constant strength source, constant strength doublets, and vortex rings.

For 2D test sections, the formulae presented are in the panel's coordinate system. Before applying the boundary conditions the induced velocities have be transformed to the global coordinate systems. The origin point of the global coordinates is located at the center of the test section. The transformation between the coordinate systems is as follows:

$$\begin{Bmatrix} u_g \\ v_g \end{Bmatrix} = \begin{bmatrix} \cos\alpha & \sin\alpha \\ -\sin\alpha & \cos\alpha \end{bmatrix} \begin{Bmatrix} u_p \\ v_p \end{Bmatrix} \tag{2-31}$$

Where the subscript g and p refer to the global and the panel coordinate systems respectively and α is the panel inclination angle as shown in Figure (2-15). Points 1 and 2 are the panel boundaries and point c is the collocation point (the center of the panel) where the boundary condition is applied to solve for the strength of the panels and n is the unit normal vector of the panel. Both c and n are calculated from the panel boundaries (points 1 and 2).

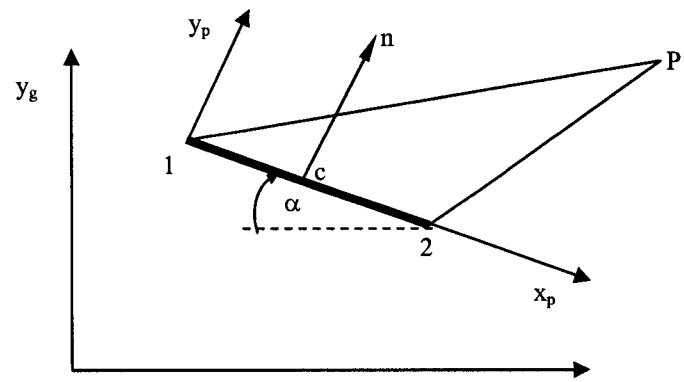

Figure (2-15) Panel and global coordinates.

The velocity components induced at any point P (x, y) by a constant strength 2D source panel, represented in the panel coordinate system (x_p, y_p), are as follows:[51]

$$u_p = \frac{\sigma}{4\pi}\ln\frac{(x-x_1)^2+y^2}{(x-x_2)^2+y^2} \tag{2-32}$$

$$v_p = \frac{\sigma}{2\pi}\left[\tan^{-1}\left(\frac{y}{x-x_2}\right)-\tan^{-1}\left(\frac{y}{x-x_1}\right)\right] \tag{2-33}$$

where, σ is the strength of the panel. The induced velocity components by a constant strength 2D doublet panel (oriented in the n direction) are obtained as follows:[51]

$$u_p = \frac{\mu}{2\pi}\left[\frac{y}{(x-x_1)^2+y^2}-\frac{y}{(x-x_2)^2+y^2}\right] \tag{2-34}$$

$$v_p = \frac{-\mu}{2\pi}\left[\frac{x-x_1}{(x-x_1)^2+y^2}-\frac{x-x_2}{(x-x_2)^2+y^2}\right] \tag{2-35}$$

where, μ is the strength of the doublet panel.

For 3D test sections, rectangular panels are used. The panel numbering starts at the downstream end of the studied domain. Figure (2-16) shows an example of dividing the boundaries of a rectangular test section into 70 surface panels. The corners of each panel are numbered in counter-clockwise direction as shown in Figure (2-17). The unit vector n for each panel is calculated as follows:

$$n = \frac{r_{13}\times r_{24}}{|r_{13}\times r_{24}|} \tag{2-36}$$

The collocation point c is located using the corners of the panels as follows:

$$r_c = \frac{r_1 + r_2 + r_3 + r_4}{4} \tag{2-37}$$

- where r is the position vector of the panel corners (1, 2, 3 and 4) and the collocation point c. Following this panel numbering approach ensures that the unit vector n for each panel is normal to its surface at the collocation point and is oriented toward the outside of the test section boundaries.

Two types of rectangular panels are used: constant strength source and vortex ring. The velocity component induced by a rectangular constant strength panel is: [51,52]

$$u = \frac{\sigma}{4\pi}\left[\begin{array}{l} \frac{y_2 - y_1}{d_{12}} \ln \frac{r_1 + r_2 - d_{12}}{r_1 + r_2 + d_{12}} + \frac{y_3 - y_2}{d_{23}} \ln \frac{r_2 + r_3 - d_{23}}{r_2 + r_3 + d_{23}} \\ + \frac{y_4 - y_3}{d_{34}} \ln \frac{r_3 + r_4 - d_{34}}{r_3 + r_4 + d_{34}} + \frac{y_1 - y_4}{d_{41}} \ln \frac{r_4 + r_1 - d_{41}}{r_4 + r_1 + d_{41}} \end{array}\right] \tag{2-38}$$

$$v = \frac{\sigma}{4\pi}\left[\begin{array}{l} \frac{x_2 - x_1}{d_{12}} \ln \frac{r_1 + r_2 - d_{12}}{r_1 + r_2 + d_{12}} + \frac{x_3 - x_2}{d_{23}} \ln \frac{r_2 + r_3 - d_{23}}{r_2 + r_3 + d_{23}} \\ + \frac{x_4 - x_3}{d_{34}} \ln \frac{r_3 + r_4 - d_{34}}{r_3 + r_4 + d_{34}} + \frac{x_1 - x_4}{d_{41}} \ln \frac{r_4 + r_1 - d_{41}}{r_4 + r_1 + d_{41}} \end{array}\right] \tag{2-39}$$

$$w = \frac{\sigma}{4\pi}\left[\begin{array}{l} \tan^{-1}\left(\frac{m_{12}e_1 - h_1}{zr_1}\right) - \tan^{-1}\left(\frac{m_{12}e_1 - h_2}{zr_2}\right) + \tan^{-1}\left(\frac{m_{23}e_2 - h_2}{zr_2}\right) \\ - \tan^{-1}\left(\frac{m_{23}e_3 - h_3}{zr_3}\right) + \tan^{-1}\left(\frac{m_{34}e_3 - h_3}{zr_3}\right) - \tan^{-1}\left(\frac{m_{34}e_4 - h_4}{zr_4}\right) \\ + \tan^{-1}\left(\frac{m_{41}e_4 - h_4}{zr_4}\right) - \tan^{-1}\left(\frac{m_{41}e_1 - h_1}{zr_1}\right) \end{array}\right] \tag{2-40}$$

- where:

$$d_{12} = \sqrt{(x_2 - x_1)^2 + (y_2 - y_1)^2}$$
$$d_{23} = \sqrt{(x_3 - x_2)^2 + (y_3 - y_2)^2}$$
$$d_{34} = \sqrt{(x_4 - x_3)^2 + (y_4 - y_3)^2}$$
$$d_{41} = \sqrt{(x_1 - x_4)^2 + (y_1 - y_4)^2}$$

$$m_{12}=\frac{y_2-y_1}{x_2-x_1},\ m_{23}=\frac{y_3-y_2}{x_3-x_2},\ m_{34}=\frac{y_4-y_3}{x_4-x_3},\ m_{41}=\frac{y_1-y_4}{x_1-x_4}$$

$$r_k=\sqrt{(x-x_k)^2+(y-y_k)^2+z^2},\quad k=1,2,3,4$$

$$e_k=(x-x_k)^2+z^2,\quad k=1,2,3,4$$

$$h_k=(x-x_k)(y-y_k),\quad k=1,2,3,4$$

For the vortex ring panels, the velocity induced (u, v, w) at any point p can be calculated as follows:[51]

$$(u,v,w)=\frac{\Gamma}{4\pi}\left[\begin{array}{l}\dfrac{r_{1p}\times r_{2p}}{|r_{1p}\times r_{2p}|}r_{12}\cdot\left(\dfrac{r_{1p}}{|r_{1p}|}-\dfrac{r_{2p}}{|r_{2p}|}\right)+\dfrac{r_{2p}\times r_{3p}}{|r_{2p}\times r_{3p}|}r_{23}\cdot\left(\dfrac{r_{2p}}{|r_{2p}|}-\dfrac{r_{3p}}{|r_{3p}|}\right)\\ +\dfrac{r_{3p}\times r_{4p}}{|r_{3p}\times r_{4p}|}r_{34}\cdot\left(\dfrac{r_{3p}}{|r_{3p}|}-\dfrac{r_{4p}}{|r_{4p}|}\right)+\dfrac{r_{4p}\times r_{1p}}{|r_{4p}\times r_{1p}|}r_{41}\cdot\left(\dfrac{r_{4p}}{|r_{4p}|}-\dfrac{r_{1p}}{|r_{1p}|}\right)\end{array}\right] \tag{2-41}$$

- where, Γ is the vortex ring panel strength and the position vector r is defined as follows:

$$r_{kp}=r_p-r_k\qquad k=1,2,3,4$$

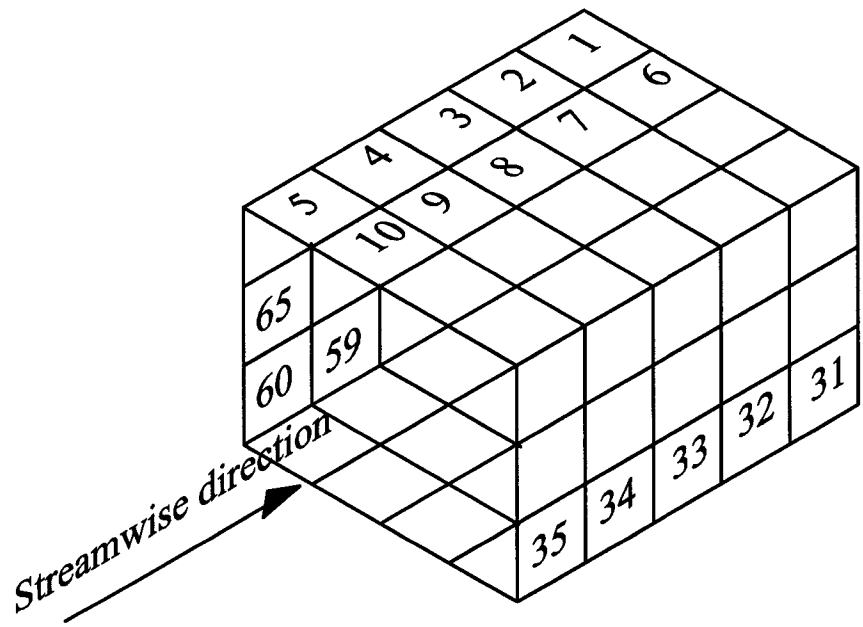

Figure (2-16) Surface panel numbering

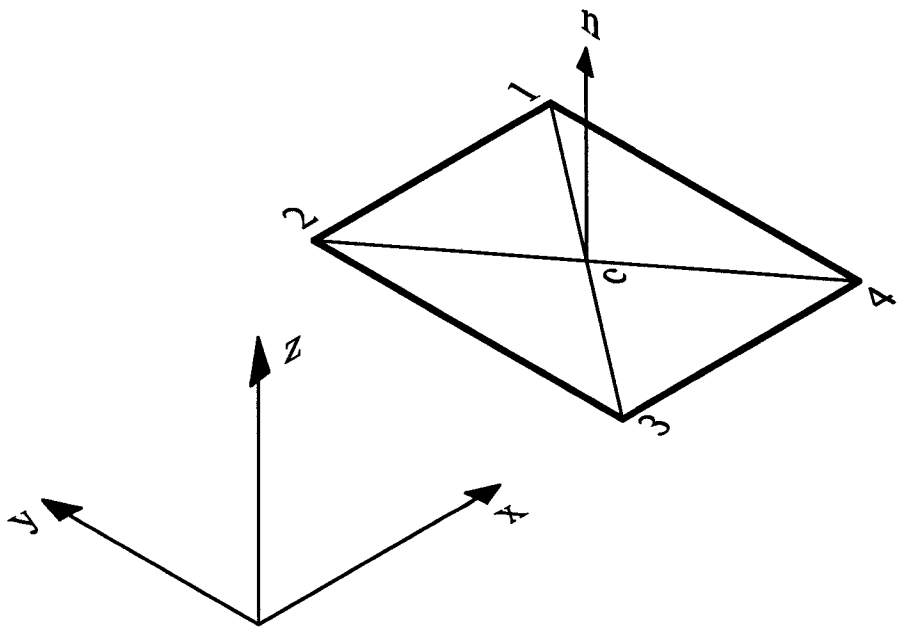

Figure (2-17) A sketch of a rectangular surface panel.

To solve for the strengths of the panels, defined above, the boundary conditions are applied at the collocation point c of each panel. For the Neumann boundary condition (zero velocity normal to the boundaries), at each collocation point the summation of the velocity component parallel to the unit vector n is equal to zero. This includes the velocity components induced by the model representation, other panels on the test section boundaries, and the velocity component of the oncoming stream U_∞. This summation leads to a set of linear algebraic equation in the form:

$$[A]\{\Gamma\} = \{RHS\} \tag{2-42}$$

The size of the matrix [A] is N×N where N is the total number of surface panels and its elements ($a_{i,j}$) are the velocity component per unit strength induced by the surface panel number j at the collocation point number i. The vector $\{\Gamma\}$ is the unknown strengths of the panels its size is N elements. The vector {RHS} is the known information including the oncoming stream component parallel to the unit normal and the velocity induced by the model representation. Due to the choice of panel singularity, the matrix A is very

well-conditioned and yields a (correct) zero solution for the empty test section case. The matrices $a_{i,j}$ and RHS_i can be defined as follows:

$$a_{i,j} = \frac{v_{i,j}}{\Gamma_j} \cdot n_i \tag{2-43}$$

$$RHS_i = (U_\infty + v_{m,i}) \cdot n_i \tag{2-44}$$

- where $v_{m,i}$ is the velocity induced by the model representation at the collocation point i. It is important to note that if the geometry of the model is complex, such as the cases presented in Chapters (4), (5) and (6), then its surface is divided into surface panels and $v_{m,i}$ does not appear in the RHS of Equation (2-44). Instead the boundary condition is applied at each collocation point of the model panels and the total number of unknowns in the left hand side is increased to include both the test section and model surface panels.

By solving the set of algebraic equations shown in Equation (2-42) the unknown strengths of the surface panels are obtained and the information required to calculate the boundary deformation is available. In the boundary deformation step of the solution, the displacement is calculated using the one-step method, described before in Equation (2-20). This displacement is introduced at the panel corners (or ends for 2D cases) starting at the downstream end of the numerical domain following the panel numbering convention discussed before, shown in Figure (2-16). Since both the collocation point c and the unit vector n for each surface panel are calculated from the panel corners, they are automatically adjusted to follow the introduced deformation. The new deformed boundaries are solved again for the strengths of the surface panels and the process is repeated until the open jet boundary condition is satisfied (constant pressure).

2.10 Selection of the surface panel size

To eliminate the effect of the panel size on the obtained results, a parametric study was performed to select the suitable number of surface panels that can adequately capture the details of the flow changes inside the test section. A set of results is developed for the same test conditions and the same model information using several sizes of surface panels. For example, consider a rectangular test section of 21.76 feet width, 14.5 feet height and 50 feet length, which are the dimensions of the test section of the NASA Langley Research Center 14 by 22 Foot Subsonic Wind Tunnel. The model is represented using a single horseshoe of strength 200 ft^2/s and span 4 feet, and the nominal tunnel speed is 30 ft/s. The horseshoe location is (25, 0, 0). Figure (2-18) shows the layout of the test section and the model representation. The detailed physical analysis of this case will be presented in Chapter (3). The focus here is to show the sensitivity of panel model to the number of surface panels used.

Five cases are presented in Figures (2-19) through (2-28) for 180, 360, 600, 1260, and 2100 surface panels. Vortex ring panels are used in this study. The results are presented in pairs, the first of which is the surface panels and the second is the predicted upwash interference factor $\Delta\alpha$ in radian on a plane passing through the test section center. Nearly no variation of the predicted upwash can be observed from the figures. For further comparison, the distributions of the upwash along the test section centerline for all the cases are presented in Figure (2-29). Again no significant variation can be observed between the different cases except near to the end of the test section starting just downstream of the maximum value. In this region, the unconstrained end of the test section decreases the accuracy of the present model. This problem will disappear when solving test sections with extended lengths or when including the collector geometry, as will be shown in the following chapters. Table (2-1) shows a summary of the surface panels used, the upwash interference factor at the model locations, and the maximum upwash magnitude and location.

Usually in numerical methods, such as finite difference approaches, this kind of grid analysis shows a greater sensitivity of the solution than the level observed here. Even for regular panel methods, where the flow is simulated to calculate the drag and lift forces, the solution typically shows more sensitivity to panel sizes. The main difference here is that the interference assessment is a second-order effect of the flow and only the far-field signature of the model is detected by boundaries. In other words, the fine details of the flow structure around the model are not captured by the boundaries.

Some of the presented work in the literature used very few surface panels such as Joppa[26] who used only 16 surface panels in his similar study. Others such as Holt and Hunt[27] used 192 surface panels while Mokry[29] used 759 surface panels in his automotive analysis. In each case of the applications presented in the following chapters, a similar parametric study was performed using different number of surface panels to ensure that the results were not grid dependent. The ranges used are within the number of surface panels reported in the literature for similar cases.

Number of panels	Panel size (ft × ft)	Upwash at the model location (x=25 ft)	Maximum upwash	
			Magnitude	Location (ft)
180	5.55 × 3.66	0.02012	0.03837	37.29
360	3.57 × 2.75	0.01986	0.03818	37.20
600	2.63 × 2.20	0.01986	0.03808	37.16
1260	1.72 × 1.57	0.01984	0.03797	37.16
2100	1.02 × 1.57	0.01996	0.03788	37.22

Table (2-1) Comparison between the upwash interference $\Delta\alpha$ (radian) developed using different panel sizes

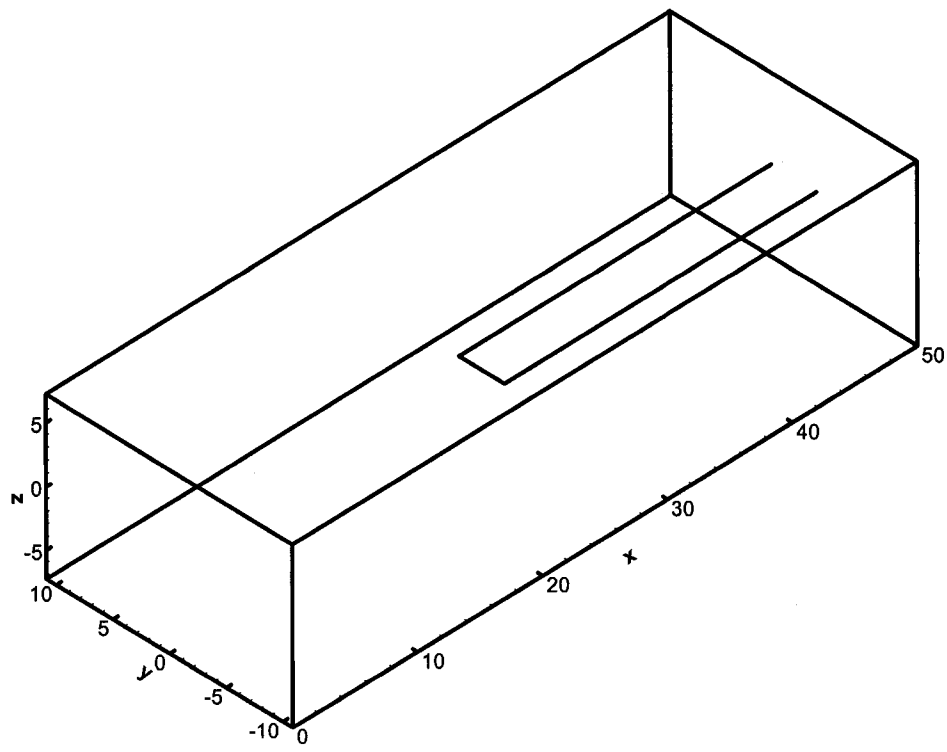

Figure (2-18) Horseshoe model representation inside a rectangular test section.

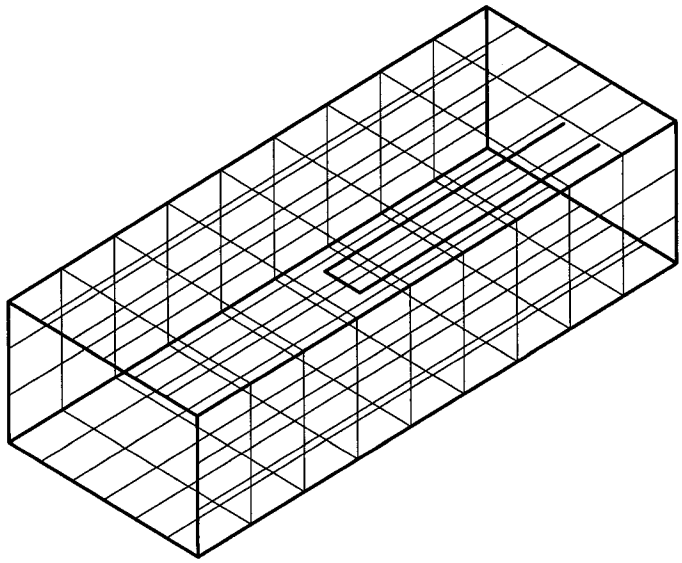

Figure (2-19) Test section boundaries divided into 180 surface panels.

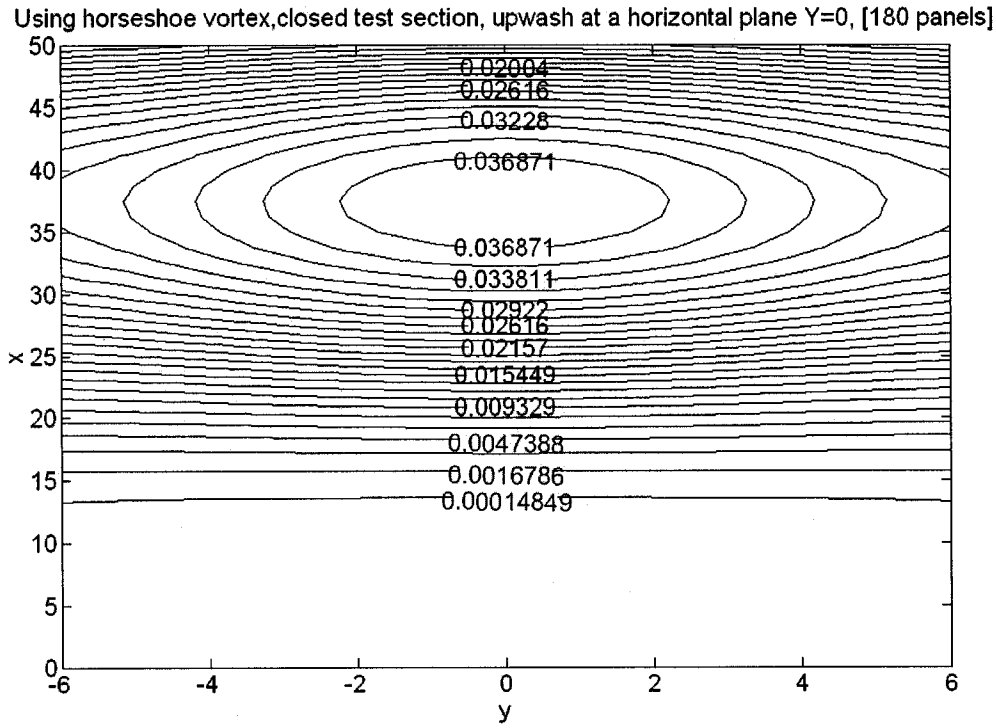

Figure (2-20) Upwash interference $\Delta\alpha$ (radian) at a horizontal plane using 180 surface panels.

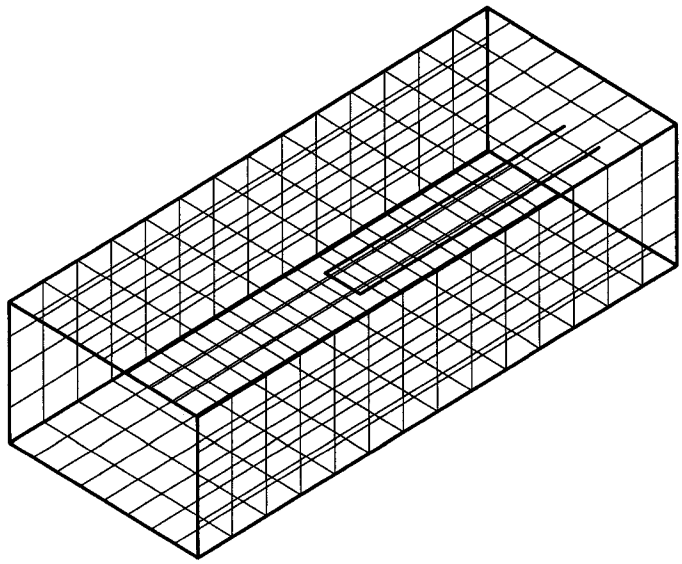

Figure (2-21) Test section boundaries divided into 360 surface panels.

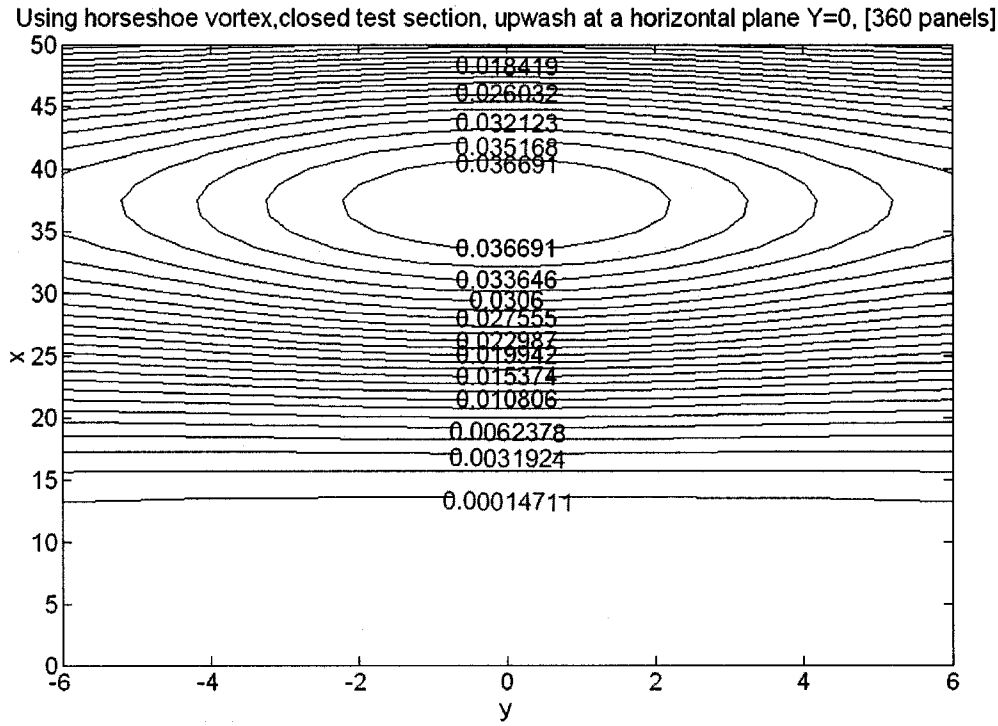

Figure (2-22) Upwash interference $\Delta\alpha$ (radian) at a horizontal plane using 360 surface panels.

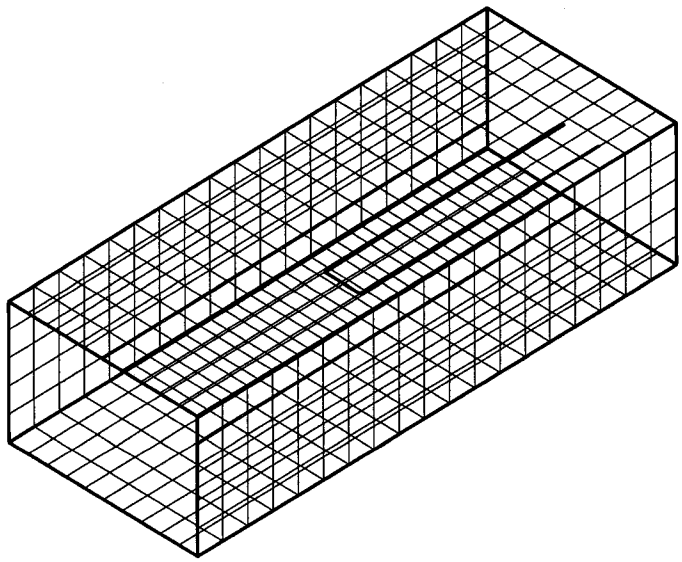

Figure (2-23) Test section boundaries divided into 600 surface panels.

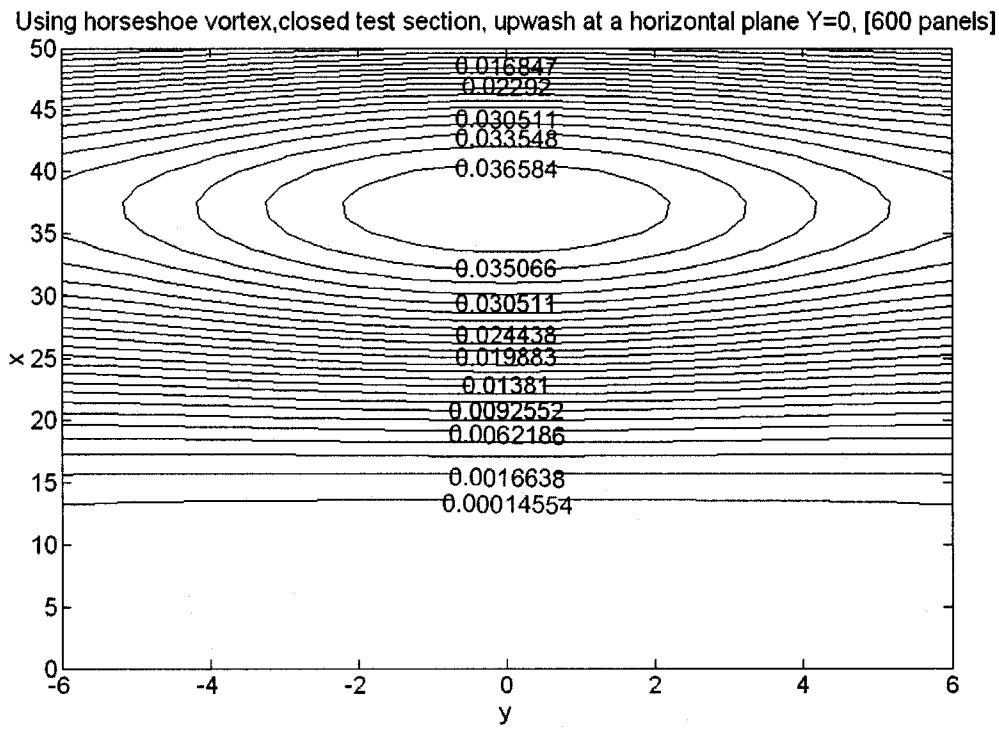

Figure (2-24) Upwash interference $\Delta\alpha$ (radian) at a horizontal plane using 600 surface panels.

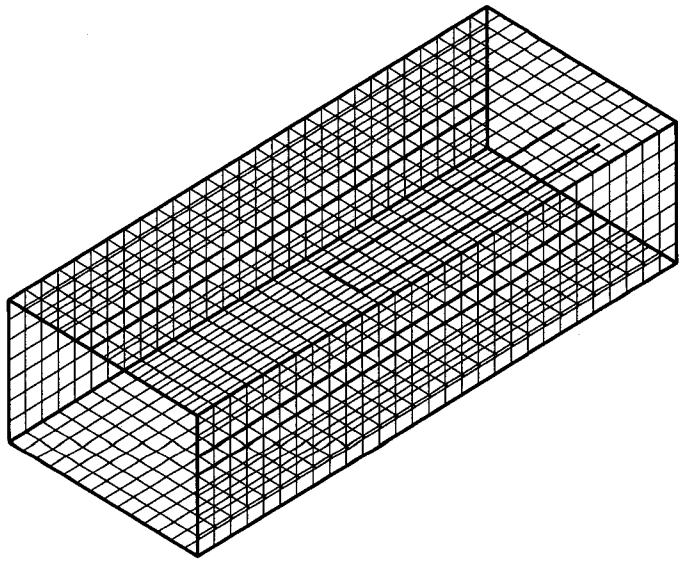

Figure (2-25) Test section boundaries divided into 1260 surface panels.

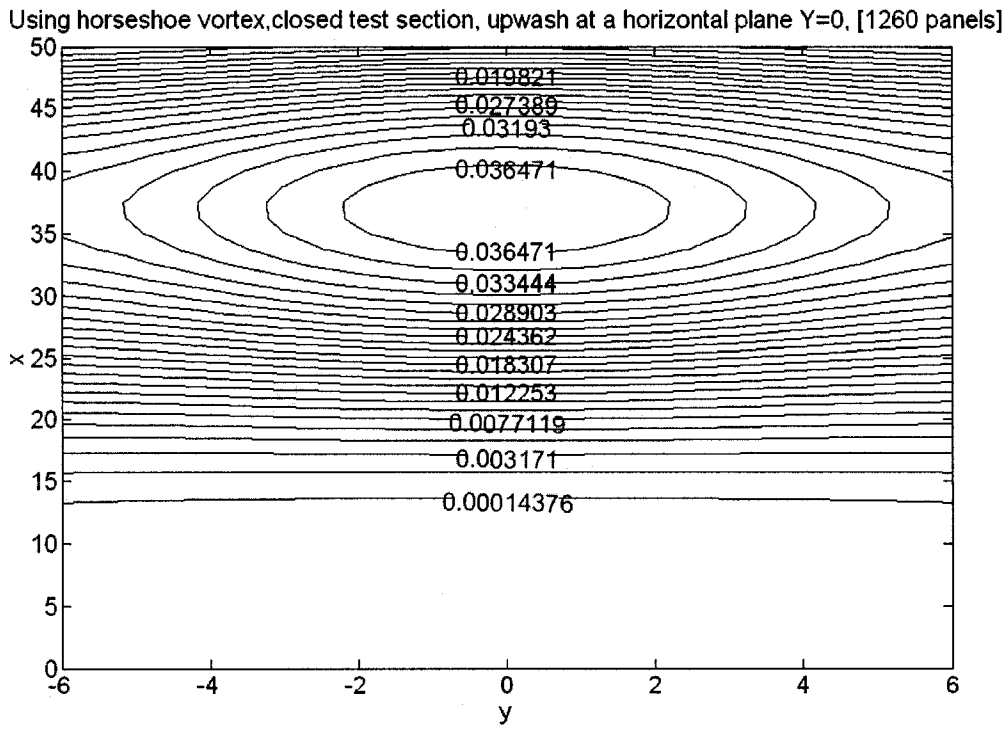

Figure (2-26) Upwash interference $\Delta\alpha$ (radian) at a horizontal plane using 1260 surface panels.

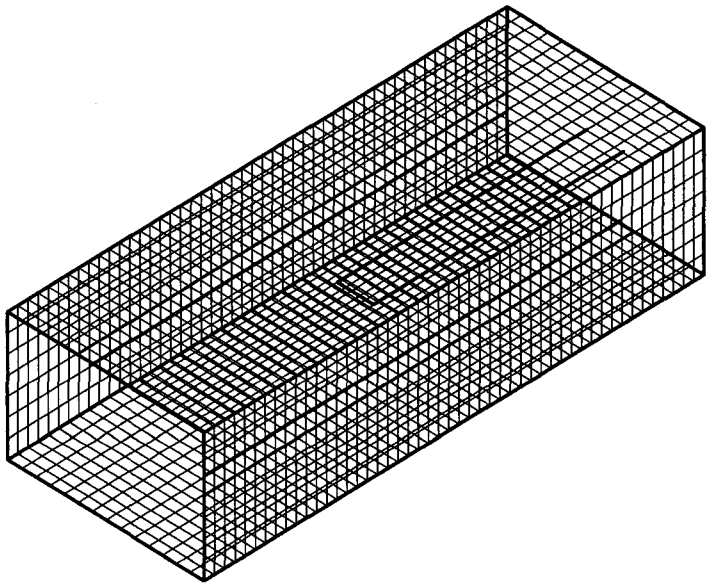

Figure (2-27) Test section boundaries divided into 2100 surface panels.

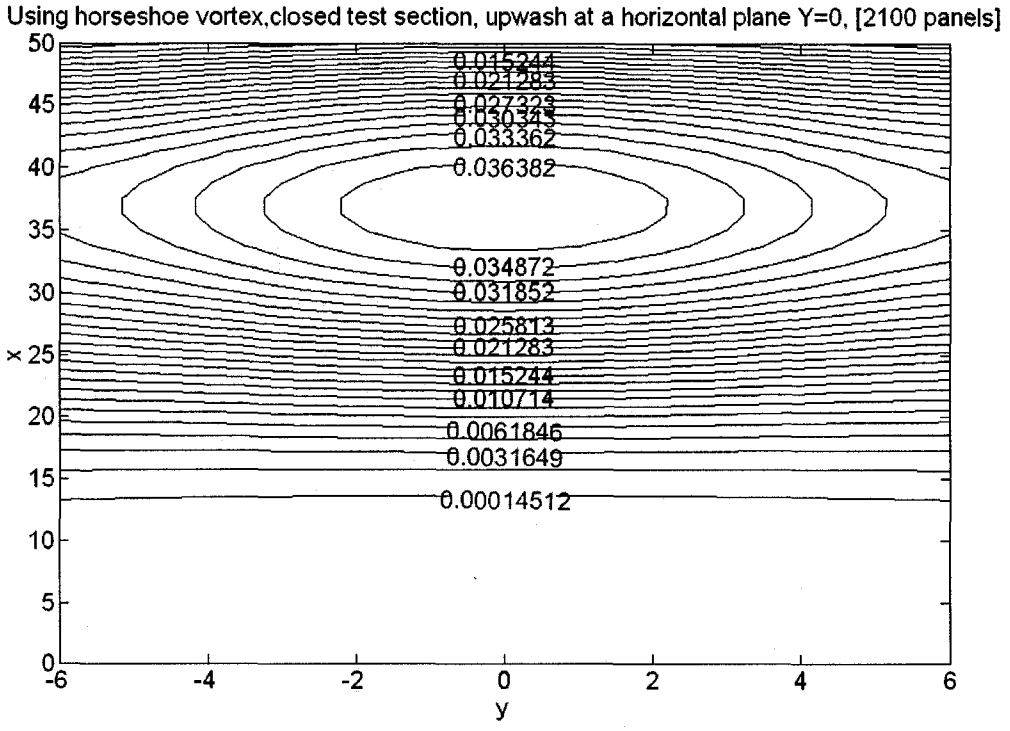

Figure (2-28) Upwash interference at a horizontal plane using 2100 surface panels.

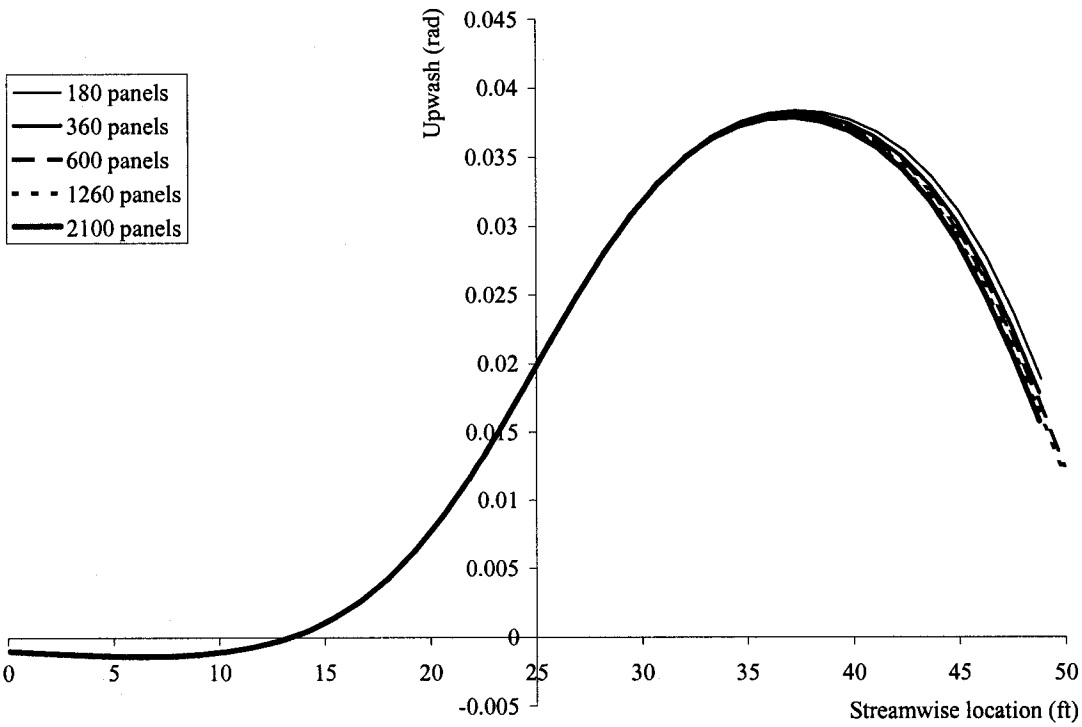

Figure (2-29) Distribution of the upwash interference $\Delta\alpha$ along the test section centerline for a model represented by a horseshoe vortex inside a rectangular test section..

CHAPTER III

III. COMPARISON TO THE METHOD OF IMAGES

The objective of this chapter is to compare the newly developed approach to the classical method of images. Several model representations are investigated using both the present method and the method of images including two- and three-dimensional test sections for both lifting and non-lifting models. The comparison between the new method and the method of images is done in three levels. First, comparison is based on closed test section cases. The objective of this comparison is to evaluate the ability of the new method to match the method of images within the latter's limitations. In the second level of comparison, open jet test section cases are used with no deformation considered. This step is a second check for the ability of the new method to match the method of images. Finally, results for fully-deformed open jet test section cases obtained by the new method are compared to those obtained by the method of images (with no deformation). The objective of this step is to show the importance of including the boundary deformation in the boundary interference assessment. Taken together, the three levels of comparison present a fair incremental evaluation of the new method against the classical method of images. The model sizes and the test section geometries are chosen to be within the limits of the accuracy of the method of images, which are discussed more fully in the following section.

3.1 Concepts of the method of images

The method of images assumes small relative model size inside an infinitely long constant cross-section test section. The far-field effect of the model is represented using elementary analytical singularities placed at its location. For example, from potential flow theory a point vortex (or in 3D a line vortex) can represent lift, a point doublet can represent model volume and a point source can represent the displacement effect of the wake.

Two boundary conditions may be imposed according to the type of the test section:

a. No flow normal to the walls for closed test sections

$$\frac{\partial \phi}{\partial n} = 0 \tag{3-1}$$

b. Constant pressure at the jet boundaries for open test sections

$$\frac{\partial \phi}{\partial x} = \text{Constant} \tag{3-2}$$

- where n is the unit normal to the walls and x is the streamwise coordinate which may be replaced by the tangential coordinate if boundary deformation is considered.

These boundary conditions can be satisfied by placing images of the singularities representing the model on the other sides of the test section boundaries. The objective is to cancel a component of the perturbation velocity; either the normal for closed wall test sections or the streamwise for open jet test sections. For example, with a 2D test section the lifting effect can be represented using a point vortex as shown in Figures (3-1) and (3-2). For closed wall boundary conditions, the normal velocity component has to be canceled by the image singularity. This means the image singularity must have the same magnitude and opposite strength, as shown in Figure (3-1). On the other hand, for open jet boundary conditions, the image singularity must have the same magnitude and strength to cancel the streamwise component as shown in Figure (3-2). It is important to note that the method of images does not account for the boundary deformation that might be expected for the open test section. In other words, **the correct boundary conditions are satisfied, but at an incorrect boundary**. Also, it is important to note that if the model is represented by any even function with respect to n and x such as a point source, to satisfy the boundary conditions in Equations (3-1) and (3-2) the strength of the images must be the same for closed walls and opposite for open jet test sections.

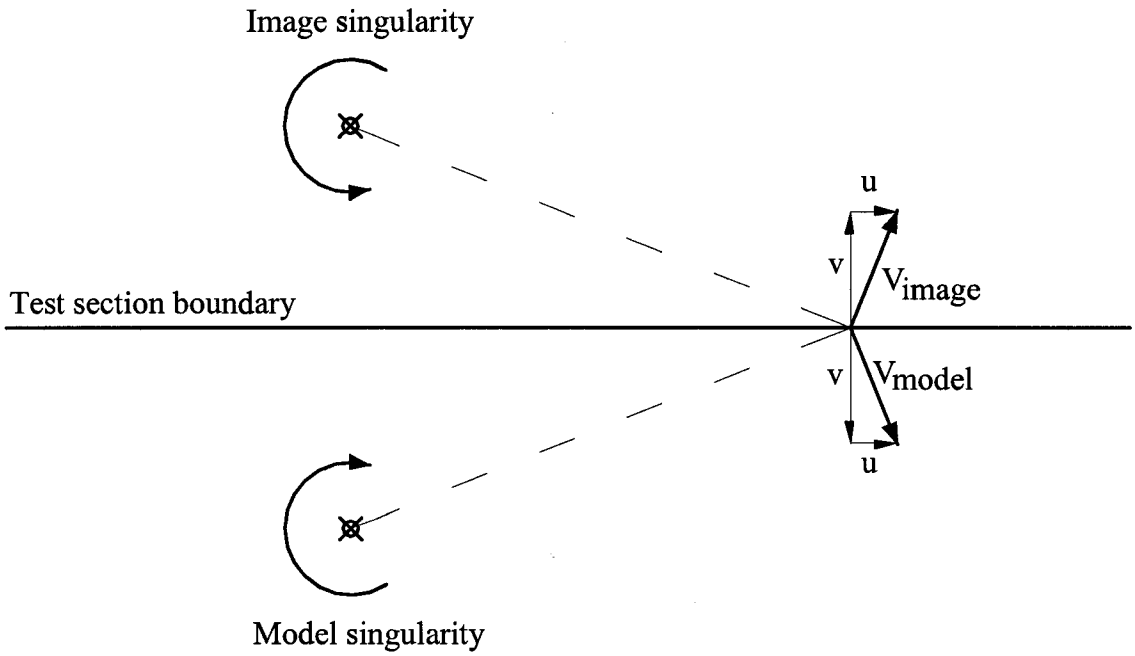

Figure (3-1) Method of images for a closed wall boundary

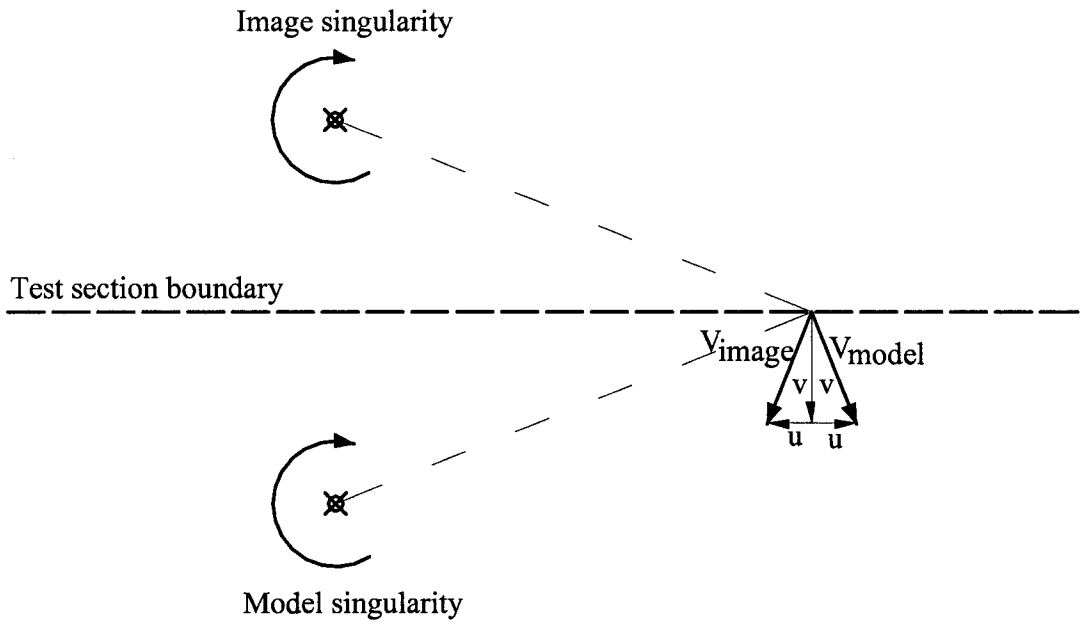

Figure (3-2) Method of images for an open jet boundary

The presence of more than one test section boundary requires the use of multiple images. In fact it is necessary, as recommended in the literature, to have an infinite array of images. For example, for a two-dimensional test section the presence of the image for the floor violates the boundary conditions on the ceiling and requires a second image above the ceiling. The same happens for the floor, which results in the generation of an infinite set of singularities, with the appropriate strengths as discussed before, equally spaced and aligned above and below the test section boundary as shown in Figure (3-3). For three-dimensional rectangular test sections a doubly infinite system of images is required with singularities in all four quadrants because of the interaction between the horizontal and the vertical boundaries. Figure (3-4) shows an example for the method of images for a three-dimensional rectangular test section. Analytic expressions representing summations of the effects of the infinite arrays of images are available for simple geometries, particularly in two dimensions.

If the model is represented using more than one singularity, the method of images can still be used if the above-discussed rules for choosing the image strengths are carefully applied. For complex test section geometry, some difficulty may exist in arranging the images to satisfy the necessary boundary conditions on the test section boundaries and more advanced methods may be needed. It should be noted, as discussed in Chapter (2), that the interference field of the image singularities can be replaced by singularity distributions along the boundaries (i.e. by paneling the boundaries).

In some cases (2D cases presented below for example) an analytic solution for the summation of the effects of the image array was available and was used. In more complex cases (Chapter (4) for example), the images are summed numerically until convergence is observed to some tolerance.

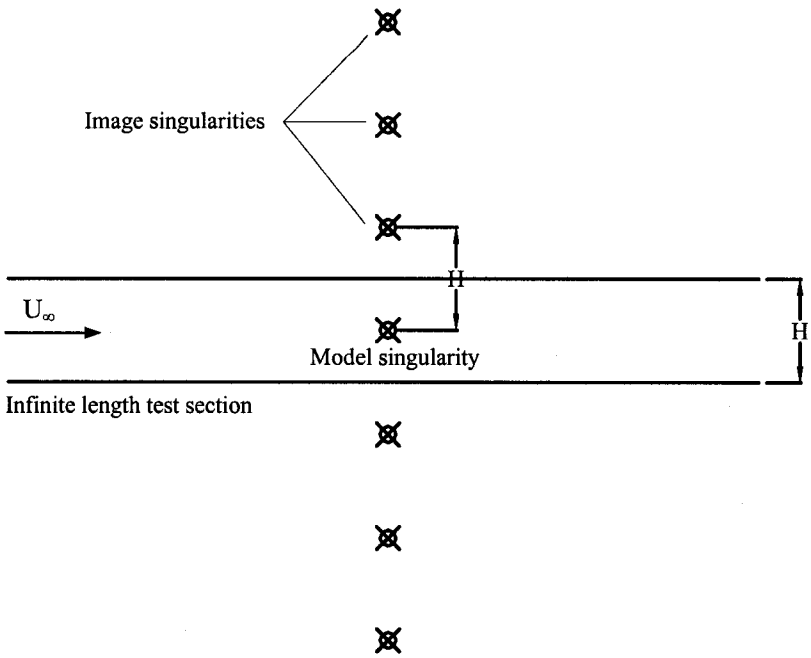

Figure (3-3) Sketch of the method of images for a 2D test section.

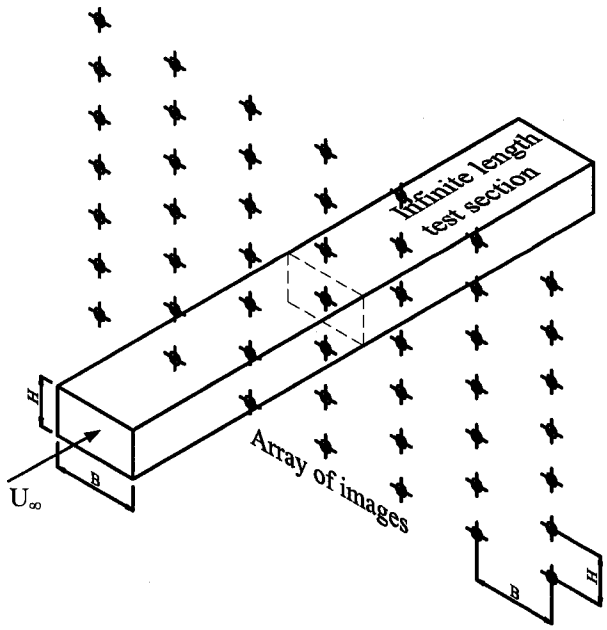

Figure (3-4) Sketch of the method of images applied to a 3D test section.

3.2 2D non-lifting model

The boundary interference of a simple 2D cylinder model on the centerline of a test section is considered. Interference from analytic image method solutions will be compared to results from paneled test section boundaries in order to evaluate the accuracy of the latter and to investigate the effect of test section length. A 2D point doublet represents the cylinder. Figure (3-5) shows the surface panels' boundaries, collocation points, and the model in the center of the test section where the dimensions shown are in feet. The size of the test section is chosen to be a two dimensional version of the Langley Full Scale Tunnel (LFST) test section with approximately equal external dimensions (30 ft height and 60 ft length), although of course the results represent generic trends for a test section of similar proportions (length/height = 2). Constant strength source panels are used. The comparison study includes both closed and open test sections with long (length/height = 20) and limited (length/height = 2) lengths.

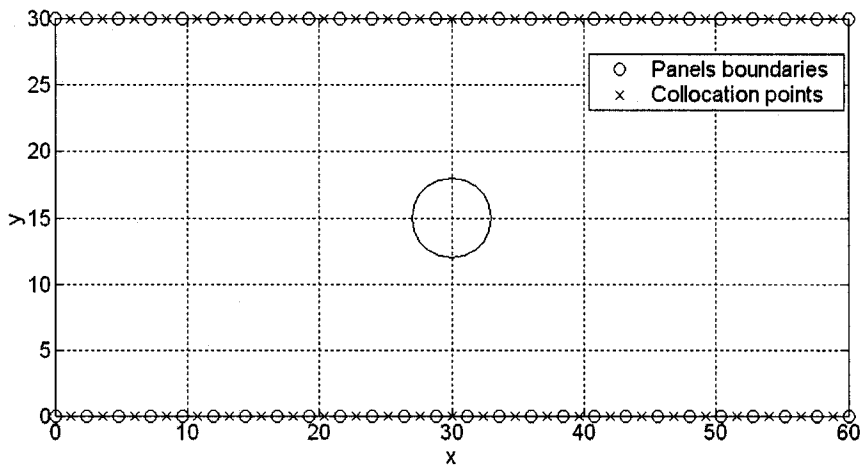

Figure (3-5) Surface panels and the model at the center of a 2D test section - dimensions are in feet.

Figure (3-6) shows the boundary interference at the center of the 2D point doublet (2D cylinder) for area ratios up to 35% for a closed wall long test section (10 times realistic length, length/height = 20), where the area ratio is the model frontal area divided by the test section cross-sectional area. The blockage and the upwash interference factors are calculated using the induced velocity components as follows:

$$\varepsilon = \frac{u_{int}}{U_\infty} \tag{3-3}$$

$$\Delta\alpha = \frac{v_{int}}{U_\infty} \tag{3-4}$$

Since the 2D doublet represents a non-lifting model, the upwash interference factor, $\Delta\alpha$, is zero. Excellent matching to the method of images can be observed through nearly the whole studied range of area ratios. The interference of a closed test section with a realistic length (length/height = 2.0) is shown in Figure (3-7). For the blockage factor ε, the obtained results agree well with the method of images. The observed small difference at high area ratios is due to the effect of the unconstrained ends of the test section solved in the present method. This effect may also exist for low area ratio models if their location is close to the test section ends. In such cases either the nozzle or/and the diffuser may have to be considered in the solution. Further details of the effect of the test section length and model location are discussed in the applications presented in Chapters (5) and (6).

For open jet test sections, the boundary interference factors (ε and $\Delta\alpha$) at the center of the test section are presented in Figure (3-8), plotted against the area ratio for a long test section (length/height = 20). Again, the upwash factor is zero due to the non-lifting model. A complete matching between the two methods is not achieved here because the method of images does not account for deformation of the test section boundaries while the present method does. As the area ratio increases, the difference between the two methods decreases. This does not mean the two methods are converging but could be due to the limited accuracy of using a point doublet to represent a cylinder at high area ratio, which has a significant effect on the predicted boundary deformation. This suggests the use of a more accurate method to represent the model at high area ratios. For example the model surface can be divided into panels with strengths obtained separately from the

measured forces or calculated during the solution for the test section panels, as will be shown in the following chapters.

Figure (3-9) shows the interference factors for a realistic length open test section (length/height = 2). Compared to the long test section results (length/height = 20) shown in Figure (3-6), the difference between the present approach and the method of images is larger. Since the only difference between the two cases is the length of the test section, it seems certain that the unconstrained ends of the test section have caused this effect. In other words, the unconstrained ends of the finite length test section add negative blockage interferences, which appear as a decrease in the predicted blockage for closed wall test sections and an increase in the negative blockage for the open jet test sections

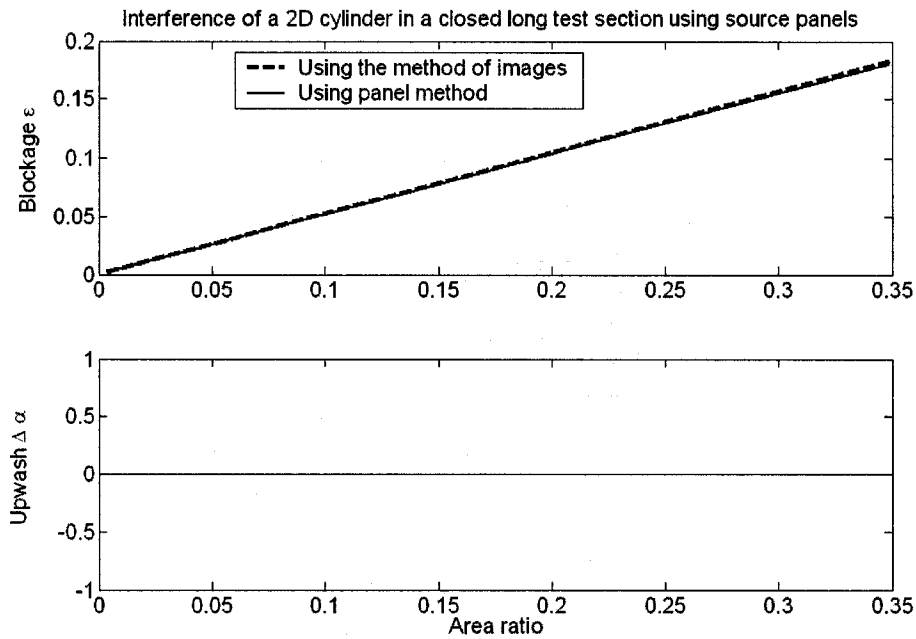

Figure (3-6) Wall interference of a 2D cylinder inside a closed long test section (Length/Height = 20)

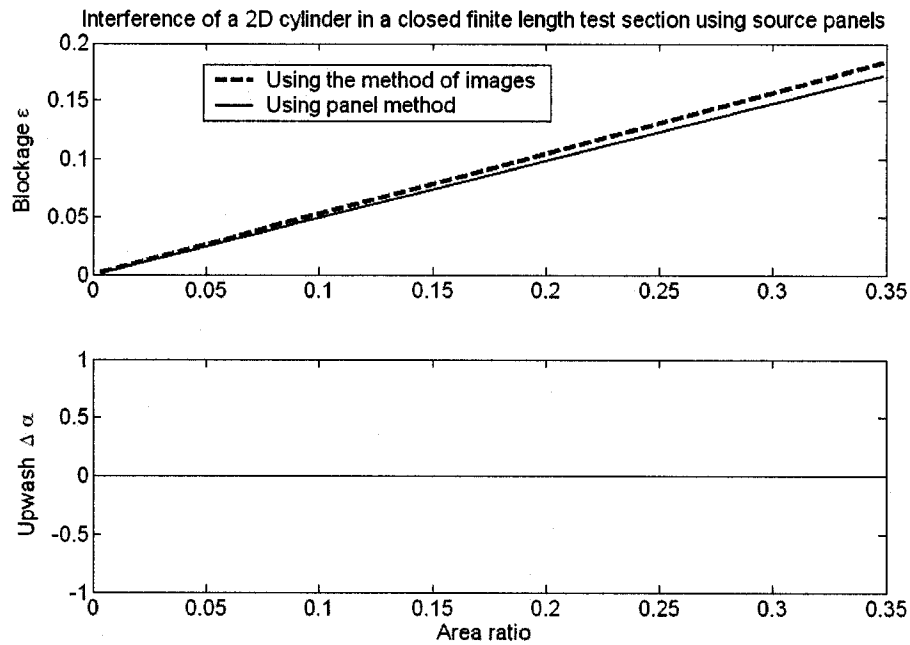

Figure (3-7) Wall interference of a 2D cylinder inside a closed finite length test section (Length/Height = 2)

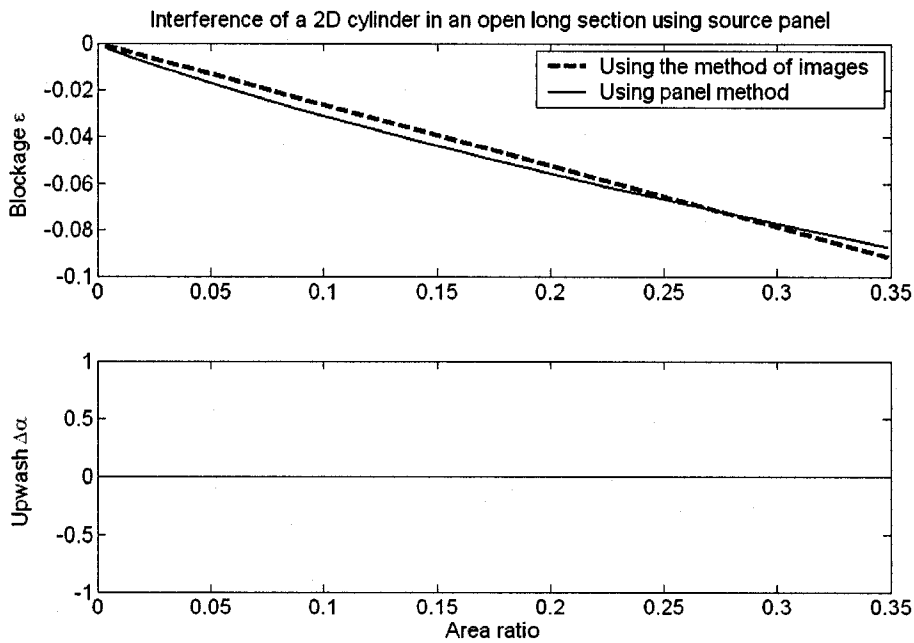

Figure (3-8) Boundary interference of a 2D cylinder inside an open long test section (Length/Height = 20)

In the results presented so far for boundary interference of a 2D cylinder, excellent matching between the new panel method and the method of images was obtained in the long closed test section case. Small differences were observed for the limited length closed test section and it was clear for this case that this difference is due to the simulated test section length because the method of images assumes infinite test section length. For the open jet test section cases, full matching was not expected because the present panel method accounts for the boundary deformation while the method of images does not. Thus, reasonable matching was achieved for long test section and less matching was observed for the finite length test section. Now to be sure that the difference observed in the open jet test section cases are only due to boundary deformation, the present method is used to predict the boundary interference for open jet test section with un-deformed boundaries.

Figure (3-10) shows the predicted boundary interference for a 2D model representation inside a long (length/height =20) open test section with un-deformed boundaries. Again excellent matching between the method of images and present method is achieved confirming that the observed difference in the fully-deformed open jet case shown in Figure (3-8) is only due to the effect of the boundary deformation, which is not accounted for in the classical method of images.

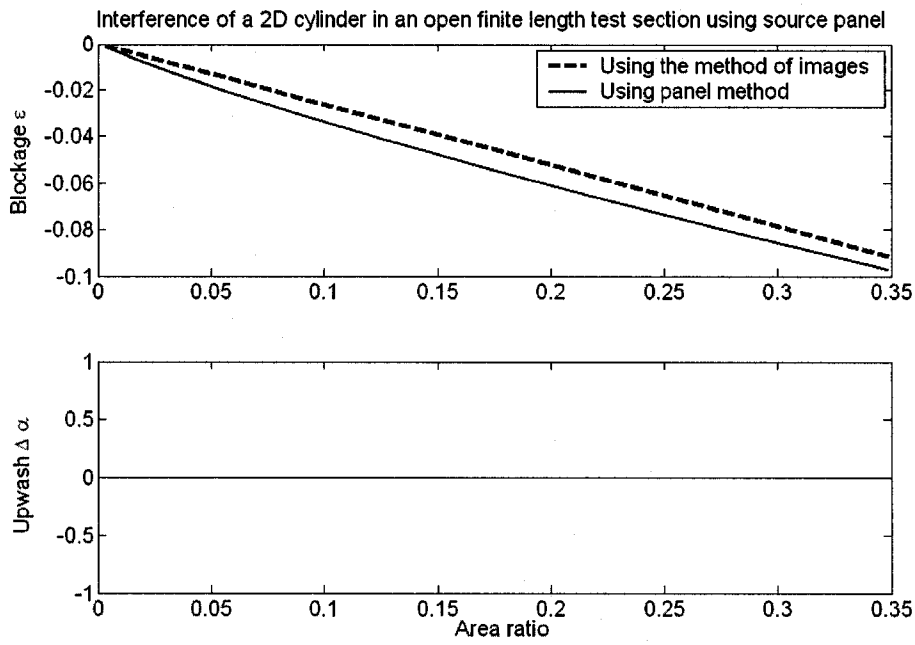

Figure (3-9) Boundary interference of a 2D cylinder inside an open finite length test section (Length/Height = 2)

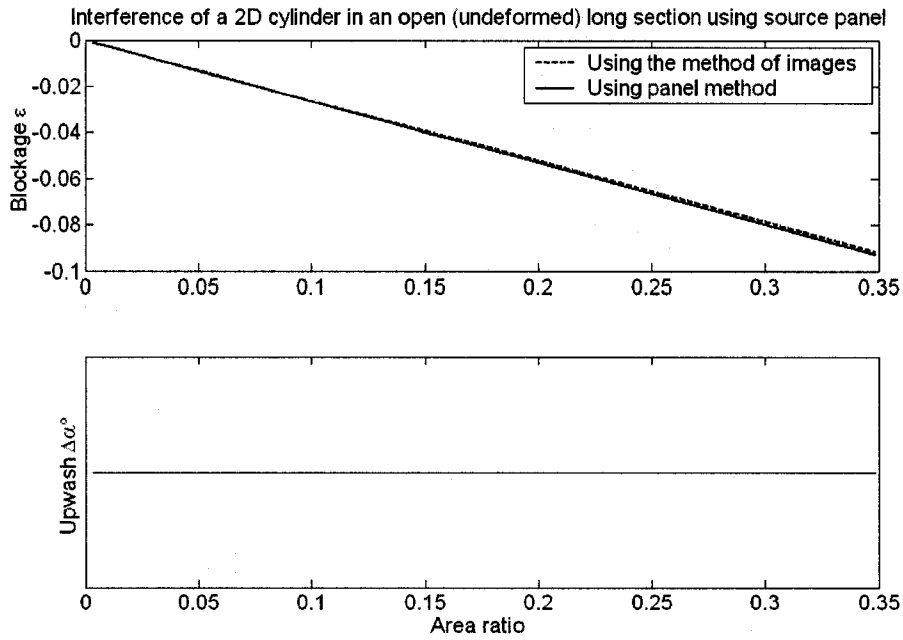

Figure (3-10) Boundary interference of a 2D cylinder inside an open (un-deformed) long test section (Length/Height = 20)

3.3 3D non-lifting model

To extend the verification of the present method against the method of images to 3D, the interference of a non-lifting sphere (represented by a 3D point doublet with its axes parallel to the oncoming stream as descried in Chapter 2) in a rectangular test section is considered. The dimensions of the test section are again taken to approximate the maximum width, the maximum height and the length of the Langley Full Scale Tunnel (LFST) (60 × 30 × 56 ft). Figure (3-11) shows the test section dimensions and the surface panels used. The model is placed at the center of the test section (28,0,0) and 1200 constant strength source surface panels are used. Results for closed and open test section configurations are presented and compared to the method of images.

Figure (3-12) shows the blockage and the upwash interference factors (ε and $\Delta\alpha$) against the area ratio for a long closed test section (three times its actual length) compared to the method of images. A good matching with the method of images is achieved through nearly all the range of area ratios studied. The interference for a realistic length test section is presented in Figure (3-13). Again reasonable matching is observed with small differences due to the unconstrained ends of the test section as discussed in the previous 2D model case.

Figure (3-14) shows the blockage factor (ε) distribution on a horizontal plane passing through the model location for a model with 15% area ratio inside a closed wall actual length test section. The maximum value of the blockage interference is at the model location, which increases the effective free stream velocity but with negligible consequent buoyancy effect on the model. The gradient in the streamwise direction is higher than the gradient in the lateral direction. The upwash factor is zero on this plane as discussed in the previous section, so it is not presented here.

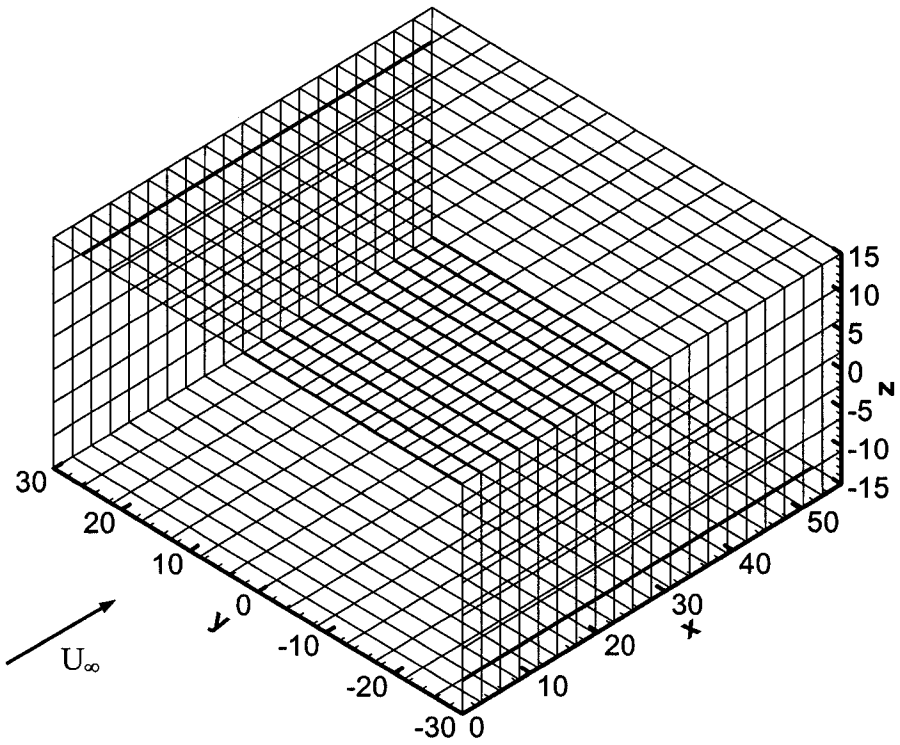

Figure (3-11) Surface panels for the rectangular test section.

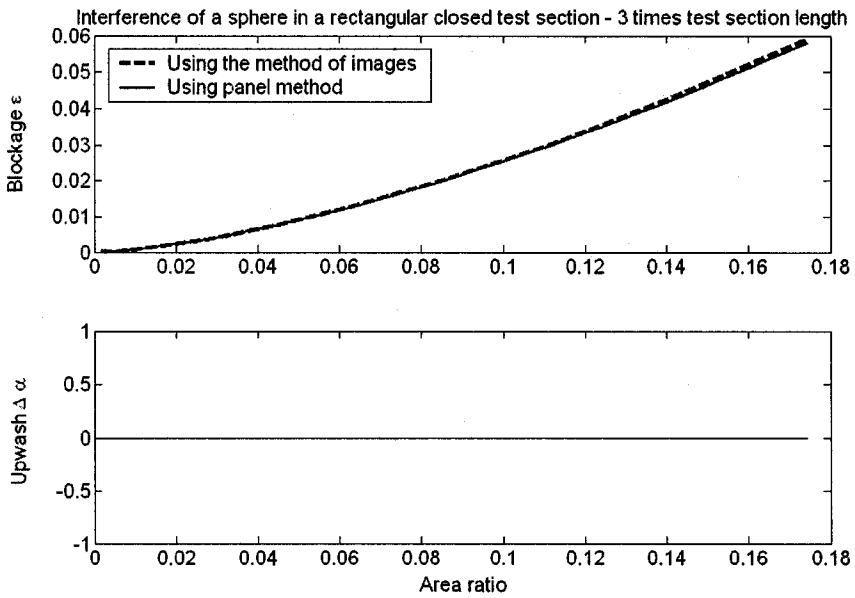

Figure (3-12) Wall interference of a non-lifting sphere representation inside a closed test section, 3 times test section length

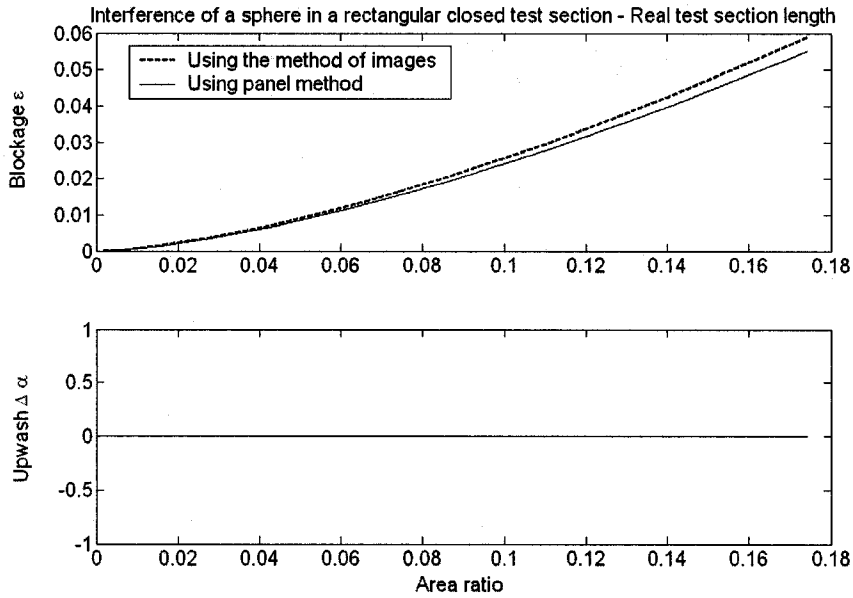

Figure (3-13) Wall interference of a non-lifting sphere representation inside a closed test section, realistic length test section.

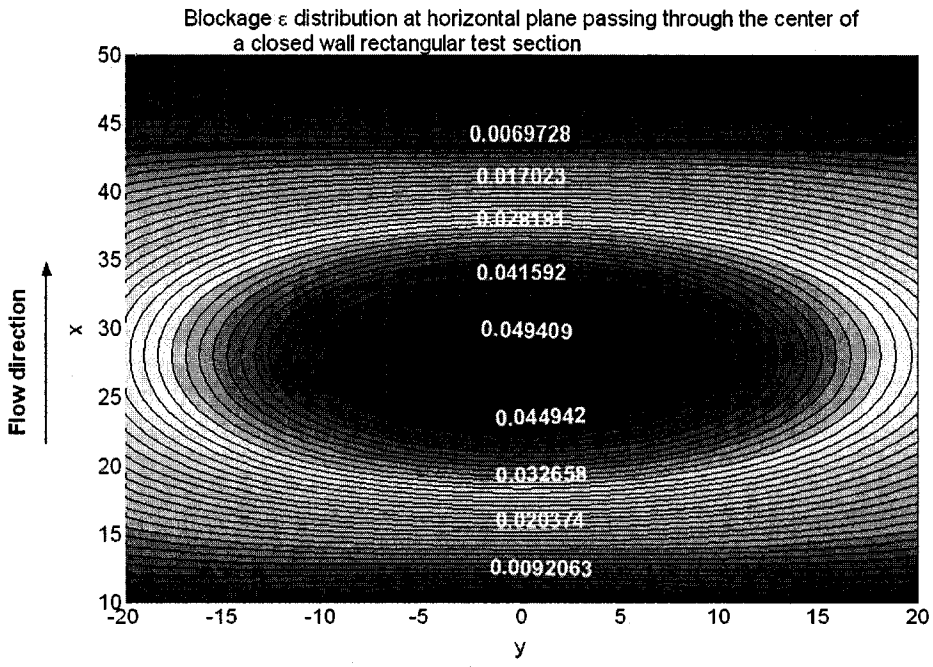

Figure (3-14) The blockage factor (ε) distribution at a horizontal plane passing through a closed test section center for a sphere model representation (Area ratio = 15%).

Turning now to an open test section case, Figure (3-15) shows the geometry of the test section boundaries at the end of the streamlining process for a 15% area ratio. A considerable amount of deformation is noticed on the upper and the lower boundaries while not much change is noticed in the lateral boundaries. The blockage factor on a horizontal plane passing through the test section center is presented in Figure (3-16). Comparing it to the equivalent results for closed walls for the same model (Figure (3-14)), it is seen to exhibit opposite sign and lower magnitudes but has similar overall streamwise and spanwise trends. Figure (3-17) shows a comparison between the interference factors obtained by the present method and the method of images for the open jet case. The agreement between the methods is acceptable keeping in mind that the present method considers the deformation in the boundaries while the method of images does not. To complete the comparison, the boundary interference of a sphere inside a rectangular open test section with un-deformed boundaries is predicted using both the present approach and method of images. Figure (3-18) shows the blockage and upwash interference factors for these cases. Excellent matching between the two methods is observed again confirming that the difference between them in the fully-deformed case, shown in Figure (3-17) is due to the boundary deformation.

To summarize the presented results for blockage effect where the model is represented using a blockage doublet; the present method matched the method of images for long closed test section for both 2D and 3D cases. This step of the comparison is important to evaluate the accuracy of the new method and to identify the limits of the test section lengths that can meet the "infinite" length assumption of the classical method of images. For the open jet test section, excellent matching was observed between the two methods for un-deformed boundaries cases. Again, this matching adds more confidence to the results predicted using the present method. It also confirms that the difference between the present method and method of images for the fully-deformed open jet cases are due to the boundary deformation only. In other words, it shows the importance of including the boundary deformation in open jet boundary interference assessment.

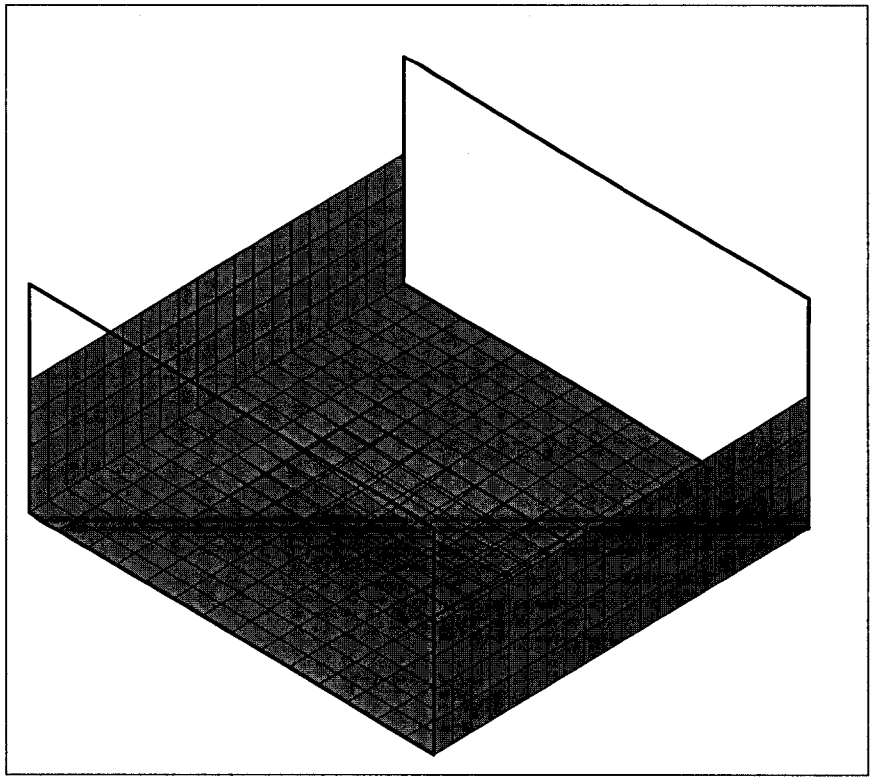

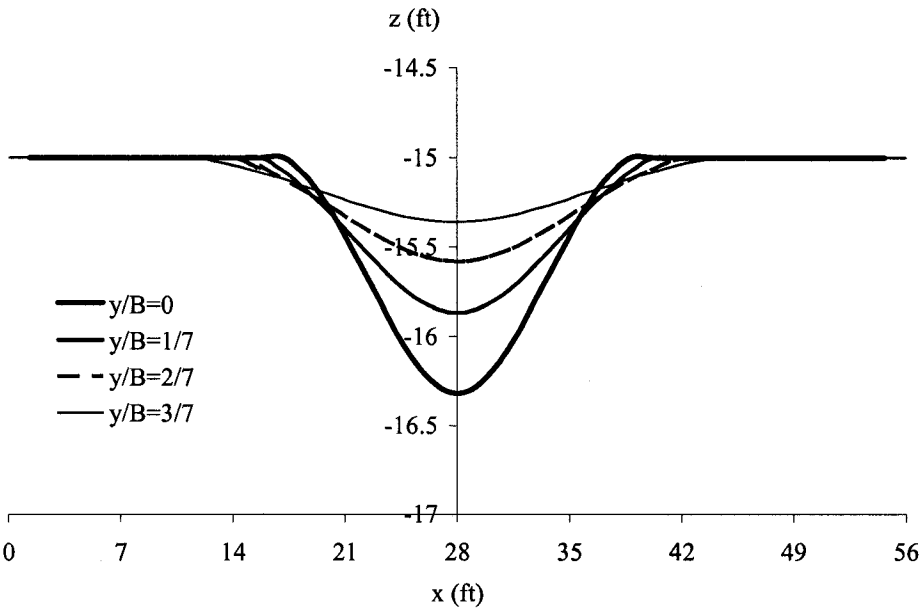

Figure (3-15) The predicted boundary deformation for open test section solutions (Area ratio = 15%).

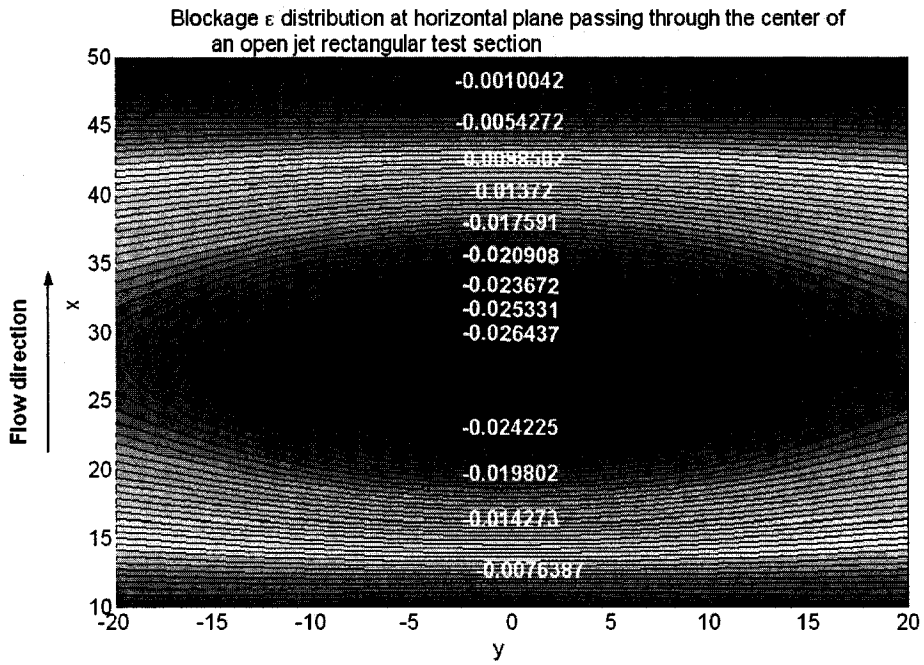

Figure (3-16) A sample of the blockage factor distribution at a horizontal plane passing through an open jet test section center for a sphere model representation.

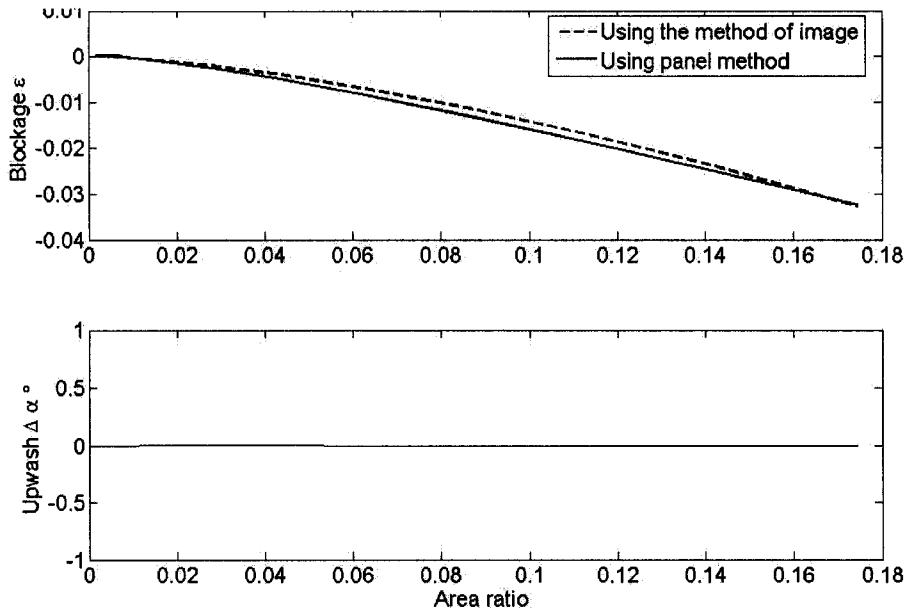

Figure (3-17) Wall interference of a non-lifting sphere representation inside an open rectangular test section.

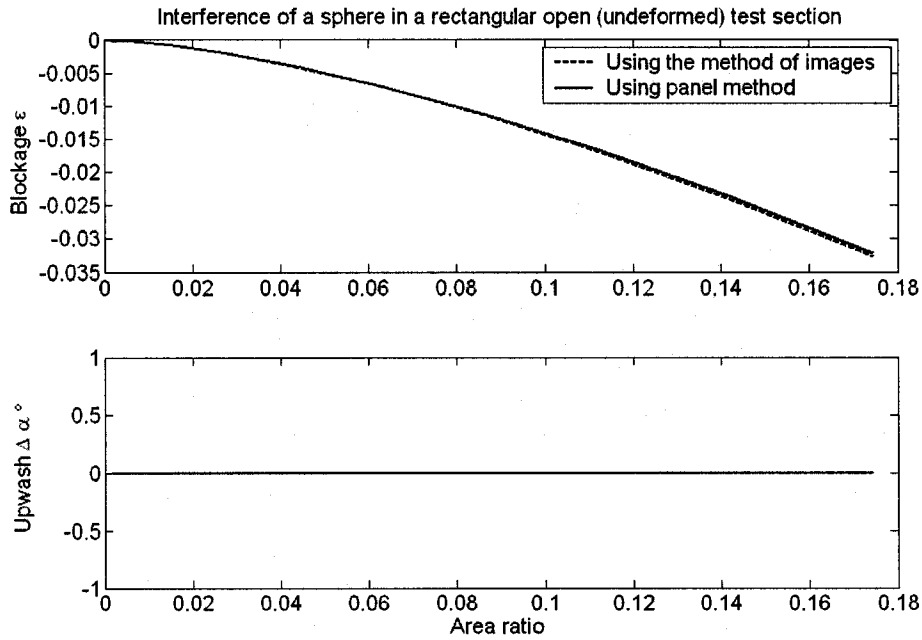

Figure (3-18) Wall interference of a non-lifting sphere representation inside an open rectangular test section, un-deformed boundaries.

3.4 2D lifting model

The lifting effect of a small airfoil tested in a 2D test section is represented by a point vortex. The reference test conditions are taken as follows: lift coefficient (C_L) is 1.5 and the air speed (U_∞) is 30 ft/s. The test section dimensions used are height (H) 30 ft and length (L) 60 ft, which approximate the external dimensions of a two-dimensional version of the Langley Full Scale Tunnel; also a generic test section of L/H ratio 2. The present method is compared to the method of images for closed and open test sections. Constant strength doublet panels are used. The normalized upwash factor δ is used in this study.

$$\delta = \frac{v_{int}}{U_\infty} \frac{H}{cC_L} \tag{3-5}$$

Where v_{int} is the vertical velocity component induced by the test section boundary panels, c is the airfoil chord length.

Figure (3-19) shows the upwash interference along the centerline of a 2D closed wall test section due to a point vortex model representation. A long test section is used (10 times its realistic length) and the model location is at x/H = 0. The upwash interference is zero at the model location with downwash and upwash interferences in the upstream and the downstream directions respectively. The upwash gradient at the model location produces additional lift due to an induced camber and angle-of-attack at the airfoil mid-chord relative to the interference-free case. A good matching between the method of images and the present method is achieved. Several test section lengths were studied to explore the minimum value that can satisfy the method of images assumptions (small model inside a long test section) and it was found that as low as three times the realistic length can produce a good agreement between the present approach and the method of images as shown in Figure (3-20). The upwash interference for a realistic length test section is shown in Figure (3-21). The method of images predicts higher upwash gradient than the present method at the model location. As discussed before, the method of images is not designed for finite length test sections but it can be a good way to get a rough estimate of the interference magnitude and trend.

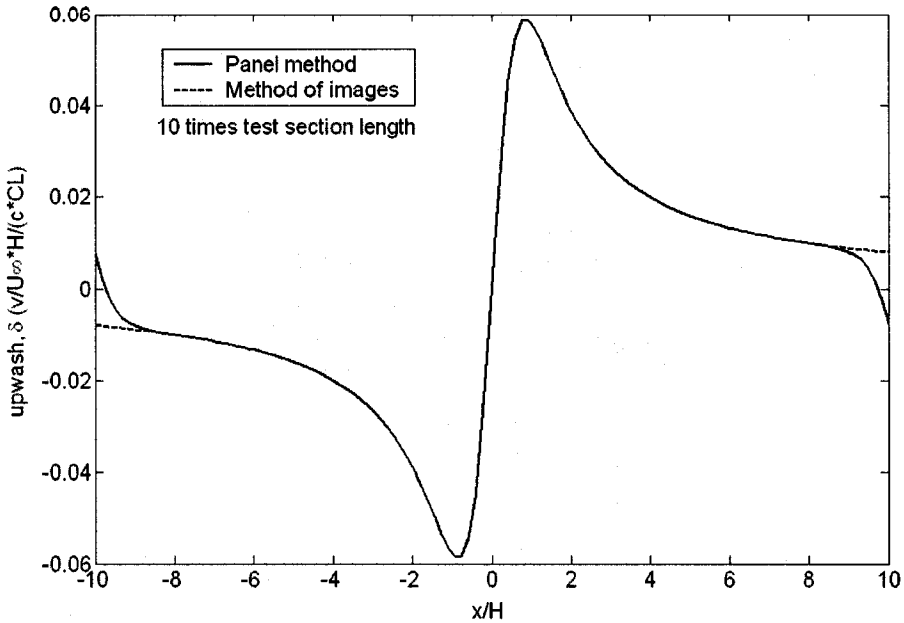

Figure (3-19) Upwash interference along the centerline for a 10 times length closed test section – 2D vortex model representation

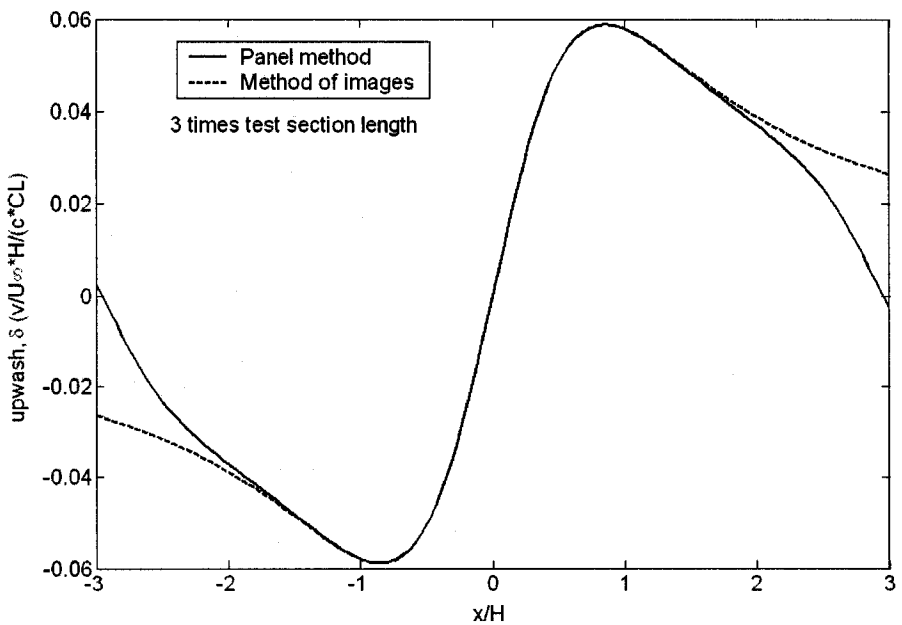

Figure (3-20) Upwash interference along the centerline for a 3 times length closed test section – 2D vortex model representation

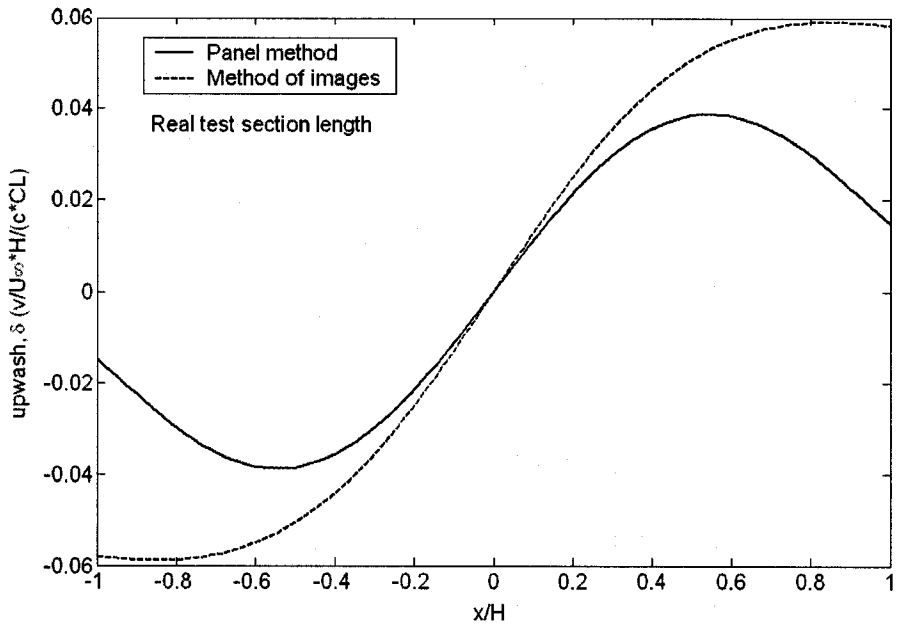

Figure (3-21) Upwash interference along the centerline for a real length closed test section – 2D vortex model representation

Turning to the open test section case, Figure (3-22) and (3-23) show the upwash interference factor δ for a long open test section (10 times its realistic length) for different chord lengths (c) and the same lift coefficient (C_L = 1.5). A good matching between the present method and the method of images is achieved for small model sizes (small relative chord lengths c/H). As the model size increases for the same lift coefficient, the generated lift force increases, which results in a change in vertical component of the momentum in the open jet, which causes increased boundary deformation as shown in Figure (3-24). The method of images does not represent this effect and predicts the same normalized upwash factor δ distribution along the test section centerline for different model sizes. For the closed wall test section shown in Figure (3-19), no boundary deformation is considered and this effect of the vertical component of the momentum does not affect the predicted normalized upwash factor δ distribution. In other words, unlike the open test sections, full matching between the present approach and the method of images can be achieved regardless of the model size for long closed-wall test sections.

It is important to note that, for large model sizes (such as c/H = 20.0%) the deformation of the lower boundary gets closer to the model location, which is a singular point, and decreases the accuracy of using a point vortex to represent the model. This problem can be eliminated if the model is represented by distributed singularities and their strengths can be directly derived from the measured forces or calculated during the solution of the test section boundary panels, as will be shown in Chapter (4).

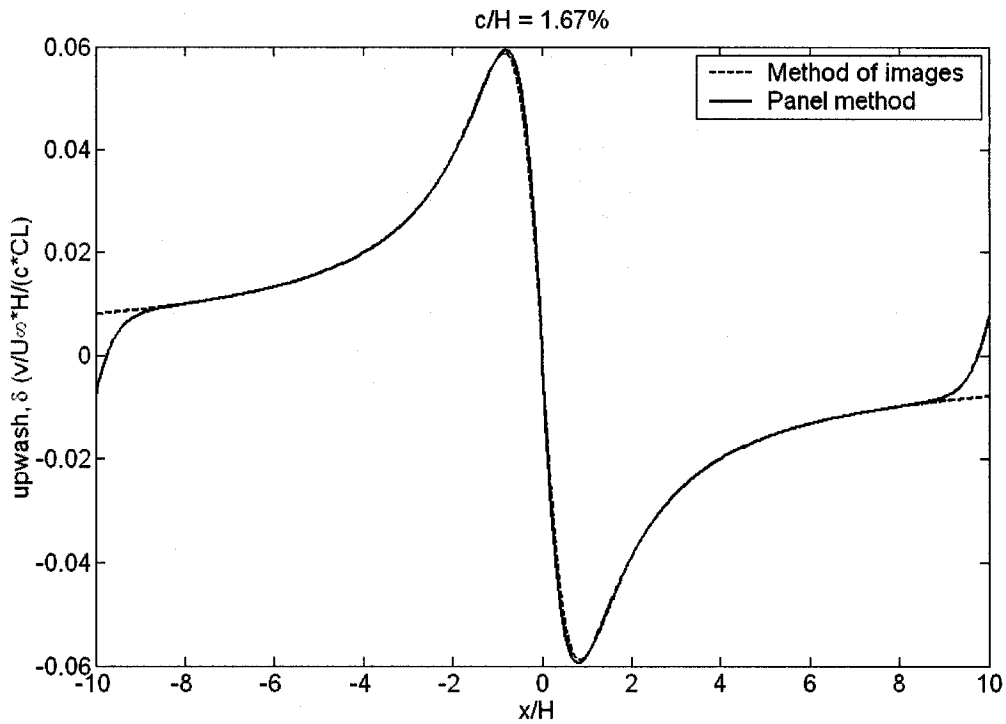

Figure (3-22) Upwash interference along the centerline for a 10 times length open test section - 2D vortex represents for c/H=1.67%.

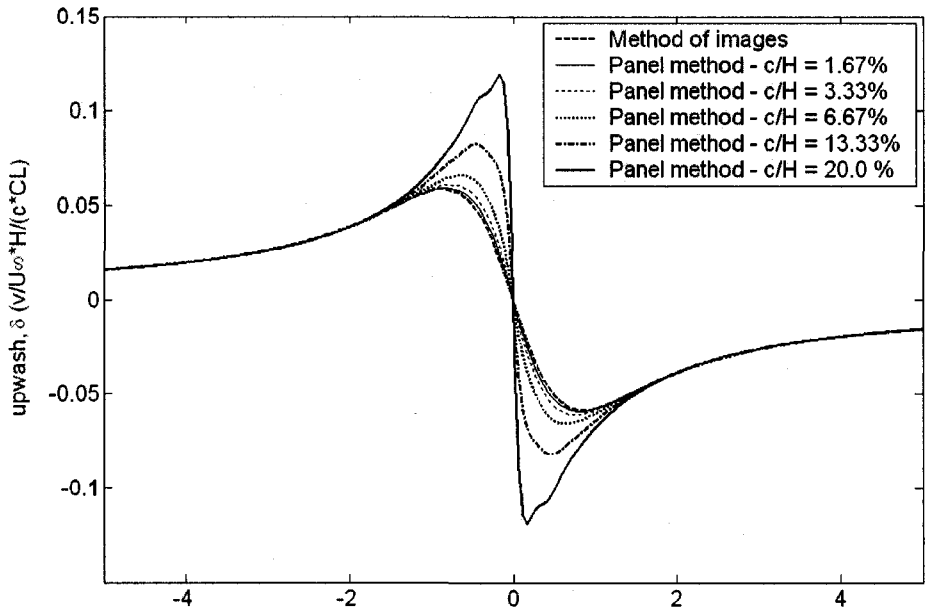

Figure (3-23) Upwash interference along the centerline for a 10 times length open test section - 2D vortex represents for different model sizes.

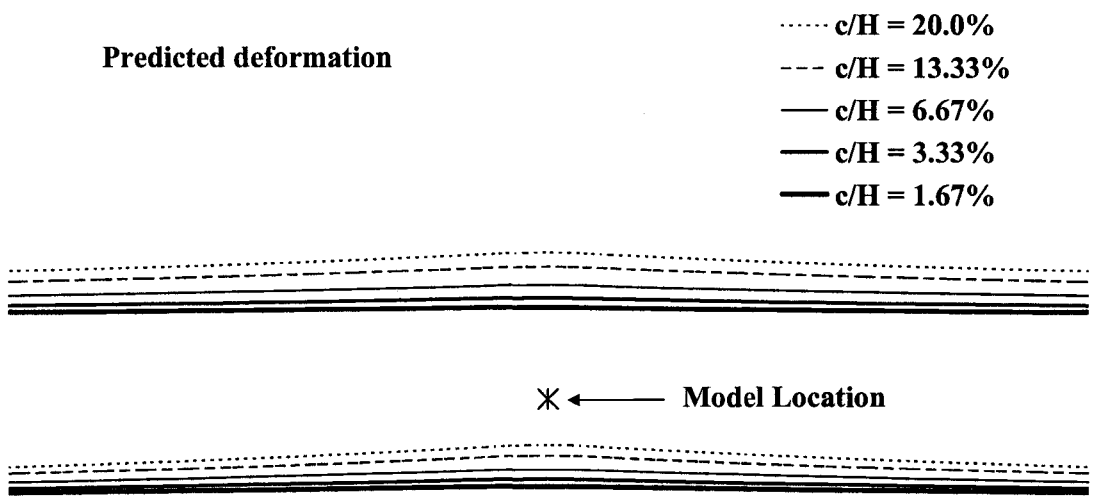

Figure (3-24) Deformation of the boundaries around the model location for different model sizes

3.5 3D lifting model

A single horseshoe vortex is used to represent the lifting effect of a small model inside a rectangular test section. The width, height and length of the test section are taken to be equal to the dimensions of the test section of the NASA Langley Research Center 14 by 22 Foot Subsonic Wind Tunnel (21.76 × 14.5 × 50 ft). Figure (3-25) shows the geometry of surface panels used, which were vortex rings (1260 panels). The model location is (25,0,0). The validations against the method of images include closed and open test sections with both long and realistic lengths. The focus will be on the upwash interference since the horseshoe vortex represents a lifting model.

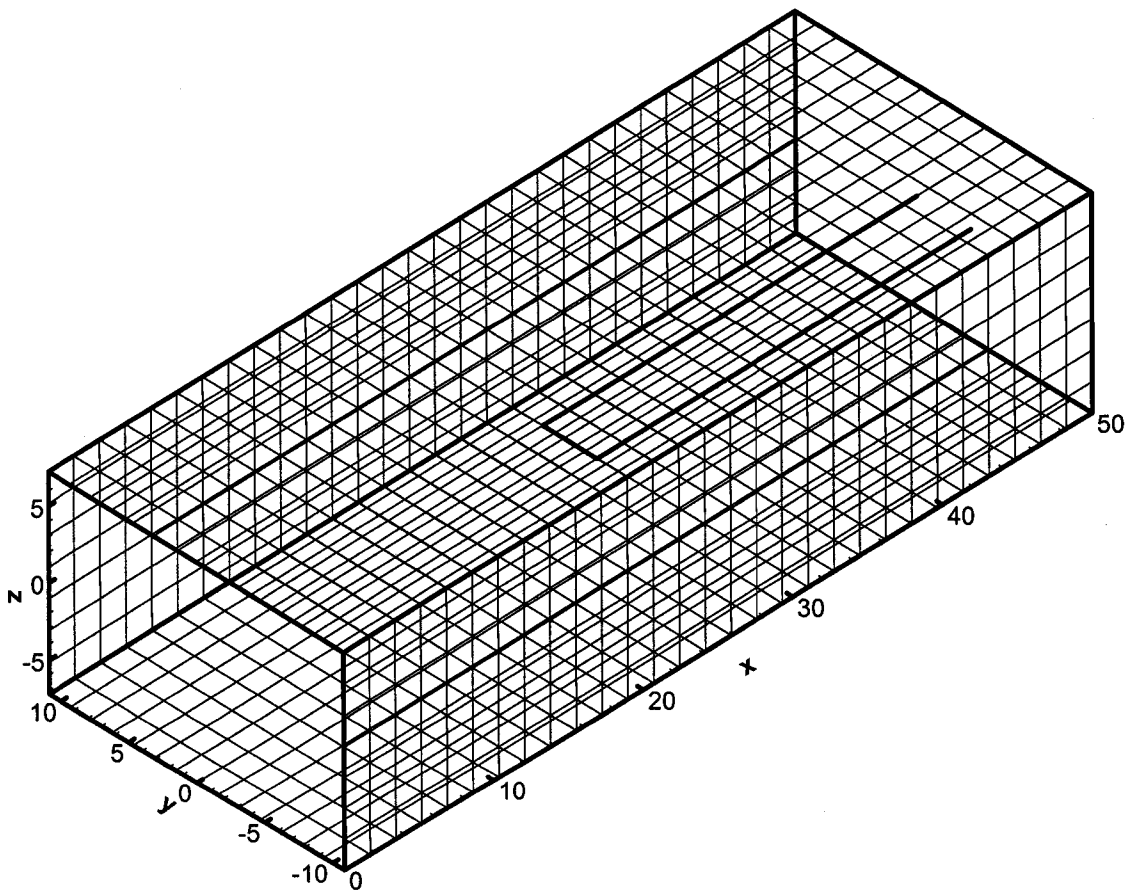

Figure (3-25) Surface panels of the rectangular test section with a horseshoe vortex model representation.

Figure (3-26) shows the upwash factor (δ) distribution along the centerline of the closed rectangular test section for several model sizes and test section lengths. For long test sections (3 times its realistic lengths), a good matching between the present method and the method of images is achieved. The upwash interference approaches zero in the upstream direction and a constant positive value in the downstream direction. The upwash interference at the model location is nearly half this value. It should be noted that the method of images predicts exactly half the upwash at the plane of the bound vortex compared to far downstream. For the realistic length test sections, also a good matching is achieved with the method of images in the upstream direction. In the downstream direction the present method does not asymptote to a constant value as does the method of images because the latter assumes infinite length test sections. For both long and short test section solutions, not much effect can be observed when different relative model sizes are used (wing span/tunnel width: b/B = 1/22, 2/22 and 4/22).

Figure (3-27) shows a sample of the upwash factor ($\Delta\alpha = \frac{w_{int}}{U_\infty}$) distribution at a horizontal plane passing through the center of a realistic length closed test section for a model size (b/B=4/22), wind speed U_∞ 30 ft/s and horseshoe vortex strength 200 ft^2/s. The maximum upwash interference is 0.038 (or 2.2°) at the centerline, about 13 ft downstream to the model. The upwash is 0.02 (or 1.1°) and its downstream gradient ($\frac{\partial(\Delta\alpha)}{\partial x}$) is 0.0026 (or 0.15 deg/ft) at the model location. These values will be compared later to open jet test section solutions.

Figure (3-28) shows the downstream distribution of the upwash interference along the centerline of an open rectangular test section. Compared to the closed test section case discussed above, the open jet test section produces an opposite sign of upwash interference (downwash), of lower magnitudes with nearly the same trends. The present method compares well with the method of images for the small model sizes. As the size increases, b/B=4/22, the present method predicts lower downwash interference which

indicates the importance of including the boundary deformation for larger model sizes as discussed in the previous section. For all the cases the magnitude of the downwash at the model location is nearly half the maximum value, which agrees with results from the classical methods.

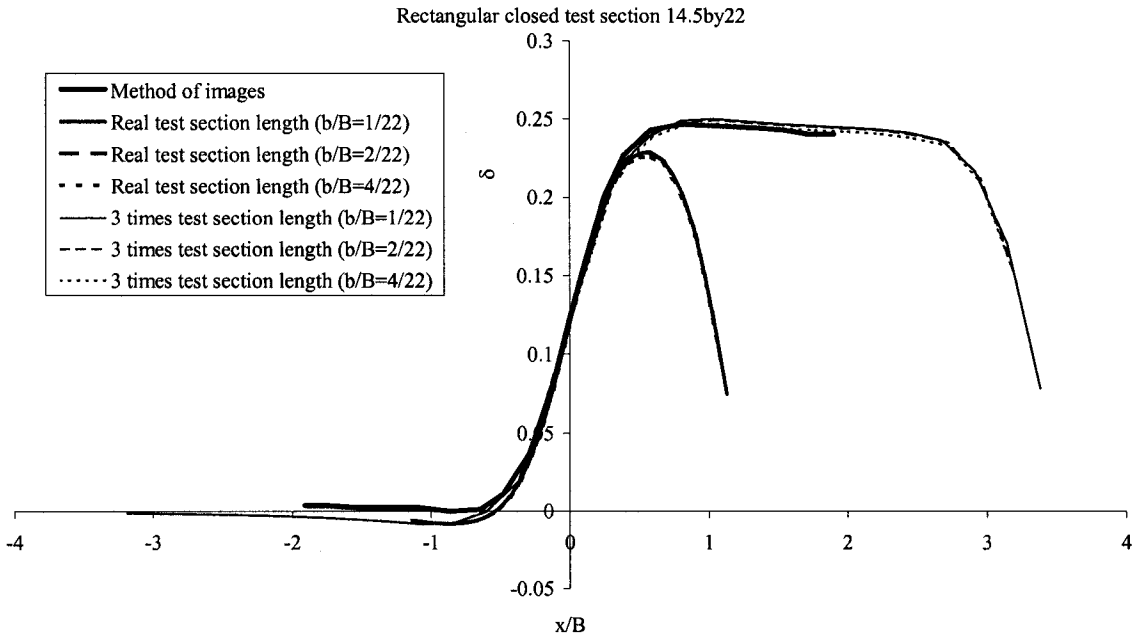

Figure (3-26) downstream distribution of the upwash factor (δ) along the centerline of a closed rectangular test section for a horseshoe vortex small span model representation – model location is at x/B = 0.

Figure (3-28) shows a sample of the predicted boundary deformation for a model size of (b/B=4/22). The major deformations are in the floor and the ceiling near to the model location. The distribution of the upwash factor ($\Delta\alpha$) at a horizontal plane passing through the open test section center is presented in Figure (3-30) for the same test conditions (wind speed U_∞ 30 ft/s and horseshoe vortex strength 200 ft^2/s) used in producing the closed test section case presented in Figure (3-27). The maximum downwash is 0.026 (or 1.5°) at about 13 ft downstream of the model location. The downwash at the model location is 0.014 (0.8°) and its gradient is 0.0029 (0.17 deg/ft). Comparing these values to those of the closed test section, it seems that the open test section produces lower

magnitudes of upwash/downwash interference and has slightly higher gradients at the model location. This statement cannot be generalized for any test section aspect ratio or geometry. In fact some open test sections may produce higher magnitudes of upwash/downwash interferences than closed ones as will be shown in the application presented in Chapter (4).

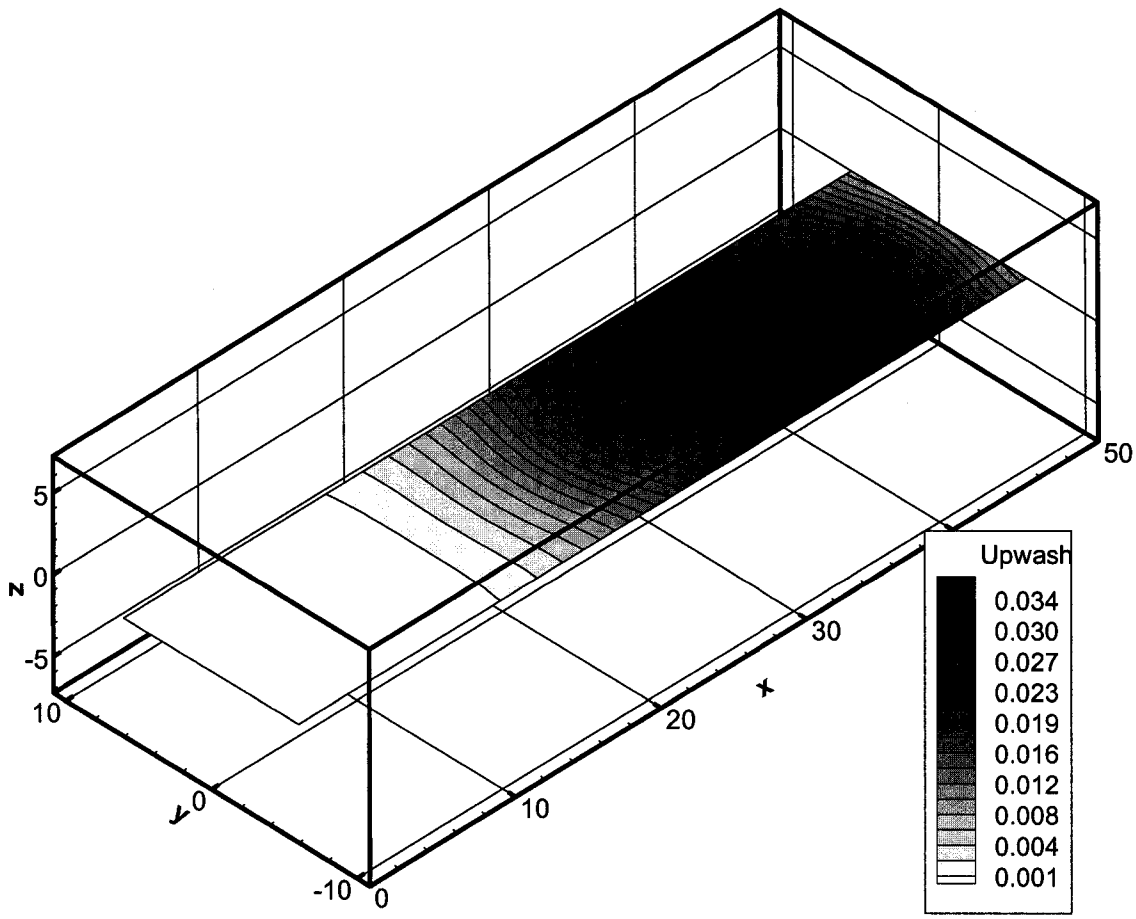

Figure (3-27) Upwash factor ($\Delta\alpha$) distribution at a horizontal plane passing through the test section center for a horseshoe vortex model representation (b/B=4/22, solving real test section length).

3.6 Summary

In this Chapter, the developed method is compared to the method of images for several model and test section configurations including two and three-dimensional lifting and non-lifting model representations. Within the limitations of the method of images, i.e. small model size inside an infinite length test section, full matching was achieved for both closed and open jet test sections. The study was extended to explore the limits of matching by changing the model size and the test section length. It was found that for test sections at least three times the real test section length, good matching could be obtained. For open test sections, as the model size increases, the effect of the boundary deformation, not accounted for in the method of images, on the predicted interference increases and full matching could not be achieved. When these cases were resolved using the present method with no boundary deformation considered, full matching was achieved confirming the importance of including the boundary deformation in the interference assessment for open jet test sections in high interference cases.

It is important to note that the range of wingspans used in this chapter was for small size wings. This size allows the use of a single horseshoe vortex to represent the rectangular wing with acceptable accuracy. For finite wingspans (more that 50% of the tunnel width), it is recommended to use more advanced method.[3] For example, the wing surface can be divided into panels and solved with the test section boundaries. Alternatively, the lifting line theory can be used to obtain the strengths of the horseshoe vortices distributed over the wingspan. In the following chapter, the present method is compared to the method of images for a finite span wing and the above methods for model representation are employed and evaluated for different test section configurations.

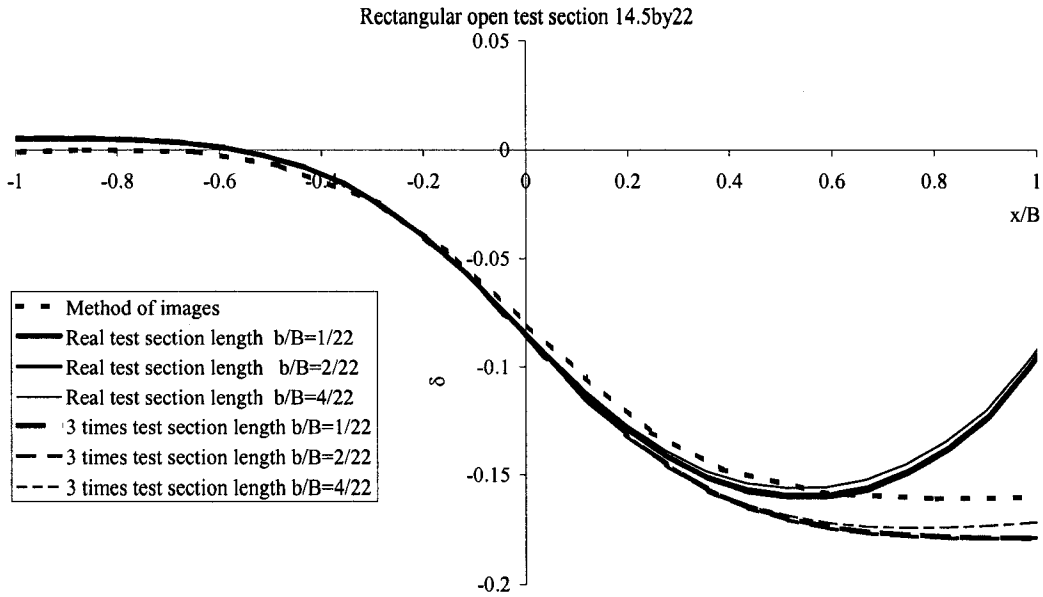

Figure (3-28) Downstream distribution of the upwash factor (δ) of an open rectangular test section for a horseshoe vortex small span model representation – model location is at x/B = 0.

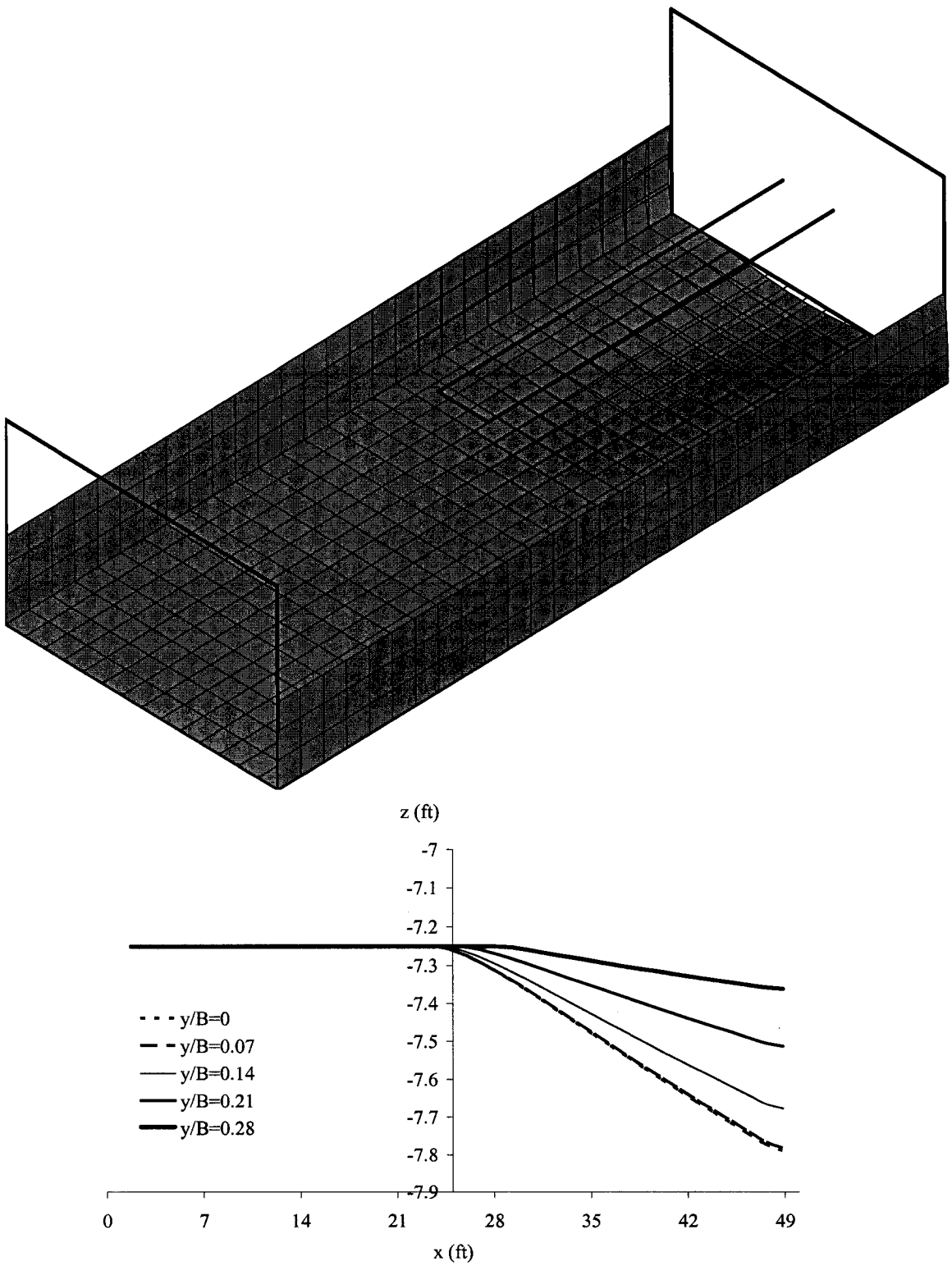

Figure (3-29) Deformed boundaries for an open test section with a horseshoe vortex model representation (b/B=4/22).

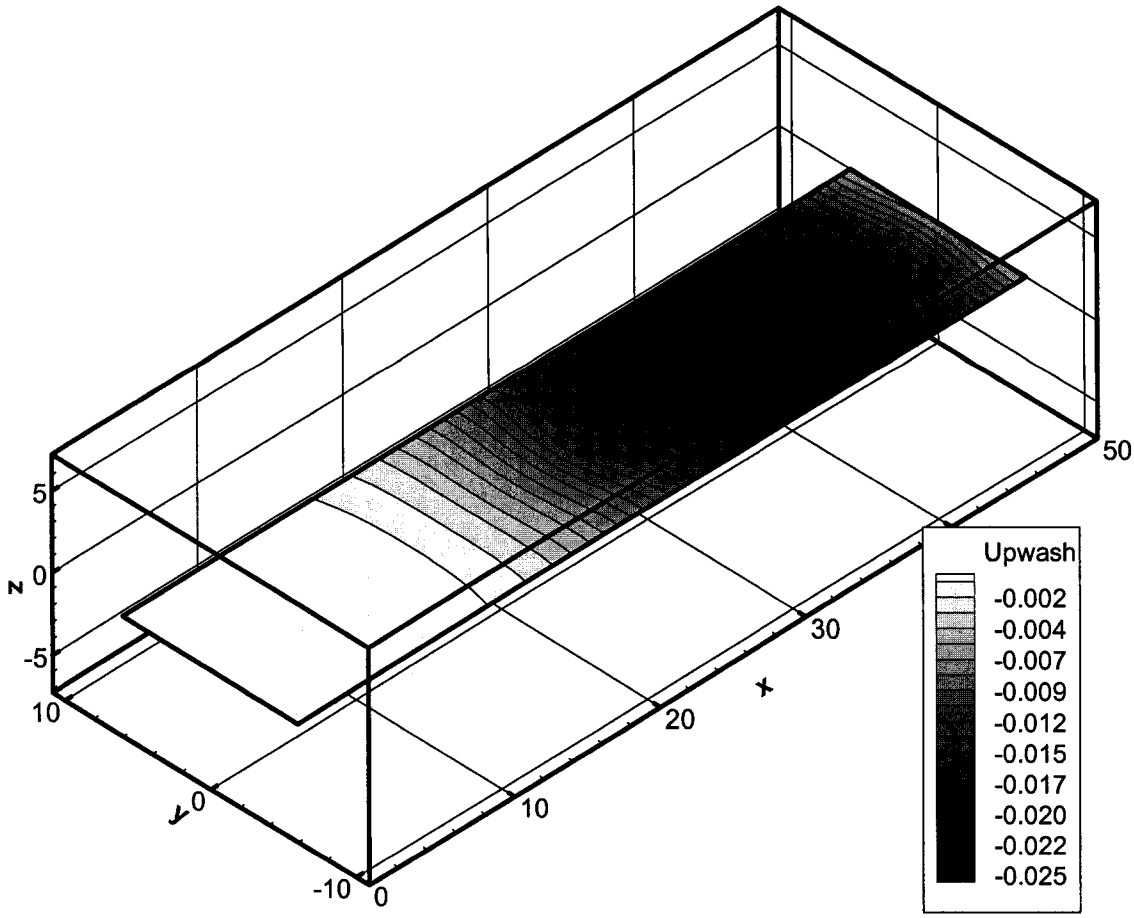

Figure (3-30) Upwash factor ($\Delta\alpha$) distribution at a horizontal plane passing through the open test section center for a horseshoe vortex model representation (b/B=4/22).

CHAPTER IV

IV. APPLICATION I – LANGLEY FULL SCALE WIND TUNNEL

The developed method for open jet wind tunnel boundary corrections is used in three applications for tests performed at the Langley Full Scale Tunnel (LFST), the NASA Langley Research Center 14 by 22 Foot Subsonic Wind Tunnel, and the $1/15^{th}$ scale Langley Full Scale Tunnel. Each application focuses on demonstration of some of the aspects of the open jet test section boundary corrections. Taken together, the three applications represent a fairly complete evaluation of the method.

The first application, which is presented in this chapter, is for a traditional aeronautical test. It addresses the effects of the model representation and different test section configurations including closed, open and 3/4 open. The second application, presented in Chapter (5), is a traditional automotive test and its focus is to study the effect of the numerical test section length and the inclusion of the nozzle on the predicted interference. The third application, presented in Chapter (6), addresses the effect of the collector and is also automotive in nature.

The objective of the study presented in this chapter is to compare the present method to the method of images for models with large wingspans tested in non-rectangular test sections. The model used is a full scale Wright Flyer replica, which is a very unique case because it has a large wingspan (about 2/3 of the test section maximum width) and a very small blockage ratio. In other words, it offers a nearly perfect lifting model case. For such large wingspans, to obtain accurate results, the model should not be represented using a single horseshoe vortex, as discussed in Chapter (3).[3] Therefore, in this application, two approaches are used to represent the model by: 1) full paneling of the lifting surfaces and 2) using distributed horseshoe vortex singularities. The effect of each approach is studied for closed, open and 3/4 open test sections.

The test is conducted inside the Langley Full Scale Tunnel (LFST), which has a non-rectangular test section. In the present method the real geometry of the test section is paneled and solved. Since the classical method of images is not suited to such a test section geometry, two rectangular test section representations are also used. In the first one, the external dimensions of the real test section cross-section are matched which results in about a 12% increase in the total cross-sectional area. In the second rectangular test section, the width is adjusted to maintain roughly the same cross-sectional area and the height is kept equal to the original test section maximum height.

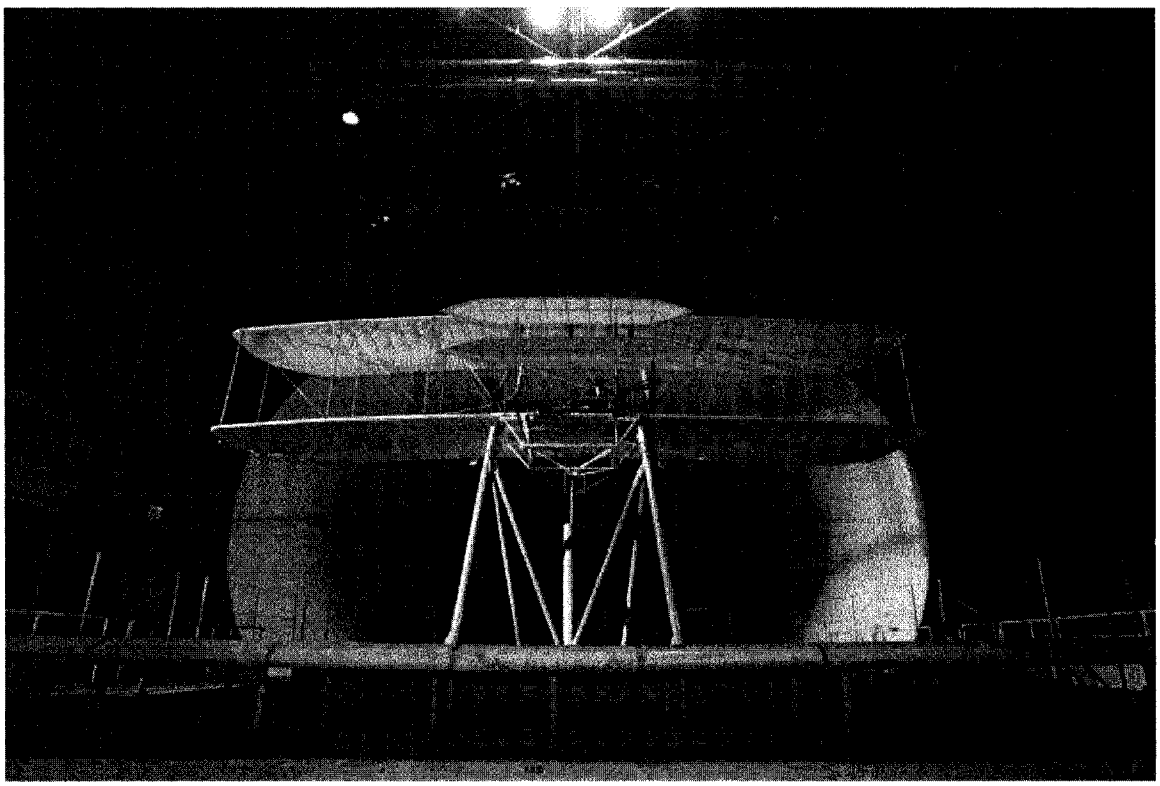

Figure (4-1) The full-scale reproduction of the 1903 Wright 'Flyer' inside the test section of the LFST

4.1 Introduction

In commemoration of the Centennial of Flight, a faithful reproduction of the 1903 Wright Brothers' 'Flyer', shown in Figure (4-1), was flown at the site of the original triumph, on December 17th, 2003. The reproduction, created by the Wright Experience under the direction of Ken Hyde, was perhaps the most accurate yet attempted. As part of the extensive preparations for the commemorative flights, the airframe was subjected to a wind tunnel test program in the Langley Full-Scale Tunnel (LFST), operated by Old Dominion University, as described in Britcher et al [54] and Kochersberger et al. [55]

The LFST is a very large, low-speed wind tunnel with a 3/4-open test section, as shown in Figure (4-2). The principal concerns relating to boundary corrections are the relatively large size of the replica with respect to the test section dimensions, coupled with the lack of modern correction techniques for aeronautical testing in open-jet test sections. A previous full-scale replica had also been wind tunnel tested, as reported by Cherne, Culick and Zell [56]. In that test, the wingspan was approximately 50% of the test section width and the wind tunnel boundaries were solid walls, so classical boundary correction techniques could be applied with some confidence. In the case of the LFST, the relatively larger wingspan, just over 67% of the test section width, coupled with the unusual 3/4-open configuration, gave rise to some concerns about the accuracy and applicability of classical correction schemes. Due to the narrow performance margins and inherent instability of the 'Flyer', the most accurate wind tunnel data set possible was required for development of flight simulators.[46] As one of the necessary steps to achieve that, the present method is employed to assess wind tunnel boundary interferences.

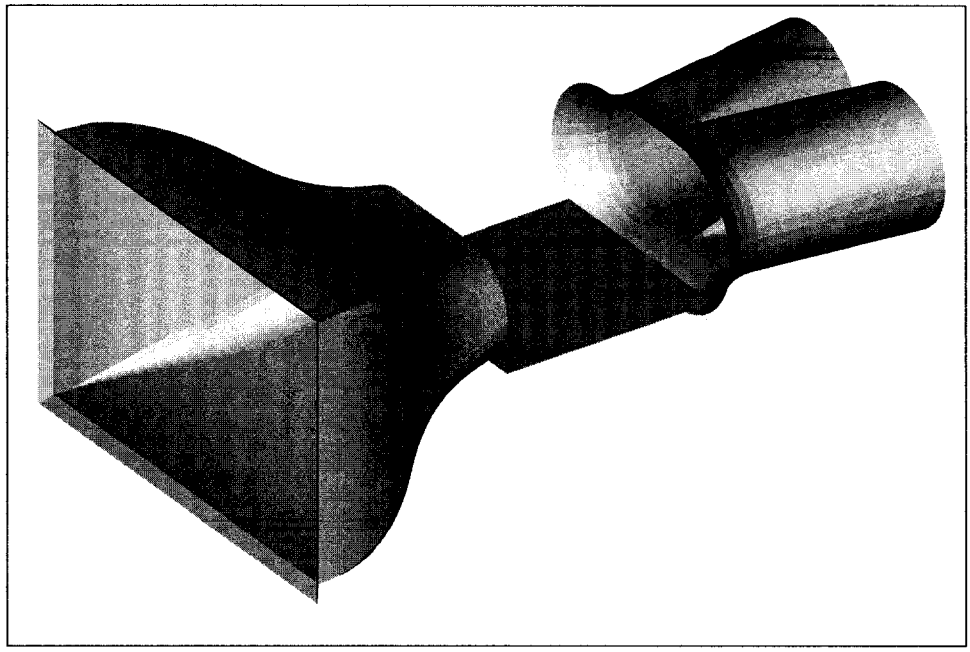

Figure (4-2) Sketch of the nozzle, test section and collector of the Langley Full-Scale Tunnel (LFST)

4.2 Methods and approaches

The 'Flyer' is represented either by simple lifting surfaces, with the accuracy of the representation checked by direct calculations using the panel code CMARC, or by an array of simple horseshoe vortex singularities. Vortex ring panels are used in the boundary correction code. A reference test condition was established; roughly corresponding to the predicted cruise conditions for the actual 'Flyer'. The nominal angle of attack measured from the reference axis of the landing skids is 1.5 degrees, and the nominal lift coefficient is 0.58. A typical airframe drag coefficient is of the order of 0.1, with a substantial upload on the canard required to trim. The reference wing area is 510 square feet with the nominal wind tunnel cross section 1607 square feet. The test section cross-section comprises two 30-foot diameter semi-circles bounding a 30 by 30 foot square and is 56 feet in length. The fixed ground intrudes into this envelope by about 2.5 feet along the lower edge, reducing the actual flow area by about 100 square feet.

A. Solution using 'Flyer' geometry

The first step in the present work is the development of a representation of the 'Flyer'. Figures (4-3) and (4-4) show plan- and side-views of the Wright 'Flyer'. Six lifting surfaces, subdivided into 720 panels are used, as shown in Figure (4-5). To ensure the accuracy of the model representation the panel code CMARC is used to solve the free air flow around the entire model and results are compared to experimental data. Figure (4-6) shows the results obtained by CMARC, compared to uncorrected experimental data. Fair agreement is achieved, keeping in mind that CMARC solves for solid (impermeable) surfaces while the real airframe is covered with unsealed fabric, which deforms with the airflow and allows small air leakage. The model representation is therefore considered adequate to be used in boundary interference calculations, with appropriate care.*

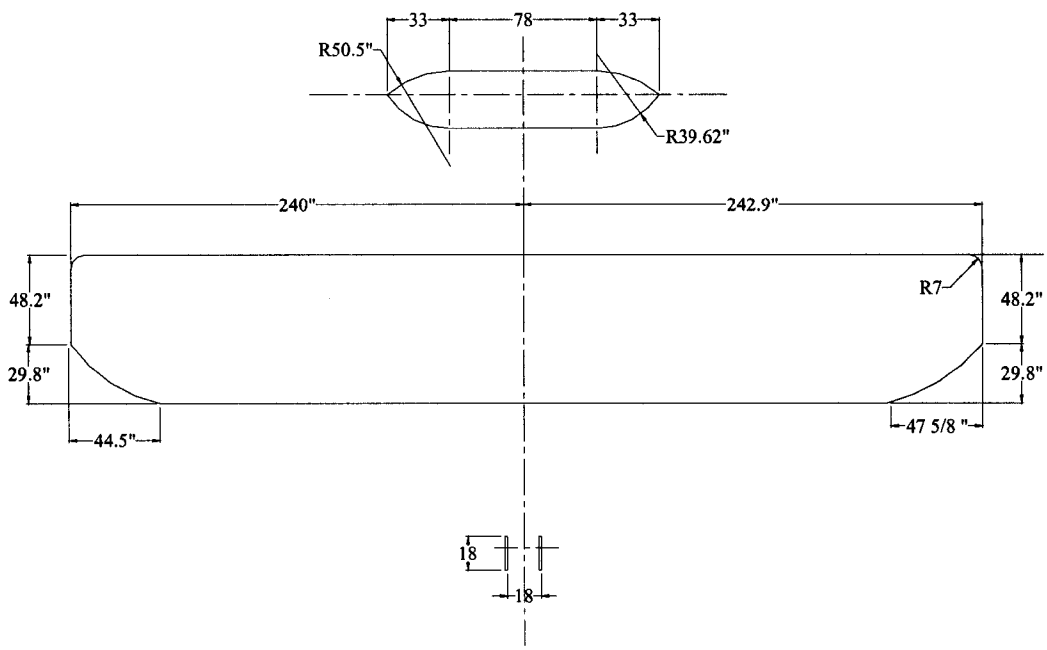

Figure (4-3) Plan-view of the Wright 'Flyer' (Dimensions in inches)

* Test conditions matched by lift coefficient, rather than angle of attack, etc.

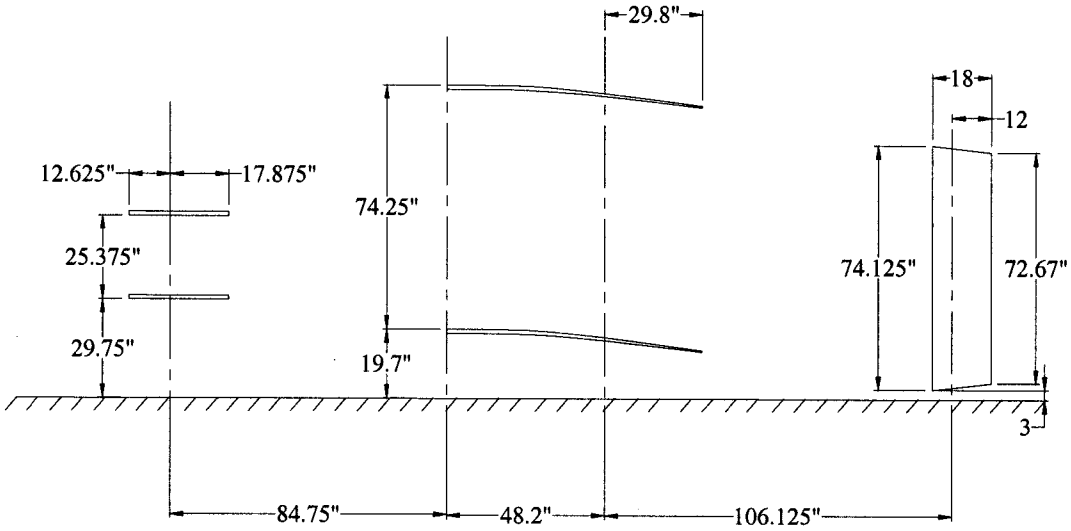

Figure (4-4) Side-view of the Wright 'Flyer' (Dimensions in inches)

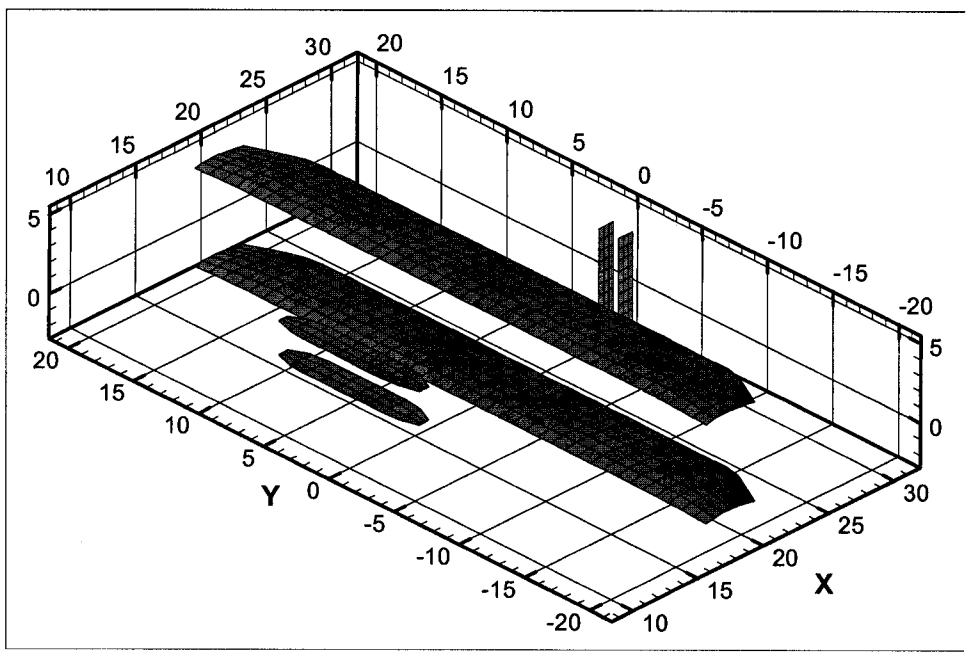

Figure (4-5) The surface panels of the Wright Flyer representation (Dimensions in feet)

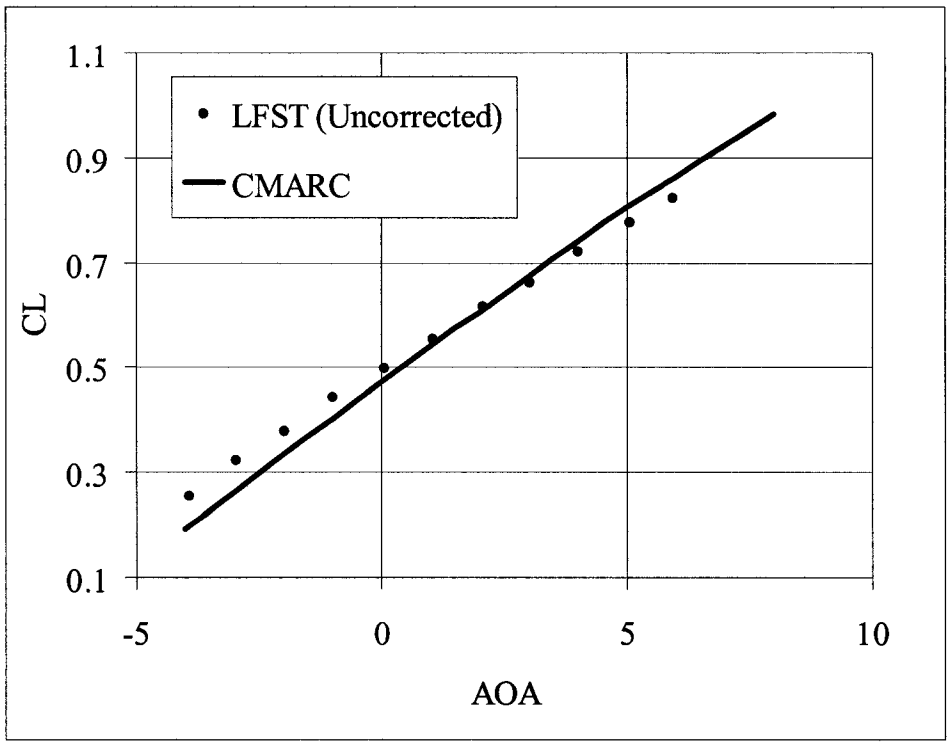

Figure (4-6) Comparison between uncorrected LFST and CMARC results

The boundary interferences, as previously described in Chapter (2), are derived in three main stages. In the first stage, the test section boundaries and the model representation are paneled, as shown in Figure (4-7), with the boundary panels' strengths solved for as solid walls with zero normal velocity. Second, the boundary deformation is predicted. Finally the interference factors are obtained using the velocity components induced by the boundary panels, as shown in Equations (4-1) and (4-2):

$$\varepsilon = \frac{u_{int}}{U_\infty} \tag{4-1}$$

$$\Delta\alpha = \frac{w_{int}}{U_\infty} \tag{4-2}$$

It should be noted that the test section representation is of finite length (equal to the actual length), leading to some sensitivity to inflow and outflow conditions. In this chapter, both the inflow and outflow cross sections are fixed, with a constant axial

velocity imposed far upstream and downstream. This is not a completely faithful representation of the conditions in the wind tunnel, where nozzle exit non-uniformity may be present and where the collector entry conditions are quite complex, but it was considered adequate for the current purpose. The effect of the nozzle and the collector will be discussed later in the applications presented in Chapters (5) and (6).

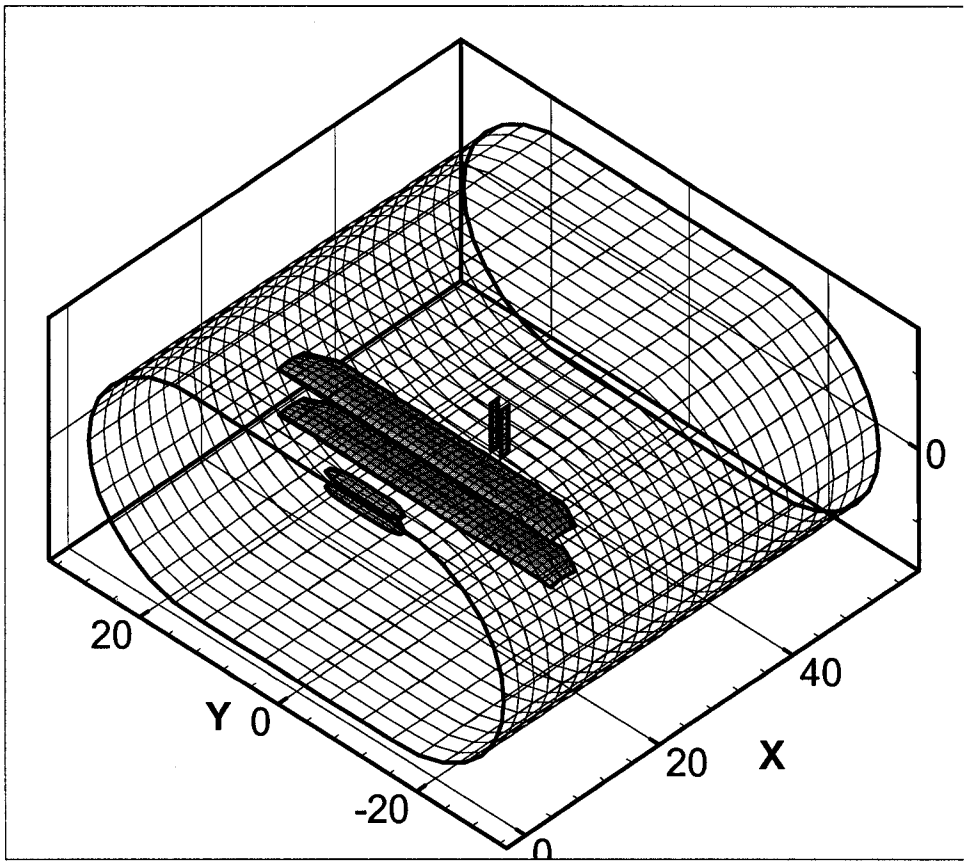

Figure (4-7) The surface panels of the Wright Flyer representation inside the test section of LFST

B. Solution using simplified representation

In order to explore the possibility of using a simple representation of the test article the 'Flyer' is represented by horseshoe vortex singularities as shown in Figure (4-8). The spanwise distribution and relative strengths are chosen based on a classical lifting line solution. The solution technique is similar to the previous case except that measured

forces are used to obtain the strengths of the horseshoe singularities for the Flyer representation. Then the boundaries are solved to obtain the corrections as before. Table (4-1) shows a summary of the horseshoe vortices used to represent the wings.

Component	Spanwise coordinate (ft)	Height above tunnel C/L (ft)	Relative strength
Lower wing	17.13 to –17.0	-1.36	1.0
	11.42 to –11.33	-1.36	0.432
	5.71 to –5.66	-1.36	0.103
Upper wing	17.13 to –17.0	4.82	1.0
	11.42 to –11.33	4.82	0.432
	5.71 to –5.66	4.82	0.103

Table (4-1) Summary of geometry of wing representation by horseshoe vortices

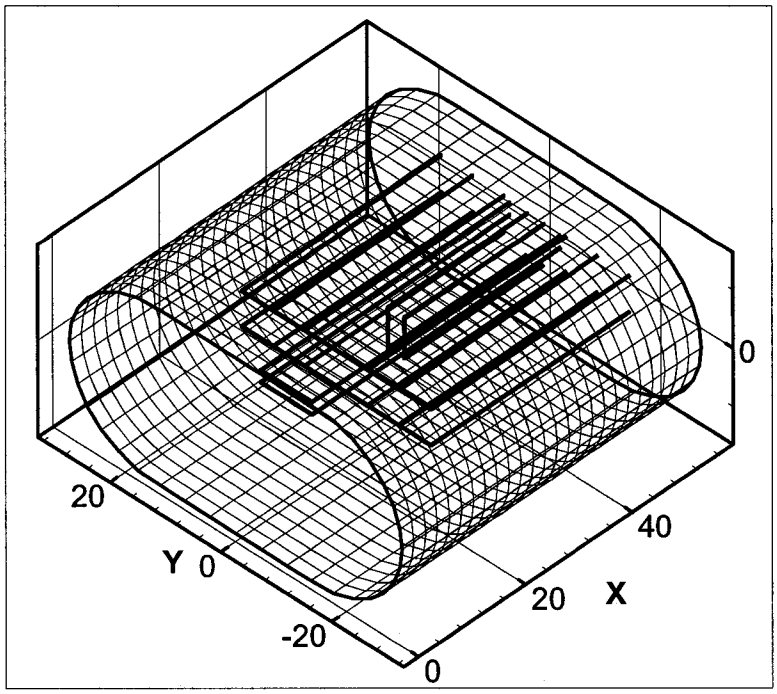

Figure (4-8) Flyer representation by horseshoe vortex singularities inside the LFST

C. Comparison to the method of images.

The horseshoe vortex representation described above is used for a numerical calculation of a 101 by 101 array of images, assuming an infinite test section length. The number of images was selected to exceed the number required for convergence to a fraction of a percent of centerline upwash. Two rectangular test sections are used in this part for comparison. In the first one, designated as test section I (30 by 60), the external dimensions of the real test section are matched so that the width is 60 feet and the height is 30 feet. In the second test section, designated as test section II (30 by 54), the width is adjusted to match the real test section cross-sectional area. Figures (4-9) and (4-10) show the two rectangular test sections used by the method of images.

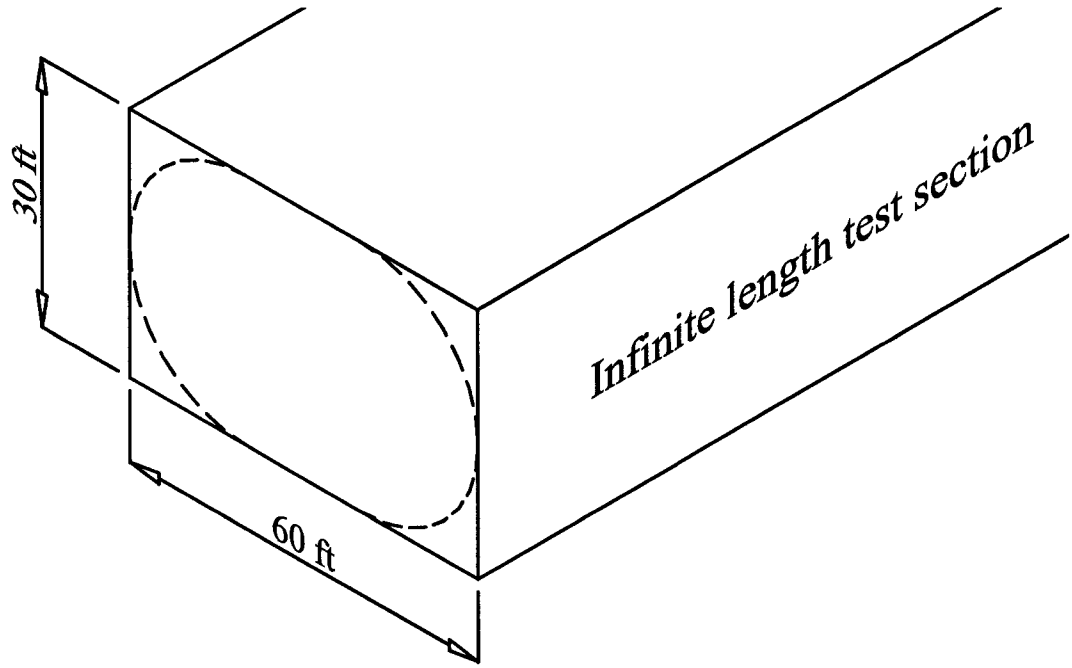

Figure (4-9) Rectangular test sections section I (30 by 60) used by the method of images to represent the LFST test section

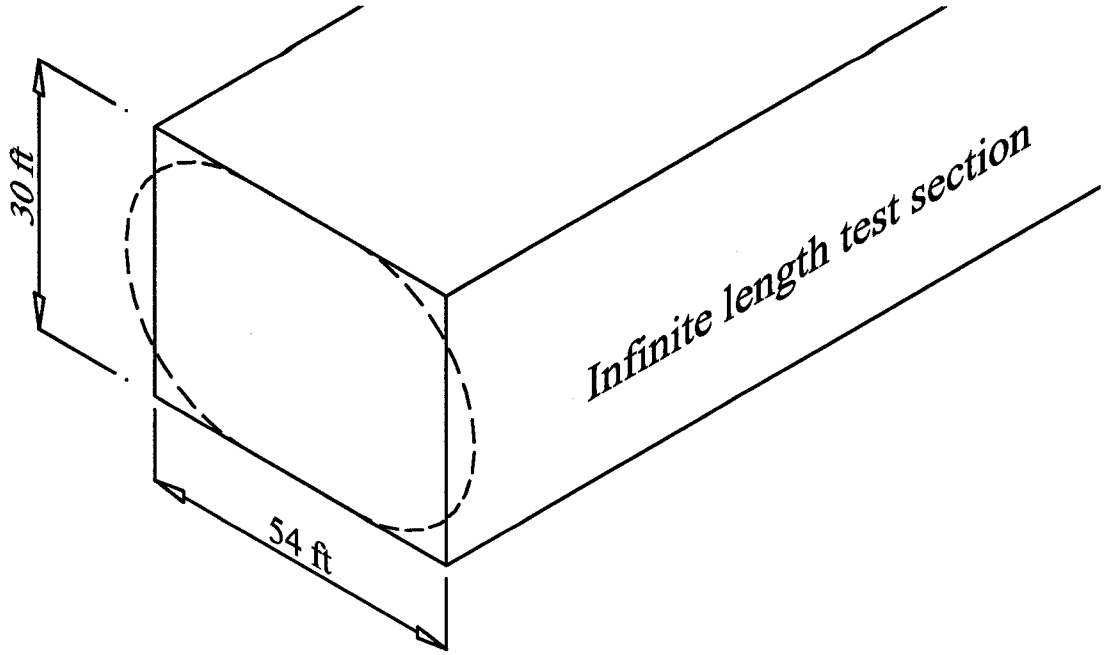

Figure (4-10) Rectangular test sections section II (30 by 54) used by the method of images to represent the LFST test section.

4.3 Interference assessment

Since the 'Flyer' consists of thin lifting surfaces, with a very low blockage ratio, upwash interference is the primary focus of this comparison study. To investigate the effect of the Flyer representation on the interference assessment, the steps of the solution are studied one by one. Figures (4-11) and (4-12) show the 'signature' of the 'Flyer' over the test section boundaries represented by the strength of the vortex ring surface panels at the end of the first step of the solution, solving for closed boundaries, with the model represented by horseshoe vortices and by surface panels respectively. The signatures produced by both methods exhibit the same overall characteristics with slight differences due to the large wingspan compared to test section width, resulting in decreased fidelity of the horseshoe vortex representation. Although the differences are relatively small they still have some effects on the following steps of the solution, as will be shown next.

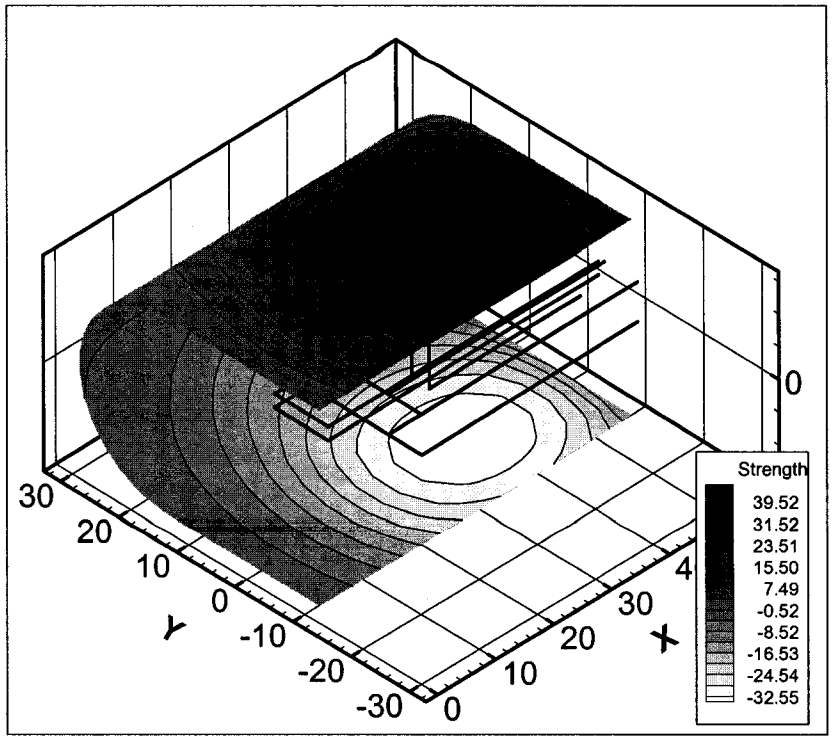

Figure (4-11) Boundary singularity strengths (ft^2/s) using the horseshoe vortex representation.

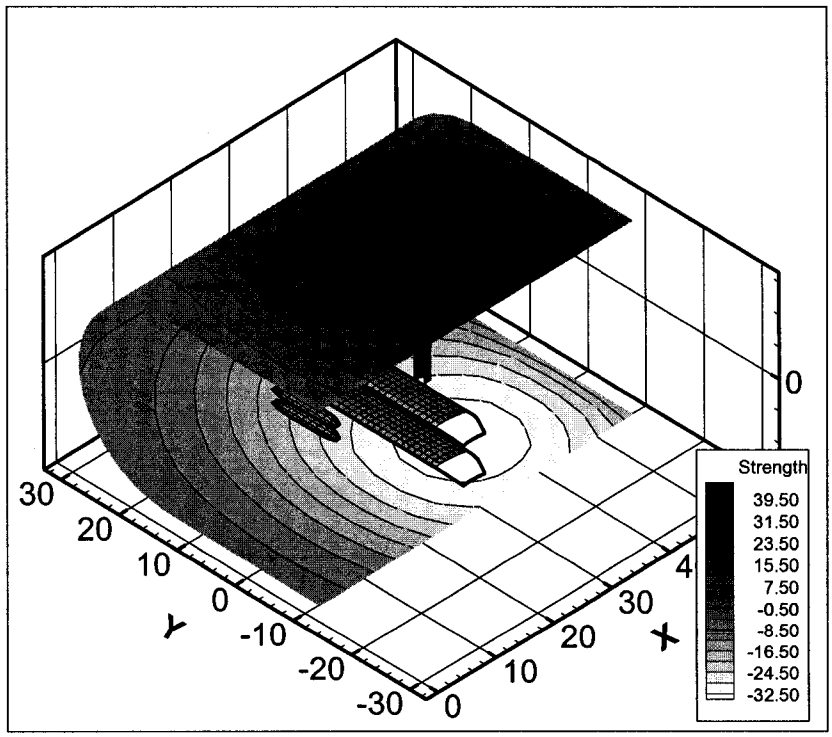

Figure (4-12) Boundary singularity strengths (ft^2/s) using the surface panel representation.

In addition to the real test section configuration (3/4 open), results for closed and fully open test sections are presented to explore the effect of the 'Flyer' representation on these cases as well. Figures (4-13) through (4-16) show the geometry of the test section at the end of the second step, boundary deformation, for both open and 3/4-open boundary configurations with the two different 'Flyer' representations. Since the boundary deformation process depends on the flow properties on the boundaries, some differences can be seen between the boundary geometries obtained using the surface panel representation of the Flyer and the one obtained using the array of horseshoe vortices.

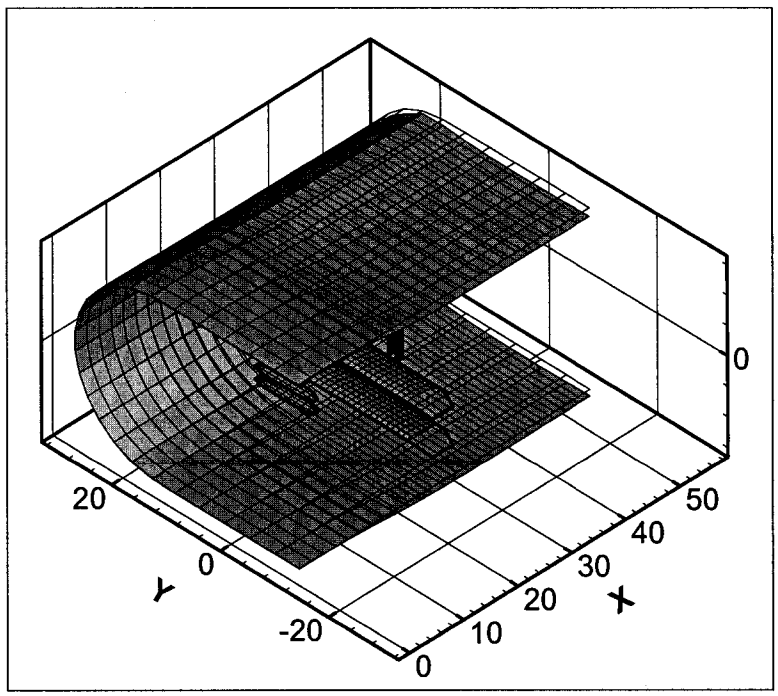

Figure (4-13) Jet distortion, fully open test section; surface panel representation.

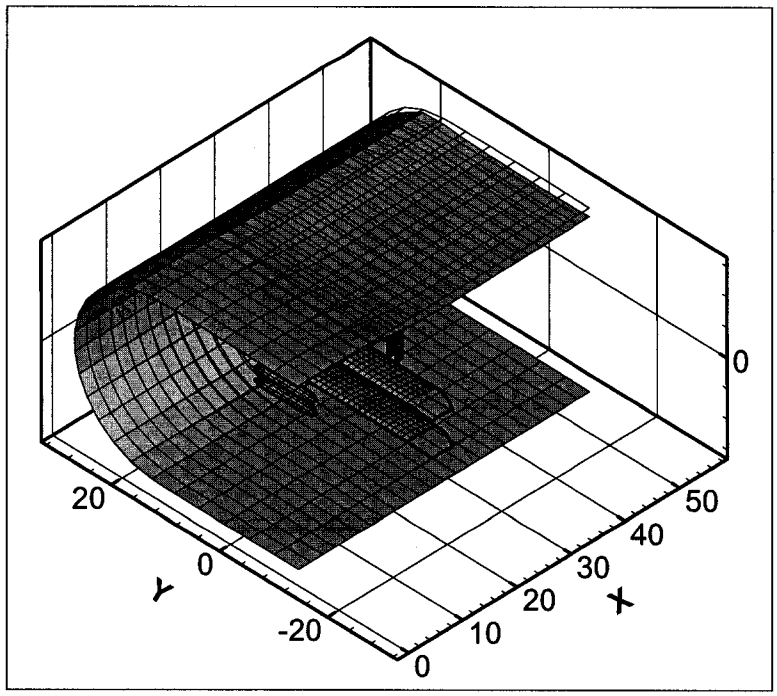

Figure (4-14) Jet distortion, 3/4 open test section; surface panel representation.

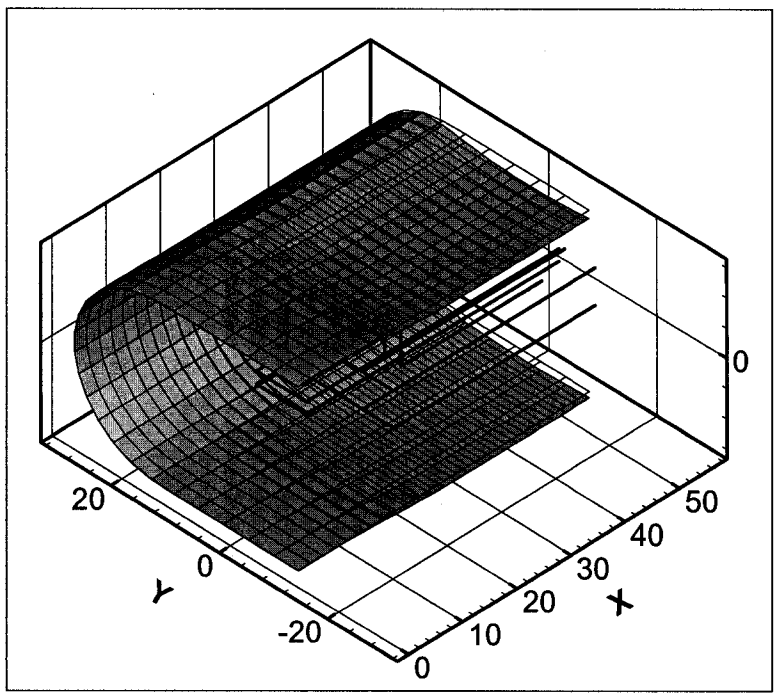

Figure (4-15) Jet distortion, fully open test section; horseshoe vortex representation.

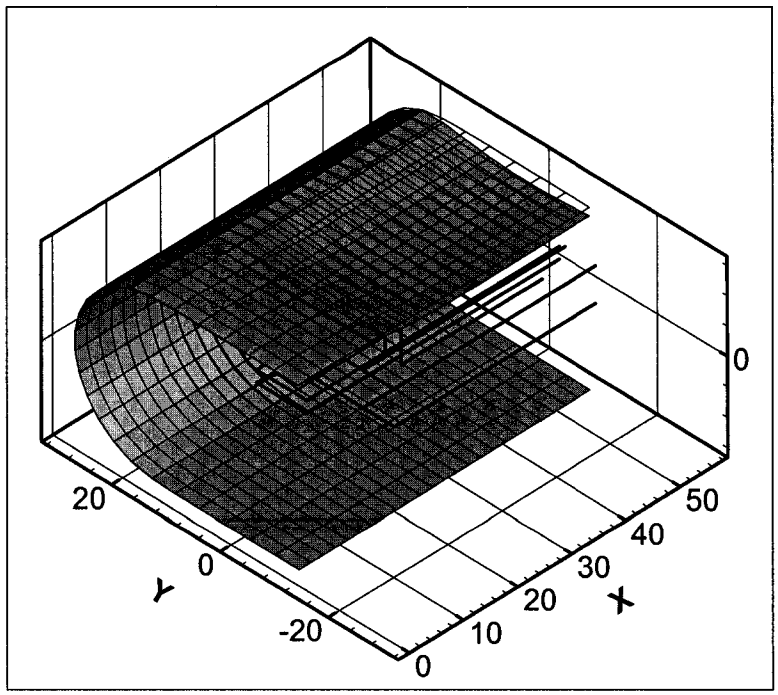

Figure (4-16) Jet distortion, 3/4 open test section; horseshoe vortex representation.

To investigate the effect of the test section boundary configuration on the interference assessment, the upwash distribution ($\Delta\alpha$) is found on horizontal and vertical planes passing through the test section centerline, for closed, open and 3/4-open test sections, using the same 'Flyer' representation (surface panels), as shown in Figures (4-17) through (4-19). The magnitude of induced upwash in the case of the closed test section is as expected slightly less than that of the open test section, with opposite sign. It is also found that in the case of the 3/4-open test section the interference of the solid ground board acts in the opposite sense to the rest of the boundaries, which greatly decreases the magnitude of the net induced upwash as shown in Figure (4-19).

For all the test section boundary configurations the maximum upwash is downstream of the centroid of the wings. Relatively little effect of the boundary configuration can be seen on the distributions of upwash in the downstream or spanwise directions.

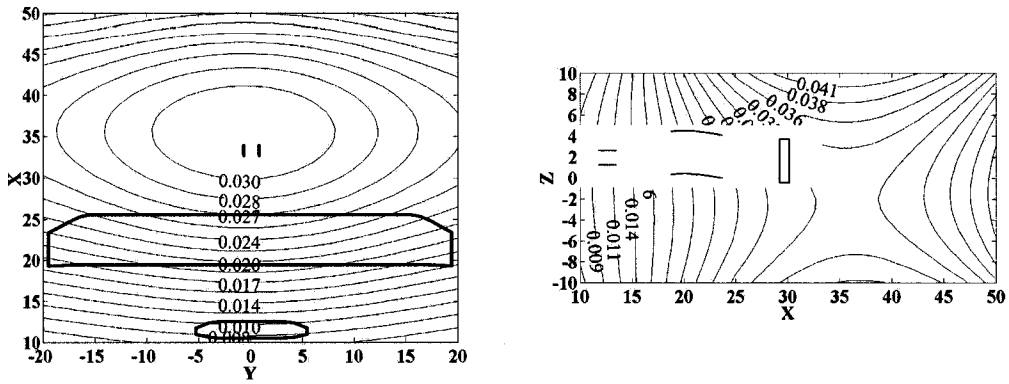

Figure (4-17) Upwash interference ($\Delta\alpha$) for closed test section; surface panel representation

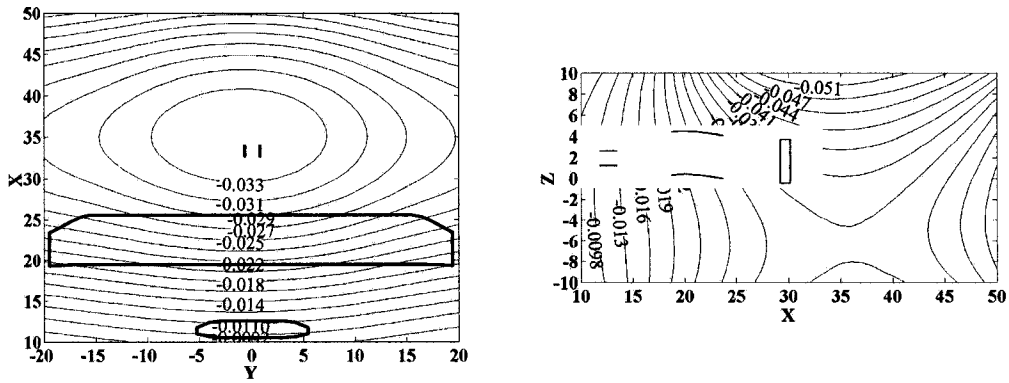

Figure (4-18) Upwash interference ($\Delta\alpha$) for open test section; surface panel representation

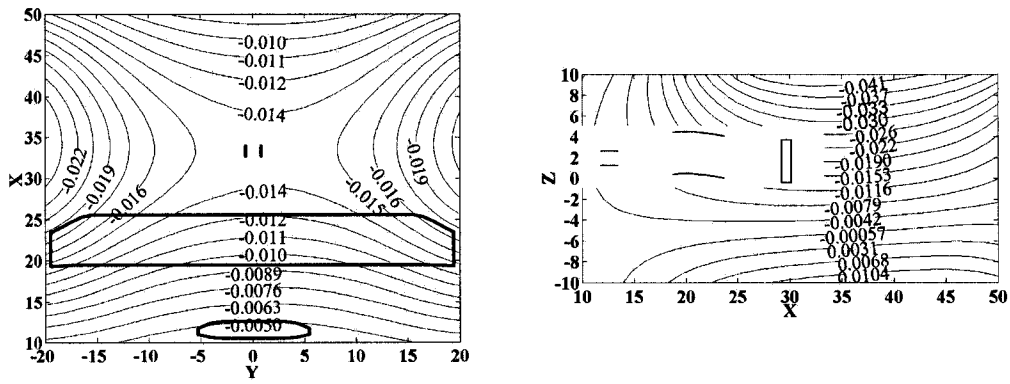

Figure (4-19) Upwash interference ($\Delta\alpha$) for 3/4 open test section; surface panel representation

For further study of the effect of the Flyer representation on the interference assessment, similar results are obtained using the horseshoe vortex representation, as shown in Figures (4-20) through (4-22). The closed test section seems to be least sensitive to the approach used for Flyer representation while in the open test section the solution is relatively more sensitive. The 3/4 open test section is the most sensitive to the Flyer representation, at least in relative terms, because it has the lowest magnitude of upwash interference.

The theoretical downstream asymptote of induced upwash in a long test section is twice the value at the location of the test article. This condition is not seen here due to the downstream constraint of the test section cross section. Calculations with increased test section lengths more closely match the theoretical asymptote as shown previously in Chapter (3).

From the previous study it is clear that existence of a ground plane in the 3/4-open test section significantly decreases the magnitude of the boundary interference but makes the solution relatively more sensitive to the 'Flyer' representation. In addition, the downstream gradients of the upwash are rather low for the 3/4-open test section, which makes it amenable to an approach where the test conditions are corrected based on the magnitude of interference at certain points (wing or canard quarter chords for example). This is not necessarily the case for fully closed or fully open test sections where the downstream gradient of the upwash is relatively high and additional care would have to be taken to include the residual variance of the interferences.

To enable a fair comparison to the method of images, the open jet test section is resolved with no boundary deformation considered. The object of this step is to evaluate the ability of the present method to match the classical method of images for the same boundary conditions applied to the un-deformed open test section. It is also presented here to show the importance of including the boundary deformation in the interference assessment. Figures (4-23) and (4-24) show the upwash interference factor on a horizontal and

vertical planes passing through the open un-deformed test section for full panel and horseshoe vortex model representation respectively.

To complete the interference assessment of the Flyer test, the blockage distribution on horizontal and vertical planes passing through the test section centerline is presented in Figure (4-25). Since the Flyer has a very low frontal area, the blockage corrections are one order of magnitude lower than the upwash interference, with negligible spanwise and low streamwise gradients.

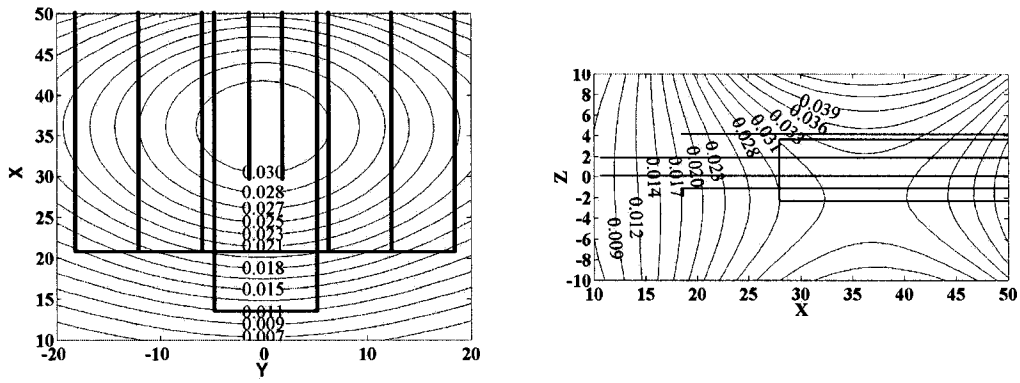

Figure (4-20) Upwash interference ($\Delta\alpha$) for closed test section; horseshoe vortex representation

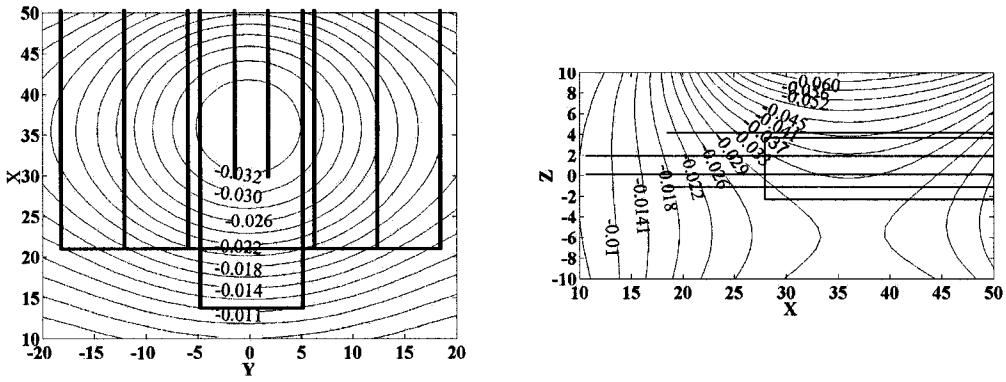

Figure (4-21) Upwash interference ($\Delta\alpha$) for open-jet test section; horseshoe vortex representation

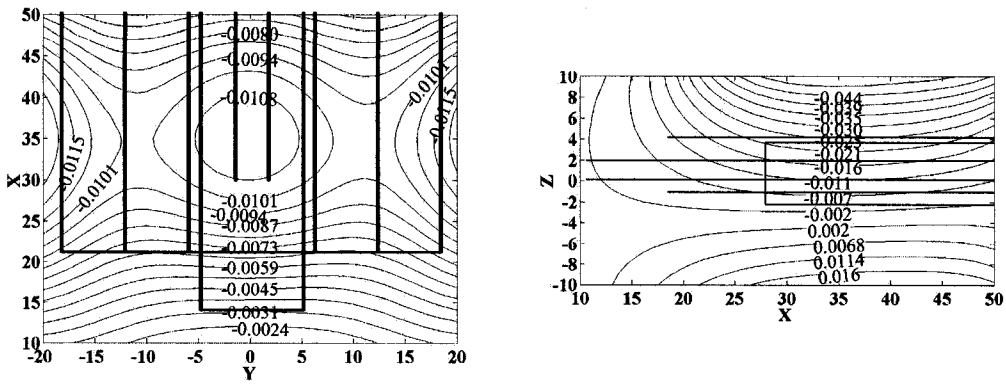

Figure (4-22) Upwash interference ($\Delta\alpha$) for 3/4 open test section; horseshoe vortex representation

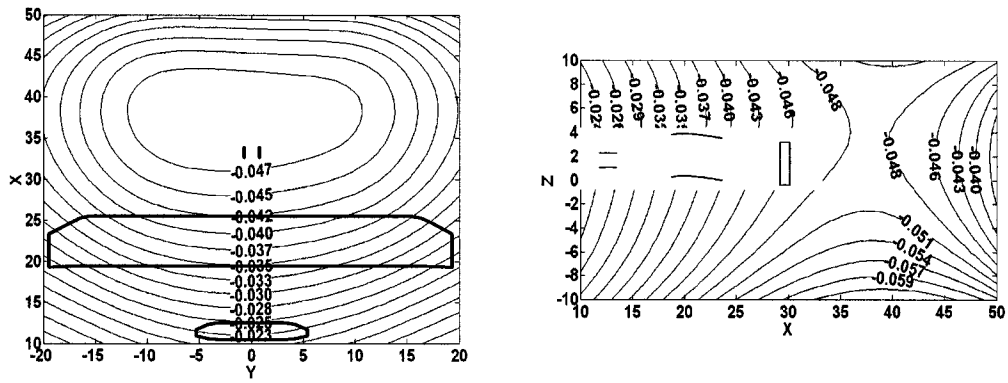

Figure (4-23) Upwash interference ($\Delta\alpha$) for un-deformed open test section; surface panel representation

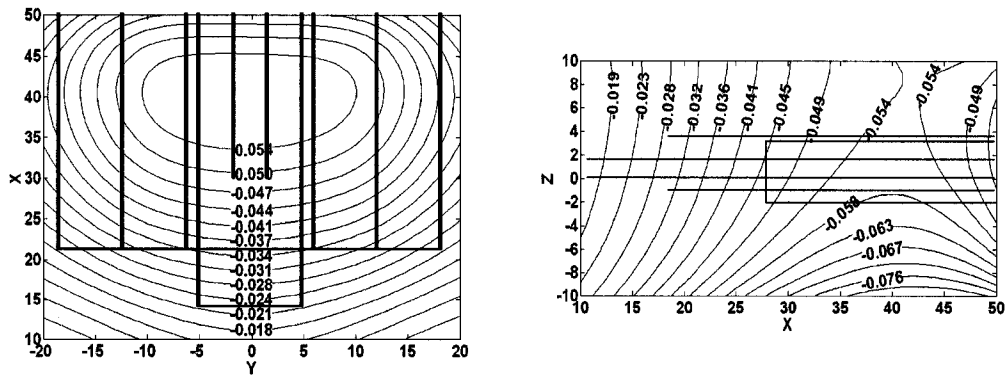

Figure (4-24) Upwash interference ($\Delta\alpha$) for un-deformed open test section; horseshoe vortex representation

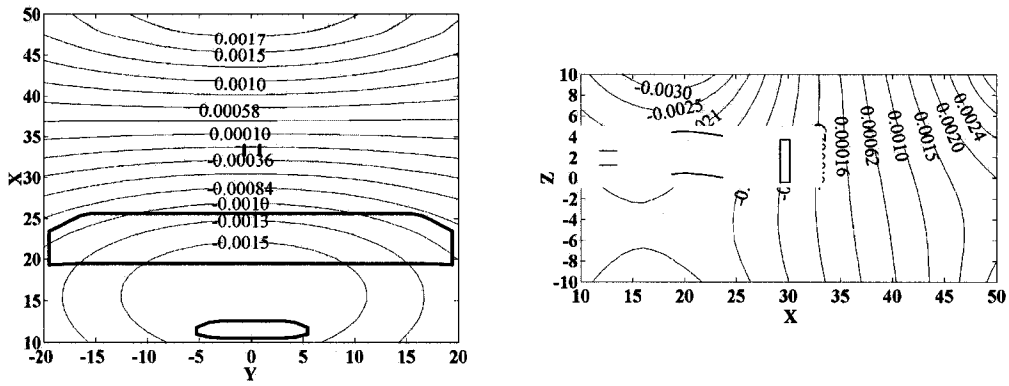

Figure (4-25) Blockage interference (ε) for 3/4 open test section; surface panel representation

4.4 Discussion of results

In this section the above interference assessment results for the different model representation and test section configurations are summarized and compared to the method of images. Table (4-2) shows a comparison between the present method and method of images for the closed test section configuration. Good matching between the methods can be observed keeping in mind that the method of images solves a rectangular test section while the present method deals with the real test section geometry. Using the rectangular test section II (30 by 54) in the method of images improved the matching since it has the same cross-sectional area.

The results for the open jet test section are summarized in Table (4-3). Compared to the previous case, less precise matching between the present method and the method of images is noticed. At the wing root the method of images over-estimated the upwash interference by about 60% when compared to the present method. Combining this statement with the above matching for the closed test section, it seems clear that the main controlling factor for this case is the boundary deformation. To confirm this conclusion, the open test section is re-solved again using the present method but with no boundary deformation to match the boundary conditions applied in the method of images. Table (4-4) shows the results for this case (un-deformed open jet test section). Good matching

between the present method and the method of images can be observed, again confirming the importance of including the boundary deformation in the open test section interference assessment.

For the 3/4 open jet test section, the difference observed between the present method and the method of images is not as clear, as shown in the results presented in Table (4-5). The order of magnitude for this case is lower and as a result the differences are so small to be resolve. Further analysis for this case is presented in a following section.

Approach		Upwash interference factor Δα: rad. (deg.)	
		At the wing root	At the wing tip
Present method	Horseshoe model	0.021 (1.2°)	0.015 (0.86°)
	Full panel model	0.022 (1.26°)	0.017 (0.97°)
Method of images	I (30 by 60)	0.018 (1.05°)	0.011 (0.65°)
	II (30 by 54)	0.019 (1.1°)	0.016 (0.9°)

Table (4-2) Comparison to the method for images for closed test section, at the wing 1/4 chord.

Approach		Upwash interference factor Δα: rad. (deg.)	
		At the wing root	At the wing tip
Present method	Horseshoe model	-0.022 (-1.26°)	-0.013 (-0.74°)
	Full panel model	-0.023 (-1.32°)	-0.018 (-1.03°)
Method of images	I (30 by 60)	-0.037 (-2.1°)	-0.024 (-1.4°)
	II (30 by 54)	-0.037 (-2.1°)	-0.026 (-1.5°)

Table (4-3) Comparison to the method for images for open jet test section, fully-deformed boundaries, at the wing 1/4 chord.

Approach		Upwash interference factor Δα: rad. (deg.)	
		At the wing root	At the wing tip
Present method	Horseshoe model	-0.0355 (-2.03°)	-0.022 (-1.26°)
	Full panel model	-0.037 (-2.1°)	-0.028 (-1.6°)
Method of images	I (30 by 60)	-0.037 (-2.1°)	-0.024 (-1.4°)
	II (30 by 54)	-0.037 (-2.1°)	-0.026 (-1.5°)

Table (4-4) Comparison to the method for images for open jet test section, un-deformed boundaries, at the wing 1/4 chord.

Approach		Upwash interference factor Δα: rad. (deg.)	
		At the wing root	At the wing tip
Present method	Horseshoe model	-0.0073 (-0.42°)	-0.0087 (-0.49°)
	Full panel model	-0.0105 (-0.6°)	-0.0155 (0.88°)
Method of images	I (30 by 60)	-0.0034 (-0.2°)	-0.007 (-0.4°)
	II (30 by 54)	-0.0052 (-0.3°)	-0.0105 (-0.6°)

Table (4-5) Comparison to the method for images for 3/4 open jet test section, at the wing 1/4 chord.

4.5 Application of corrections

In this section, some statements concerning the order-of-magnitude of the boundary interferences are made, based on the reference case described above, followed by correction of a representative angle-of-attack sweep. The wing quarter-chord line of the 'Flyer'' was located at around the 21-foot station in x, with the aircraft wings nearly equidistant above and below the y-axis. Figure (4-19) indicates that the average induced upwash across the wing quarter chord locations is around -0.0105 or -0.60 degrees. Since the measured lift curve slope, $C_{L\alpha}$, is approximately 0.054 per degree, this suggests a lift coefficient correction of only 0.032, which is around 5% of the nominal value. The corresponding drag coefficient correction would be only 0.006, again only a few percent of the nominal value. Figure (4-26) shows the effect of applying the corrections for induced upwash on a representative lift curve. It should be noted that the upper and lower wings are exposed to different levels of upwash, and that a spanwise upwash gradient exits, with maximum values on centerline, falling to near zero at the tips. For reference, the induced twist is around 0.3 degrees, averaged over the two wings. The effects of the induced twist are typically not considered correctable.

The stream-wise gradient in upwash is rather small. Figure (4-19) shows an induced upwash at the canard location of perhaps -0.005, or -0.29 degrees, leading to small corrections of canard angle to trim, since this is less than the average value at the wing. Figure (4-27) shows the effect of the canard angle corrections. It is seen that the magnitudes of the effect of the structural deflections of the canard under load are larger than the boundary-induced corrections. These deflections arise due to the canard being pivoted about the 50% chord location, resulting in increased "nose-up" deflection as aerodynamic loads increase. Blockage effects on aerodynamic results are negligible.

It should be noted that empty test section flow uniformity was surveyed most recently by Alvarez (unpublished). Angularity, total and static pressures were measured on various cross-sections. Unfortunately, axial gradient information is not considered sufficiently reliable for use here.

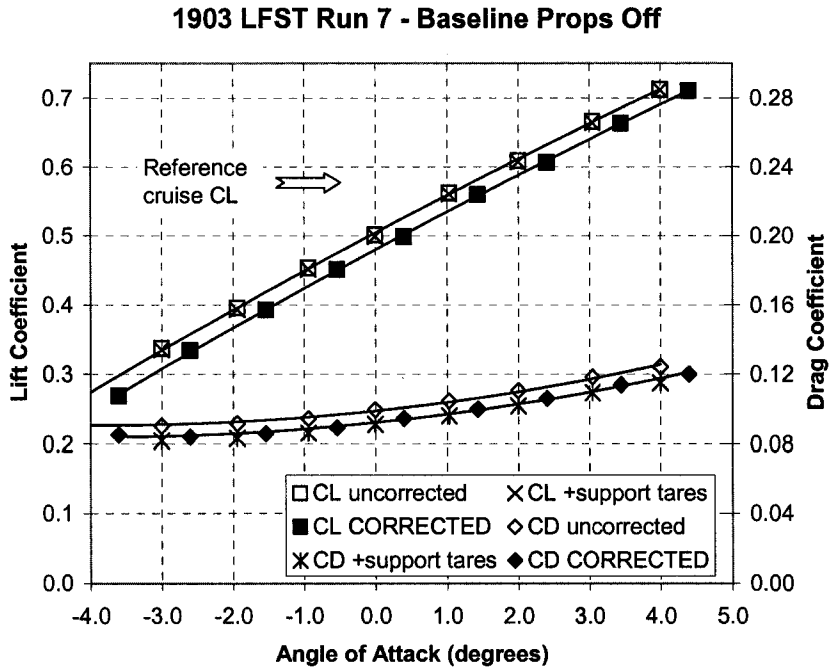

Figure (4-26) Corrected lift curve

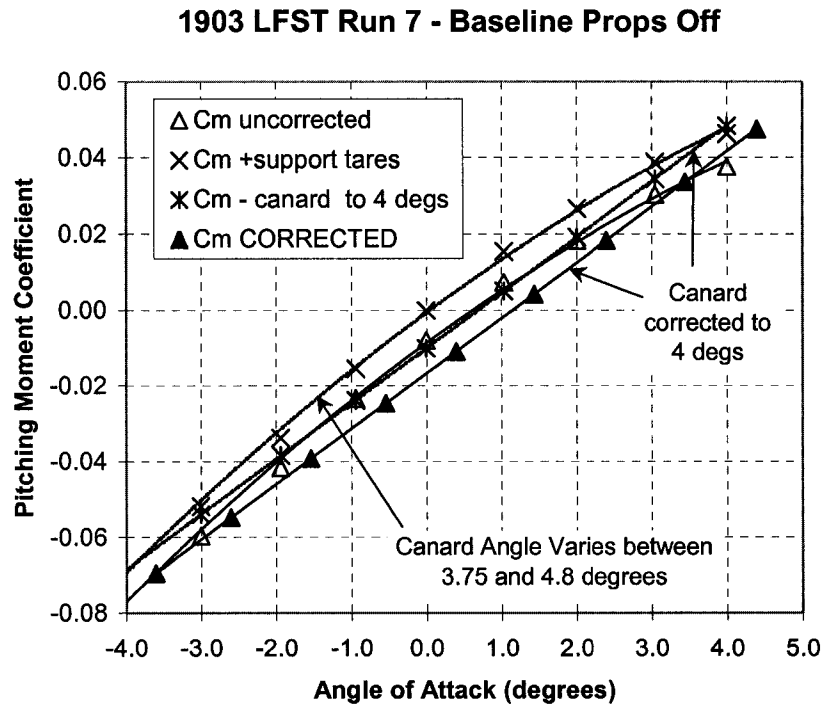

Figure (4-27) Corrected Pitching moment curve

4.6 Summary

In this chapter the present method is compared to the classical method of images for the interference assessment of a relatively large span model (full scale Wright Flyer replica, the span is about 67% of test section maximum width) tested in a non-rectangular test section (LFST). The comparison study included closed, open with full-deformed boundaries, open with un-deformed boundaries and 3/4 open test section configurations. Two methods are used to represent the model using full paneling of the surfaces and using horseshoe vortex. For the method of images, the test section is represented using two approaches: 30 by 60 foot and 30 by 54 foot rectangular cross-sections. The first one matches the external dimensions of the LFST test section, which makes it about 12% larger in cross-sectional area. The second one matches the real test section area.

Good matching between the method of images and the present method is found for the closed test section cases. For the open jet test section, the results from the classical method of images compared very well with the present method for the un-deformed boundaries test section. However, for the fully-deformed boundary case, the method of images over-estimated the upwash interference by nearly 60%. These two sets of results for open jet test sections with and without boundary deformation confirm the importance of including the boundary deformation in the interference assessment. They also show the ability of the present method to match the classical method of images by modifying the boundary conditions applied.

The effect of the model representation (using full panels or horseshoe vortices) seems to be small for the closed and open test sections. It is relatively more significant for the 3/4 open test section case, which has a lower level of upwash interference.

CHAPTER V

V. APPLICATION II – NASA LANGLEY RESEARCH CENTER 14 BY 22 FOOT SUBSONIC WIND TUNNEL

In the Fall of 2003 a proof-of-concept automotive test was undertaken in the NASA Langley Research Center 14 by 22 Foot Subsonic Wind Tunnel*. The test was a collaboration between Old Dominion University, who supplied the automotive balance, NASA, who provided wind tunnel time, and Penske Racing South, who provided the instrumented test vehicle (a full scale NASCAR vehicle). During that test, back-to-back measurements were taken for the closed and the 3/4 open test section configurations. Figures (5-1) and (5-2) show views of the tested NASCAR vehicle inside the closed and the 3/4 open test sections respectively. The test section is 21.76 feet in width, 14.5 feet in height and 50 feet in length. The size of the vehicle is approximately 5.6 feet maximum width, 4.17 feet maximum height and 16 feet maximum length. Its reference area is 23.35 ft^2. The nominal blockage is 7.4%. During the test, the front of the vehicle was 10.7 feet downstream of the nozzle exit section along the centerline of the ground board. In other words, the front of the vehicle was about 0.67 times its length downstream of the nozzle and its back was 1.46 times its length upstream of the beginning of the diffuser (or the collector in the open jet test section).

In this chapter, the present approach is used to assess the boundary interference for the 3/4 open test section and a pressure signature method is used to assess interference for the closed test section. The study is also extended to include the upstream effect by the inclusion of the real nozzle geometry in the solution or by adding an extra upstream length to the test section equal to the nozzle length. The focus of the study is the blockage interference.

* A follow-up test with a new automotive balance was conducted in December 2005 and January 2006. Results from this test were not released in time to be included in this dissertation.

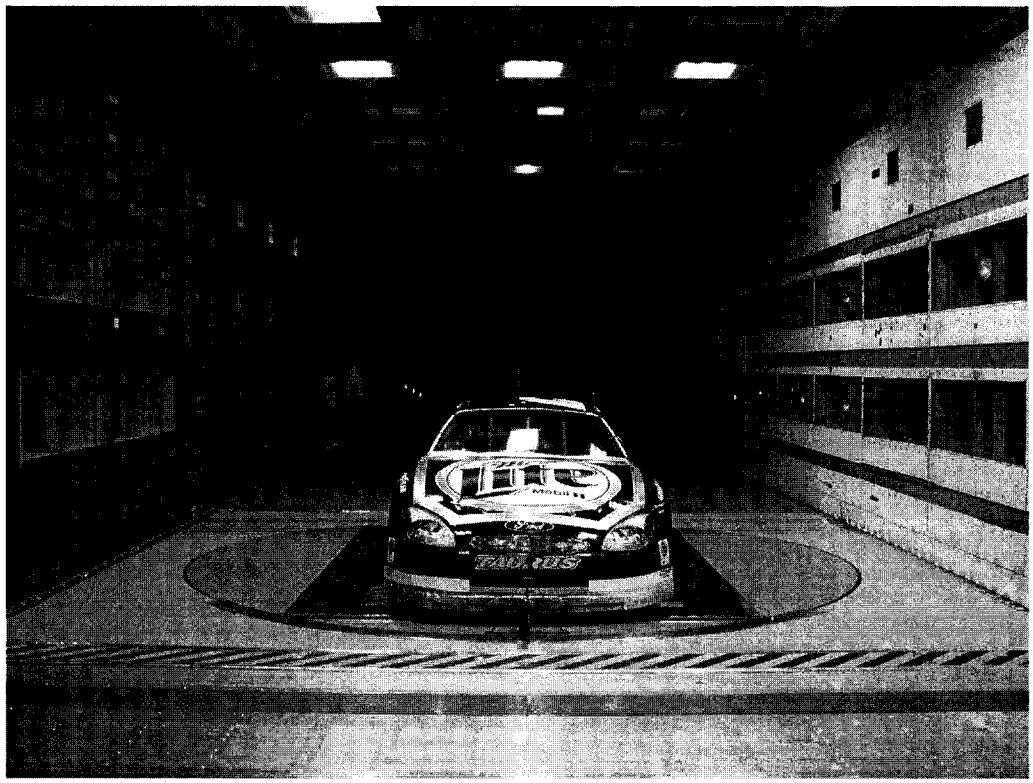

Figure (5.1) Vehicle in closed wall test section

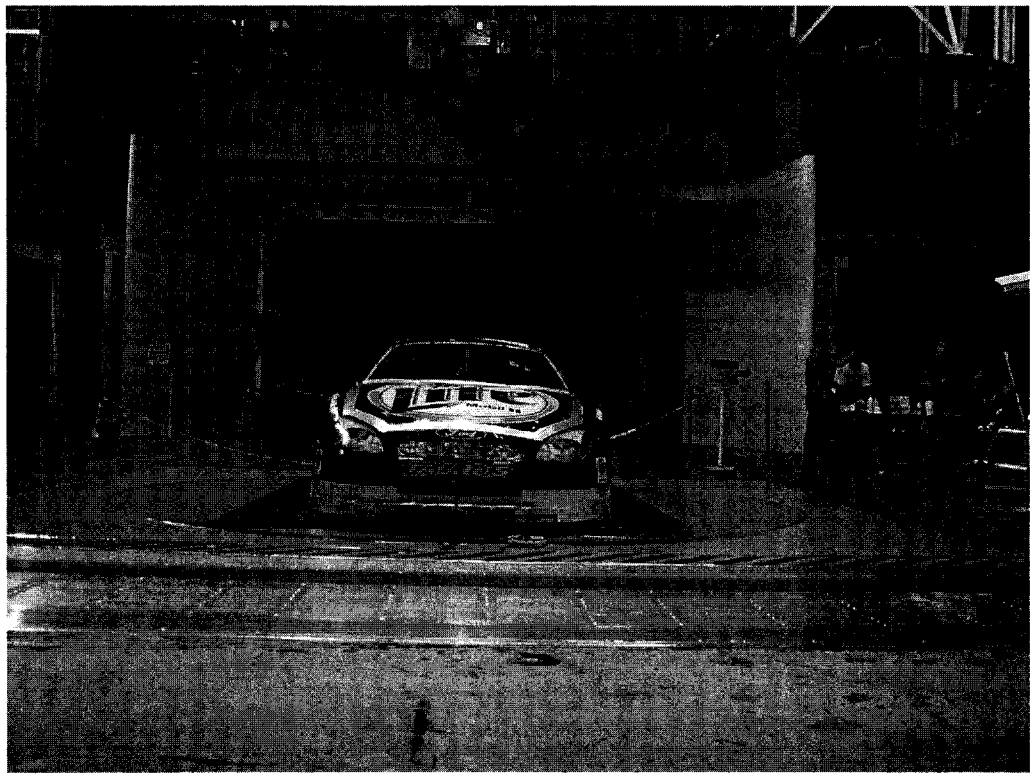

Figure (5.2) Vehicle in open jet test section

5.1 Closed test section interference

During the test with the closed wall configuration, the surface pressure on the sidewalls and the ceiling was measured using an array of 373 pressure taps located along the axes of filled wall slots. A schematic of the tap locations is shown in Figure (5-3). A typical measured pressure signature is presented in Figure (5-4). In the classical pressure signature method, discussed in Chapters (1) and (2), this measured wall pressure is used to obtain the strength of a set of singularities representing the tested model. Then the wall interference is obtained by calculating the velocity induced by a finite number of images of these singularities. A similar approach is used in the present work but instead of using images to calculate the wall interference, the test section boundaries are divided into surface panels with strengths derived by applying the wall boundary condition (Neumann boundary condition). The interference is then obtained by calculating the velocity induced by the boundary panels.

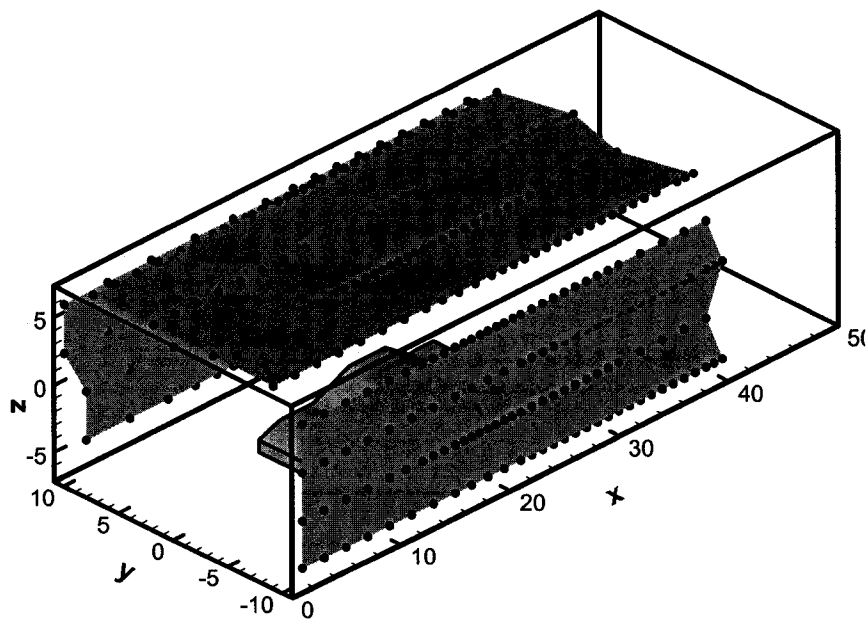

Figure (5-3) Schematic of the pressure tap locations

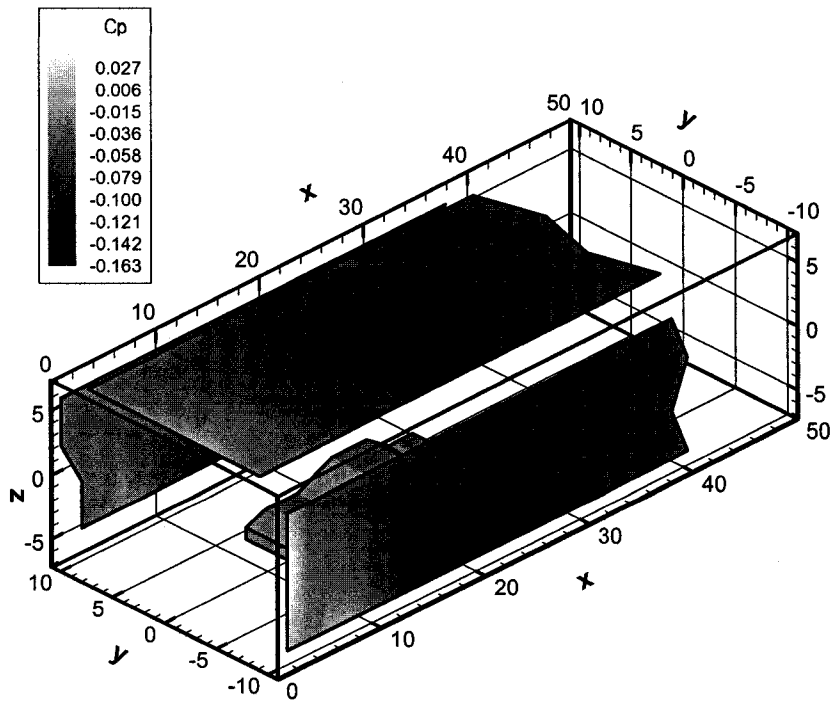

Figure (5-4) Typical wall pressure signature for the NASA Langley Research Center 14 by 22 Foot Subsonic Wind Tunnel

The far field effect of the NASCAR model is approximated by 420 point-source singularities distributed over its geometry, as shown in Figure (5-5). The same number of collocation points are distributed over the sidewalls and the ceiling and a best surface fitting technique is used to obtain the surface pressure at each collocation point using the measured pressure signature. The strengths of the singularities representing the vehicle model are obtained by applying Dirichlet boundary conditions at each collocation point. Three numerical configurations are studied for the closed test section. In the first one, the sidewalls and the ceiling of the test section are divided into 342 surface panels. In the second configuration, both the test section and the nozzle walls are divided into surface panels, which makes a total of 520 surface panels. In the third configuration, the nozzle is replaced by an extra constant area duct added to the test section, with the same total number of surface panels as the second configuration (520 surface panels). For all cases vortex ring surface panels are used. Figures (5-6), (5-7) and (5-8) show the surface panels for the test section only, the test section plus nozzle and the long test section configurations respectively.

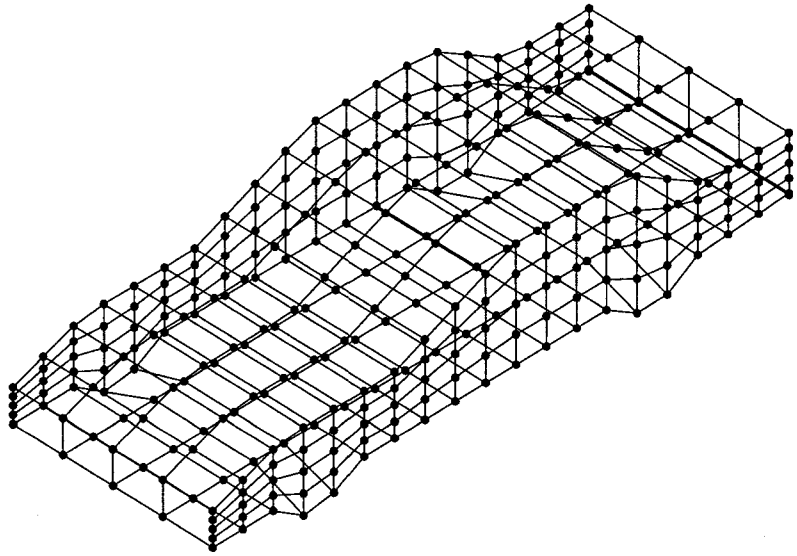

Figure (5-5) Distributed singularities over the car model geometry

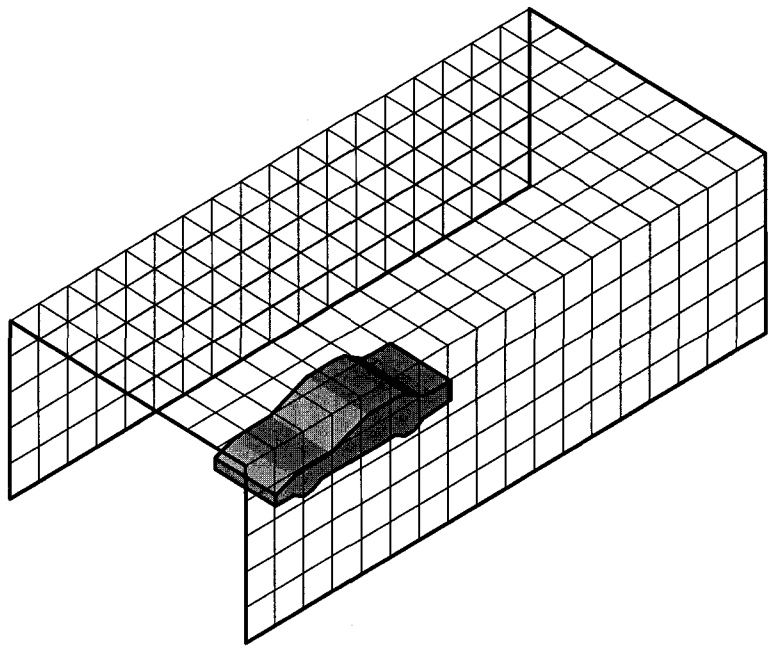

Figure (5-6) Surface panels for test section walls.

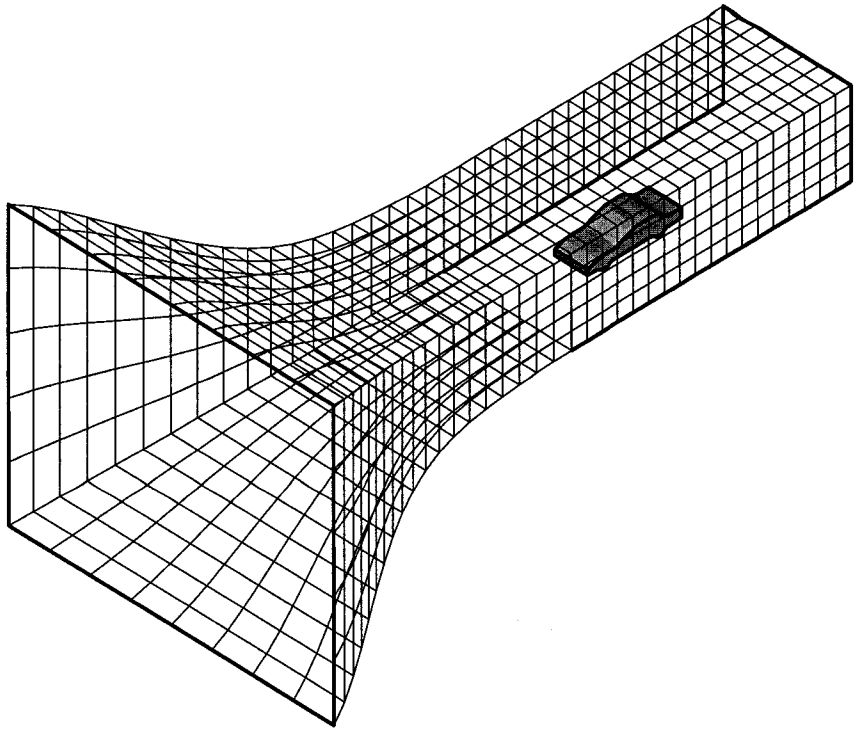

Figure (5-7) Surface panels for test section walls + nozzle.

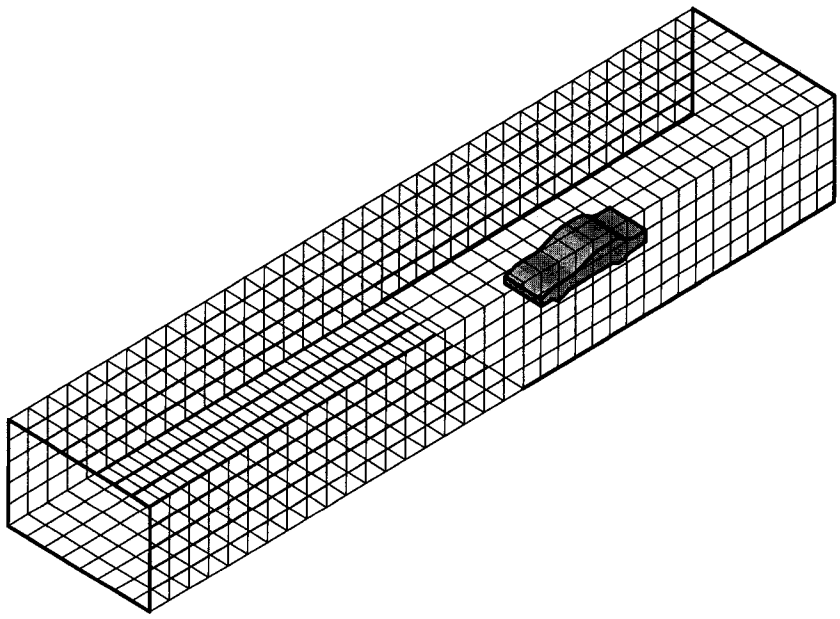

Figure (5-8) Surface panels for the long test section.

The strengths of the surface panels are obtained by applying the Neumann boundary condition at the boundaries. Figures (5-9) through (5-11) show the derived vortex ring panel strengths when solving the test section only, the test section plus nozzle and the long test section respectively. The results shown are for an air speed equal to 30 ft/s and the panel strength is in ft^2/s. The addition of the nozzle or an extra length to the test section slightly changes the derived panel strength but has almost no effect on the distribution over the sidewalls or the ceiling. This difference will be more visible in the following steps of the solution.

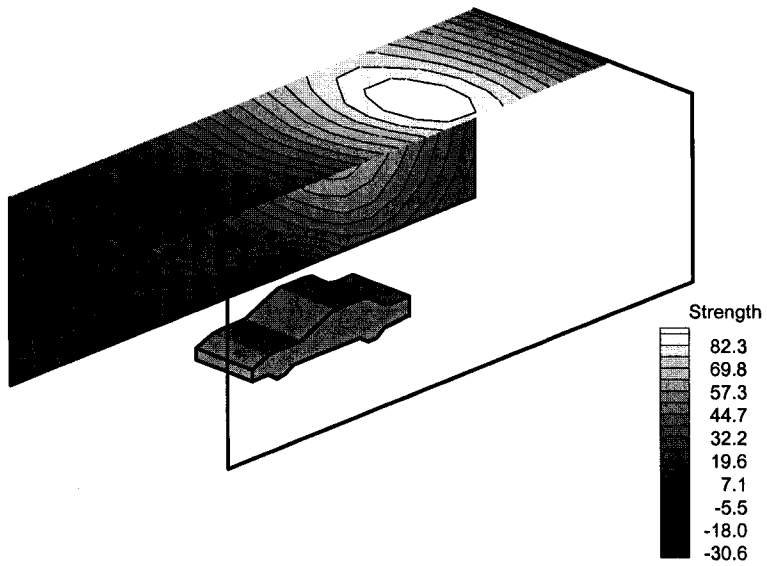

Figure (5-9) Strength of the vortex ring surface panels (ft^2/s), solving test section walls.

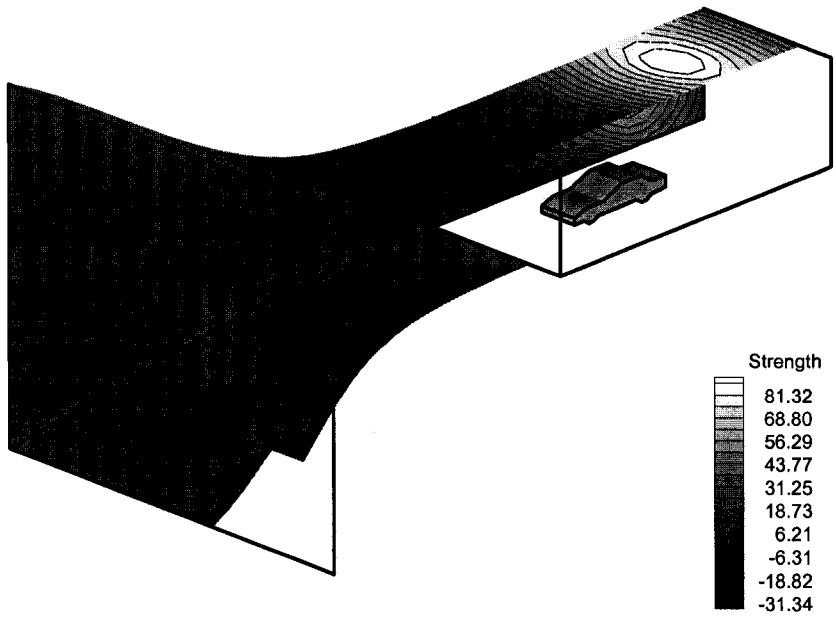

Figure (5-10) Strength of the vortex ring surface panels (ft^2/s), solving test section walls + nozzle.

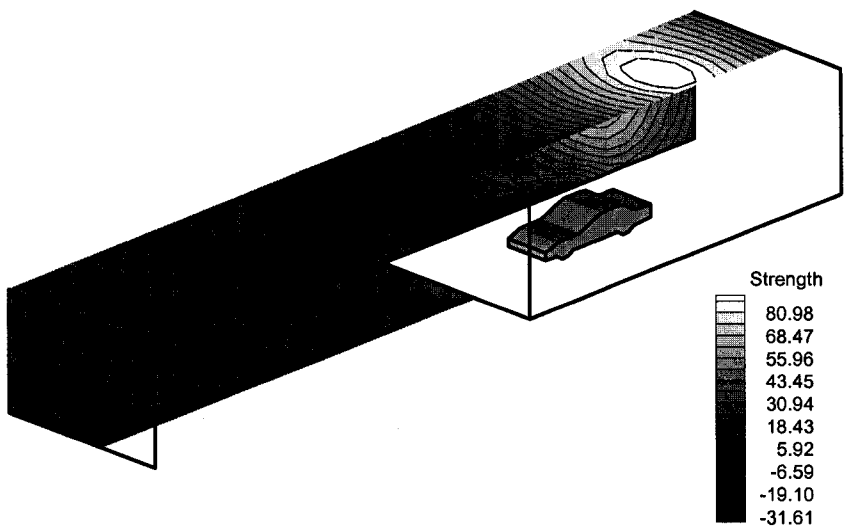

Figure (5-11) Strength of the vortex ring surface panels (ft^2/s), solving a long test section.

The final step in this investigation of the upstream effect represented by adding the nozzle or increasing the test section length is the comparison between the predicted blockage interference factor obtained from the different numerical configurations. Figures (5-12), (5-13) and (5-14) show the blockage factor (ε) distribution on a horizontal plane passing through the car for the different test section configurations studied. The overall distribution of the predicted blockage interference is nearly the same for all cases. A small increase in the predicted blockage interference is observed when the nozzle is added or the test section length is increased. This may be due to the additional upstream constraints imposed by these walls compared to the unconstrained upstream end when solving the test section only. The gradient in the lateral direction is very small compared to the streamwise direction. The maximum blockage interference is at about 80% of the car length.

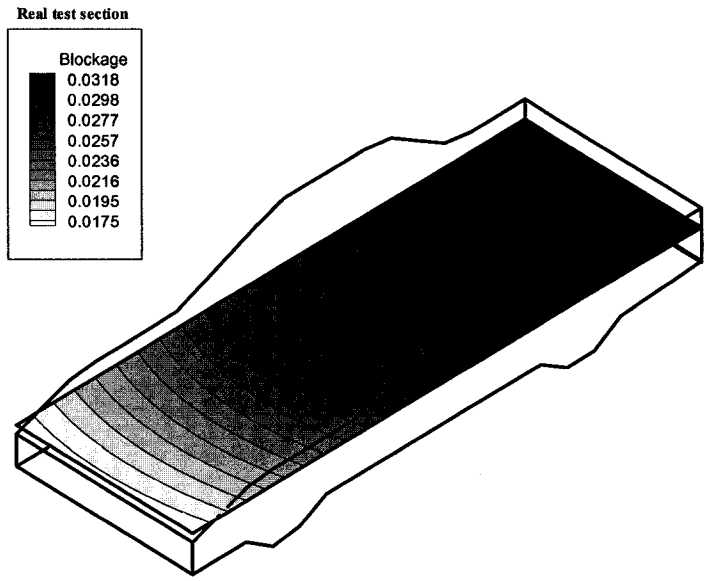

Figure (5-12) Blockage factor (ε) distribution at a horizontal plane, solving the test section walls.

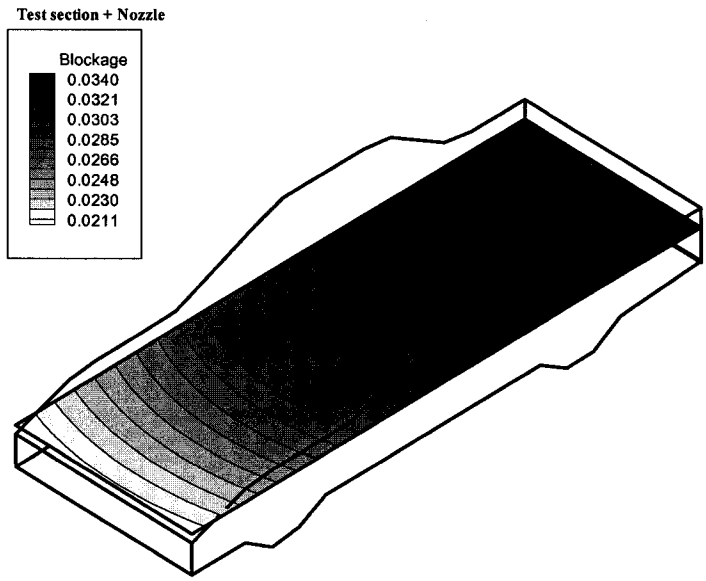

Figure (5-13) Blockage factor (ε) distribution at a horizontal plane, solving the test section walls + the nozzle.

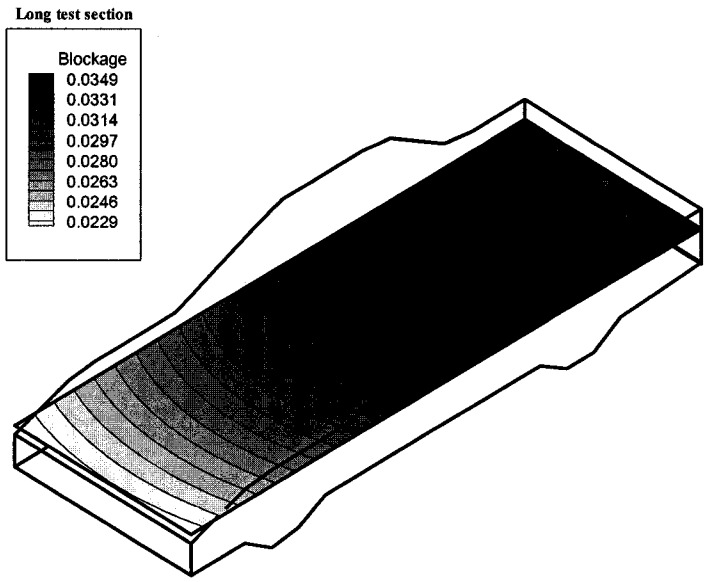

Figure (5-14) Blockage factor (ε) distribution for at a horizontal plane, solving a long test section.

Figure (5-15) shows the blockage interference distribution along the car centerline for the different test section numerical configurations. Again the overall trend and the location of the maximum value are nearly the same for all cases. The difference between the blockage interference predicted by adding the nozzle and by increasing the test section length is decreasing in the downstream direction. Figure (5-16) shows the distribution of the percentage increase in the blockage factor when the nozzle or an extra length is added to the test section. It is clear that the two solutions are converging in the downstream direction. Table (5-1) shows the maximum predicted blockage factor for the different numerical test section configurations.

Test section numerical configuration	Maximum blockage factor
Test section only	0.0322
Test section + nozzle	0.0343
Long test section	0.0352

Table (5-1) Maximum blockage factor, solid walls.

The difference between the values in the table may indicate that the upstream effect is not very significant. This is not true for any model location or any model size relative to the test section. The presented results are for a model located roughly one model-length downstream of the nozzle and roughly two model-lengths upstream of the diffuser measured from the model center. For example, if the model is moved upstream, the flow at the nozzle exit section will be more strongly affected and the nozzle representation will have to be included in the solution. The same applies to the diffuser if the model is moved downstream toward the end of the test section. Also as the relative model size increases, the effect of the nozzle and the diffuser on the interference increases. The effect of both the model size and its location is coupled as reported by Cooper[57]. He recommended that model not be positioned closer to the nozzle than $2\sqrt{S_b}$ and at least $4\sqrt{S_b}$ upstream of the diffuser, where S_b is the area of the separated region on the base of the model.

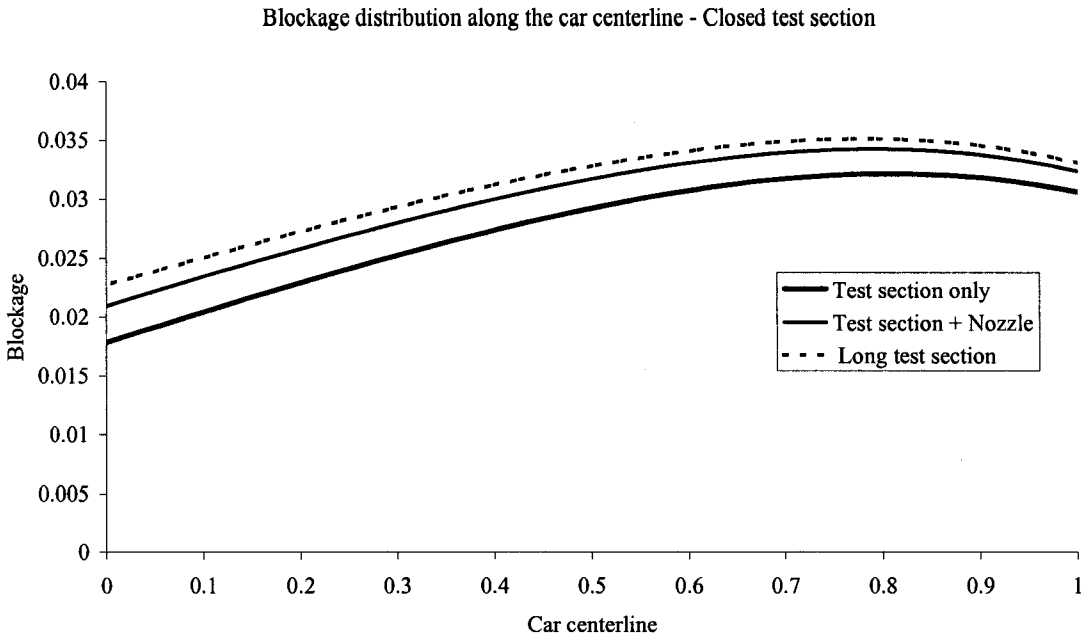

Figure (5-15) Blockage factor (ε) distribution along the car centerline for different test section configurations.

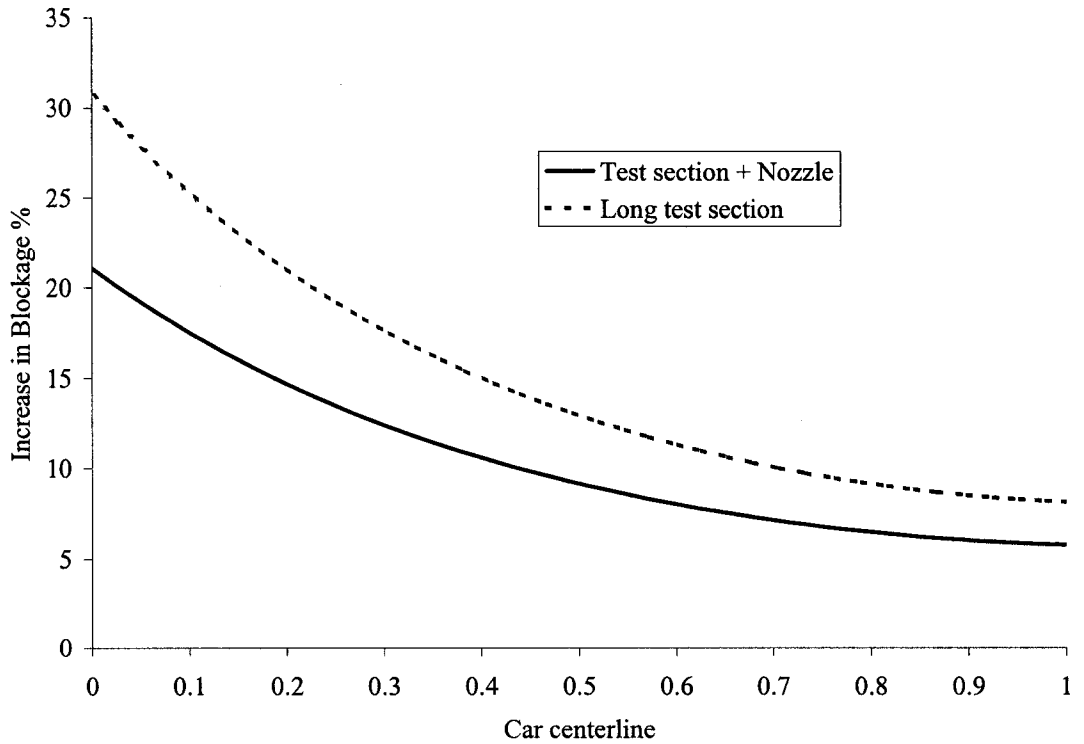

Figure (5-16) Distribution of the percentage increase in the blockage factor (ε) when adding the nozzle or increasing the test section length.

5.2 Open jet test section interference

In this section, the upstream effect represented by adding the nozzle or extending the test section length is studied for an open jet test section. The same surface panels and the same model representation used in the previous section are used here. The present method for open test section boundary interference assessment, discussed in Chapter (2), is employed. Figure (5-17) shows the predicted boundary deformation when solving the test section boundaries only. The major deformation is observed in the side boundaries near to the model location while a lower magnitude of deformation is observed at the ceiling. Figures (5-18) and (5-19) show the predicted deformation for the test section plus nozzle and the long test section configurations respectively. Although little difference in the predicted boundary deformation between the two cases can be observed, it still has some effect on the boundary interference as will be shown next.

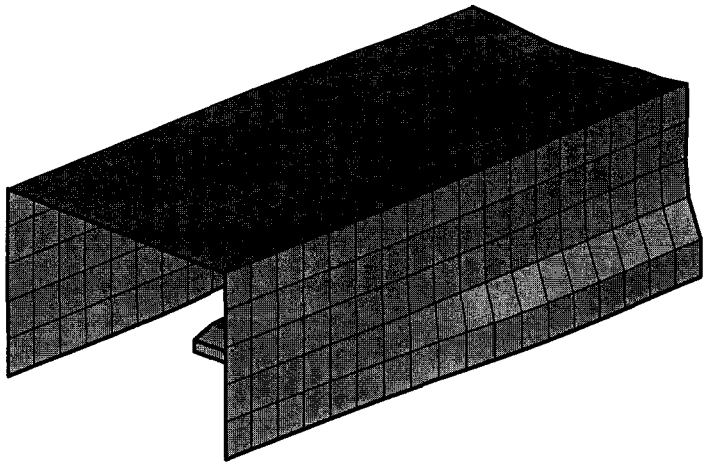

Figure (5-17) Predicted boundary distortion for open jet test section (test section only).

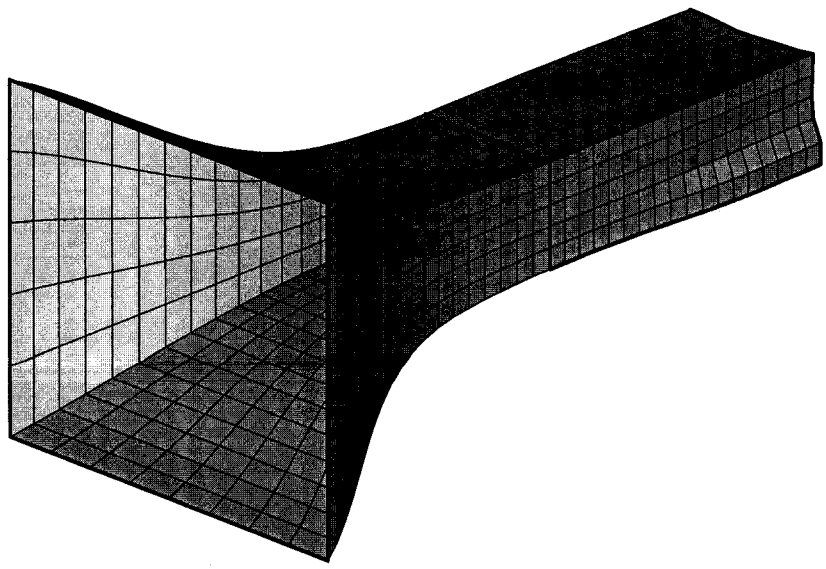

Figure (5-18) Predicted boundary distortion for open jet test section (test section + nozzle).

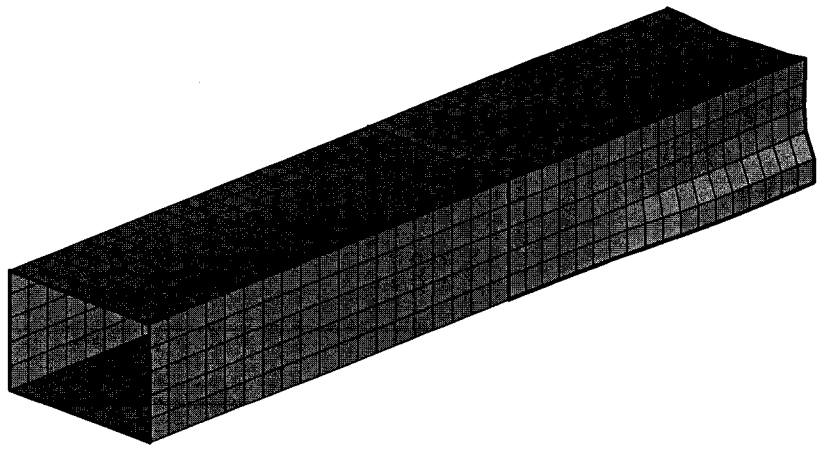

Figure (5-19) Predicted boundary distortion for open jet test section (long test section).

Figures (5-20) through (5-22) show the blockage factor (ε) distribution on a horizontal plane passing through the car model. Comparing these results to those for the closed test section, Figures (5-12) through (5-14), the open jet test section produces lower magnitude of blockage interference with opposite sign. The spanwise gradient is very small compared to the streamwise gradient. The location of the maximum blockage magnitude is at approximately 80% of the car length.

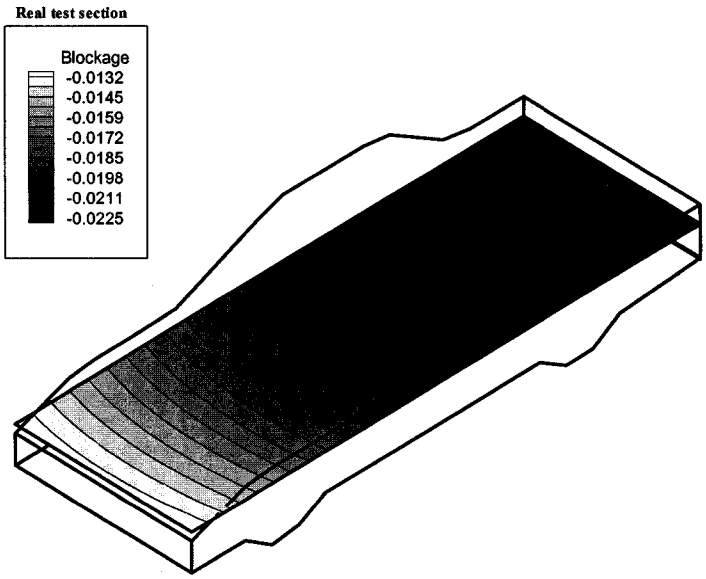

Figure (5-20) Blockage factor at a horizontal plane obtained using the present approach for open jet test section (test section only).

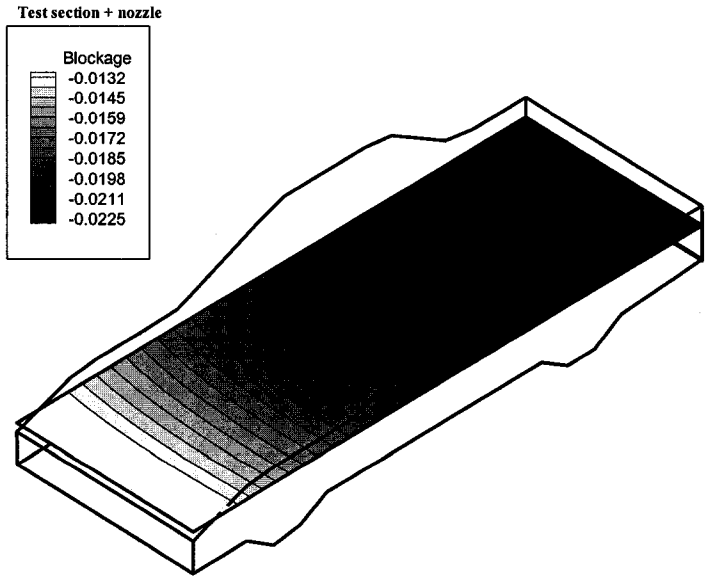

Figure (5-21) Blockage factor at a horizontal plane obtained using the present approach for open jet test section (test section + nozzle).

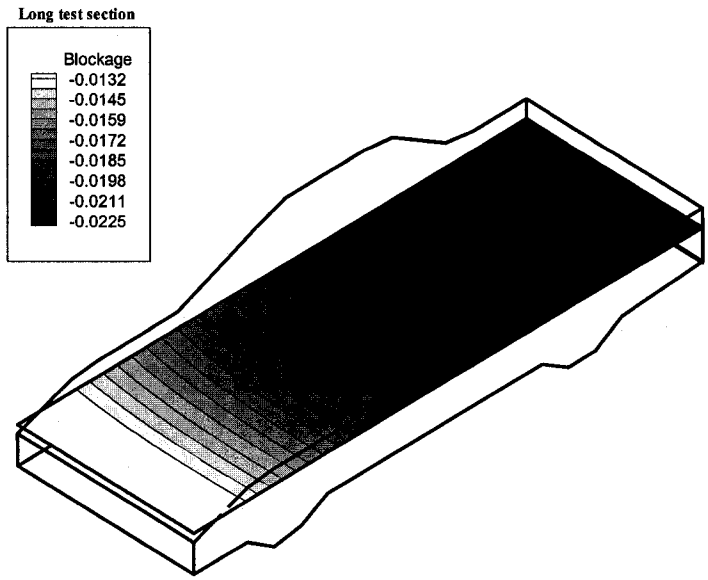

Figure (5-22) Blockage factor at a horizontal plane obtained using the present approach for open jet test section (long test section).

Figure (5-23) shows the centerline blockage distribution for the different open test section numerical configurations. Unlike the closed test section case, the additional upstream constraints (nozzle or extra length) decrease the magnitude of the blockage interference because solid walls of the added lengths produce positive blockage interference. This simple statement could be enough to explain the differences observed near to the front face of the model but it is not enough to explain the differences near to the rear of the model where an opposite effect can be observed. It seems that the existence of these upstream boundaries affects the boundary deformation as well, which increases the blockage gradient and shifts the location of the maximum blockage magnitude in the downstream direction. Figure (5-24) shows the percentage changes of the blockage interference when adding the nozzle or an extra length to the test section. Table (5-2) shows the maximum blockage factor magnitudes for the different cases studied.

Test section numerical configuration	Maximum blockage factor
Test section only	-0.0228
Test section + nozzle	-0.0233
Long test section	-0.0234

Table (5-2) Maximum blockage factor, open jet test section

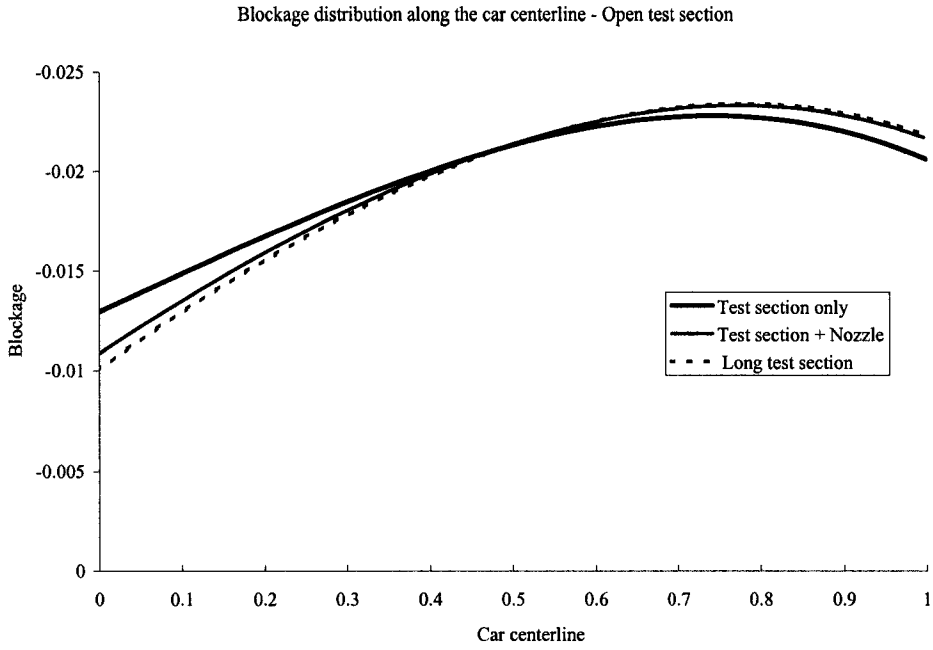

Figure (5-23) Blockage factor along the car centerline obtained using the different numerical configurations for open test section.

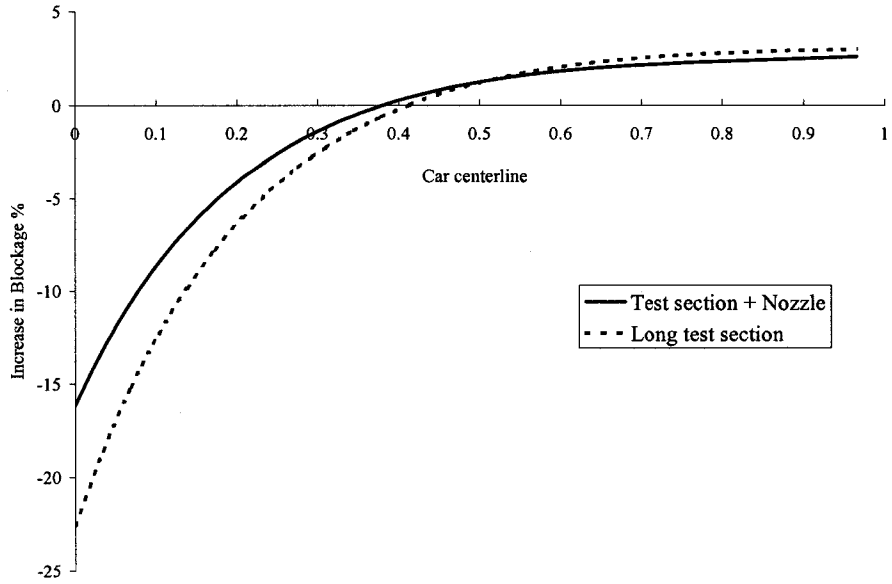

Figure (5-24) Distribution of the percentage change in the blockage factor (ε) when adding the nozzle or increasing the test section length.

5.3 Application of corrections

In this section, the developed method is used to correct the drag force measured during the closed and open jet test section configurations. Results are compared to the classical method of images,[1,2,3,41,57] the modified method of images developed by Wickern,[41] and the semi-empirical method developed by Mercker et al.[42,43,46,49,57] The formula for the drag coefficient for open jet tunnels can be expressed as:[39]

$$C_{Dc} = \frac{C_{D\,m} + \Delta C_D}{q_c / q_\infty} \tag{5-1}$$

Where, $C_{D\,c}$ and $C_{D\,m}$ are the corrected and the measured drag coefficient respectively. ΔC_D is the drag coefficient correction due to the effect of the empty test section pressure gradient. This effect has to be introduced into the correction procedure before any dynamic pressure correction is applied[39]. For the present case, the 14 by 22 tunnel exhibits a weak streamwise pressure gradient in the closed jet case. The gradient is 0.04 psf/ft in the region of the forward cart (model location during the test) at a dynamic pressure 40 psf, based on empty section surveys with a static pipe.[58] The volume of the test article in this case is estimated to be around 265 ft^3 resulting in a buoyancy correction to drag coefficient (ΔC_D) of around –0.011 at a dynamic pressure of 45 psf. This value is then multiplied by a factor of 1.5 or greater for automotive geometries as recommended in the literature.[39] The streamwise pressure gradient for the open jet tunnel case is small.[58] In addition, the effect of the gradients of the blockage factor predicted for both the closed and the open jet sections are also included in ΔC_D. q_c and q_∞ are the corrected and the uncorrected dynamic pressure. Where

$$q_c = q_\infty (1+\varepsilon)^2 \tag{5-2}$$

Figure (5-25) shows the uncorrected and the corrected drag coefficient against the yaw angles through the range from –6 to +6°. The correction factor obtained from the test

section plus nozzle case is used since this case represents the real geometry of the wind tunnel. For the uncorrected drag, the average of the measured values for the open jet case is 83.9% of the closed jet case*. After applying the corrections to both cases the average became 97.5%. Full matching between the two cases is not expected since some other effects such as collector interaction, discussed in Chapter (6), are not included in the methods used.

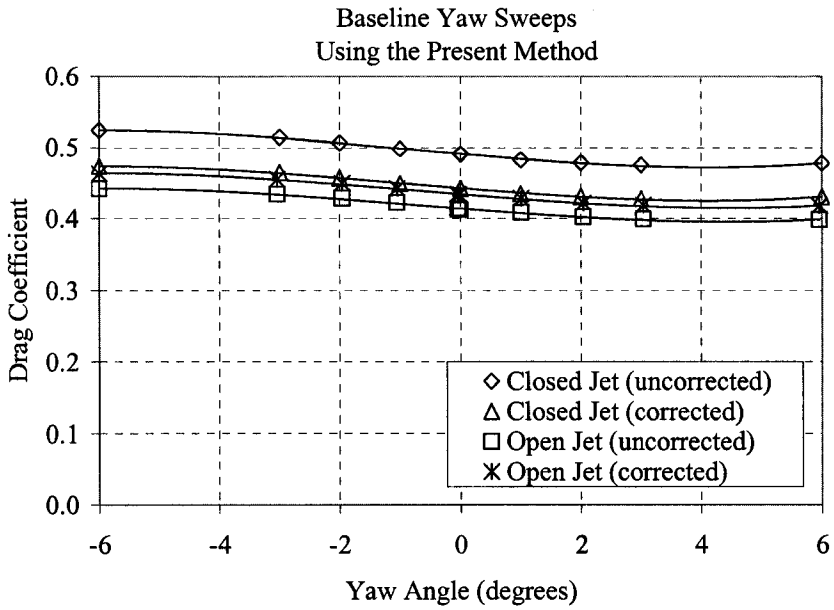

Figure (5-25) Application of the boundary corrections to NASCAR vehicle using the present method.

Now for further evaluation of the developed method, the same data will be corrected using three of the well-developed methods used in automotive wind tunnels. These methods were outlined in Chapter (1) and here further details are presented. The first is the classical method of images[1,2,3,41,57], where the model is represented by simple singularity (point doublet) and the effect of the boundaries is simulated by creating images of this singularities. A duplex test section is used to account for the ground board where a mirror image of the model is used to represent the ground and the images are

* The balance strictly measured axial force, but with an expected sideforce value of around 0.032 per degree, the difference between drag and axial force coefficients is below 1% for yaw angles below 3°.

then created for both the model and its mirror. Using the classical method of images, the blockage factor for both closed and open jet test sections can be calculated as follows:[41]

$$\varepsilon = \tau \left(\frac{A_M}{A_N} \right)^{\frac{3}{2}} \tag{5-3}$$

Where, A_M and A_N are the model frontal area and the nozzle exit area respectively. τ is for closed and open test sections are follows:[3,41]

$$\tau_{closed} = \frac{1}{2\pi^{3/2}} \left(\frac{H}{B} \right)^{3/2} \sum_{\substack{n=-\infty \\ \text{excluding} \\ n=m=0}}^{n=\infty} \sum_{m=-\infty}^{m=\infty} \frac{1}{\left[n^2 + \left(m \frac{H}{B} \right)^2 \right]^{\frac{3}{2}}} \tag{5-4}$$

$$\tau_{open} = \frac{1}{2\pi^{3/2}} \left(\frac{H}{B} \right)^{3/2} \sum_{\substack{n=-\infty \\ \text{excluding} \\ n=m=0}}^{n=\infty} \sum_{m=-\infty}^{m=\infty} (-1)^{m+n} \frac{1}{\left[n^2 + \left(m \frac{H}{B} \right)^2 \right]^{\frac{3}{2}}} \tag{5-5}$$

Alternatively τ can be obtained analytically as follows:[41]

$$\tau_{closed} = 0.406 \left(\frac{B}{H} + \frac{H}{B} \right) \tag{5-6}$$

$$\tau_{open} = -0.03 \left(\frac{B}{H} + \frac{H}{B} \right)^3 \tag{5-7}$$

Where B and H are the width and the height of the test section. Using the above equations, it is found that the blockage factor is 0.0177 for the closed test section and – 0.0061 for the open jet test section. Following the same correction procedure as used for the present method[39] (Equations (5-1) and (5-2)) the measured drag for closed and open test sections are corrected again using the classical method of images as shown in Figure (5-26). The average ratio between the open and closed test sections change from 83.9% to

91% after the application of the corrections. Compared to the present method it is clear that the method of images underestimated the correction factors for both the closed and open test sections. The reasons for that are the effects of the finite length of the test section combined with the boundary deformation, neither of which is accounted for in the classical method of images. In addition to that the use of a point doublet to represent the model is not sufficiently accurate. This result is presented here to serve as a reference case for the comparison to the present method and the other methods discussed later.

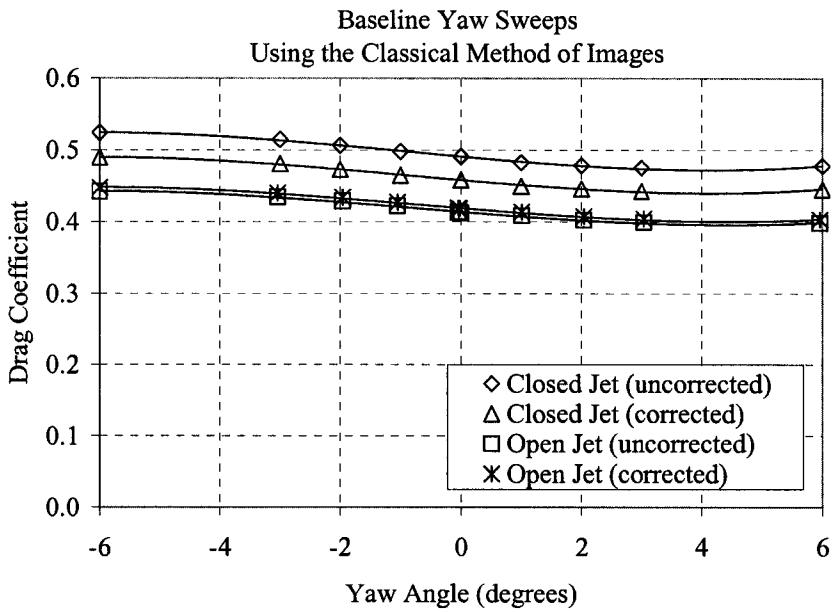

Figure (5-26) Application of the boundary corrections to NASCAR vehicle using the classical method of images. [1,2,3,41,57]

Wickern[41] modified the classical method of images to better represent the model by introducing a body shape factor in Equation (5-3) that depends on the volume of the tested model. The blockage factor for his method is defined as follows:

$$\varepsilon = \tau\lambda\left(\frac{A_M}{A_N}\right)^{\frac{3}{2}} \tag{5-8}$$

- where, the coefficient τ is calculated using Equations (5-4) though (5-7) similar to the classical method of images. The shape factor λ (developed originally by Lock)[3] is defined as follows:[41]

$$\lambda = G\frac{\sqrt{\pi}}{2}\frac{V_M}{(A_M)^{\frac{3}{2}}} \tag{5-9}$$

- where V_M and A_M are the model volume and front area respectively. G is the Glauert[1] factor, which depends on the fineness ratio l/t:

$$G = 1 + 0.4\frac{t}{l} \tag{5-10}$$

- where, l is the length of the model and t is the equivalent diameter of the model calculated from the frontal area A_M:

$$t = \sqrt{\frac{A_M}{\pi}} \tag{5-11}$$

Using Wickern's modified method of images, the blockage factor for closed and open jet test sections was found to be 0.0368 and –0.0125 respectively. Compared to the present method, good matching was found for the closed test section. For the open jet test section, Wickern's method does not include boundary deformation and as a result it underestimates the correction factor. Figure (5-27) shows the uncorrected and corrected drag coefficient for closed and open jet test section. The correction used is the modified method of images developed by Wickern following the same correction procedure in Equation (5-1) and (5-2). After applying the corrections the ratio for the drag coefficient between open jet and closed test sections changed from 83.9% to 95.7%. It is clear that this method improved the model representation. However, the open jet corrections still appear to be under-estimated.

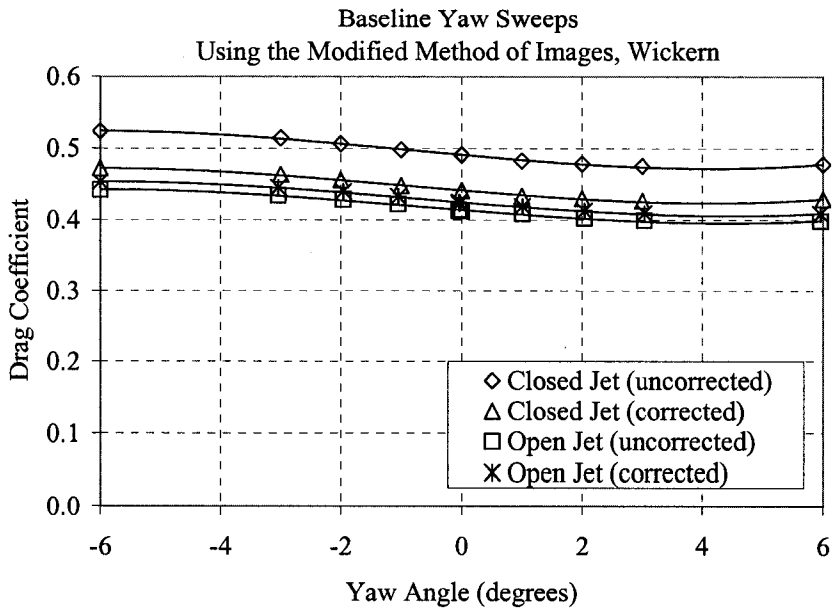

Figure (5-27) Application of the boundary corrections to NASCAR vehicle using the modified method of images, Wickern.[41]

Mercker et al [42,43,46,49,57] developed a method based on the modified method of images of Wickern[41] for open jet test sections. This method is a semi-empirical approach where the correction factor includes the effect of the jet expansion calculated using the modified method of images and the solid blockage of the nozzle and collector calculated using a point source located a the model center and two vortex rings positioned a the nozzle exit and the collector entrance. Several improvements of this method were presented in the literature, as discussed in Chapter (1); following is the outline of the method.

The blockage factor is defined as follows:

$$\varepsilon = \varepsilon_S + \varepsilon_C + \varepsilon_N \tag{5-12}$$

Where ε_S is the blockage factor due to the jet expansion. It is calculated using the method of images. Equation (5-8) is modified to better represent the model as follows:

$$\varepsilon_S = \tau \sqrt{\frac{V_M}{L_M}} \left(\frac{A_M}{A^*} \right)^{\frac{3}{2}} \tag{5-13}$$

- where, the coefficient τ is calculated using Equations (5-4) though (5-7) similar to the classical method of images. The shape factor λ in Equation (5-8) is replaced by a constant calculated using the model volume V_M and length L_M instead of the model volume V_M, front area A_M, G factor, and fineness ratio l/t used in Equations (5-9) and (5-11) for Wickern's method. The nozzle A_N area is replaced by A^* which is reference area calculated using the velocity at infinity U^* and the nozzle exit velocity U_N as follows:

$$A^* U^* = A_N U_N \tag{5-14}$$

The blockage factor ε_c in Equation (5-12) represents the solid blockage of the collector. It is defined as follows:

$$\varepsilon_C = \frac{\varepsilon_W R_C^3}{\left[(L_{TS} - x_M)^2 + R_C^2 \right]^{\frac{3}{2}}} \tag{5-15}$$

- where, L_{TS} is the test section length and x_M is the distance from the nozzle exit to the model center. R_C is the duplex collector radius calculated using the collector area A_C.

$$R_C = \sqrt{\frac{2A_C}{\pi}} \tag{5-16}$$

ε_w is the wake blockage defined as a function of the model front area A_M, the collector area A_C, and the measured drag coefficient $C_{D\,m}$. Based on wind tunnel measurements, Mercker et al developed the following semi-empirical formula:[42,43]

$$\varepsilon_W = \frac{A_M}{A_C}\left(\frac{C_{Dm}}{4} + 0.41\right) \tag{5-17}$$

The third effect included in the blockage factor, Equation (5-12), is the nozzle solid blockage ε_N. It is defined as follows:

$$\varepsilon_N = \frac{\varepsilon_{QN} R_N^3}{\left[R_N^2 + x_M^2\right]^{\frac{3}{2}}} \tag{5-18}$$

- where, R_N is the equivalent duplex nozzle radius calculated from the area.

$$R_C = \sqrt{\frac{2A_N}{\pi}} \tag{5-19}$$

ε_{QN}.is defined as follows:

$$\varepsilon_{QN} = \frac{A_M}{2A_N}\left(1 - \frac{x_S}{\sqrt{x_S^2 + R_N^2}}\right) \tag{5-20}$$

- where, x_S is the distance from the nozzle exit to the point source which represents the model effect:

$$x_S = x_M - \frac{L_M}{2} + \sqrt{\frac{A_M}{2\pi}} \tag{5-21}$$

Recently Mercker and Cooper presented an iterative empirical method to calculate x_S by taking two wind tunnel measurements.[49] The details of this method were discussed in Chapter (1). In this section, Equation (5-21) is used to calculate x_S because the newly developed method[49] needs additional wind tunnel measurements, which are not available for the current data presented here.

Using Equations (5-12) through (5-21), it was found the blockage factor for the open jet test section is –0.016. Following the same procedures to correct the drag coefficient, Equations (5-1) and (5-2), the uncorrected and correction data are presented in Figure (5-28). The modified method images of Wickern[41] is used to correct the closed test section case while the semi-empirical method of Mercker et al [42,43,46,49,57] is used to correct the open jet case. After applying the corrections to the drag coefficient the ratio of the open jet to closed test section changed from 83.9% to 96.3%. It is clear that Mercker's method improved the open jet results compared to Wickern's method. The main factors here are the inclusion of the nozzle and collector effect in the interference assessment. These results compared well with present method. In addition, the present method has the advantage of including the boundary deformation and it is not based on empirical formulas as the other methods.

Tables (5-3) and (5-4) summarize the comparison study between the present approach and the other methods discussed above. For the present method, the corrections presented in Table (5-4) are performed using the blockage factor obtained from the test section plus nozzle case because it represents the real geometry of the wind tunnel. As shown in Table (5-3), the present method matches the modified classical method of images developed by Wickern for closed test section especially for the solution obtained using the long test section. It is important to note that Wickern's method simplifies the model representation while the present method uses the real geometry of the NASCAR model. The classical method of images underestimates the correction factors for both the closed and open jet test sections. For open jet test section both Wickern's and the Mercker's methods improved the correction factors. However, neither method accounts for the boundary deformation.

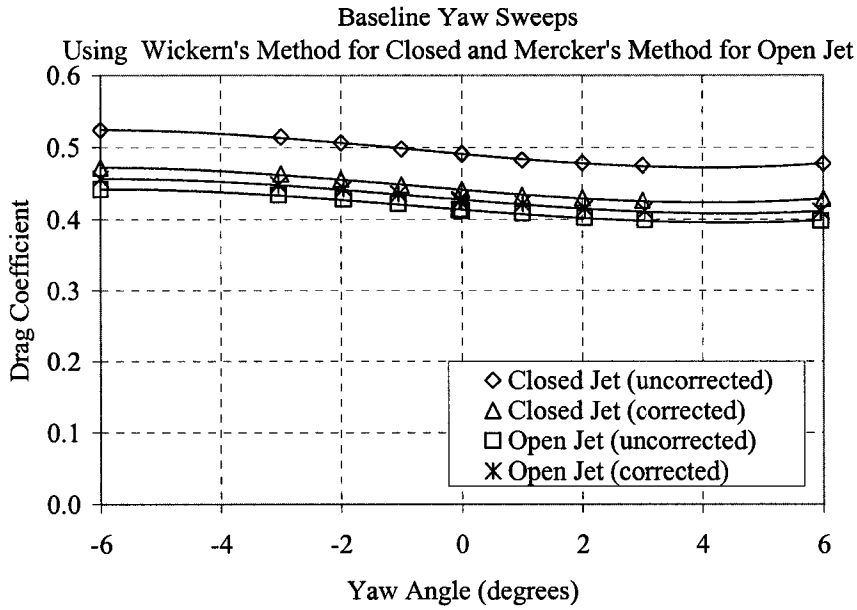

Figure (5-28) Application of the boundary corrections to NASCAR vehicle using the modified method of images (Wickern[41]) for closed and the semi-empirical method (Mercker et al [42,43,46,49,57]) for open jet test sections.

Approach		Blockage factor ε	
		Closed	Open jet
Present method	Test section only	0.0322	-0.0228
	Test section + nozzle	0.0343	-0.0233
	Long test section	0.0352	-0.0234
Classical method of images[1,2,3,41,57]		0.0177	-0.0061
Wickern's method[41]		0.0368	-0.0125
Mercker's method [42,43,46,49,57]		n/a	-0.0160

Table (5-3) Blockage factor for open and closed test sections obtained using different methods.

Approach	Average drag coefficient C_D		$\frac{C_{D,Open}}{C_{D,Closed}}\%$
	Closed	Open jet	
Uncorrected	0.493	0.414	83.9%
Present method (test section + nozzle)	0.445	0.434	97.5%
Classical method of images[1,2,3,41,57]	0.460	0.419	91.0%
Wickern's method[41]	0.443	0.424	95.7%
Wickern's method[41] (closed) + Mercker's method [42,43,46,49,57] (open)	0.443	0.427	96.3%

Table (5-4) Application of the correction factors.

5.4 Summary

In this chapter, the use of the present method for an automotive application was explored for both closed and open test section with several numerical configurations. The study indicated that the method could be modified to take advantage of the wall pressure signature measured during the closed test section configuration in developing the model representation. It can also solve complex model and test section geometries including nozzle walls. Compared to the other methods used in automotive tunnels, the method offers more information about the problem to extend the correction from the one-point, one force component technique to a more comprehensive and integrated approach that is close to the real flow inside the test section. Also, it offers more flexibility in terms of the model and test section geometries.

CHAPTER VI

VI. APPLICATION III – 1/15TH SCALE LANGLEY FULL SCALE WIND TUNNEL

A test was undertaken inside the 1/15th Scale Langley Full Scale wind Tunnel (LFST)[†], where the main objectives were to apply the developed boundary correction method to a relatively high blockage ratio model configuration, to visualize the boundary deformation and to validate the computation of the boundary deformation. A secondary objective was an examination of the conditions at the flow interface to the collector.

The geometry of the 1/15th scale LFST is very similar to the original (full-scale) wind tunnel. It has a 3/4 open test section with a 44.8 inch length, 24 inch height and 48 inch maximum width. A "Davis"[39, 40] generic truck model was specially manufactured for the test. Figure (6-1) shows a view of the model inside the test section. The model is 34 in maximum length, 9.6 in maximum height and 12.8 in width. The nominal blockage ratio is approximately 20.6%, which is a very high ratio for a wind tunnel test of external aerodynamics. The model's front face is 4 in downstream of the nozzle exit plane and its back face is approximately 7.3 in upstream of the collector entry plane.

This chapter consists of three main sections. First, two sets of measurements are presented for the open jet boundaries with and without the model inside. The objective of this section is to visualize the boundary deformation in the test section region. Second, a simplified CFD simulation is presented to show more details about the behavior of the test section boundary (shear layer) and the jet interaction with the collector. Finally the boundary interference is assessed using the developed panel method. In this part, four approaches are used to model the wind tunnel.

[†] The wind tunnel test was conducted in summer 2004. The measurements were taken by Megan Miller, a summer intern student, and John Bledsoe, an LFST staff engineer, under the supervision of Professor Colin Britcher.

Each one of them presents a different level of approximation starting with a simple long test section with no collector, progressing to a fully deformed test section where the collector and the jet growth are represented. In this part, results from the CFD simulation are used in conjunction with the developed panel method.

6.1 Wind tunnel measurements

A rake of 21 Pitot tubes, shown in Figure (6-1), was used to survey the test section boundaries in four vertical planes normal to the test section axis. Figures (6-2a) and (6-2b) show the velocity survey for an empty test section and for the test section with the model inside respectively. It should be noted that measurements ore only available for the four planes depicted in Figure 6-2, with a measurement spacing of 1.0 inches in both the vertical and lateral directions. For both cases (with and without the model inside) the thickness of the shear layer at the test section boundaries increases in the downstream direction. This increase occurs at nearly the same rate for both cases, which suggests that the model does not have significant effect on the growth rate. Since the jet boundary is at practically constant pressure, this is thought to be reasonable. As the jet exits from the nozzle a thin mixing layer is developed around the jet boundaries, which grows in the downstream direction by entraining air from the plenum chamber. As the jet reaches the collector the entrained air is spilled back to the plenum chamber creating large vortices near the collector mouth as will be shown in the following section. Another view of the pressure contours for the measurements taken with the model inside is shown in Figure (6-3a). Figure (6-3b) is a sketch highlighting the important physical features of the flow field. It can be seen now that the boundaries of the test section interact with the surrounding air creating this mixing layer, which makes it technically difficult to detect the effective test section boundaries and hence makes it more difficult to take accurate flow property measurements. These results will be used in the following section as a reference for the boundary deformation.

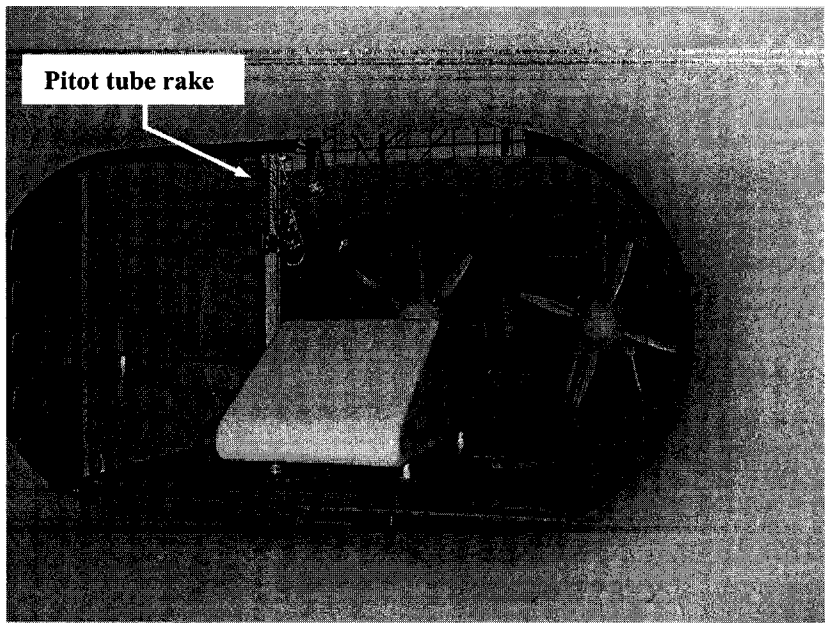

Figure (6-1) View of the "Davis" model inside the 1/15th scale LFST.

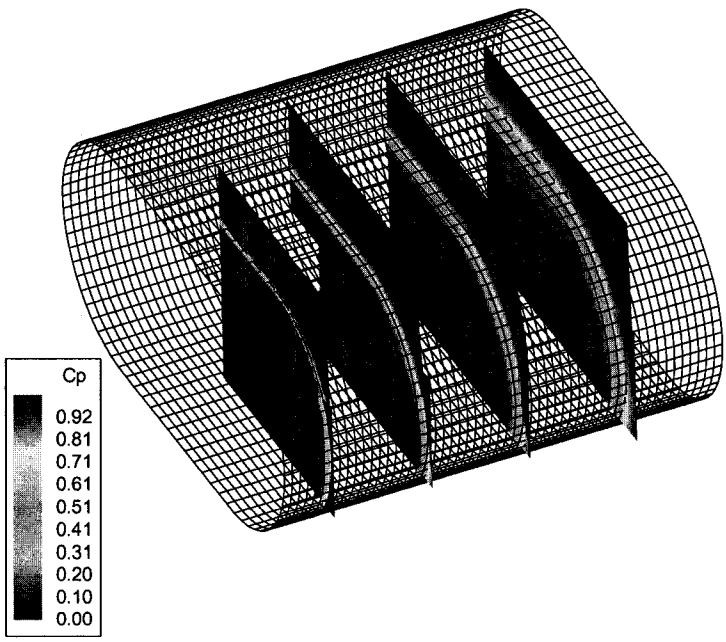

Figure (6-2a) Velocity survey for an empty test section.

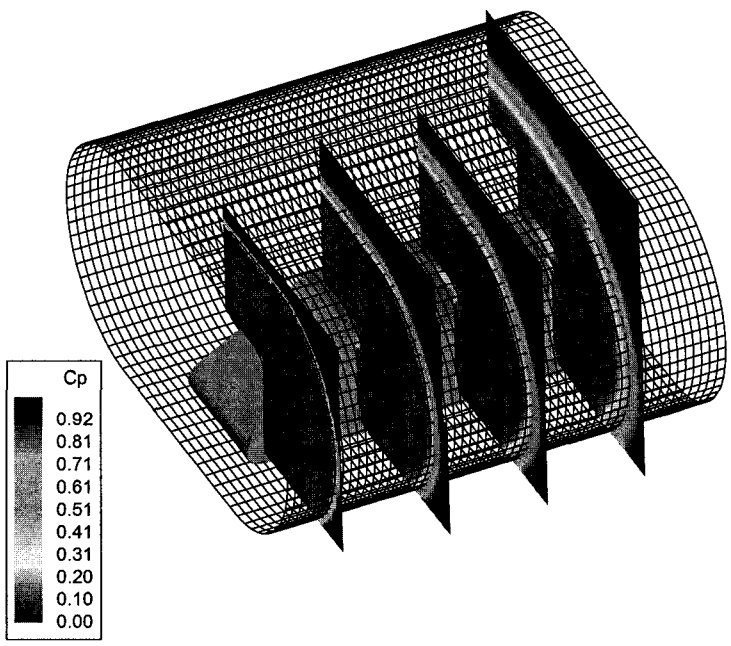

Figure (6-2b) Velocity survey for the test section with the model inside.

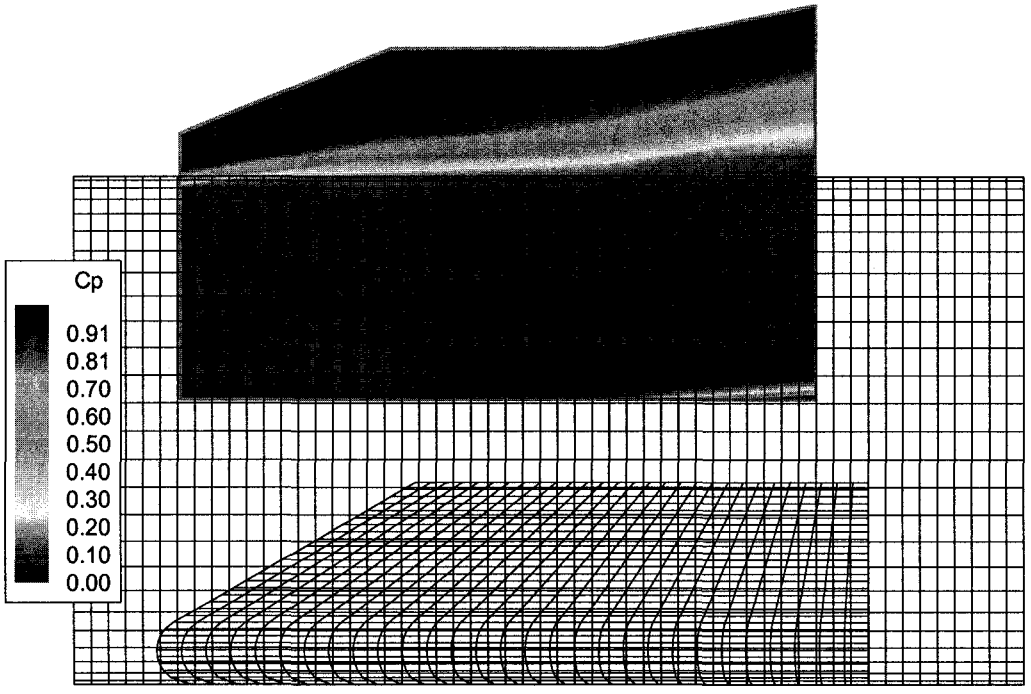

Figure (6-3a) Velocity survey on a streamwise vertical plane passing through the test section centerline.

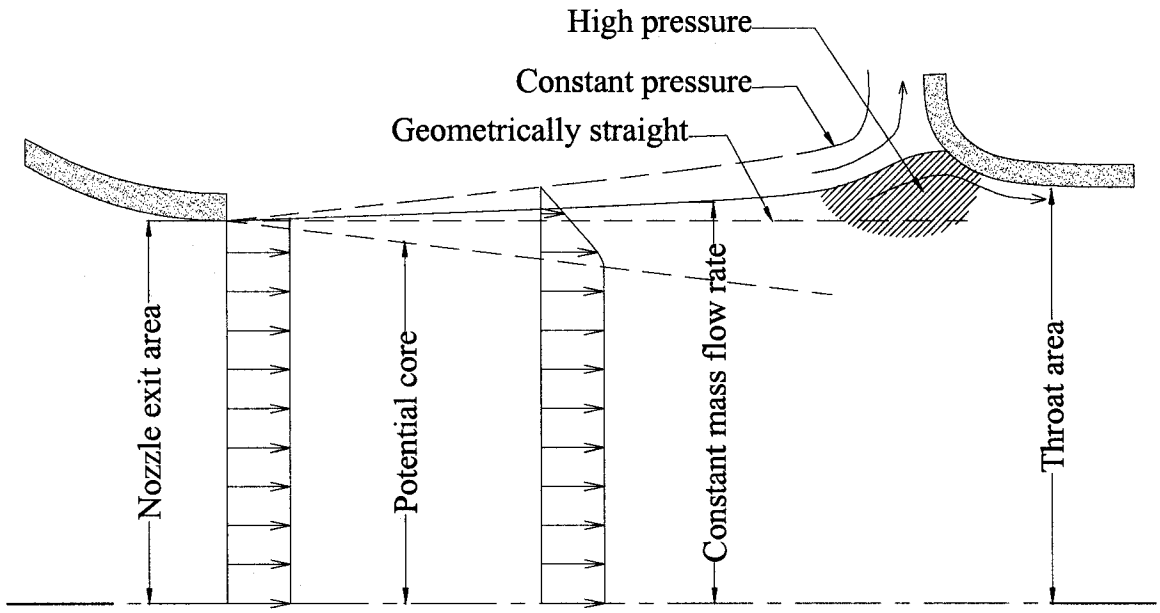

Figure (6-3b) Sketch of flow field features.

6.2 CFD simulation

A 2D CFD study is performed using CFL3D. The principal objective of this study is to add more insight into the observations presented in the previous section through a full simulation of both the test section and the plenum chamber. Two cases are studied: the empty test section and the test section with the "Davis" model inside. The computational domain includes the nozzle, the test section, the collector and the plenum chamber. A two-block structured grid is generated for each case with clustering near the nozzle, the collector surfaces, and the test section boundaries, as shown in Figures (6-4) and (6-5). A no-slip boundary condition is imposed on the nozzle, the collector, the ground board, and the model surfaces. Inflow boundary conditions are applied at the nozzle inlet and inflow/outflow boundary conditions are applied at the collector exit section. Inviscid wall boundary conditions are applied to the plenum chamber walls.

The CFL3D code [59] is a computational method for structured grids developed at NASA Langley Research Center. It uses an upwind finite volume formulation and neglects viscous cross-derivative terms, which results in the thin-layer Navier-Stokes equations in specified coordinate directions. Third-order upwind-biased spatial differencing on the convective and pressure terms, and second-order differencing on the viscous terms are used; it is globally second-order spatially accurate. Upwind-biased spatial differencing is used for the inviscid terms, and flux limiting is used to obtain smooth solutions in the vicinity of shock waves, when present. No limiter was employed for this study. Viscous terms are centrally differenced. The flux difference-splitting (FDS) method of Roe is employed to obtain fluxes at the cell faces. [60] The CFL3D code advances in time with an implicit three-factor approximate factorization method. The implicit derivatives are written as spatially first-order accurate, which results in block tri-diagonal inversions for each sweep. However, for solutions that use FDS, the block tri-diagonal inversions are further simplified with a diagonal algorithm. Turbulence equations are solved uncoupled from the mean equations. The Menter's k-w Shear Stress Transport (SST) turbulent model is used in the study. [61]

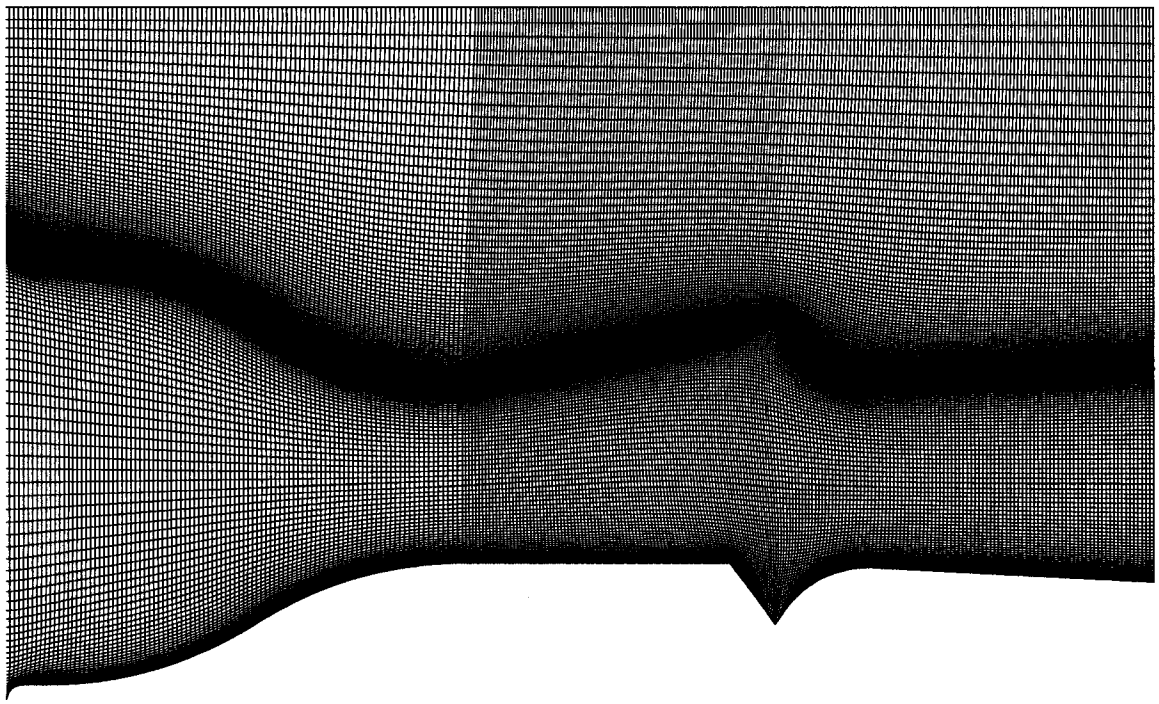

Figure (6-4) Two-block structured grid for empty test section.

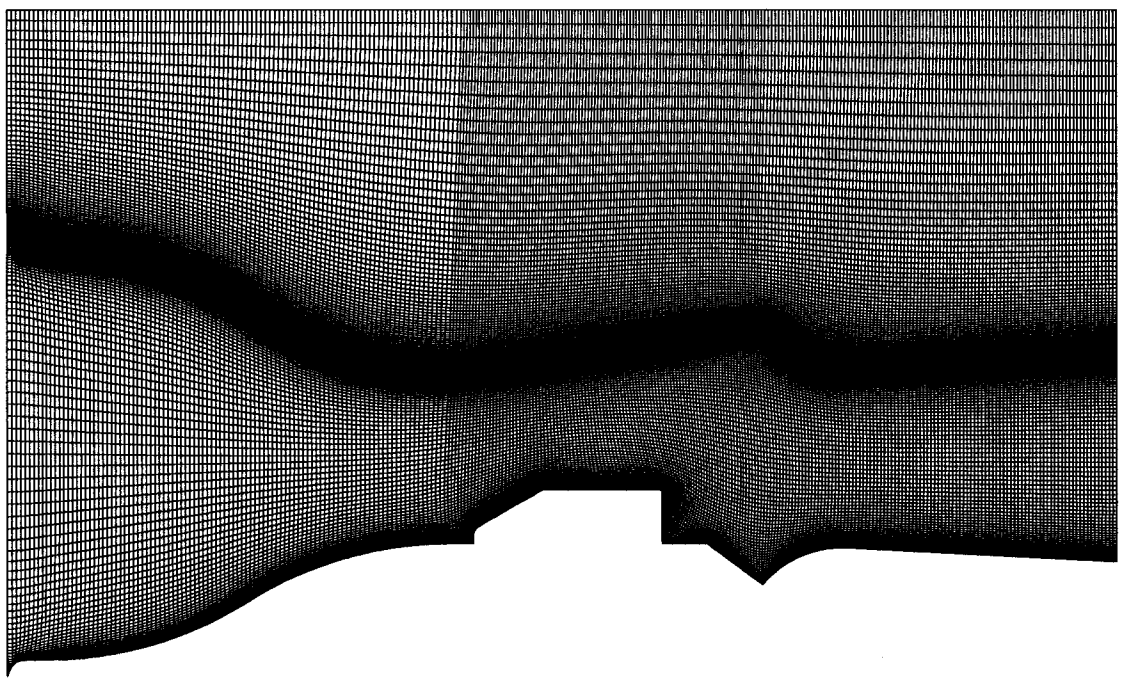

Figure (6-5) Two-block structured grid for the test section with the model inside

Figures (6-6) and (6-7) show the computed pressure contours for the empty test section and the test section with model inside respectively. For the empty test section, the growth of the mixing layer outside the jet boundary can be seen and the reflection of the entrained air near to the collector entrance is generating a small upward jet into the plenum chamber. A pressure gradient is generated due to the stagnation point, which occurs within the collector entrance. Due to the constant pressure condition acting just outside the jet (in the plenum chamber), the rising pressure along the stagnation streamline causes an outward deformation of the upper boundary of the open jet just before entering the collector. For the second case where the model is inside the test section shown in Figure (6-7), the wake of the model extends inside the collector, blocking part of its area, which increases the mean velocity of the air as it enters the collector. This increased blockage just ahead of the collector face causes an outward movement of the stagnation point and other changes in the deformation of the shear layer and in the detail structure of the flow field as shown in Figure (6-7).

Figures (6-8a) and (6-8b) show the computed flow near the collector entrance for the test section without and with a model inside respectively. The trace-lines shown are derived from the velocity field. Both the trace-lines and the pressure distribution at the collector wall are used to locate the stagnation point, as shown in the Figures. Figure (6-9) shows the stagnation lines located experimentally, with tufts applied to the internal surfaces of the collector. Direct comparison to the CFD results is not possible (3D experiments versus a 2D CFD case) but broad qualitative agreement is evident. This information will be used in the following section with the panel method. It is important to note that the 2D representation of the model and the test section, used in the CFD study, increased the blockage ratio to 40% instead of the true value in the 3D case (20.6%). However, this serves the purpose of the study and allows the use of these results as the upper limit for model size as will be shown in the following section. Both the experimental and numerical results support the idea that numerical methods may have to be used to calculate the flow properties on the test section boundaries due to the strong interactions observed between the jet boundary and the surrounding air. In the following section results from the developed panel method are presented.

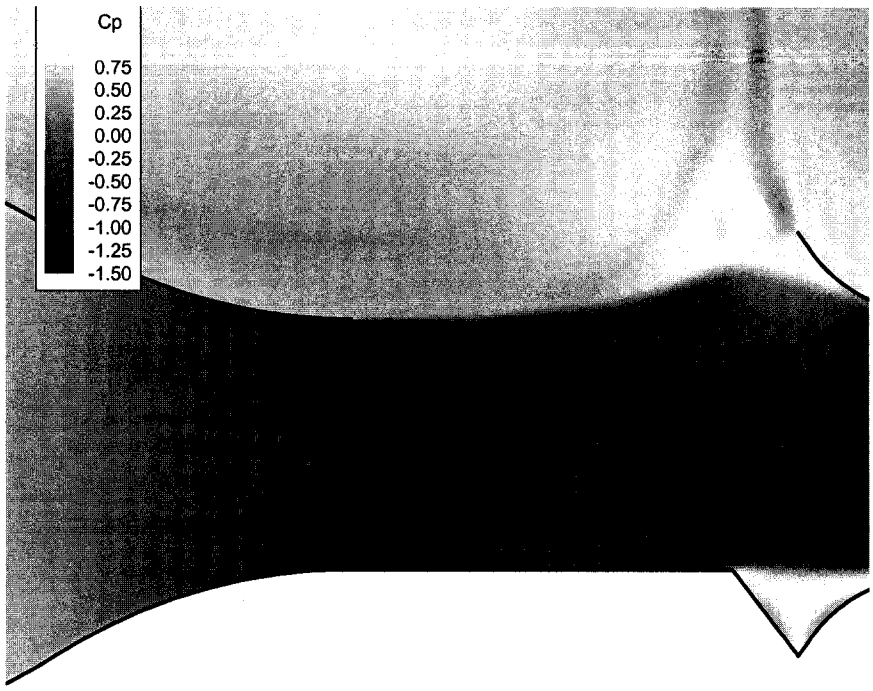

Figure (6-6) Computed pressure contours for empty test section.

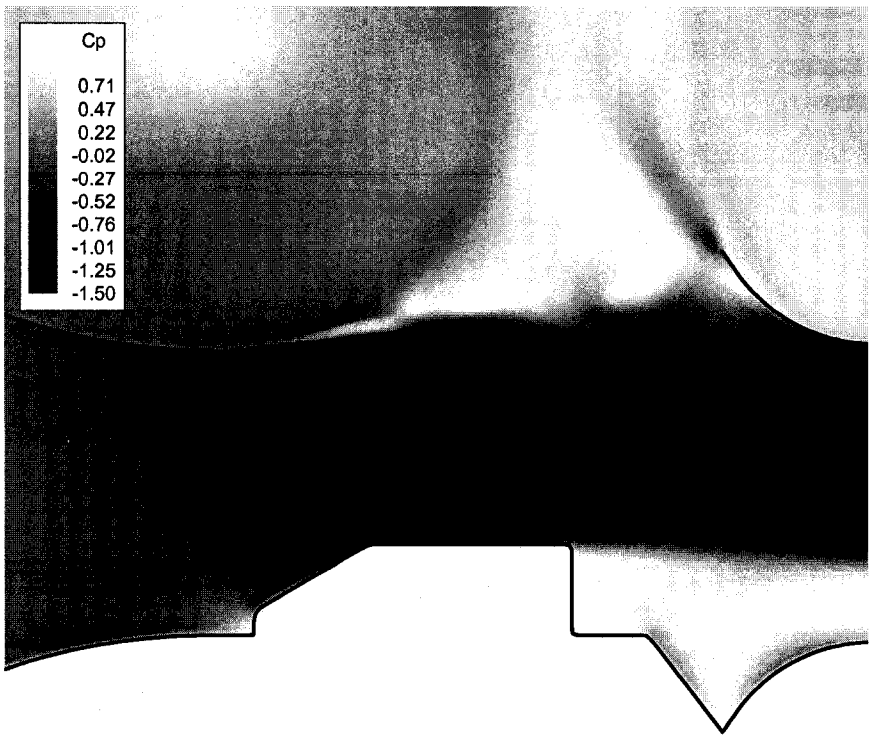

Figure (6-7) Computed pressure contours for test section with the model inside.

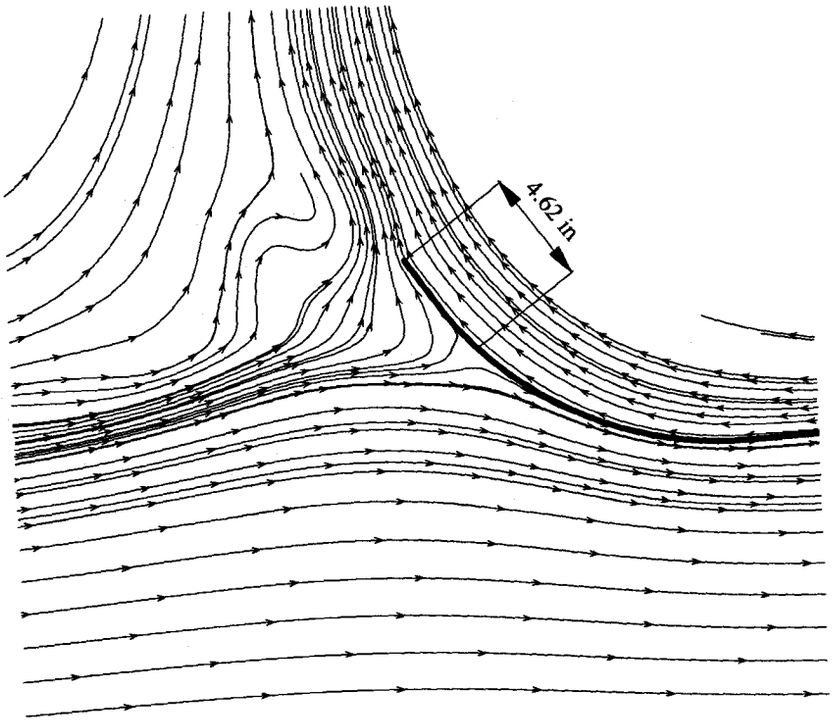

Figure (6-8a) Trace line near the collector entrance for the empty test section derived from the CFD results

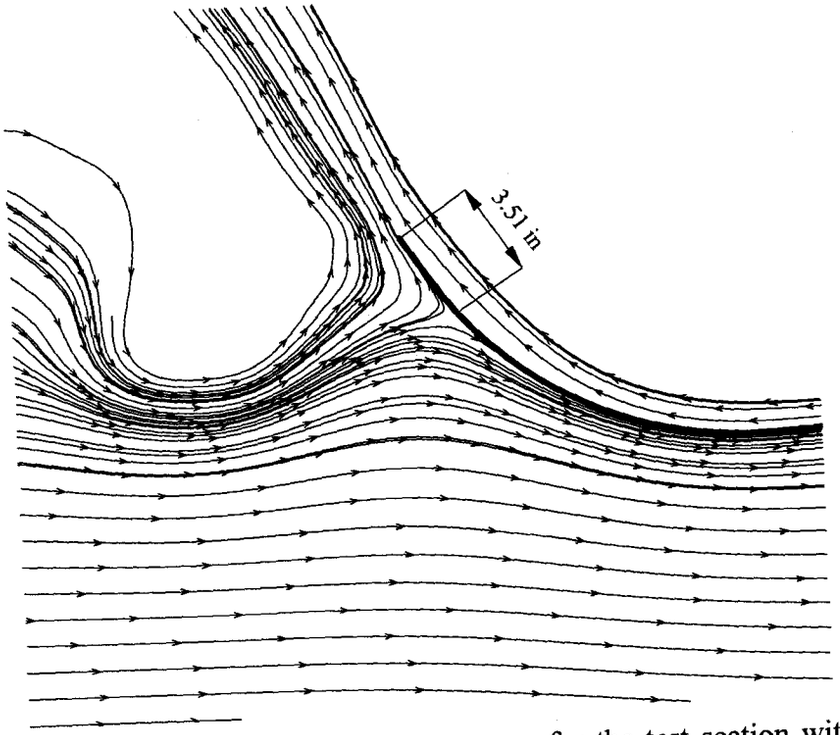

Figure (6-8b) Trace line near the collector entrance for the test section with the model inside derived from the CFD results

(a) Empty test section.

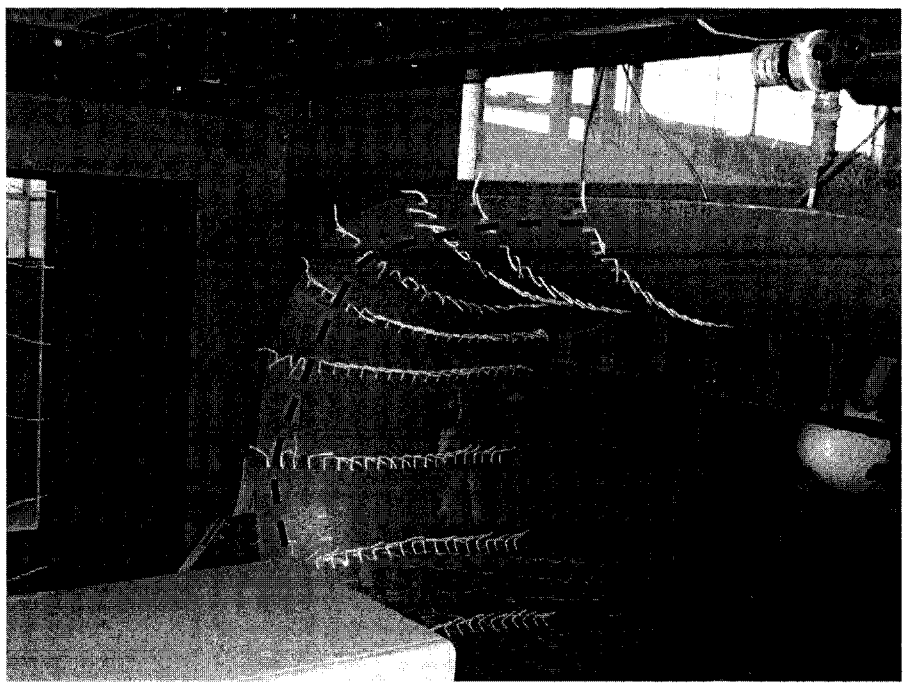

(b) Test section with the model inside.

Figure (6-9) The stagnation lines located experimentally with tufts.

6.3 Wind tunnel boundary interference assessment

Four approaches are used to tackle the problem. In the first one, a long test section is solved (three times the actual length). Since the nozzle effect was studied in the previous chapter, it is replaced by a constant area duct, which is one third of the total length of the long test section, and is solved as solid walls. The rest of the length is solved as an open jet, thereby placing any downstream constraint far from the model. The surfaces of both the model and test section boundaries are divided into panels. 486 surface panels are used for the model and 2000 surface panels are used for the tunnel boundaries. Figures (6-10) and (6-11) show the surface panels for the model and the test section boundaries respectively. In the second approach, the collector is represented and the length of the open jet is decreased to be equal to the actual test section length with a similar length solid walled duct upstream (to replace the nozzle). 486 surface panels are used for the model, 1200 surface panels are used for the test section boundaries (including the nozzle) and 518 surface panels are used for the collector as shown in Figure (6-12). In this configuration, the test section representation extends in the downstream to the beginning of the collector with no representation for the jet growth or the deformation due to jet interaction with the collector. The interface between the test section and the collector is rather abrupt, but the panel solutions remain stable.

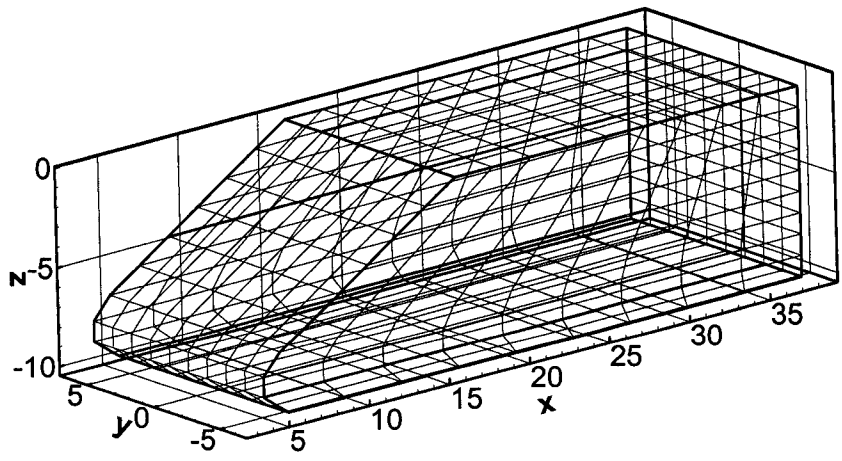

Figure (6-10) Surface panels used for the model. (Vortex ring panels)

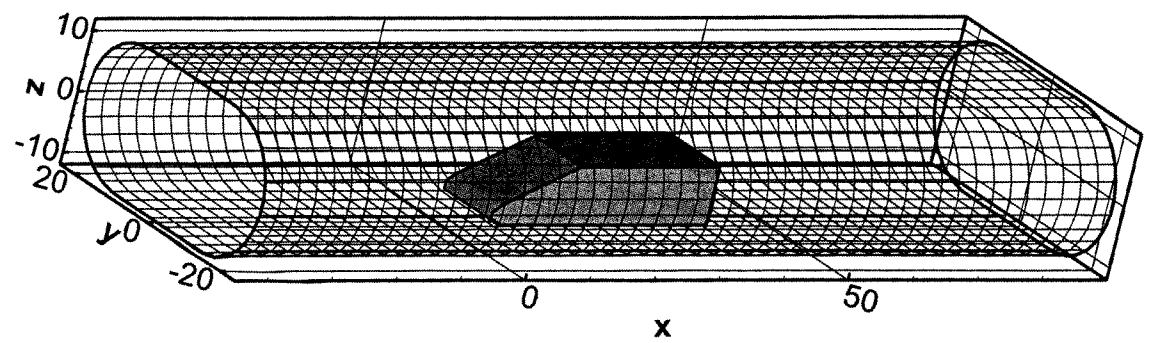

Figure (6-11) Surface panels used for the long test section configuration. (Vortex ring panels)

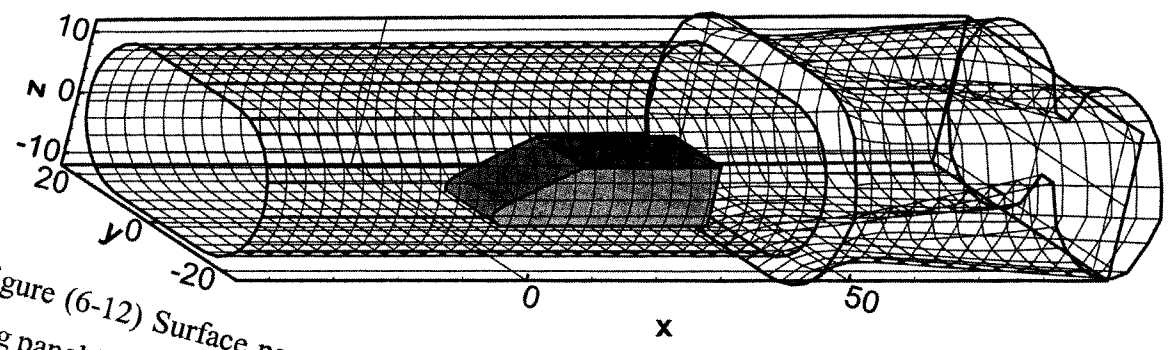

Figure (6-12) Surface panels used for the test section + collector configuration. (Vortex ring panels)

Two more methods are used to represent the test section based on the CFD results presented before in Figures (6-6) through (6-8). For both of them, the same number of surface panels is used for the model, the test section and the collector representation as in the previous case. The objective is to represent the jet growth and the jet interaction with collector entrance. In the first case, a pre-deformed test section boundary, designated as test section I and shown in Figure (6-13), represents the jet deformation near to the collector, the jet growth, and the stagnation point location predicted from the CFD solution for the empty test section. This case will serve as a lower bound for the pre-deformation. For the upper bound, the test section boundaries are similarly pre-deformed to match the CFD solution of the test section with the model inside. The surface panels for this case, designated test section II, are shown in Figure (6-14). It can be noted that the interface between the test section and the collector is now somewhat "smoother" than in the first case described earlier.

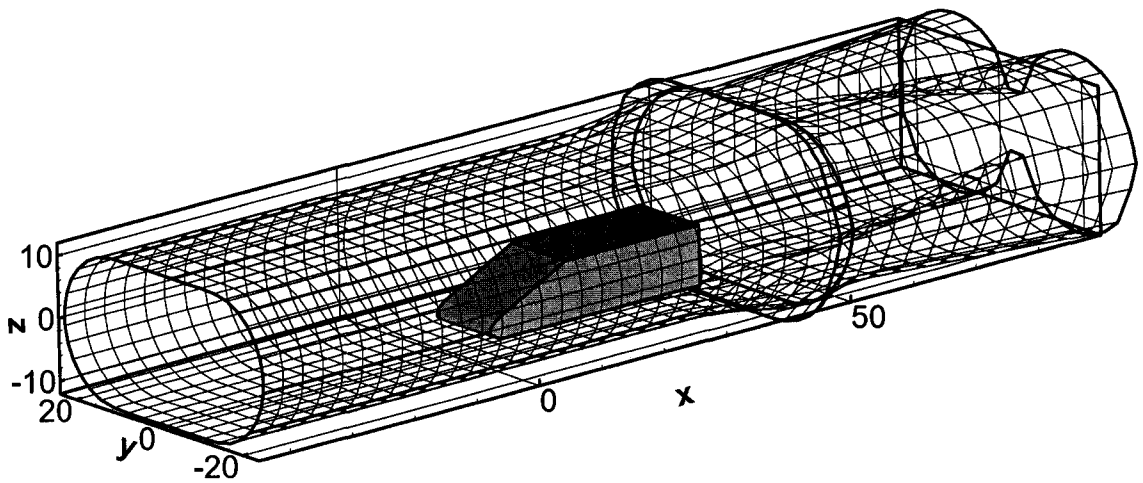

Figure (6-13) Surface panels used for the pre-deformed test section I + collector configuration. (Vortex ring panels)

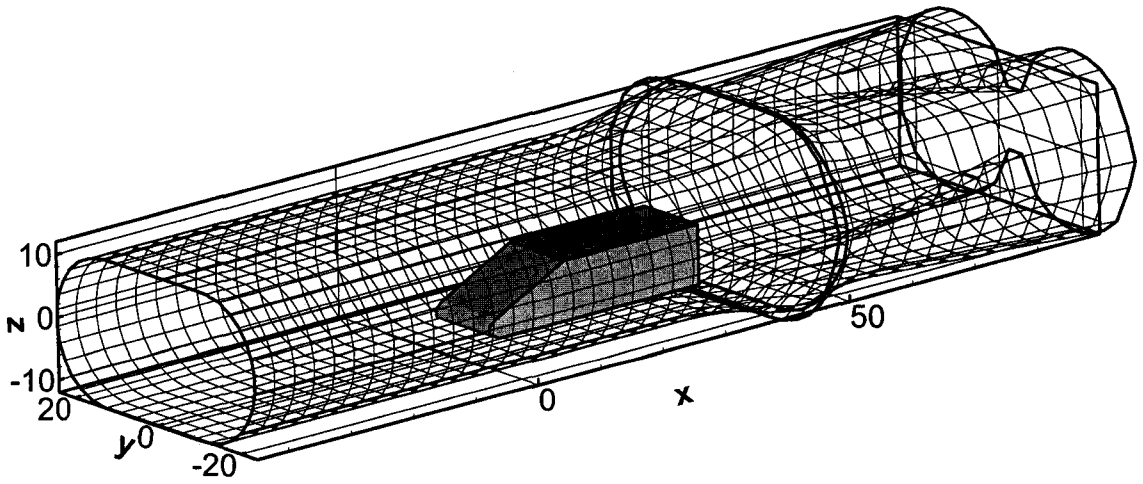

Figure (6-14) Surface panels used for the pre-deformed test section II + collector configuration. (Vortex ring panels)

It is important to note that the approach used to represent the model in this application is slightly different from the approach used in the application presented in Chapter (5). In the latter, the strengths of the singularities representing the model were derived directly from the pressure measurements taken on the test section walls. In this application (inside the $1/15^{th}$ scale LFST), the flow inside the test section is solved to obtain the strengths of both the model and the test section boundary panels simultaneously. This approach might be computationally more expensive but it is more general than the alternative because not all closed test sections have pressure taps on the walls and there are technical difficulties in taking these boundary measurements for open test sections as discussed in Chapters (1) and (2).

The developed method consists of three main steps as outlined in Chapter (2). First the boundaries are solved as closed walls with no deformation considered, except the pre-deformation in the third and the fourth cases. The Neumann boundary condition is applied to all surfaces panels including the model, the test section boundaries and the collector to obtain their strengths. Here, the objective of this step is to obtain a boundary

signature. The Neumann boundary condition applied to the panels at the back surface of the model is modified to account for its drag by allowing a 50% leakage of the air through the model as recommended by Mokry[29] in his similar study which represented the wake displacement. The boundary deformation is then predicted using the signature developed in the previous step of the solution. No deformation is performed at the ground board, the collector walls, or upstream of the test section ($x < 0$). For the third and fourth cases, the locations of the stagnation points at the collector entrance, predicted from the CFD and the experimental studies, are kept fixed during the boundary deformation. Finally the interference is assessed from the flow induced by the test section boundary panels, including the collector panels. The panels of the ground board are not included in this step. The focus of this study is the blockage interference.

Figures (6-15) through (6-18) show the predicted and measured boundary deformation for the long test section, test section plus collector, pre-deformed test section I plus collector, and pre-deformed test section II plus collector respectively. The maximum relative deformation is at the upper boundary close to the model centerline. Less deformation is observed at the side boundaries. The predicted relative deformations for all the test section configurations are nearly the same and compare reasonably well with the wind tunnel measurements. It is important to note that the Figures show relative deformations and that the two cases shown in Figures (6-17) and (6-18) already have pre-deformation before starting the solution to account for the jet growth and the collector entrance interaction. The results suggest that the method is somewhat consistent in predicting the relative deformation due to the model blockage.

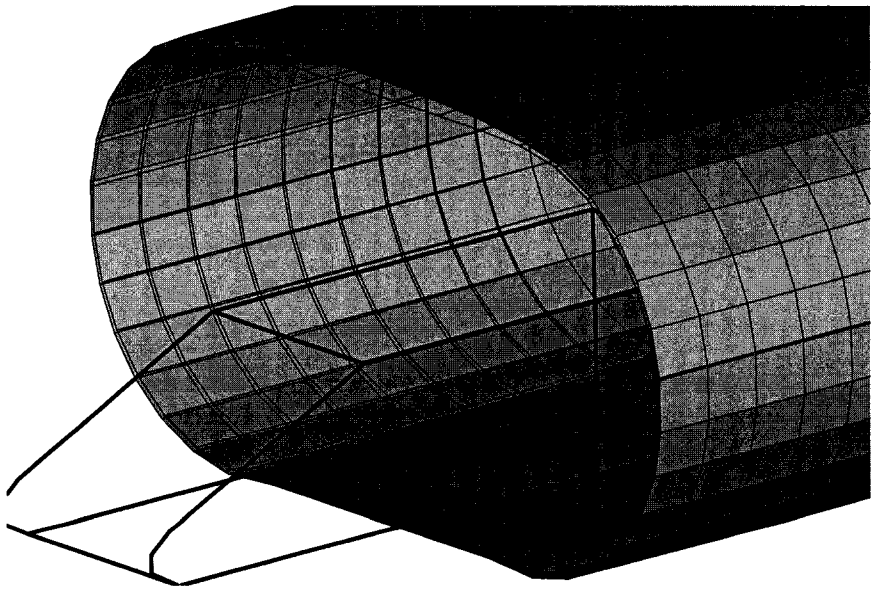

Figure (6-15-a) Predicted boundary deformation, solving long test section

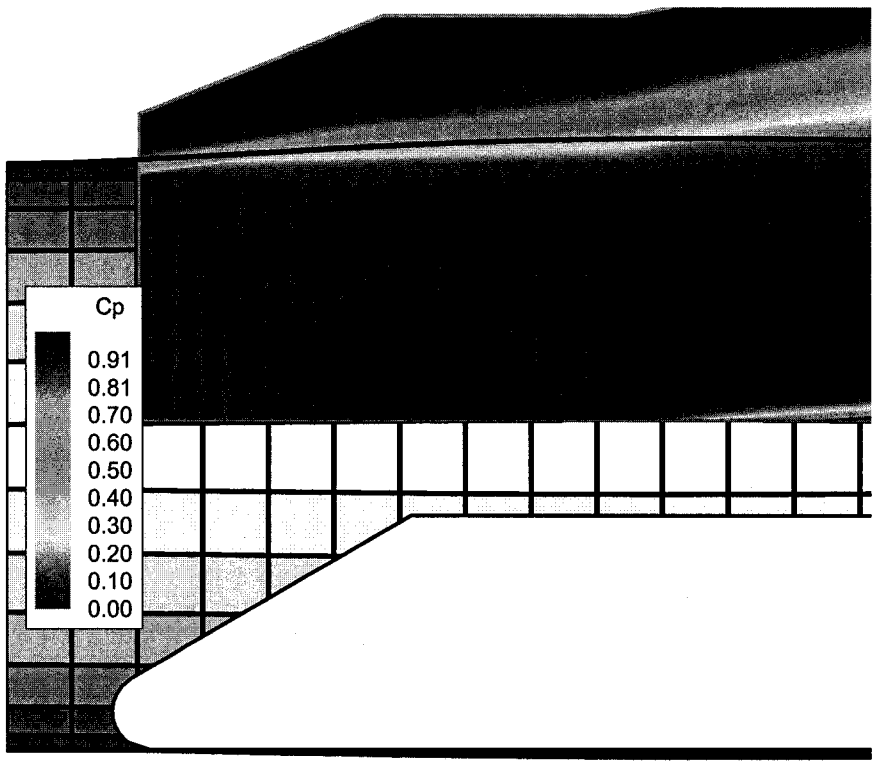

Figure (6-15-b) Predicted and measured boundary deformation, solving long test section

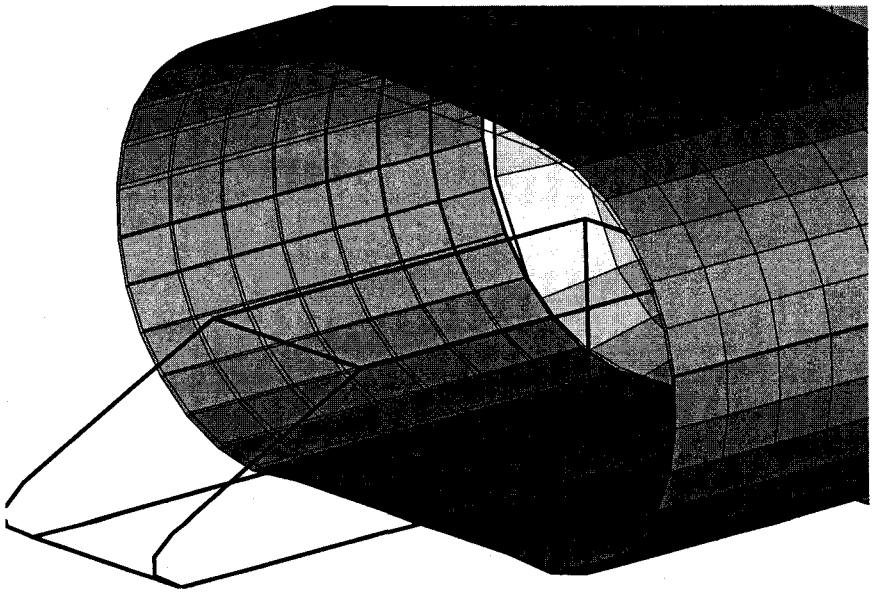

Figure (6-16-a) Predicted boundary deformation, test section + collector

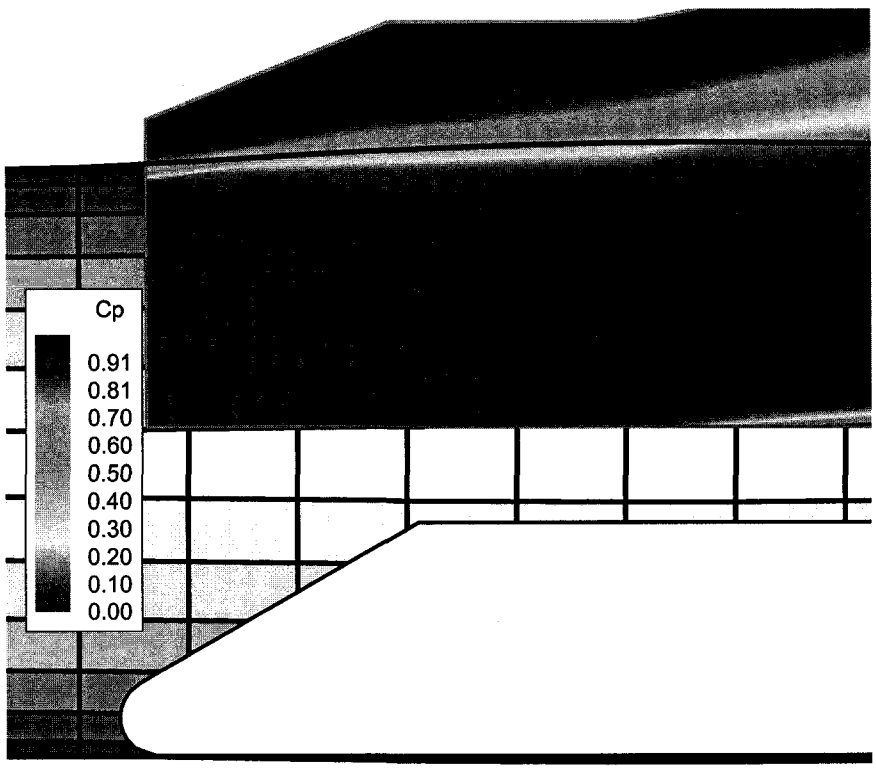

Figure (6-16-b) Predicted and measured boundary deformation, solving test section + collector

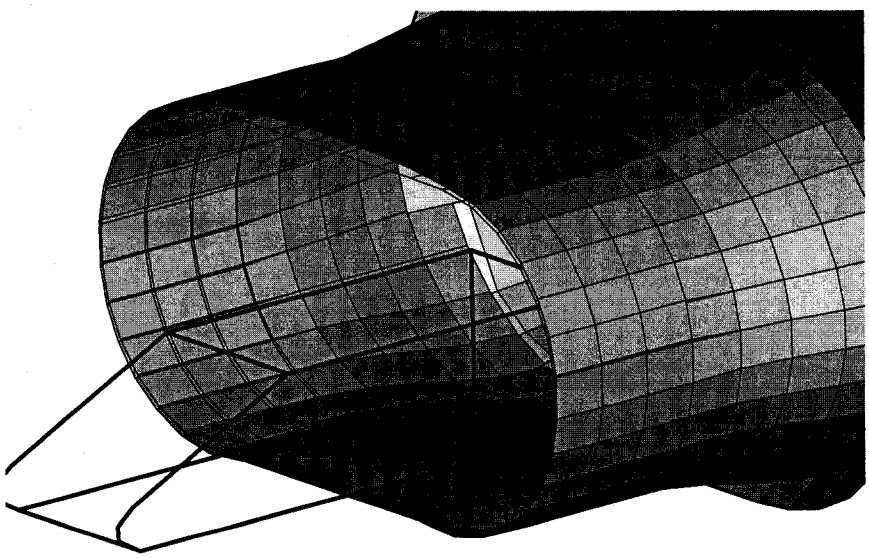

Figure (6-17-a) Predicted boundary deformation, pre-deformed test section I + collector

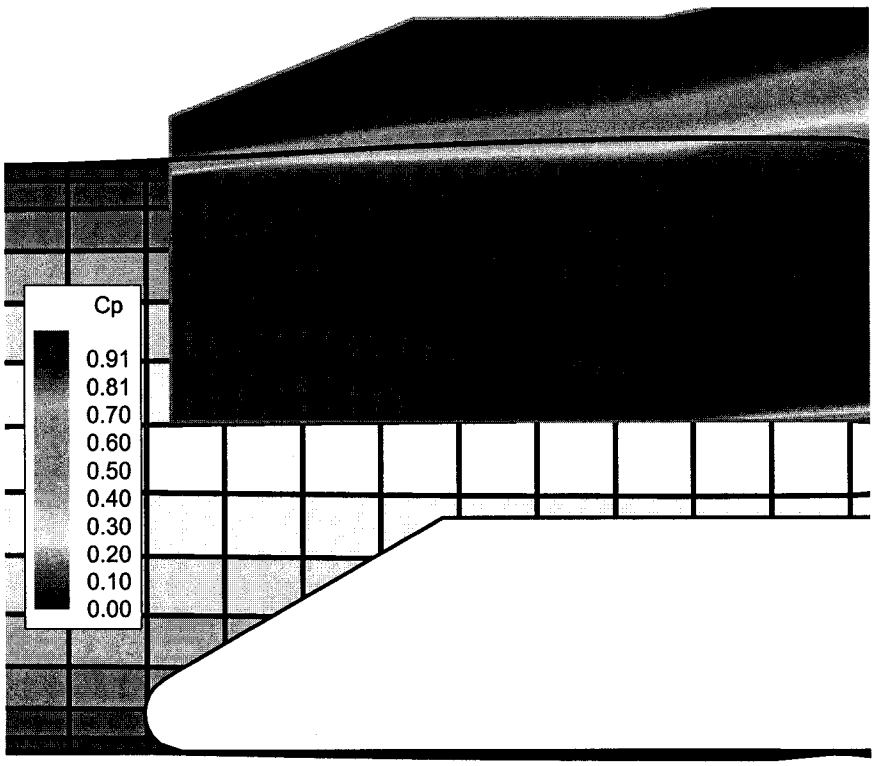

Figure (6-17-b) Predicted and measured boundary deformation, pre-deformed test section I + collector

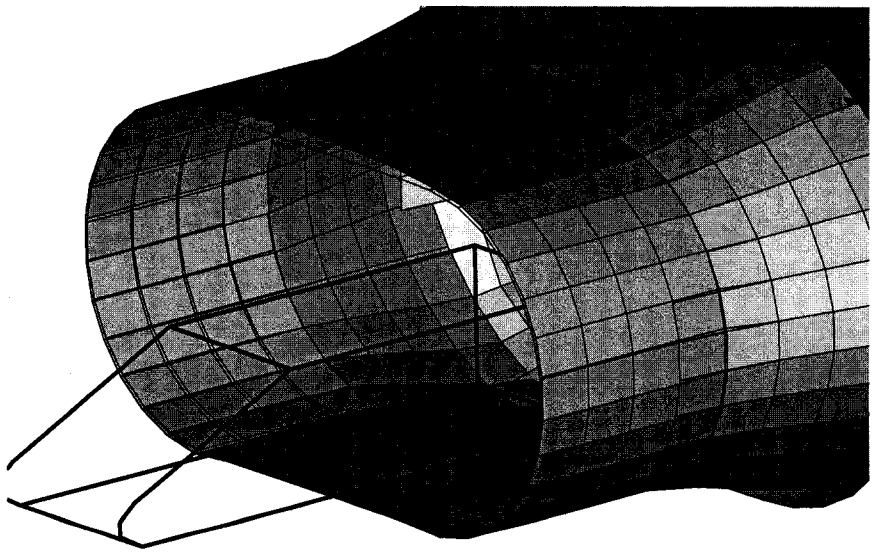

Figure (6-18-a) Predicted boundary deformation, pre-deformed test section II + collector

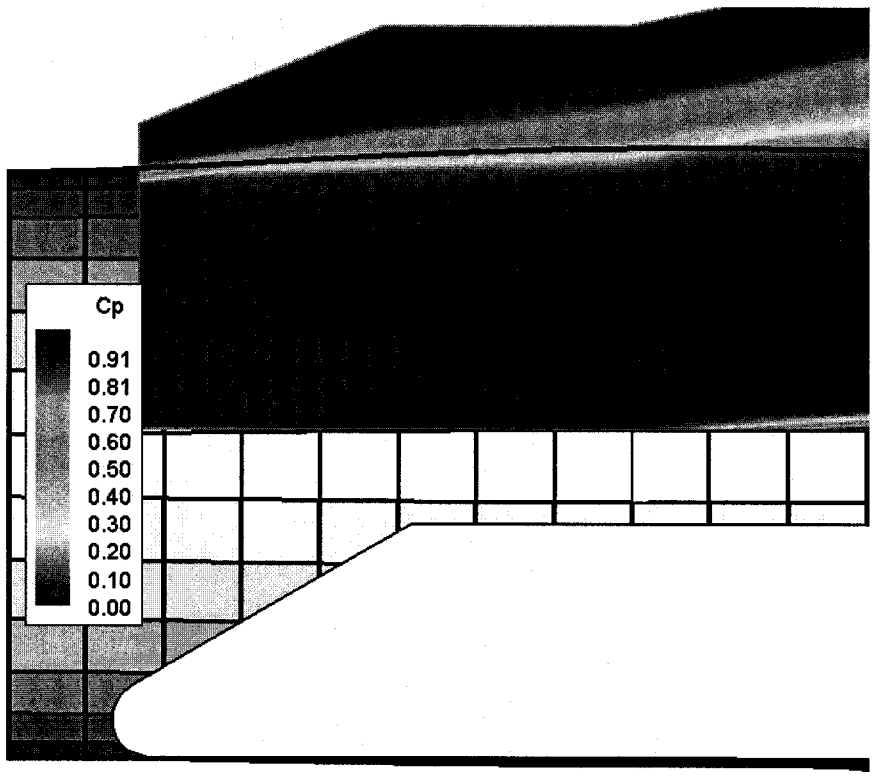

Figure (6-18-b) Predicted and measured boundary deformation, pre-deformed test section II + collector

Figure (6-19) shows the predicted blockage factor distribution on a horizontal plane for the long test section with no collector representation. The blockage factor for the over-expanded jet boundary is negative and has lower values near to the front and the back of the model and a maximum value located near to the midpoint of the vehicle centerline. Its gradient in the lateral direction is smaller than in the downstream direction. It is nearly symmetric in the downstream direction around its maximum value. This case accounts for the jet over-expansion only and will serve as a reference case to study the collector effect.

The predicted blockage factor for the second configuration is shown in Figure (6-20). In this case the collector is represented downstream of the test section with no account for the jet growth or the interaction with the collector entrance. The primary effect on the solution will therefore be the change in duct area and cross-section downstream of the entrance and the imposition of solid boundary conditions. The trend of the distribution very much follows the trend observed in the previous case; however, the maximum blockage decreases about 21% and its location moves toward the front of the car. The largest reduction is near the back of the car and it decreases in the upstream direction. The reason for that is the fact that the solid walls of the collector induce positive blockage, which acts in the opposite direction against the negative blockage induced by the over-expanded test section boundaries.

As discussed in the previous two sections, there is a growth of the test section jet in the downstream direction generated by the air entrained from the plenum chamber which needs to be considered in the panel method. Also as the jet reaches the collector entrance, this entrained air is reflected back to the plenum chamber generating a positive pressure gradient near to the collector, which causes a deformation of the jet boundary. To account for these two factors, the results from the CFD simulation are used to calculate the necessary boundary deformation near the collector. The CFD runs, Figures (6-6) through (6-9), are for empty test section (pre-deformed test section I) and for a test section with 40% blockage ratio model (pre-deformed test section II). These represent approximate upper and lower bounds of the boundary pre-deformation for nearly any model size that

may be tested inside most of the open jet wind tunnels used for external aerodynamic testing. It should be noted that the expansion of the jet well ahead of the collector is not modeled, since the panel method does not specifically account for mass flow entrainment. The jet expansion close to the collector can be regarded as a secondary effect of this entrainment.

Figures (6-21) and (6-22) show the predicted blockage factor for the pre-deformed test section I and pre-deformed test section II cases respectively. Both of them have similar trends of distribution as the previous cases. The jet growth and the pre-deformation near to the collector increase the negative blockage while the solid walls of the collector act in the opposite sense. Also in the second case, pre-deformed test section II, a greater area of the collector is subjected to the flow because the stagnation point, predicted from the CFD simulation, is about 1.0 in farther upstream toward the edge of the collector entrance. This increases the influence of the collector walls.

Combining these factors together helps in understanding the difference between the centerline blockage distributions shown in Figure (6-23). The pre-deformed test section I case includes jet growth and account for the collector walls, so it generates blockage higher than the second case (no jet growth or pre-deformation) and lower than the long test section along most of the car length. The pre-deformed test section II case includes more jet growth, which increases the predicted blockage near to the front of the car. It also has more area of the collector walls, which decreases the blockage near to the back of the car. The maximum values of the blockage factor along the vehicle centerline are summarized in Table (6-1) for the different configurations.

Configuration	**Maximum blockage**	**Downstream location**
Long test section	-0.0492	51.3%
Test section + collector	-0.0385	33.3%
Pre-deformed test section I + collector	-0.0433	32.1%
Pre-deformed test section II + collector	-0.0467	37.9%

Table (6-1) Maximum blockage factors.

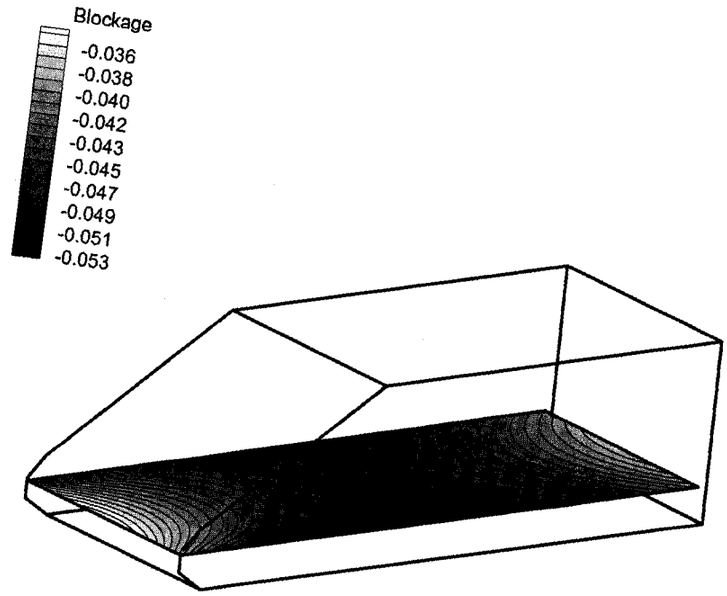

Figure (6-19) Distribution of the blockage interference at a horizontal plane for long test section configuration.

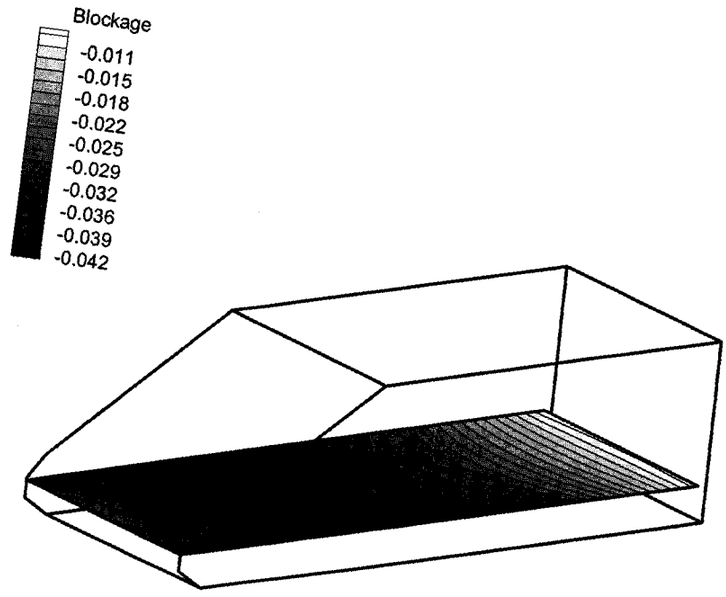

Figure (6-20) Distribution of the blockage interference at a horizontal plane for test section + collector configuration.

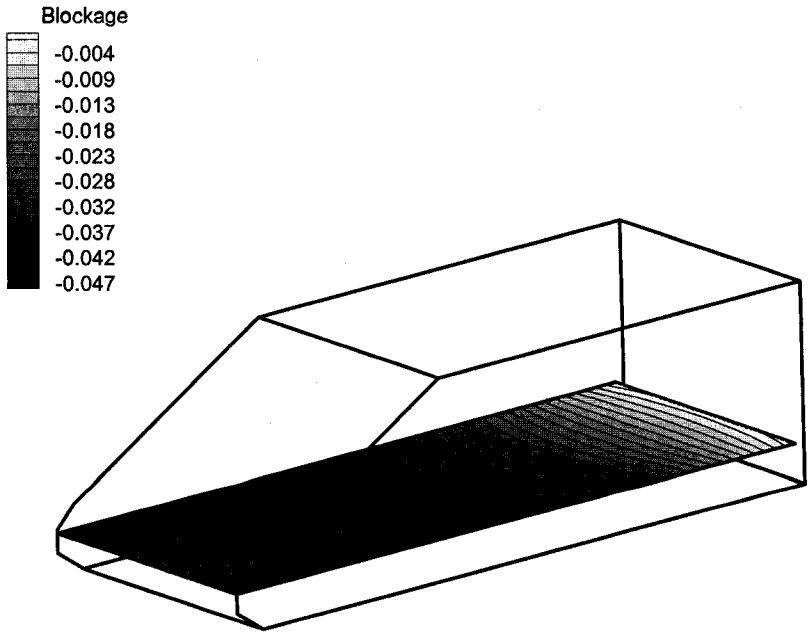

Figure (6-21) Distribution of the blockage interference at a horizontal plane for pre-deformed test section I + collector configuration.

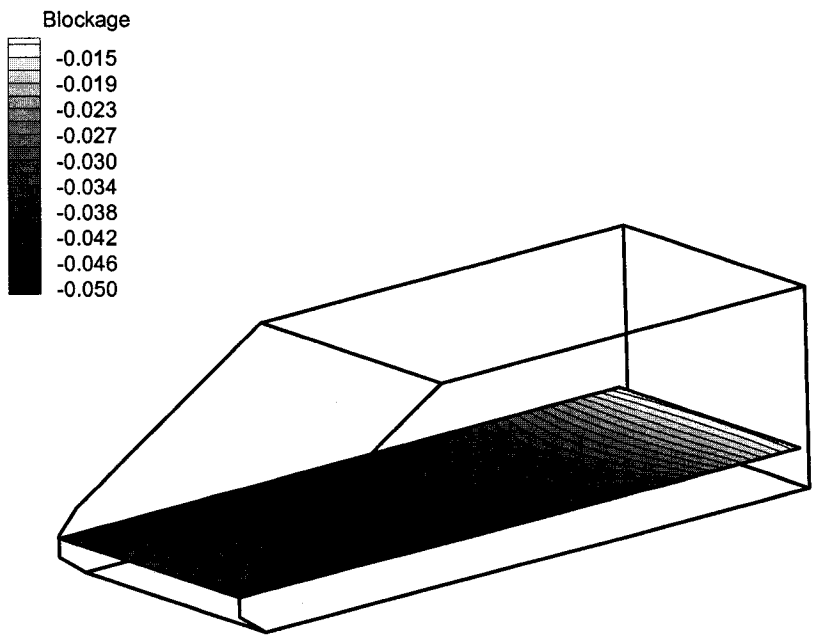

Figure (6-22) Distribution of the blockage interference at a horizontal plane for pre-deformed test section II + collector configuration.

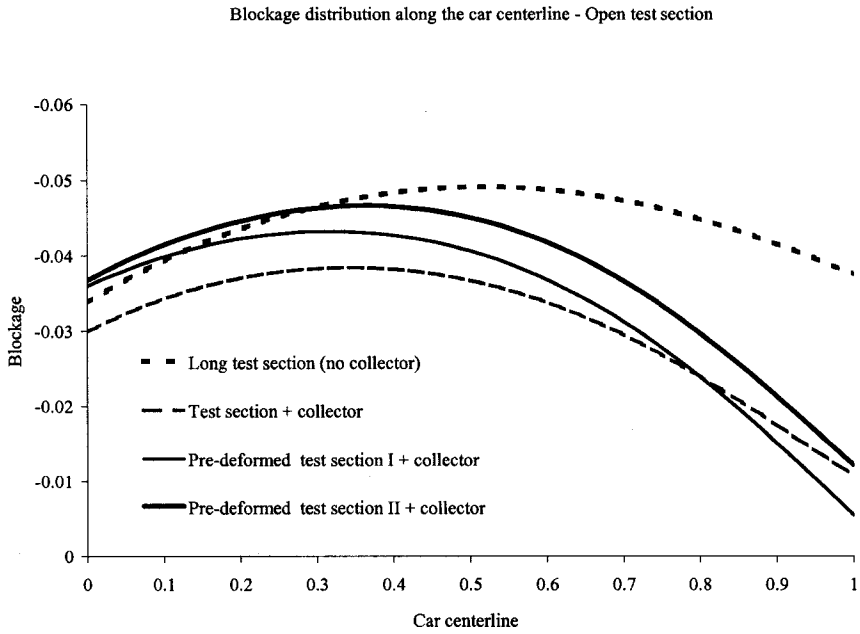

Figure (6-23) Blockage factor along the car centerline.

6.4 Summary

In this chapter, experimental measurements were used to evaluate the boundary deformation predicted by the present method. Fairly good matching was found for several test section configurations solved by the present method. A CFD study is performed to investigate effect the jet/collector interaction and the jet growth. Both effects are due to viscous interaction, which is not included in the panel method used in the present work. Thus a Navier-Stokes solution is needed to capture these flow structures. Results from CFD were used to evaluate the boundary deformation predicted by the present method and to estimate the necessary boundary pre-deformation to represent the jet growth and the jet collector interaction.

The collector effect was studied using four approaches. First a reference case was presented where the wind tunnel was represented using long test section with no collector. Then three levels of approximation were used to represent the collector, the jet

growth and the jet collector interaction. By comparing the four methods introduced to solve the problem, it is clear that it is important to include the pre-deformation (or some equivalent technique) in the panel method to account for both the jet growth and the jet interaction with the collector entrance for such large models. The pre-deformation used in the second case (pre-deformed test section II) is for a 40% blockage ratio model, which is a very high value. For smaller model sizes it might be enough to consider the pre-deformation obtained from the empty test section CFD solution since the difference between the two curves in Figure (6-23) is not very large. It is important to note that the sizes of the models used in this test and in the CFD simulation are well beyond the usual model sizes allowed inside open jet test sections. They are chosen for this study for the purpose of testing the new developed panel method. In practice with smaller models, it might not be necessary to include the pre-deformation.

This automotive application inside the $1/15^{th}$ scale Langley Full Tunnel adds further evidence for the ability of the developed method to correct large model sizes inside a relatively complex test section (with the collector included). The method shows consistent results with applications presented in the previous chapters. The method shows more flexibility and better representation of the real flow inside the test section compared to the methods currently used in automotive wind tunnels.

CHAPTER VII

VII. CONCLUSIONS

A new method to assess the boundary interferences for open jet test sections has been introduced. The main motivation was to overcome some of the limitations in the classical and/or currently used methods for aeronautical and automotive wind tunnels. The key addition in the present technique compared to the others is the specific inclusion of boundary deformation, which is shown to be important under certain circumstances. The starting point was to take advantage of two well-developed approaches used in closed wall test sections, namely the boundary measurements approach and adaptive wall wind tunnels. A low-order panel code was developed because it offers a relatively efficient solution from the computational point of view within the required measurement accuracy. It also gives the method more flexibility to deal with variations in model geometries and test section cross sections. The method was first compared to the classical method of images then used in three tests conducted inside the Langley Full Scale Tunnel, the NASA Langley Research Center 14 by 22 Foot Subsonic Wind Tunnel and the $1/15^{th}$ scale Langley Full Scale Tunnel. Some important conclusions are summarized in this Chapter starting with some statements for the open jet test section boundary interference derived from the parametric analyses performed during the wind tunnel tests presented. Then some general comments about the introduced method compared to the other methods are discussed.

A full matching between the present method and the classical method of images was achieved for lifting and non-lifting model representations inside both closed wall and open jet test sections within the limits of the underlying assumptions of the method of images (small model size relative to test section; long test section with rigid boundaries). In addition, for open jet test sections, comparison was performed for un-deformed and deformed boundaries and it was found that classical method of images matches only the un-deformed boundary cases, as expected. However, for large model sizes, there is a significant difference between the solutions with un-deformed and deformed boundaries.

This difference is not captured by the classical method of images, confirming the importance of including boundary deformation in the interference assessment of open jet test sections in cases where blockage or lift effects are large. In other words, the present method successfully detects the effect of boundary deformation while the classical method of images ignores the effect.

Each one of the three wind tunnel applications focuses on some aspects of the open jet test section boundary interference problem. The objective of the suite of three is to explore both the capabilities of the developed method to handle different problems and to individually explore some of the characteristics of open jet test section interferences. Following are some of the conclusion derived from these applications.

In the Langley Full Scale Tunnel application, the focus was to explore several methods to represent the model (full scale reproduction of the 1903 Wright Flyer replica) and the effect of the different test section boundary configurations. In addition, the large relative model size (large span) together with the very small blockage ratio offers a unique test case for upwash interference assessment using the present method. Good matching between the present method and the classical method of images was found for the closed and the un-deformed-boundary open jet test sections. For the open jet test section with a fully deformed boundary, the classical method of images significantly over-estimated the upwash interference. These two cases for open jet test sections (deformed and un-deformed boundaries) show the limitation of the classical method of images in predicting the correction factors for models with large wingspans and they also show the importance of including boundary deformation in the upwash interference assessment of such cases.

Regarding the model representation approach, the study indicated that the closed test section is less sensitive to the method of model representation while the 3/4-open test section is the most sensitive to it. For aeronautical applications, 3/4-open test sections have the advantage of producing less overall interference because the ground board produces interference with opposite sign to that of the open boundaries. This advantage

does not exist in automotive testing because the ground board is considered a part of the tested model.

The automotive test conducted in the NASA Langley Research Center 14 by 22 Foot Subsonic Wind Tunnel is used to explore the effect of flow upstream to the test section for closed and open jet conditions. It was found that for the studied model blockage ratio (7.4%), it is important to include the effects of the upstream walls either using the real nozzle geometry or by extending the test section. The open jet was less sensitive to the upstream configurations (nozzle or duct), at least for this case. Although these statements are for the studied model size only, it gives an indication of the importance of the upstream configurations for other model sizes. The test also offers a good chance to present a modified version of the developed method because in this application the measured wall pressure signature in the closed wall test configuration was used in developing the model representation. The present method was compared to some of the classical and current methods used in automotive wind tunnels for boundary corrections. It was found that the classical method of images seems to underestimate the correction factors for both closed and open test sections. Currently used methods are typically semi-empirical approaches based on a combination between wind tunnel measurements and a modified version of the classical method of images. Analysis shows that whereas these methods overcame some of the limitations in the classical method of images, such as the model representation, finite test section length and the effect of the nozzle and the collector solid blockage, the model is still simplified to point-singularity representations and the boundary deformation is not included. On the other hand, the present method deals with the real model geometry and specifically includes the boundary deformation in the interference assessment. The comparison study showed that the present method compared acceptably well with methods currently used in automotive wind tunnels boundary corrections and showed some advantages of including the boundary deformation in the interference assessment in certain cases.

The collector effect was studied in the third application during an automotive test inside the $1/15^{th}$ scale Langley Full Scale Tunnel. The model was built and the test was

conducted specifically to support the present study. This is another unique test of the developed method because the model size is very large for external aerodynamic studies (20.6% blockage ratio). The study confirmed the crucial role of the collector especially for such a large model. Also the measured boundary deformation compared acceptably well with the predicted ones calculated using the developed method.

In conclusion, the developed method showed reliability when compared directly to the classical method of images. It offers the advantage of explicitly including the boundary deformation, which was shown to be important in certain cases. It has enough flexibility to solve both aeronautical and automotive models and arbitrary test section configurations with enough computational efficiency. Finally, it is important to acknowledge that there are some aspects of open jet test section boundary interference not accounted for in the developed method. Some future work will still be needed to explore these other effects. The following chapter summarizes some of these possible research topics.

CHAPTER VIII

VIII. FUTURE WORK

"*The subject of wall interference dates back over 75 years. Developments in understanding and in methodology of applying wall corrections have more or less kept pace with progress in developmental testing of aircraft to the point that wind tunnel testing programs, in general, have not come to grief for want of better methods. The future is changing and, as competition heightens the need for higher quality data to reduce uncertainty, we discover more and more that wind tunnels are indeed difficult things. This is practically true when testing models of large size.*", Steinle et al[62]

The above statement was present in the conclusions of AGARDograph 336 which summarized the methods used for wind tunnel corrections, focusing mainly on aeronautical applications. The present method addresses the problem of large models and how the corrections can be improved by including the boundary deformation in the assessment procedures. However, the topic is not yet closed, especially with the use of open jet test sections in automotive wind tunnels. The present method can be considered one step along the road and more research is still needed. In this section, some of the future work and recommendations are summarized.

Considering the theoretical bases of the methods, linear theory showed success in developing correction methods for both closed and open jet test sections. As the need to improve the accuracy of the measurements and to capture more details of the flow inside the wind tunnel increases, advanced methods appear to be required. Several levels of approximation can be employed depending on the desired computational efficiency, such as full potential flow solvers, Euler equation solvers with and without boundary layer representation, and thin layer or full Navier-Stokes equation solvers.

Now turning to the open jet test section problem, for aeronautical applications support interference in some applications plays an important roll in the boundary interference and

has to be well represented in the correction method. Support stings or struts look like a model to the test section boundaries and to obtain interference-free results, the effects of the support mechanism have to be corrected. In addition, viscous wakes of the struts complicate the computational problem. Panel methods have shown some success in solving this problem by predicting the support and the boundary interferences and correcting the results for each of them separately. An integrated approach, where both effects can be included in one correction step and accounts for the interaction between them, would be a good advance.

Some challenging problems still exist, such as the unsteadiness of the flow near to the collector entrance. High-lift testing is also one of the challenges where the inclusion of the viscous effect is crucial. CFD (Navier-Stokes) methods are good alternatives; however, the turbulence modeling is a limiting factor.

For the use of open jet test sections in automotive wind tunnels, the problem includes other details, for example: moving and fixed grounds, boundary layer treatment upstream to the model and its effect on the test section pressure gradients, and full modeling of the jet growth and jet/collector interaction. Again most of these effects need a method that includes the viscous effect. CFD is a good candidate but turbulence modeling is also a limitation.

Finally, the computational efficiency of the method is another challenge. Online corrections where the method is fast enough to correct the wind tunnel conditions during the test (point-by-point in quasi real-time) is desired. Very fast corrections may be required if the correction procedure is integral to the tunnel set-point control. Currently most of the methods that meet this requirement are based on empirical approaches. Future work could improve the computational efficiency of one of the advanced numerical methods (CFD) to obtain the corrections factors during the test and correct the wind tunnel conditions in real-time.

REFERENCES

1. Glauert, H., "The elements of aerofoil and airscrew theory" Cambridge science classics, Chapter XIV, pp 189-198, 1926.
2. Theodoresen, T., "The theory of wind-tunnel wall interference" NACA Report No 410, pp 219-227, 1931.
3. Krynytzky, A. and Ewald, B., "Conventional wall correction for closed and open test sections", AGARD, AG-336, pp 2.1-2.66, 1998.
4. Ashill, P., "Boundary-flow measurements methods for wall interference assessment and correction- classifications and review" AGARD CP-535, pp 12.1-12.21, 1994.
5. Ashill, P., Hackett, J. E., Mokry, M. and Steinle, F., "Boundary-flow measurements methods" AGARD AG-336, pp 4.1-4.61, 1998.
6. Hackett, J., "Tunnel-induced gradients and their effect on drag" AIAA Journal, vol. 34, no. 12, pp 2575-2581, 1996.
7. Hackett, J. and Wilsden, D., "Determination of low speed blockage corrections via tunnel wall static pressure measurements" AGARD-CP-174, pp 22.1-22.9, 1976.
8. Britcher, C. and Mokhtar, W. "Comparison of aerodynamic measurements on a full-scale NASCAR in open and closed-jet test sections", presented at the SAE World Congress, SAE paper no 2005-01-0548, published at the Vehicle Aerodynamics SAE Transaction: SP-1931, April 2005 and SAE Transactions Journal of Passenger Cars – Mechanical systems, March 2006.
9. Rizk, M and Smithmeyer, M, "Wind-tunnel wall interference corrections for three-dimensional flows", J. Aircraft, vol. 19, no. 6, pp 465-472, 1982.
10. Iyer, V, Kuhl, D and Walker, E, "Wall interference study of the NTF slotted tunnel using bodies of revolution wall signature data", AIAA 24th Aerodynamic Measurement Technology and Ground Testing Conference, AIAA paper no. 2004-2306, June 2004.
11. Ulbrich, N and Boone, A, "Real-time wall interference correction system of the 12 ft pressure wind tunnel", AIAA 36th Aerospace Science Meeting and Exhibit, AIAA paper no. 98-0707, Jan 1998.

12. Wedemeyer, E., Taylor, N. and Holst, H., "Adaptive wall techniques", AGARD, AG-336, pp 10.1-10.48, 1998.
13. Mokry, M., (Editor), "Limits of adaptation, residual interference", AGARD, AR-269, pp 66-90, 1990.
14. Goodyer, M., (Editor), "The aims and history of adaptive wall wind tunnels", AGARD, CP-269, pp 1-7, 1990.
15. Goodyer, M, "A low speed self streamlining wind tunnel", AGARD, CP-174, pp 13.1-13.8, 1976.
16. Erickson, J., (Editor), "Streamlining algorithms for complete adaptation", AGARD, CP-269, pp 21-41, 1990.
17. Wolf, S., "Adaptive wall technology for improved wind tunnel testing techniques – a review", Progress in Aerospace Sciences, no. 31, pp. 85-136, 1995.
18. Meyer, O. and Nitsche, W. "Update on progress in adaptive wind tunnel wall technology", Progress in Aerospace Sciences, no. 40, pp. 119-141, 2004.
19. Wolf, S and Goodyer, M., "Predictive wall adjustment strategy for two-dimensional flexible walled adaptive wind tunnel – A detailed description of the first one-step method", NASA, CR – 181635, 1988.
20. Ladson, C., (Editor), "Adaptive wind tunnels walls: technology & application – facilities", AGARD, CP-269, pp 8-20, 1990.
21. Bottin, B., Carbonaro, M. and Schroder, W., "First runs of the adaptive wind tunnel T'3 at VKI: calibration and application of a flexible wall adaptation technique on NACA0012 airfoil", 4th Belgian Congress on Theoretical and Applied Mechanics, Leuven, Belgium, May, 1997.
22. Russo, G., Zuppardi, G. and Basciani, M., "Adaptive wind tunnel walls vs. wall interference correction methods in 2D flows at high blockage ratios", AGARD, CP-535, July, 1994.
23. Mineck, R., "Comparison of a two-dimensional adaptive-wall technique with analytical wall interference correction techniques", NASA TP-3132, April, 1992.
24. Mokry, M. and Ohman, L., "Application of Fast Fourier Transform to two-dimensional wind tunnel wall interference", J. Aircraft, vol. 17, no. 6, pp 402-408, 1980.

25. Hauxing, L., Jiaju, H. and Peichu, Z., "A further study on adaptive wall strategy for half model testing", AIAA-95-1903-CP, pp 1150-1158, 1995.
26. Joppa, R., "A method of calculating wind tunnel interference factor for tunnels of arbitrary cross section", NASA CR-845, 1967.
27. Holt, D. and Hunt, B., "The use of panel method for the evaluation of subsonic wall interference", AGARD, CP-335, pp 2.1-2.16, 1982.
28. Lee, K., "Numerical simulation of the wind tunnel environment by a panel method", AIAA J., vol. 19, no. 4, pp 470-475, 1981.
29. Mokry, M., "Wall interference correction to drag measurements in automotive wind tunnels", J. Wind Engineering. Industrial. Aerodynamics, Elsevier, no. 56, pp 107-122, 1995.
30. Ulbrich, N., "Determination of a rolling moment coefficient correction due to wall interference effects", AIAA 43rd Aerospace Science Meeting and Exhibit, AIAA paper no. 2005-0904, Jan 2005.
31. Mokry, M., Digney, J. and Poole, R., "Double-panel method for half-model wind tunnel corrections", J. Aircraft, vol. 24, no. 5, pp 322-327, 1987.
32. Qian, X. and Lo, C., "Two-variable method for blockage wall interference in a circular tunnel", J. Aircraft, vol. 31, no. 5, pp 1130-1134, 1994.
33. Qian, X, "A study of wind tunnel aerodynamic data correction with panel method and two-variable method", PhD dissertation, University of Tennessee, Knoxville, Dec. 1994.
34. Glazkov, S., Gorbushin, A., Ivanov, A. and Semenov, "Recent experience in improving the accuracy of wall interference corrections in TsAGI T-128 wind tunnel", Progress in Aerospace Sciences, 37, pp 263-298, 2001.
35. Hackett, J, "Recent developments in the calculation of low-speed solid-walled tunnel wall interference in tests on large models Part I: evaluation of three interference assessment methods", Progress in Aerospace Sciences, 39, pp 537-583, 2003.
36. Hsing, C. and Lan, C., "Low speed wall interference assessment/correction with vortex flow effect." J. Aircraft, Vol. 34, No. 2, pp220-227, 1997.

37. Lomobardi, G., Salvetti, M. V. and Moerlli, M., "Correction of wall interference in wind tunnels: A numerical investigation." J. Aircraft, Vol. 38, No. 5, pp944-949, 1997.
38. Lessard, W., "Analysis of post-support and wind tunnel wall interference on flow field about subsonic high-lift high-speed research configuration", NASA/TP-2000-210555, November 2000.
39. SAE international, "Aerodynamic testing of road vehicle in open jet wind tunnel", SP-1465, 1999.
40. SAE international, "Aerodynamic testing of road vehicles – open throat wind tunnel adjustment", SAE surface vehicle information report J2071, Society of Automotive Engineering, Warrendale, PA, USA 1994.
41. Wickern, G, "On the application of classical wind tunnel corrections for automotive bodies", SAE 2001-01-0633, Society of Automotive Engineering, Detroit, MI, USA, 2001.
42. Mercker, E. and Wiedemann, J., "On the correction of interference effects in open jet wind tunnels" SAE 96061, Society of Automotive Engineering, Detroit, MI, USA, 1996.
43. Mercker, E., Wickern, G. and Wiedemann, J., "Views on nozzle interference effect in open jet wind tunnels" SAE 970136, Society of Automotive Engineering, Detroit, MI, USA, 1997.
44. Wickern, G. and Schwartekopp, B., "Correction of nozzle gradient effect in open jet wind tunnels" SAE 2004-01-0669, Society of Automotive Engineering, Detroit, MI, USA, March 2004.
45. Wiedemann, J., Fischer, O. and Jiabin, P., "Further investigation on gradient effects" SAE 2004-01-0670, Society of Automotive Engineering, Detroit, MI, USA, March 2004.
46. Mercker, E., Cooper, K., Fischer, O. and Wiedemann, J., "The influence of a horizontal pressure distribution on aerodynamic drag in open and closed wind tunnels" SAE 2005-01-0867, Society of Automotive Engineering, Detroit, MI, USA, April 2005.

47. Hoffman, J., Martindale, B., Arnette, S., Williams, J. and Wallis, S., "Effect of test section configuration on aerodynamic drag measurements", SAE 2001-01-0631, Society of Automotive Engineering, Detroit, MI, USA, March 2001.
48. Hoffman, J., Martindale, B., Arnette, S., Williams, J. and Wallis, S., "Development of lift and drag corrections for open jet wind tunnel tests for an extended range of vehicle shapes", SAE 2003-01-0934, Society of Automotive Engineering, Detroit, MI, USA, March 2003.
49. Mercker, E. and Cooper, K."A two-measurement correction for the effects of pressure gradient on automotive, open jet, wind tunnel measurements" SAE 2006-01-0568, Society of Automotive Engineering, Detroit, MI, USA, April 2006.
50. Mokry, M., "Assessment of boundary interference in open test section wind tunnels using successive over-relaxation", AIAA 43rd Aerospace Science Meeting and Exhibit, AIAA paper no. 2005-0906, Jan 2005.
51. Katz, J. and Plotkin, A., "Low-speed aerodynamics", Cambridge University Press, 2nd Edition, 2001.
52. Hess, J. and Smith, A., "Calculation of potential flow about arbitrary bodies", Progress in Aeronautical Science, Vol. 8, pp. 1-138, 1967.
53. Barlow, J., Rae, W., Pope, A. "Low speed wind tunnel testing", 3rd edition, Wiley, 1999.
54. Britcher, C, Landman, D, Ash, R and Hyde, K, "Predicted flight performance of the Wright "Flyer" based on full-scale tunnel data", 42nd AIAA Aerospace Sciences Meeting and Exhibit, AIAA Paper 2004-104, Jan 2004.
55. Kochersberger, K, Britcher, C, Crabill, N, Player, J. and Hyde, K, "Flying qualities of the Wright 1903 Flyer: from simulation to flight test", 42nd AIAA Aerospace Sciences Meeting and Exhibit, AIAA Paper 2004-105, Jan 2004.
56. Cherne, J, Culick, F and Zell, P, "The AIAA 1903 Wright 'Flyer' project prior to full-scale tests at NASA Ames research center", AIAA 38th Aerospace Science Meeting, AIAA paper no. 2000-0511, Jan 2000.
57. Cooper, K, "Bluff-body blockage correction in closed and open test section wind tunnels", AGARD, AG-336, pp 6.1-6.33, 1998.

58. Gentry, G.L.; Quinto, P.F.; Gatlin, G.M.; Applin, Z.T.: The Langley 14- by 22-foot Subsonic Wind Tunnel: Description, Flow Characteristics and Guide for Users. NASA TP-3008, September 1990

59. Krist, S., Biedron, A. and Rumsey, C., "CFL3D user's manual (Version 5.0)", NASA TM-1998-208444, 1998.

60. Roe, P., "Approximate Riemann solvers, parameter vectors, and difference schemes," J. Computational Physics, Vol. 43, 1981.

61. Menter, F.R., "Zonal two equation k-w turbulence models for aerodynamic flows", AIAA Paper 93-2906, 1993.

62. Steinle, F., Crites, R., Krynytzky, A., and Binion, T. "Wind tunnel wall corrections – future necessary work", AGARD, AG-336, pp 12.1-12.25, 1998

VITA

Wael Ahmed Mokhtar
Department of Aerospace Engineering, Old Dominion University, Norfolk, VA, 23529

Education

Ph.D. May 2006, Old Dominion University, VA.

B.S. July 1994, M.S. May 2001, Alexandria University, Egypt

Professional experience

Assistant professor: August 2005-present, Lake Superior State University, MI.

Graduate research assistant: May 2001-August 2005, Old Dominion University, VA.

Graduate teaching assistant: February 1997-May 2001, Alexandria University, Egypt.

Graduate teaching assistant: March 1996-February 1997, Asuit University, Egypt.

Relevant publications

Wael A. Mokhtar and Colin P. Britcher, "Boundary Distortion and Interference of Open Jet Test Sections", AIAA 25th Aerodynamics Measurements Technology and Ground Testing Conference, AIAA paper no. 2006-3641, June 2006.

Wael A. Mokhtar and Colin P. Britcher, "Wind Tunnel Boundary Corrections for a Full Scale 1903 Wright Flyer Replica." AIAA Journal of Aircraft, vol. 43, no. 1, pp. 64-71, 2006.

Colin P. Britcher and Wael A. Mokhtar "Comparison of Aerodynamic Measurements on a Full-Scale NASCAR in Open and Closed-Jet Test Sections", SAE World Congress, SAE paper no 2005-01-0871, Vehicle Aerodynamics SAE transaction: SP-1931, pp: 203-213, April 2005, SAE transaction journal of passenger car, March 2006.

Wael A. Mokhtar and Colin P. Britcher, "Study of Real Time Wind Tunnel Boundary Corrections Using Panel and Pressure Signature Methods", AIAA 43rd Aerospace Science Meeting and Exhibit, AIAA paper no. 2005-905, Jan 2005.

Wael A. Mokhtar and Colin P. Britcher, "Wind Tunnel Boundary Corrections for a Full Scale 1903 Wright Flyer Replica", AIAA 24th Aerodynamics Measurements Technology and Ground Testing Conference, AIAA paper no. 2004-2309, June 2004.

Wael A. Mokhtar and Colin P. Britcher, "Boundary Interference Assessment and Correction for Open Test Section Wind Tunnels Using Panel Methods", AIAA 42nd Aerospace Science Meeting and Exhibit, AIAA paper no. 2004-609, Jan 2004.